Superconducting quantum circuits for hybrid architectures

Zur Erlangung des akademischen Grades eines
DOKTORS DER NATURWISSENSCHAFTEN
von der KIT-Fakultät für Physik des
Karlsruher Instituts für Technologie (KIT)

genehmigte
Dissertation
von

M. Sc. Patrick Winkel

Tag der mündlichen Prüfung:	03. Juli 2020
Referent:	Prof. Dr. Wolfgang Wernsdorfer
Korreferent:	Prof. Dr. Gerhard Kirchmair
Betreuer:	Dr. Ioan M. Pop

Contents

1 Introduction

Discovering and unveiling the unknown has ever since been an important, maybe the most important driving force behind human endeavor. In the world of physics, understanding the fundamental principles that govern the dynamics of the world surrounding us, on the small as well as on the large scale, is certainly one of the greatest unknowns. The tools used by generations of scientists to disclose nature's secrets have evolved during the centuries alongside with the sophistication of the faced questions, from simple mechanical machinery like slide rules, to complex and powerful electrical machinery like supercomputers. Science and technology have stimulated each other ever since, and by that, have changed and improved human lives on a global scale. During the last century, a new phenotype was added to the collection of tools available for humankind, summarized under the term quantum technologies.

In quantum technologies, our developed understanding of nature within the framework of quantum mechanics [63] is translated into new applications, directed towards the substitution of classical technology with better performing quantum devices, for instance in medical surgery [84], or the development of fundamentally new concepts utilizing unique quantum phenomena like quantum entanglement [14, 100, 102, 200], quantum superposition [199], and quantum tunneling [35, 146]. New technology branches arising from these phenomena are quantum sensing [1, 72], quantum computing [17, 73, 137], and quantum communication [18, 65, 69, 82, 112].

The technological prerequisit for the implementation and operation of quantum technologies is the preparation, control and readout of a quantum state $|\Psi\rangle$ stored in a specifically engineered hardware. Although designed for the same conceptual purpose, the physical systems used for the implementation of such quantum platforms are manifold, and range from microscopic systems like individual electron spins in silicon [109, 139, 159, 223] and quantum dots [70, 96, 104, 175], magnetic molecules [5, 28, 83, 132, 205, 213], ultracold atoms [88], trapped ions [16, 25, 26, 44, 130], nitrogen-vacancies in diamonds [66, 95], and polarized photons [115, 176], as well as macroscopic systems like superconducting quantum circuits [42, 116, 148, 149, 166]. Similar to natural atoms, the quantum hardware is associated with a discrete energy spectrum, but require different conditions for their operation, for instance in terms of the ambient temperature. Despite a myriad of promising theoretical ideas, exploiting the full potential of quantum hardware constitutes an immense technological challenge. A major task remains the preservation of quantum coherence, meaning that the time evolution of the prepared quantum state is known and predictable, while allowing for a fast manipulation and detection of the quantum state at the same time.

Superconducting quantum circuits [45, 58, 59, 121] (SQCs) are among the most versatile quantum hardware platforms as they offer a unique degree of freedom and control in shaping the energy spectrum of the system. Successfully realized applications range from particle detection [50, 182] to low-loss amplification [38, 212, 233, 235] to the storage and processing of quantum information. Especially the latter two constitute fundamental building blocks on the road map of quantum sensing and quantum computing with superconducting circuits. In 2019, the first programmable superconducting quantum processor has achieved quantum supremacy — the demonstration of a calculation performed on a quantum device which wouldn’t have been feasible on a classical computer [6]. At the core of SQCs are low-loss and nonlinear microwave circuits built from superconducting materials, which, determined by their shape, host collective oscillations of the superconducting condensate in the low gigahertz regime. Despite the macroscopic scale of SQCs not uncommonly spanning over hundreds of micrometers or even millimeters, in combination with the large number of particles participating in the collective motion, the dynamics of such circuits can still be described by effective circuit models with only a small number of quantum degrees of freedom (DOF). The elementary building blocks of these models are capacitors, resistors, as well as linear and nonlinear inductors. The properties of a circuit are controlled by connecting different circuit elements to an electrical network, similar to classical integrated circuits, with the DOF being related to the oscillating currents and voltages.

Similar to the position and momentum coordinate of a quantum particle, the quantum nature of a circuit with a single DOF manifests in the relation between current and voltage, which become conjugate variables in the quantum mechanical sense, and cannot be measured with infinite precision at the same time. As a consequence, the energy spectra of SQCs are discrete, with the spacing between neighboring energy levels typically on the order of a few gigahertz, with some remarkable exceptions [237]. Transitions between the different eigenstates are induced by the application of propagating microwave photons of similar energy. Since current and voltage are ultimately linked to the electromagnetic fields, the oscillations of the condensate can be thought of as stationary microwave photons. Therefore, nonlinear circuits for which transitions can be addressed individually are referred to as artificial atoms.

A common property of natural and artificial atoms is the anharmonicity of the energy spectrum, implying that consecutive transitions are not of the same energy. In the context of quantum computing, separating two states from the infinite Hilbert space to form a quantum two-level system — a quantum bit or qubit — is one of the main challenges. The key element to engineer the energy spectrum is the Josephson junction (JJ) [108]. A typical JJ is implemented by a tunneling contact between two superconducting electrodes, which are separated by a thin insulating barrier. Since charges tunnel only in discrete numbers across the barrier, the action of a JJ placed inside a circuit is that of a nonlinear inductor. The corresponding inductance is referred to as kinetic inductance, as the presence of the tunneling barrier enhances the inertia of the superconducting condensate. A similar effect can be obtained in disordered superconductors with high normal-state resisitivity, enabling to build compact circuits with high impedance [91, 148, 210].

Owing to the macroscopic size, SQCs couple to uncontrolled mesoscopic systems that degrade the coherence of the circuit [114, 131, 135, 195, 203]. Although many mesoscopic systems have been identified during the last decades, ranging from defects in interfaces [135, 163], adsorbates and organic residuals from the fabrication process [51], non-equilibrium, collective excitations of the superconducting ground state [56, 180, 188, 227], denoted quasiparticles, and magnetic vortices [211], successfully mitigating them is considerably more difficult. A substantial effort is invested into material science and new qubit concepts less susceptible to such disturbances [180], and the development of quantum error correction schemes [12, 36, 110, 170, 187].

Another very interesting approach is to combine different quantum degrees of freedom in a hybrid architecture [232]. As most quantum degrees of freedom have rather distinct advantages and disadvantages, in the ideal case, combinations of these systems acquire the advantages, while discarding the disadvantages of the underlying subsystems. Recent examples for such fruitful marriages are hybrid systems of SQCs and magnetic molecules [22, 23, 83], and SQCs and semi-conducting spin qubits [154, 194]. The benefits of SQCs are their fast and precise control, as well as their ability to couple to other quantum system via the electrical and the magnetic field.

In many hybrid architectures, the counterparts of SQCs require the application of strong external magnetic fields on the order of several tens to hundreds of millitesla [23, 194]. Although superconducting materials which are able to sustain these fields are known and frequently used for the implementation of SQCs, in the vast majority of circuits, the nonlinear elements are still Josephson tunnel junctions made from thin film aluminum. The main disadvantage of such conventional JJs are interference effects occurring inside the tunnel junction in external magnetic fields, similar to the interference pattern of an optical single slit experiment, which cause the suppression of the JJ's critical current with field [196]. For that reason, a new type of nonlinear element is required in the context of hybrid systems, an element that offers enough nonlinearity to realize a sufficiently anharmonic energy spectrum for the implementation of qubits, but which can sustain external magnetic fields at the same time.

In the scope of my thesis, I investigated the applicability of granular aluminum (grAl) [54] for the implementation of superconducting qubits designed for hybrid architectures. Granular aluminum is a member of the class of granular superconductors and exhibits a superconductor-to-insulator transition as the resistivity of the material is increased [133, 181], and is particularly interesting for the application in hybrid system due to its large critical field [29, 43, 47, 53]. The microstructure of grAl films is composed of similarly sized crystalline aluminum grains [55], with diameters on the order of a few nanometers, which are embedded into an insulating, non-stoichiometric aluminum-oxide matrix. Therefore, the circuit quantum electrodynamcs of grAl resonators can be described as an effective array of Josephson junctions [144, 172], and in analogy to conventional Josephson junction arrays, the grAl film gives rise to a nonlinear kinetic inductance, which is controlled by the resistivity of the material and the film dimensions. For the purpose of my study, I substituted the conventional Josephson tunnel junction in a superconducting transmon qubit [116] with a small volume of grAl [230]. By measuring the resonance fluorescence response of the *granular aluminum transmon* in spectroscopy and time-domain, the properties of the film and the circuit were characterized, in particular in terms of the microwave losses in external magnetic fields, the quantum coherence, and the obtained nonlinearity.

For the purpose of improving the signal-to-noise ratio (SNR) of the measurement setup and to reduce the required measurement time, a low-loss Josephson parametric amplifier (JPA) was developed additionally. In a typical SQCs setup, several amplifier stages are required to elevate the signal strength to a level detectable at room temperature. Although each amplifier inherently degrades the SNR by adding noise to the signal, the total SNR of the measurement setup is dominated by the first stage, if signal and noise incident to the first amplifier are sufficiently amplified. JPAs have repeatedly proven to reach the quantum limit of added noise, the fundamental lower bound on the added noise as determined by the principles of quantum mechanics [40].

The presented JPA concept is based on long Josephson junction arrays, which are engineered to allow for non-degenerate parametric amplification with pairs of eigenmodes, denoted dimers. Therefore, the device is referred to as the *dimer Josephson junction array amplifier* (DJJAA) [231]. The key features of the DJJAA concept are the potentially large operational bandwidth due to the use of different dimers of the same device in adjacent frequency domains, and the saturation power offered by the use of long JJ arrays. The implementation of the DJJAA concept is demonstrated on several devices, all fabricated based on a simple and cheap optical-lithography process, which were characterized in spectroscopy and time-domain. For one device, the measurement efficiency of the experimental setup — the measure on how close our setup approaches the quantum limit — was calibrated with the aid of a transmon qubit.

The thesis is organized as follows: First, an introduction into the main concepts of superconducting quantum circuits and their mathematical description is given, followed by a section summarizing the demands on SQCs for hybrid systems, and the amenities offered by superconducting granular aluminum. The introductory part is concluded with a discussion about the requirements and the working principle of superconducting parametric amplifiers. In chapter 2 and 3, the main results obtained on the granular aluminum transmon and the dimer Josephson junction array amplifiers are reported. The main part of the thesis is completed with a conclusion and an outlook. For all main chapters, additional information is provided in corresponding appendices.

1.1 Superconducting quantum circuits

Superconducting quantum circuits are electrical networks composed of linear and nonlinear circuit elements, deliberately connected to form artificial media for microwave quantum electrodynamics. Because three different fields find application in the same context, there are three different perspectives on the same physical system: the solid-state perspective, the (quantum) electrical engineer perspective, and the quantum optics perspective. While the first perspective is helpful for a better understanding on a microscopic level, the second perspective is useful for the designing process of devices and the development of new concepts on a higher level, and the third perspective is particularly convenient to describe the interaction between propagating and stationary electromagnetic fields used for manipulation, storage, and readout.

The solid-state perspective

On a microscopic scale, the properties of a superconducting quantum circuit reflect the properties of the charge carriers in the superconductor, particularly the properties of their collective motion. In a conventional (metallic) superconductor, and according to the Bardeen-Cooper-Schrieffer (BCS) theory [10], the electrons condensate into Cooper pairs, which occupy a common ground state. The collection of Cooper pairs is referred to as the superconducting condensate, and its ground state is described by a macroscopic complex wavefunction, whose amplitude is related to the number of Cooper pairs, while its phase reflects the phase coherence between the electronic states on a macroscopic scale. In a superconductor, the corresponding Cooper pair number operator $\hat{N}$ and the phase operator $\hat{\varphi}$ are conjugate variables with a non-zero commutation relation

$$[\hat{N}, \hat{\varphi}] = -i. \tag{1.1}$$

Consequently, they underlie the uncertainty principle similar to the position and momentum coordinates of the electrons in the potential of a natural atom. However, the fluctuations of these two quantities are not predetermined by natural constants, but are controlled by the shape and the material properties of the superconductor, which is one of the main reasons for the immense versatility of superconducting quantum circuits.

The electrical engineering perspective

In quantum circuit theory, the shape and the material properties of the superconductor are mapped onto an effective circuit model, and the collective motion of the Cooper pairs is described by the currents and voltages through and across the circuit elements. Although many particles participate in the collective motion, the properties of the system are described by a small set of degrees of freedom (DOF). For linear circuits, there is a one-to-one correspondence between the quantum circuit and its classical equivalent. Finding the (independent) DOF of a circuit based on the circuit topology is the subject of the circuit quantization. Since the currents and voltages are ultimately related to the Cooper pair number and the macroscopic phase, they are conjugate variables in the same quantum mechanical sense, and the resulting energy spectrum of the circuits is discrete.

The quantum optics perspective

Driving transitions between the energy levels of the circuit corresponds to the manipulation of the quantum state stored in the circuit, and is performed by the application of propagating microwave photons. In contrast to quantum optics, the propagating microwave photons are guided to the system through coaxial cables and eventually interact with the collective oscillation inside the superconductor via their electrical or magnetic field. For that reason, a useful analogy is to consider the collective plasma oscillation hosted by the circuit as a stationary microwave photon, similar to the electromagnetic field confined between the two concave mirrors of an optical cavity. Hence, the exchange of information between the system and its environment is described by the exchange of microwave photons.

In the following, I will further illustrate the relation between the different perspectives with the aid of the quantum harmonic oscillator.

1.1.1 The quantum harmonic oscillator

A simple but very relevant implementation of a superconducting quantum circuit is the LC-oscillator, which is formed by a parallel circuit of an inductor L and a capacitor C. In Fig. 1.1, the left-hand panel depicts an optical microscopy image of a physical realization of the LC oscillator, fabricated from a single thin film aluminum layer (white) on a sapphire substrate (grey).

From a wire to a quantum circuit

Despite the quite peculiar shape noticed at a first glance, the whole circuit is formed by a single, continuous superconducting wire, which means that every segment is galvanically connected to all other segments. However, due to the arrangement of the wire, the circuit contains a region of enhanced capacitance on the right-hand side, where the two ends of the wire are parallel and close in distance. The galvanic connection between the capacitor electrodes is considerably narrower in width, and forms the inductor of the circuit. Hence, if the capacitor is charged, an electric field will occur between the capacitor plates, and analogously, if the capacitor discharges via the inductor, the induced current will give rise to a magnetic field surrounding the inductor. On resonance, the energy stored in the magnetic field equals the energy stored in the electric field, and both field components are oscillating at the natural resonance frequency of the circuit. Finding the corresponding eigenfrequencies of a circuit is subject to (quantum) circuit theory.

The circuit model

The lumped-element electronic schematic of the physical circuit is shown on the right-hand side of Fig. 1.1. In the lumped-element representation of a circuit, the physical properties associated to a segment of the superconducting thin film, and the corresponding electromagnetic fields, are condensed into a single or multiple two-port circuit elements. In the given example, the contribution of the long wire forming the inductor is compressed into a single inductive element. During this

Figure 1.1: Quantum harmonic oscillator. Optical microscopy image of a superconducting LC oscillator. The circuit is formed by a single superconducting wire made from thin film aluminum (white) evaporated on a sapphire substrate (grey), which is arrangend in such a way to form a meander shaped inductor on the left-hand side and a capacitor on the right-hand side. The right-hand panel shows the corresponding lumped-element circuit diagram composed of a parallel circuit of an effective capacitance C and an effective inductance L. The red and the blue arrows indicate the electric and magnetic field, respectively, associated with the charges on the capacitor plates and the current threading the inductance. The condition for resonance is reached when the energy stored in the electrical field equals the energy stored in the magnetic field, which occurs at the natural resonance frequency $\omega_0 = 1/\sqrt{LC}$ of the circuit.

process, the distribution of the current along the wire is lost, and the effective circuit model does not account for higher harmonics present in the physical system.

The circuit model of the quantum harmonic oscillator has a single degree of freedom. In the node representation of electrical networks, the node flux $\hat{\Phi}$, which is defined as the time integral of the voltage drop $\hat{V}(t)$ across the capacitor

$$\hat{\Phi}(t) = \int_{-\infty}^{t} \hat{V}(t')\mathrm{d}t', \tag{1.2}$$

becomes the position coordinate of the system. The spectrum of the node flux operator is continuous, and by comparing its relation to the voltage operator with the classical definition of Faraday's law of induction reveals, that the classical node flux is indeed equal to the magnetic flux Φ_B through the inductor

$$V(t) = \dot{\Phi}_\mathrm{B} = \dot{\Phi}. \tag{1.3}$$

In general, following the canonical quantization [222], the quantum Hamiltonian of a circuit is deduced from the classical Hamiltonian of its equivalent circuit. For the quantum LC-oscillator, the Hamiltonian is

$$\hat{H} = \frac{\hat{Q}^2}{2C} + \frac{\hat{\Phi}^2}{2L}, \tag{1.4}$$

where $\hat{Q}$ is denoted the node charge operator. The node charge constitutes the conjugate variable of the node flux, and becomes the momentum coordinate of the system. Therefore, the two operators obey the canonical commutation relation

$$[\hat{\Phi}, \hat{Q}] = i\hbar, \tag{1.5}$$

in analogy to the position and momentum coordinate of a quantum particle. While for the given example, the node charge determines the charge on the capacitor plates, in more complex systems with more than one DOF, the node charge corresponds to the combined charges residing on all capacitors connected to the respective node. Nevertheless, in the node representation the kinetic energy of the system is associated with the capacitive elements, and the potential energy to the inductive elements. Although arbitrary for the LC oscillator, this choice becomes convenient in the treatment of nonlinear inductors, i.e. the Josephson junction [222].

According to the definition of the node flux operator, the voltage and current operators are

$$\hat{V}(t) = \frac{\hat{Q}}{C} \qquad \text{and} \qquad \hat{I}(t) = \frac{\hat{\Phi}}{L}, \tag{1.6}$$

revealing that both operators satisfy the constitutive relations of a linear capacitor and a linear inductor, respectively.

Stationary microwave photons

Since the node flux and charge operators do not commute with the Hamiltonian, they do not share a common eigenbasis. In order to find the energy eigenstates of the circuit, the canonical coordinates $\hat{\Phi}$ and $\hat{Q}$ are expressed in terms of creation and annihilation operators $\hat{a}^\dagger$ and $\hat{a}$, respectively,

$$\hat{\Phi} = \Phi_{\text{ZPF}} \left(\hat{a} + \hat{a}^\dagger\right) \qquad \hat{Q} = -iQ_{\text{ZPF}} \left(\hat{a} - \hat{a}^\dagger\right). \tag{1.7}$$

Here, Φ_{ZPF} and Q_{ZPF} are the zero-point fluctuations of the node flux and the node charge, respectively. By definition, they determine the magnitude of the ground-state fluctuations in both variables in the absence of excitations, and are the manifestation of the uncertainty principle between both variables. In a superconducting circuit, the size of these fluctuations is controlled by the relative size of the circuit elements. For the quantum harmonic oscillator, the zero-point fluctuations are

$$\Phi_{\mathrm{ZPF}} = \sqrt{\frac{\hbar Z_0}{2}} \qquad\qquad Q_{\mathrm{ZPF}} = \sqrt{\frac{\hbar}{2Z_0}}, \tag{1.8}$$

where $Z_0 = \sqrt{L/C}$ is the circuit's characteristic impedance. According to the definitions of the zero-point fluctuations, the suppression of the fluctuation in one variable by changing the characteristic impedance of the circuit, enhances the fluctuation in the other variable.

Since the node flux and the charge of the harmonic oscillator are ultimately related to electromagnetic fields created by the current flowing through the inductor and the charges residing on the capacitor plates, the creation and annihilation operators correspond to single-mode field amplitude operators, which obey the bosonic commutation relation

$$[\hat{a}, \hat{a}^{\dagger}] = 1. \tag{1.9}$$

The quantization of the electromagnetic fields is subject of the second quantization, and inserting Eq. 35 and Eq.36 into Eq. 34, yields the quantum optics Hamiltonian of the quantum harmonic oscillator

$$\hat{H} = \hbar\omega_0 \left(\hat{a}^{\dagger}\hat{a} + \frac{1}{2}\right), \tag{1.10}$$

where $\omega_0 = 1/\sqrt{LC}$ is the resonance frequency. The operator $\hat{n} = \hat{a}^{\dagger}\hat{a}$ is the occupation number operator, which has a discrete eigenbasis, denoted the Fock basis, spanned by the discrete set of elementary excitations of the electromagnetic field, the photons:

$$\hat{n}\left|n\right\rangle = n\left|n\right\rangle. \tag{1.11}$$

Here, $n \in \mathcal{Z}^{\geq 0}$ is a positive integer number representing the number of photons inside a Fock state. The eigenenergies of the quantum harmonic oscillator are

$$E_n = \hbar\omega \left(n + \frac{1}{2}\right), \tag{1.12}$$

where n is thus the number of photons inside the oscillator. The energy spacing between consecutive energy levels is detemined by the resonance frequency of the circuit and does not depend on the number of photons inside the oscillator. The constant term reflects the zero-point fluctuations of the system, which are present even without any excitation, and are of the same type as the quantum fluctuations of the vacuum. Although the quantum harmonic oscillator is a relevant system, as every linear system can be decomposed into a set of independent harmonic modes, for quantum computing and many other applications, nonlinear elements are required. Even in bosonic approaches on quantum computing, for instance the cat codes [219] or the Gottesmann-Kitaev-Preskill (GKP) code [86], in which the quantum state is actually stored inside a linear oscillator, non-linear drives are required to prepare the states.

1.1.2 The Josephson junction

The key element and the reason for the high amount of flexibility of superconducting quantum circuits is the Josephson junction (JJ). A JJ is formed when two superconducting electrodes are connected by a weak link, for instance if the electrodes are separated by a thin insulating tunneling barrier, or even by a narrow bridge. In both cases, the superconducting condensate is locally weakened and the properties of the JJ are fundamentaly related to the relationship of charge and phase in a superconductor. While the wavefunctions of the superconducting electrodes are well defined in the case of a tunnel junction, which simplifies the mathematical treatment significantly, for a bridge or constriction, the wavefunction can become a complicated function of space [134]. In general, the physical laws governing

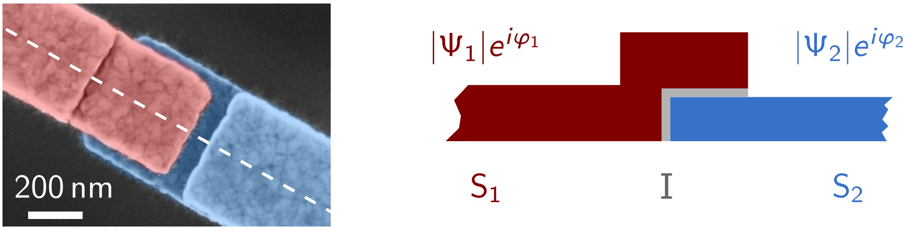

Figure 1.2: Josephson tunnel junction Scanning electron microscopy image of a Josephson junction formed by the overlap area of two superconducting electrodes (aluminum on silicon), which are separated by a thin insulating barrier. For clarity, the electrodes are false color-coded in red and in blue, and an artistic illustration of the cross section is shown in the right-hand panel. Since the superconductors are separated, the condensate in each electrode is described by a complex wavefunction $\Psi_i = |\Psi_i|e^{i\varphi_i}$.

a constriction depend on the geometric dimension of the wire, and the material properties of the superconductor. For that and other reasons, the predominant sources of nonlinearity in superconducting quantum circuits are JJ formed by a tunnel contact. Yet, every superconducting wire is to some extent nonlinear as the nonlinearity arises from the superconducting condensate.

The Josephson equations

In a JJ, a dissipationless current of Cooper pairs, denoted the supercurrent, can be induced by a difference in the macroscopic phases of the superconducting electrodes $\hat{\varphi} = \hat{\varphi}_1 - \hat{\varphi}_2$, and is sustained by the element up to a critical current I_c. Figure 1.2 depicts an example for a tunnel contact formed between two superconducting electrodes, false color-coded in red and blue, with an artistic illustration of the corresponding cross section of the contact.

The transfer of Cooper pairs from one electrode to the other is discrete, and since the number of Cooper pairs and the phase of the macroscopic wavefunction are conjugate variables, which are by definition Fourier transform duals, the discreteness of the charge transport engenders the phase response to be periodic. The corresponding relation between the supercurrent and the phase difference is referred to as the current-phase relation, and for the ideal contact it takes the form of the first Josephson equation [108]

$$\hat{I}(\hat{\varphi}) = I_\mathrm{c} \sin(\hat{\varphi}). \tag{1.13}$$

For weak links not formed by a tunnel contact, the current-phase relation can deviate from the sinusoidal form significantly [134]. The time evolution of the phase difference is determined by the voltage drop across the element, and expressed by the second Josephson equation

$$\hat{V}(t) = \frac{\hbar}{2e} \frac{\mathrm{d}\hat{\varphi}}{\mathrm{d}t}, \tag{1.14}$$

revealing a close similarity to the definition of the node flux operator. However, the phase operator is defined on the unit circle only, which is why the two operators are not necessarily identical. As U. Vool argues in his PhD thesis [221], a way of relating the node flux and the phase difference is to introduce an infinitely large inductance in parallel to the junction, which does not affect the solutions on the small scale, but breaks the periodicity of the phase operator and assures the vanishment of the wavefunctions at infinity.

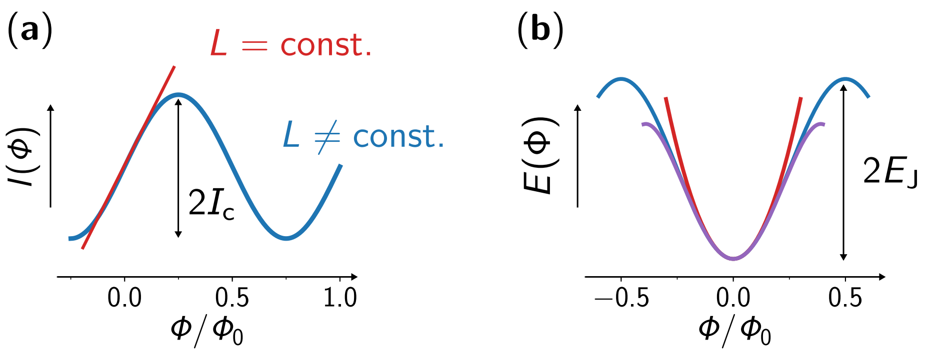

Figure 1.3: Josephson tunnel junction: Current-flux relation and energy potential. a) Current-flux relation of an ideal JJ (solid blue line) and an ideal linear inductor (red dashed line), plotted against the generalized flux across the elements Φ. The modulation amplitude is determined by the critical current I_c of the JJ. **b)** Energy potential of an ideal JJ $E \propto \cos(\Phi/\varphi_0)$ (blue), together with the Taylor expansion around the origin up to the quadratic Φ^2 (red) and the quartic term Φ^4 (purple). The linear inductance corresponding to the quadratic curve is denoted the Josephson inductance $L_J = \Phi_0/(2\pi I_c)$.

The Josephson potential

Under the assumption that the JJ is shunted by an infinitely large inductor, the phase operator becomes the normalized flux operator $\hat{\varphi} = \hat{\Phi}/\varphi_0$, with $\varphi_0 = \hbar/(2e)$ being the reduced magnetic flux quantum. The potential energy associated to the Josephson element is

$$E_{\text{pot}} = -E_J \cos(\hat{\varphi}) \approx -E_J + \frac{E_J}{2}\hat{\varphi}^2 - \frac{E_J}{24}\hat{\varphi}^4 + \mathcal{O}(\hat{\varphi}^6), \tag{1.15}$$

where $E_J = \hbar I_c/(2e)$ is the Josephson energy.

The expansion of the Josephson potential for small phase differences ($\varphi \ll 1$) shows, that the JJ contributes to the circuit as a nonlinear inductance. Neglecting the energy offset, the first term of the expansion corresponds to the harmonic potential of a linear inductor, with the associated coefficient denoted the Josephson inductance $L_J = \Phi_0/(2\pi I_c)$. The quartic term constitutes the first nonlinear term of the JJ, and is usually sufficient to explain the dynamics governing a nonlinear circuit if the phase fluctuations across the JJ are small.

In general, the phase fluctuations across the JJ determine the dynamics of the JJ, and are controlled by the shunting element(s). This circumstance is utilized to build different flavors of quantum bits, where either the charge or the phase are considered a good quantum number.

The Josephson Hamiltonian

For a tunnel junction, the two superconducting electrodes give rise to an additional shunt capacitance, referred to as the junction capacitance C_J. Figure 1.4 depicts the corresponding circuit diagram of a JJ, composed of a tunneling element with sinusoidal current-phase relation (cross) and a capacitor (left-hand panel), as well as the compact representation (right-hand panel).

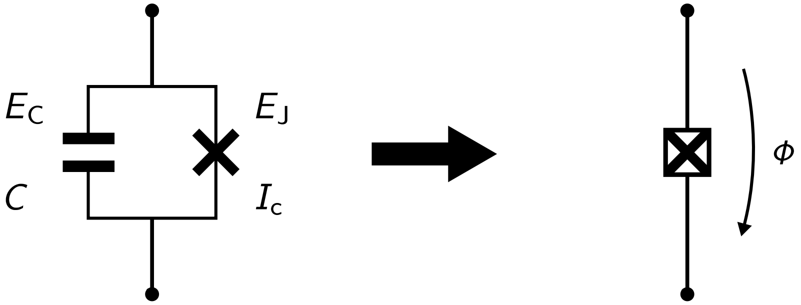

Figure 1.4: Josephson tunnel junction: Circuit diagram. The circuit representation of a single Josephson junction, formed between two superconducting electrodes separated by a thin insulating barrier (see Fig. 1.2), is a parallel circuit of a capacitor with charging energy $E_\mathrm{c} = e^2/(2C_\mathrm{J})$, where C_J is the junction capacitance arising between the electrodes, and a tunnel contact (cross) with Josephson energy $E_\mathrm{J} = \Phi_0/(2\pi I_\mathrm{c})$, where I_c is the critical current of the junction. The critical current determines the maximal supercurrent the JJ can sustain without dissipation, i.e. without a voltage drop across the element. Therefore, the circuit representation is only valid for bias currents smaller than the critical current. The self-resonant frequency of the equivalent circuit is referred to as the plasma frequency $\omega_\mathrm{pl} \approx \sqrt{8E_\mathrm{J}E_\mathrm{c}}$. A more compact and commonly used representation of a JJ is shown on the right-hand side.

The Hamiltonian of the JJ including the kinetic term due to the junction capacitance is

$$\hat{H} = \frac{\hat{Q}^2}{2C_\mathrm{J}} - E_\mathrm{J}\cos(\hat{\Phi}/\varphi_0), \tag{1.16}$$

which can be rewritten in the form

$$\hat{H} = 4E_\mathrm{c}\hat{N}^2 - E_\mathrm{J}\cos(\hat{\Phi}/\varphi_0), \tag{1.17}$$

by introducing the normalized charge operator $\hat{N} = \hat{Q}/(2e)$, and the charging energy $E_\mathrm{c} = e^2/(2C_\mathrm{J})$. Despite its simplicity, the JJ Hamiltonian is sufficient to describe the vast majority of systems studied within the scope of my thesis, ranging from parametric amplification to the implementation of qubits, as it describes different dynamics depending on the relative size between the charging energy and the Josephson energy.

1.1.3 The superconducting charge qubit

The superconducting charge qubit is not only the first superconducting qubit implemented [30, 166], but also one of its manifestations, the transmon qubit [116], has become the most widely used qubit flavor until now. Conceptually, the idea of the charge qubit is to encode the logical states in the charge states of a superconducting island, connected to a charge reservoir via a JJ, therefore allowing only discrete numbers of Cooper pairs on the island. If the island is small in size, the charging energy, which is a measure of the Coulomb expulsion of two charged particles on the island, dominates the dynamics of the circuit. In this regime, the charge qubit is referred to as the Cooper pair box [206]. For large islands, the dynamics are dominated by the superconducting phase.

The circuit diagram of the superconducting charge qubit is similar to the circuit diagram of the JJ introduced in the previous section, with the main difference being an additional capacitance C_g connecting the superconducting island to a voltage source. The application of a gate voltage changes the chemical potential of the island continuously, and determines the equilibrium point of the charge. The charge qubit Hamiltonian is

$$\hat{H} = 4E_\mathrm{c}(\hat{N} - N_\mathrm{g})^2 - E_\mathrm{J}\cos(\hat{\Phi}/\varphi_0), \tag{1.18}$$

where $N_\mathrm{g} = V_\mathrm{g}C_\mathrm{g}/(2e)$ is the normalized offset charge due to the gate voltage V_g, and is equivalent to a number of Cooper pairs. Notably, the contribution of the gate capacitor changes the charging energy $E_\mathrm{c} = e^2/(2[C_\mathrm{J} + C_\mathrm{g}])$ of the island. Since charge transfer is conducted via a tunneling contact, only discrete numbers of Cooper pairs can tunnel onto the island. Figure 1.5 depicts the corresponding circuit diagram, in which the superconducting island is highlighted in red.

In general, there are two complementary bases for the Hilbert space representation of the charge qubit Hamiltonian: the eigenbasis of the normalized charge operator, and the eigenbasis of the phase operator. Although both bases reproduce the same results, the natural choice is to use the charge eigenbasis in the limit $E_\mathrm{c} \geq E_\mathrm{J}$, and the phase eigenbasis in the limit $E_\mathrm{c} \ll E_\mathrm{J}$.

In the charge eigenbasis the Hamiltonian becomes

$$\begin{aligned}\hat{H} = 4E_{\mathrm{c}} &\sum_{N=-\infty}^{\infty} (N - N_{\mathrm{g}})^2 \left|N\right\rangle \left\langle N\right| \\ &- \frac{E_{\mathrm{J}}}{2} \sum_{N=-\infty}^{\infty} \left(\left|N\right\rangle \left\langle N+1\right| + \left|N+1\right\rangle \left\langle N\right|\right),\end{aligned} \tag{1.19}$$

which again does only hold if individual Cooper pairs are transferred across the JJ at a time. While the first term determines the kinetic energy associated to the Coulomb expulsion, the second term determines the finite coupling between the superconducting island and the charge reservoir of the environment.

Energy spectrum

Figure 1.5 depicts the energy spectrum of the charge qubit up to the fourth energy eigenstate, numerically calculated as a function of the offset charge $N_{\mathrm{g}} \in [-1, 1]$ for two ratios of the Josephson energy and the charging energy $E_{\mathrm{J}}/E_{\mathrm{c}} = 1.0$ and 50, representative for the two limits of the circuit. For clarity, the energies E_i are expressed in a frequency scale and are offset by the minimum of the ground state energy E_0.

In the first case, the spectrum is composed of a family of parabolas, which are horizontally offset by integer values and represent the energies of the charge eigenstates. Due to the finite tunneling, the parabolas split at the intersection points, with the splitting between the ground and the first excited state being the Josephson energy E_{J}. The point of operation for the charge qubit in this regime, denoted the charge sweet spot, is at $N_{\mathrm{g}} = 0.5$, as the slope of the first two eigenenergies vanishes simultaneously. Representing the ground state in the charge basis (bottom panel) reveals that the eigenstate at the charge sweet spot is an equal superposition state between zero and a single Cooper pair on the island, with only a small contribution of other states, justifying the choice of basis.

The obtained spectrum is highly anharmonic, meaning that the transition energy E_{01} between the ground and the first excited state differs significantly from the transition energy E_{12} between the first and the second excited state. In general, the *anharmonicity* α of an energy spectrum is determined by

$$\hbar\alpha = E_{12} - E_{01}. \tag{1.20}$$

However, as it turned out in various experiments, stabilizing the charge qubit at the desired point of operation proved elusive due to fluctuations in the uncontrolled

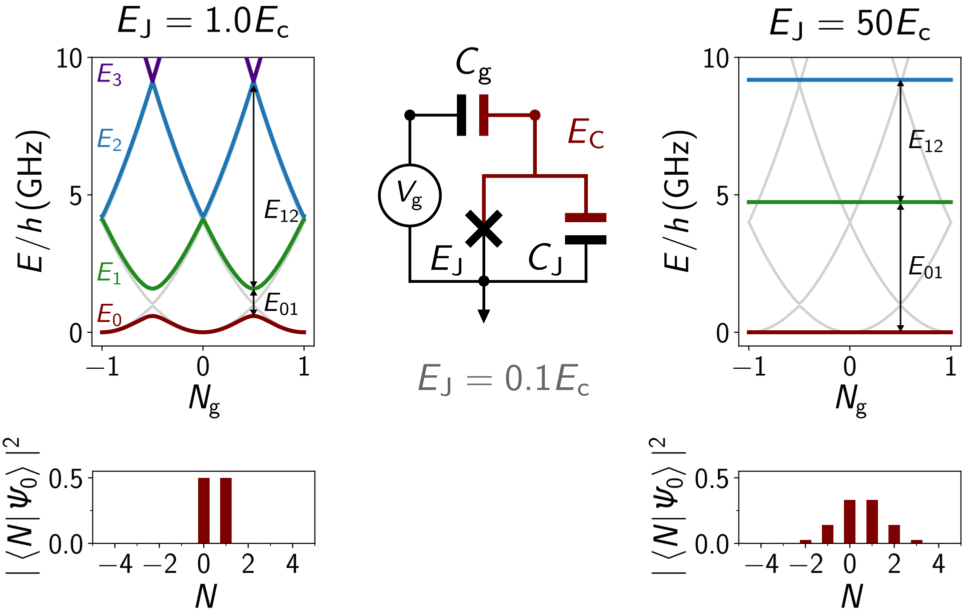

Figure 1.5: Superconducting charge qubit: Circuit diagram and energy spectrum. The circuit diagram of the superconducting charge qubit consists of a superconducting island, indicated in red, for which the charge transfer with the environment is conducted via a Josephson junction — a tunneling contact (cross) associated with the Josephson energy $E_J = \Phi_0/(2\pi I_c)$ in parallel with the concomitant junction capacitance C_J — and is therefore discrete. However, the equilibrium point of the charge is controlled by an external voltage source V_g that determines the offset charge $N_g = V_g C_g/(2e)$ on the islands. The total charging energy of the island is $E_c = e^2/(2[C_g + C_J])$. The left-hand and the right-hand panels depict the energy spectrum of the circuit, numerically calculated for the two ratios $E_J/E_c = 1$ and 50, as a function of the offset charge. Additionally, the case $E_J/E_c = 0.1$ is plotted in light gray, and serves as a reference. The first four energy levels are indicated by different colors. The comparison between both plots emphasizes the distinct dependence of the energy spectrum on the value of the offset charge observed in the regime in which the charging energy dominates or both energy scales are comparable. With increasing ratio E_J/E_c, the dependence on the offset charge, the offset charge dispersion, is exponentially suppressed. The lower panels indicate the ground state wavefunction in the charge number basis for $N_g = 0.5$. For small ratios E_J/E_c the charge number is a good quantum number and the eigenstates of the charge qubit are almost identical to the charge number eigenstates. With increasing ratio, the spread of the wavefunction increases.

electromagnetic environment of the circuit, significantly limiting the quantum coherence of the charge qubit [105].

Mitigating the effect of the offset charge on the qubit spectrum is achieved by increasing the ratio $E_\mathrm{J}/E_\mathrm{c}$, shown in the right-hand panel of Fig. 1.5, as the splitting at the intersection points flattens the dependency of the eigenenergies on N_g. This causality is the idea behind the transmon qubit [116].

The Transmon regime

The transmon qubit is a type of superconducting charge qubit operated in the regime $E_\mathrm{J}/E_\mathrm{c} \geq 50$, which is most commonly achieved by shunting a single JJ with an additional capacitor. As a consequence, the circuit's susceptibility to offset charges is exponentially suppressed with $\sqrt{E_\mathrm{J}/E_\mathrm{c}}$, significantly enhancing the time stability of the operational frequency. However, at the same time the anharmonicity of the energy spectrum decreases.

In the transmon regime, the potential well due to the JJ is much larger than the kinetic energy. Therefore, the representation of the dynamics in the phase basis becomes more intuitive, drawing the picture of an effective phase particle trapped in a cosine potential. Since the phase fluctuations across the JJ are small, the potential energy is well approximated by the terms of a Taylor expansion up to the fourth order. Neglecting the constant term of the expansion and the offset charge in the kinetic energy, the approximated transmon Hamiltonian is

$$\hat{H} \approx 4E_\mathrm{c}\hat{N}^2 + \frac{E_\mathrm{J}}{2}\hat{\varphi}^2 - \frac{E_\mathrm{J}}{24}\hat{\varphi}^4, \tag{1.21}$$

which is the Hamiltonian of a harmonic oscillator with quartic perturbation. Therefore, a suitable description of the system are the bosonic single-mode field amplitude operators introduced for the harmonic oscillator:

$$\hat{\varphi} = \varphi_\mathrm{ZPF}\left(\hat{a} + \hat{a}^\dagger\right) \tag{1.22}$$

$$\hat{N} = -iN_\mathrm{ZPF}\left(\hat{a} - \hat{a}^\dagger\right). \tag{1.23}$$

Here, $\varphi_\mathrm{ZPF}^2 = \sqrt{2E_\mathrm{c}/E_\mathrm{J}}$ and $N_\mathrm{ZPF}^2 = \sqrt{E_\mathrm{J}/(32E_\mathrm{c})}$ are the zero-point fluctuations of the phase and the normalized charge. Applying the rotating-wave-approximation, i.e. keeping only terms that conserve energy, and using the bosonic commutation relation to perform a normal mode ordering, yields the Hamiltonian of the transmon qubit in second quantization

$$\hat{H} \approx \underbrace{\left(\sqrt{8E_\mathrm{J}E_\mathrm{c}} - E_\mathrm{c}\right)}_{=\omega_0'} \hat{a}^\dagger \hat{a} \; \underbrace{-\frac{E_\mathrm{c}}{2}}_{=\hbar K/2} \hat{a}^\dagger \hat{a}^\dagger \hat{a}\hat{a}, \tag{1.24}$$

where ω_0' is the resonance frequency of the fundamental transition. In quantum optics, the obtained type of Hamiltonian is known as the Kerr Hamiltonian, where K is the Kerr coefficient and determines the anharmonicity of the energy spectrum. Mapping the charge qubit Hamiltonian onto the Kerr Hamiltonian reveals, that the anharmonicity in the transmon limit, i.e. performing an expansion of the Josephson potential up to the fourth order, is set by the charging energy of the shunt capacitor.

$$\alpha \approx \frac{E_\mathrm{c}}{\hbar} \tag{1.25}$$

This result constitutes the compromise between the offset charge dispersion and the anharmonicity encountered in the charge qubit.

Despite its small anharmonicity compared to the Cooper pair box and other qubit flavors, the transmon qubit has been successfully used for the first demonstration of the so-called quantum supremacy [6], and persuades by its conceptual simplicity.

1.1.4 Bloch-sphere representation

In the qubit limit, the infinite Hilbert space of a superconducting quantum circuit is truncated and mapped onto a two-dimensional space spanned by the logical ground state $|g\rangle$, or $|0\rangle$ alternatively, and the logical excited state $|e\rangle$ or $|1\rangle$. While in many implementations the logical ground and excited state coincide with the two lowest physical energy eigenstates of the system, in bosonic codes, the infinite Hilbert space of the harmonic oscillator is used to encode quantum information, and the ground and excited state can be more complex superposition states [36, 219].

A sufficient condition for the qubit limit of a multi-level system is, that transitions between the energy eigenstates forming the computational basis are induced at a significantly slower rate than the anharmonicity of the energy spectrum. However, even for weakly anharmonic systems like the transmon, there are pulse sequences designed to avoid the population of higher energy eigenstates outside the computational basis [161], or which even exploit the higher dimensionality of the underlying Hilbert space for the preparation of a logical quantum state $|\Psi\rangle$ inside the computational basis [61].

The Bloch-sphere representation shown in Fig. 1.6 is a common way of displaying the logical state $|\Psi\rangle$ of a quantum bit in the three-dimensional space

$$|\Psi\rangle = \cos\left(\frac{\theta}{2}\right)|0\rangle + \sin\left(\frac{\theta}{2}\right)e^{i\phi_\mathrm{q}}|1\rangle\,, \tag{1.26}$$

where θ is the mixing angle between the ground and the excited state, and ϕ_q is the phase of the state with respect to a yet undefined reference. The corresponding Hamiltonian of an ideal qubit is

$$\hat{H}_0 = \frac{\hbar\omega_\mathrm{q}}{2}\hat{\sigma}_z, \tag{1.27}$$

where $\hat{\sigma}_z$ is a Pauli operator, and $\omega_\mathrm{q} = (E_1 - E_0)/\hbar$ is the transition frequency between the ground state $|0\rangle$ with energy E_0 and the first excited state $|1\rangle$ with energy E_1.

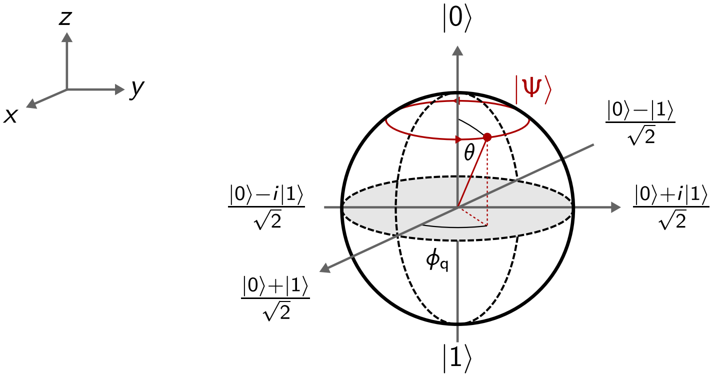

Figure 1.6: Bloch-sphere. Graphical representation of the two-dimensional Hilbert space spanned by the logical states $|0\rangle$ and $|1\rangle$ of a qubit. The six cardinal points and the corresponding states are indicated along the three coordinate axes. Any quantum state $|\Psi\rangle$ (red dot) on the surface of the Bloch sphere is determined by two angles θ and ϕ_q. In the Schroedinger picture, the state of the qubit precesses around the z-axis at the transition frequency ω_q of the qubit. In statistical quantum mechanics, the surface of the Bloch sphere hosts pure states, while mixed states reside in the interior.

Rabi-oscillations

In the Schroedinger picture, the time evolution of a system is described by the a unitary operation $\hat{U}(t, t_0)$ acting on the initial quantum state of the system. If the system Hamiltonian is time independent, the evolution of the quantum state over time is

$$|\Psi(t)\rangle = e^{i\hat{H}(t-t_0)}\,|\Psi(t_0)\rangle\,. \tag{1.28}$$

For an ideal qubit, the state $|\Psi(t_0)\rangle$ initialized at time t_0 precesses around the z-axis of the Bloch sphere at the qubit frequency ω_q, as illustrated in Fig. 1.6. In order to induce transitions between the ground and the excited state, an additional drive term has to be added to the unperturbed Hamiltonian $\hat{H}_0$, resulting in the Rabi-Hamiltonian

$$\hat{H}_\mathrm{Rabi} = \frac{\hbar\omega_\mathrm{q}}{2}\hat{\sigma}_z + \Omega\hat{\sigma}_x\cos(\omega t)\,. \tag{1.29}$$

Here, Ω is the drive amplitude, ω is the drive frequency, and $\hat{\sigma}_x$ is a Pauli operator. The presented form of coupling is referred to as a transversal coupling, as it does not preserve the eigenbasis of the initial Hamiltonian. In a frame rotating at the drive frequency, obtained by the unitary transformation $\hat{U} = \exp(i\omega\hat{\sigma}_z t/2)$, the Hamiltonian becomes

$$\hat{H}_\mathrm{Rabi} = \frac{\hbar\Delta_\mathrm{q}}{2}\hat{\sigma}_z + \frac{\Omega}{2}\hat{\sigma}_x, \tag{1.30}$$

with the frequency detuning $\Delta_\mathrm{q} = \omega_\mathrm{q} - \omega$ between the drive and the qubit. The new eigenenergies of the so-called *dressed* Hamiltonian $\hat{H}_\mathrm{Rabi}$ are $E_\pm = \pm\frac{1}{2}\sqrt{\Omega + \Delta_\mathrm{q}^2}$, and since the corresponding eigenstates $|\pm\rangle$ of the Rabi-Hamiltonian are superposition states of the bare eigenstates $|0\rangle$ and $|1\rangle$, the action of the additional term is to drive transitions between $|0\rangle$ and $|1\rangle$ at a rate given by the generalized Rabi frequency

$$\Omega_\mathrm{R} = \sqrt{\Omega^2 + \Delta_\mathrm{q}^2}. \tag{1.31}$$

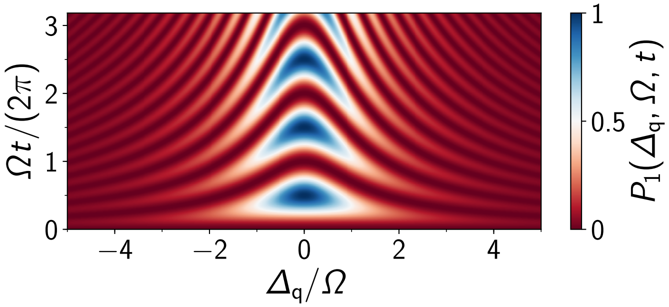

Figure 1.7: Rabi cycle. Time evolution of the probability P_1 of finding a qubit in the excited state $|1\rangle$, if a continuous microwave drive of amplitude Ω and frequency detuning $\Delta_\mathrm{q} = \omega_\mathrm{q} - \omega$ is applied at time $t_0 = 0$.

Figure 1.7 depicts the probability P_1 of finding the qubit in the excited state as a function of the normalized time t and the frequency detuning $\mathit{\Delta}_\mathrm{q}$ after preparing the qubit in the ground state at $t = 0$. While the Rabi frequency increases with increasing detuning, the contrast of the oscillation reduces at the same time. The obtained pattern is known as the Chevron pattern.

1.1.5 Open quantum systems

So far, the discussion about superconducting quantum circuits has been carried out on the basis of closed quantum systems — systems that are completely decoupled from their environment. The quantum state of such an isolated quantum system evolves indefinitely with time under the action of the corresponding Hamiltonian of the system. Moreover, if the system is prepared in a superposition state, for instance a state on the equator of the Bloch sphere $(|0\rangle + |1\rangle)/\sqrt{2}$, the phase relation between the states remains well defined, which is referred to as *quantum coherence*.

In reality, every quantum system exchanges information with its environment, sharing its quantum state with a set of observers. For the study of a quantum system we, the scientists, become observers, too, by delibaretly opening a communication channel to the system. In the field of superconducting quantum circuits, the communication is carried out by propagating microwave photons with energies $E_\mathrm{ph}/h \approx 0.1 - 20\,\mathrm{GHz}$. If the state of all other observers and their time evolution would be known to us, the total system including the observers would remain coherent in the quantum mechanical sense [164]. However, all quantum systems interact with uncontrolled degrees of freedom, which are usually not accessible, therefore causing quantum decoherence — the loss of information about the quantum state over time.

The extent of the interaction of a system with its environment is captured by two characteristic time scales, the energy relaxation time T_1 and the dephasing time T_2^*. In both cases, introducing the corresponding relaxation rates as the inverse, $\mathit{\Gamma}_1 = T_1^{-1}$ and $\mathit{\Gamma}_2^* = T_2^{*-1}$, becomes convenient when dealing with multiple decay mechanisms.

Energy relaxation

In most cases the total energy relaxation into the equilibrium state of the system is due to a combination of different physical effects, but can be categorized into a decay rate κ caused by the interaction of the system with the input port used to collect information, and the decay rate γ caused by the interaction with uncontrolled and unobserved degrees of freedom:

$$\mathit{\Gamma}_1 = \kappa + \gamma. \tag{1.32}$$

The corresponding relaxation times are $T_{1,\kappa} = \kappa^{-1}$ and $T_{1,\gamma} = \gamma^{-1}$. In a direct measurement of the system, κ is the rate at which information about the quantum state is obtained.

For a qubit, the energy relaxation time determines how fast the qubit reaches its equilibrium state on average after it has been excited. Notably, depending on the temperature of the environment, the equilibrium state is not necessarily the ground state of the system, which is why two additional rates are distinguished: The rate $\mathit{\Gamma}_\uparrow$ at which the environment excites the qubit from the ground state into the excited state ($|0\rangle \to |1\rangle$), and the rate $\mathit{\Gamma}_\downarrow$ at which the excited state spontaneously decays into the ground state ($|1\rangle \to |0\rangle$):

$$\mathit{\Gamma}_1 = \mathit{\Gamma}_\uparrow + \mathit{\Gamma}_\downarrow. \tag{1.33}$$

The equilibrium state depends on the relative size of both rates.

In general, the relaxation rates reflect the property of a time ensemble — a statistical ensemble of identical copies of the system. If the state of the qubit is continuously traced over time, usually fast transitions between the two states can be observed, as shown in Fig. 1.8 (right-hand panel). Although such transitions are denoted *quantum jumps*, implying a discontinuous quantum trajectory, recent experiments

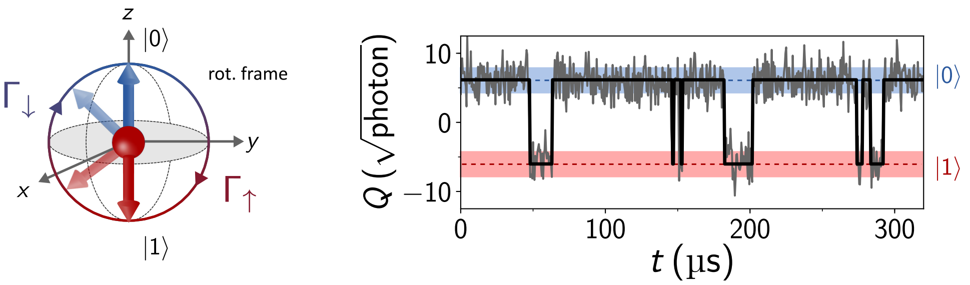

Figure 1.8: Energy relaxation. Bloch sphere representation of energy relaxation processes, illustrated in the rotating frame of the qubit transition frequency. On average, the qubit state transits from the ground (blue) to the excited state (red) at a rate $\mathit{\Gamma}_\uparrow$, and in the opposite direction at a rate $\mathit{\Gamma}_\downarrow$. The rates are defined as the inverse of the duration the qubit spends in the respective state. The continuous tracking of the qubit state (grey lines) over time reveals fast transitions between the two states, referred to as quantum jumps [155, 218]. The black line indicates the qubit state inferred from the system response Q, which is explained in more detail in Sec. 3.9.

have confirmed that the transitions are coherent Rabi transitions induced by the environment, usually taking place much faster than the time resolution of the measurement [155].

Dephasing

The dephasing rate is a measure of how fast the phase coherence of a prepared superposition state decays with time, i.e. how fast a pure quantum state becomes a statistical mixture, and is usually caused by a combination of energy relaxation and the fluctuation of the system's transition frequency expressed in the pure dephasing rate $\mathit{\Gamma}_\phi$. For a qubit prepared in a superposition state between the logical ground and first excited state, the dephasing rate is

$$\mathit{\Gamma}_2^* = \frac{\mathit{\Gamma}_1}{2} + \mathit{\Gamma}_\phi. \tag{1.34}$$

In the ideal case, the dephasing of a qubit is dominated by energy relaxation ($\mathit{\Gamma}_\phi \to 0$), and the dephasing time becomes

$$T_2^* = 2T_1. \tag{1.35}$$

According to conventional terminology, the asterisk indicates the dephasing time extracted from a Ramsey fringes experiment [186], as exemplarily shown in Fig. 1.9. In comparison, the time T_2 refers to the dephasing time obtained in a Hahn-echo experiment, an experiment designed to filter the low-frequency components of pure dephasing processes [94].

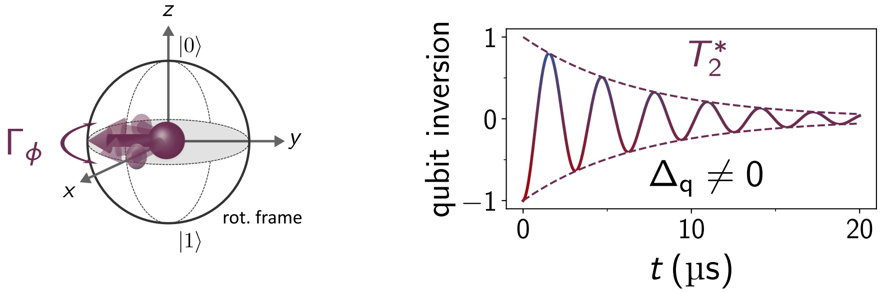

Figure 1.9: Dephasing. Bloch sphere representation of pure dephasing in the rotating frame of the (fixed) qubit transition frequency. For every component of the time ensemble representing the statistical average, the qubit frequency is slightly different, causing a rotation in the rotating frame, as indicated by the faint arrows. The projection onto the computational basis shows an exponentially decaying oscillation between the logical ground and excited state, where the oscillation frequency depends on the detuning $\mathit{\Delta}_\mathrm{q}$ between the rotating frame and the qubit transition frequency, and the characteristic time scale of the envelope is T_2^*.

Reflection coefficient

For superconducting quantum circuitry, a common way of characterizing a system is to measure the reflection coefficient $\Gamma(\omega)$ — the ratio between the outgoing and the incident field — through a dedicated input port in close vicinity to the resonance frequency of the system

$$\Gamma(\omega) = S_{11}(\omega) = \frac{\langle \hat{B}_{\mathrm{out}} \rangle}{\langle \hat{B}_{\mathrm{in}} \rangle}. \tag{1.36}$$

Here, $\hat{B}_{\mathrm{in}}$ and $\hat{B}_{\mathrm{out}}$ are the bosonic single-mode field amplitude annihilation operators of the fields propagating inside the input port. Referring to electrical engineering, the reflection coefficient is often denoted S_{11}, the first entry in the scattering matrix of a multi-port network.

In general, the reflection coefficient is a complex function of the probe frequency ω and power $P_{\mathrm{in}} = \hbar\omega \, \langle \hat{B}^{\dagger}_{\mathrm{in}} \hat{B}_{\mathrm{in}} \rangle$, and allows not only to distinguish between internal and external energy decay, but also to measure the frequency fluctuations of a system causing dephasing. While the reflection coefficient remains independent of the applied probe power for harmonic systems, the response of anharmonic systems can be highly nonlinear.

1.1.6 Circuit quantum electrodynamics

In analogy to cavity quantum electrodynamics (CQED) [142, 185], the experimental framework in which natural atoms interact with the quantized light confined in a three-dimensional superconducting cavity, in circuit qunatum electrodynamics (cQED), artifical atoms built from superconducting thin films are coupled to dedicated readout resonators [24, 224]. Figure 1.10 shows an illustration of the conceptual resemblance between both fields. Notably, for cQED experiments, the harmonic mode can be an on-chip 2D resonator [11, 33, 224] or a 3D cavity [171, 180]. In both cases, the corresponding Hamiltonian describing the interaction between the quantized electromagnetic light and the (artificial) atom is known as the quantum Rabi Hamiltonian [183, 184]

$$\hat{H}_{\mathrm{R}} = \frac{\hbar\omega_{\mathrm{q}}}{2}\hat{\sigma}_z + \hbar\omega_{\mathrm{r}}\hat{a}^{\dagger}_{\mathrm{r}}\hat{a}_{\mathrm{r}} + g\hat{\sigma}_x \left(\hat{a}_{\mathrm{r}} + \hat{a}^{\dagger}_{\mathrm{r}} \right), \tag{1.37}$$

where $\hat{a}^{\dagger}_{\mathrm{r}}$ and $\hat{a}_{\mathrm{r}}$ are the creation and annihilation operators of the cavity mode, respectively, with a bare transition frequency ω_{r}, and g is the coupling rate between the resonator and the qubit. In the presented from, the coupling is transversal, for instance induced by a finite coupling via the electrical fields of both modes, and does not preserve the eigenstates of the uncoupled systems. Although not further

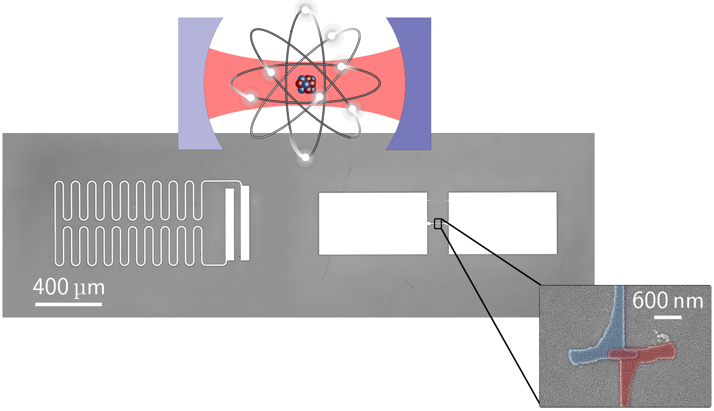

Figure 1.10: Circuit quantum electrodynamics (cQED). Similar to the field of cavity quantum electrodynamics (CQED), where natural atoms are coupled to the quantized light confined in a cavity [101, 142, 185], as illustrated by the artistic sketch, in cQED, an artificial atom is coupled to the electrical or magnetic field of a microwave cavity. The circuit visible on the left-hand side of the optical microscopy image constitutes the harmonic cavity, while the artificial atoms is a transmon qubit visible on the right-hand side. The inset shows an SEM image of the JJ, where the two superconducting electrodes on both sides are false color-coded in red and blue similar to Fig. 1.2.

discussed, the coupling scheme preserving the bare eigenstates is referred to as a longitudinal coupling [62].

Provided the coupling rate is significantly slower than the transition frequency of qubit and cavity ($g \ll \omega_\mathrm{q}, \omega_\mathrm{r}$) the application of the rotating wave approximation is justified, yielding the Jaynes-Cummings Hamiltonian [106, 226]

$$\hat{H}_\mathrm{JC} = \frac{\hbar\omega_\mathrm{q}}{2}\hat{\sigma}_z + \hbar\omega_\mathrm{r}\hat{a}_\mathrm{r}^\dagger\hat{a}_\mathrm{r} + g\left(\hat{\sigma}_+\hat{a}_\mathrm{r} + \hat{a}_\mathrm{r}^\dagger\hat{\sigma}_-\right). \tag{1.38}$$

The interaction term reveals that individual excitations are exchanged between the cavity and the qubit at a rate g. In the dispersive limit of cQED, the frequency detuning $\Delta_\mathrm{qr} = \omega_\mathrm{q} - \omega_\mathrm{r}$ between both systems is significantly larger than the coupling rate $\Delta_\mathrm{qr} \gg g$, and the Jaynes-Cummings Hamiltonian can be approximately diagonalized [24]

$$\hat{H}_\mathrm{JC} \approx \frac{\hbar}{2}\left(\omega_\mathrm{q} + \chi_\mathrm{qr}\right)\hat{\sigma}_z + \hbar\left(\omega_\mathrm{r} + \chi_\mathrm{qr}\hat{\sigma}_z\right)\hat{a}_\mathrm{r}^\dagger\hat{a}_\mathrm{r}. \tag{1.39}$$

The information about the qubit state is encoded in the frequency of the readout resonator, where $\chi_\mathrm{qr} = g^2/\Delta_\mathrm{qr}$ is the qubit state induced dispersive shift. Moreover, the dispersive measurement technique of the qubit state is quantum non-demolition (QND), meaning that the projected state of the qubit remains preserved after

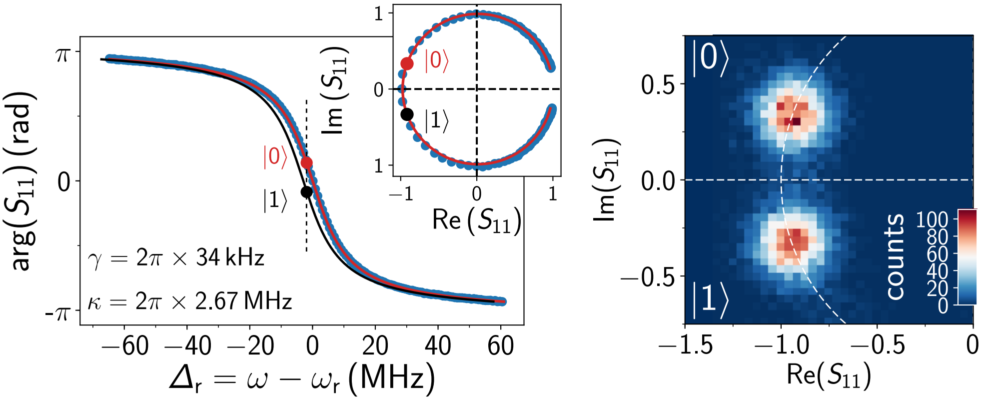

Figure 1.11: cQED:dispersive readout. Phase $\arg(S_{11})$ of the reflection coefficient measured around the resonance frequency ω_r of a readout resonator with internal and external decay rates γ and κ, respectively. The solid lines indicate the expected response if the qubit is in the ground state $|0\rangle$ (red), and the excited state $|1\rangle$ (black), assuming a dispersive shift $2\chi_\mathrm{qr} = -2\pi \times 480\,\mathrm{kHz}$. In the limit $\kappa > \gamma$, the resonator response in the complex plane covers all four quadrants (inset), and, for a fixed frequency readout tone (vertical black dashed line), the information about the qubit state is encoded in the reflected phase. The right-hand panel shows an example of a measured histogram of the reflection coefficient, when the qubit has been prepared in a superposition state on the equator. The two circular regions correspond to the coherent states prepared in the readout resonator if the qubit is in the ground and the first excited state.

the readout. However, above a critical photon number inside the resonator, the dispersive approximation breaks down [24]. Moreover, in many cQED experiments, the breakdown of the QND property of the readout is found to occur for even significantly smaller photon numbers inside the resonator [155].

The main advantage of the dispersive readout is the independent control of the energy decay of the qubit into the input port, and the rate at which information about the qubit state is collected, which is now determined by the coupling rate of the resonator. An example of the dispersive readout of a transmon qubit is shown in Fig. 1.11.

ac Stark shift and measurement-induced dephasing

Another aspect of the Jaynes-Cummings Hamiltonian becomes visible if the individual terms are arranged in a different order. In the same way the quantum state of the qubit is encoded in the resonance frequency of the resonator, the number of photons inside the resonator is reflected by the qubit transition frequency, an effect known as the ac Stark effect. The resonator induced frequency shift is

$$\omega_\mathrm{q}(\bar{n}_\mathrm{r}) = \omega_\mathrm{q,0} + \bar{n}_\mathrm{r} 2\chi_\mathrm{qr}, \tag{1.40}$$

where $\bar{n}_\mathrm{r}$ is the average photon number in the resonator. If the dispersive shift is calibrated from histograms similar to Fig. 1.11, measuring the qubit frequency allows for a precise calibration of $\bar{n}_\mathrm{r}$.

In most cQED experiments, instead of the application of Fock states, which are more complicated to prepare [99], the state of the readout resonator is measured with a coherent state, a Poisson distributed superposition of Fock-states (see App. B). Since the Poisson distribution broadens with increasing readout power, the linewidth of the qubit transition increases in addition to the frequency shift, as shown in Fig. 1.12. This effect is known as measurement induced dephasing.

Provided the dispersive shift per photon $2\chi_\mathrm{qr}$ is significantly larger than the linewidth of the qubit, individual qubit transitions can be observed for each Fock state occupied in the readout resonator. As an example, in the case of a coherent state stored in the resonator, its Poisson distribution in the Fock basis can be recovered from the qubit spectrum [79, 201].

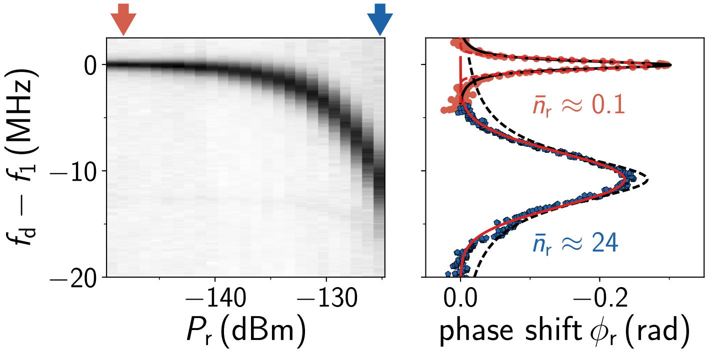

Figure 1.12: Measurement induced detuning in cQED. Dispersive shift of the readout resonator measured on resonance with an increasing on-chip readout power P_r. An additional drive tone is applied at frequency f_d in order to excite the qubit. With increasing readout power, the transition frequency of the qubit decreases (AC-Stark effect), while the transition broadens at the same time due to measurement induced dephasing, as indicated by the Gaussian (red) and Lorentzian (black) fits.

Beyond the qubit approximation

For qubits with small relative anharmonicity ($\alpha/\omega_{\mathrm{q}} \ll 1$), the two-level approximation does not describe the observed behavior of the system accurately. The transmon qubit is such an example, where the dispersive shift of the readout resonator is lower compared to the two-level approximation due to the presence of higher energy levels. Including the third level, the dispersive shift is [116]

$$\chi_{\mathrm{qr}} = \chi_{01} - \frac{\chi_{12}}{2}, \tag{1.41}$$

with $\chi_{j,j+1} = g_{j,j+1}^2/((E_{j+1} - E_j)/\hbar - \omega_{\mathrm{r}})$. The coupling rates between the transmon transitions and the readout resonator are determined by the off-diagonal matrix elements of the charge number operator $g_{j,j+1} \propto \langle j|\hat{N}|j+1\rangle$. In the limit $E_{\mathrm{J}} \gg E_{\mathrm{c}}$, the matrix elements of the two lowest transitions are $g_{12}^2 \approx 2g_{01}^2 = 2g^2$, and the dispersive shift can be approximated by

$$\chi_{\mathrm{qr}} \approx \frac{g^2}{\Delta_{\mathrm{qr}}} \frac{\alpha}{\Delta_{\mathrm{qr}} + \alpha}. \tag{1.42}$$

The corresponding Jaynes-Cummings Hamiltonian becomes [116]

$$\hat{H} = \frac{\hbar}{2} \underbrace{(\omega_{01} + \chi_{01})}_{=\bar{\omega}_{\mathrm{q}}} \hat{\sigma}_z + \hbar \left(\underbrace{\omega_{\mathrm{r}} - \frac{\chi_{12}}{2}}_{=\bar{\omega}_{\mathrm{r}}} + \underbrace{\left[\chi_{01} - \frac{\chi_{12}}{2}\right]}_{=\chi_{\mathrm{qr}}} \hat{\sigma}_z \right) \hat{a}_{\mathrm{r}}^{\dagger} \hat{a}_{\mathrm{r}}. \tag{1.43}$$

Here, the dressed transmon and resonator frequencies $\bar{\omega}_{\mathrm{q}}$ and $\bar{\omega}_{\mathrm{r}}$, respectively, are offset owing to the finite coupling rate and quantum fluctuations in both systems [74, 81]. Therefore, the induced shifts are referred to as Lamb-shifts [21, 124], which are generally not identical for both systems.

In the spirit of the quantum optics description of the transmon qubit (see Eq. 1.24), the cQED system can also be described solely based on bosonic field amplitude operators for both systems [168]:

$$\begin{aligned} \hat{H}/\hbar &= \tilde{\omega}_{\mathrm{q}} \hat{a}_{\mathrm{q}}^{\dagger} \hat{a}_{\mathrm{q}} + \frac{\alpha_{\mathrm{q}}}{2} \left(\hat{a}_{\mathrm{q}}^{\dagger}\right)^2 \hat{a}_{\mathrm{q}}^2 + 2\chi_{\mathrm{qr}} \hat{a}_{\mathrm{q}}^{\dagger} \hat{a}_{\mathrm{q}} \hat{a}_{\mathrm{r}}^{\dagger} \hat{a}_{\mathrm{r}} \\ &+ \tilde{\omega}_{\mathrm{r}} \hat{a}_{\mathrm{r}}^{\dagger} \hat{a}_{\mathrm{r}} + \frac{\alpha_{\mathrm{r}}}{2} \left(\hat{a}_{\mathrm{r}}^{\dagger}\right)^2 \hat{a}_{\mathrm{r}}^2. \end{aligned} \tag{1.44}$$

Here, $\hat{a}_{\mathrm{q}}^{\dagger}$ and $\hat{a}_{\mathrm{q}}$ are the bosonic field amplitude operators of the qubit mode with fundamental transition frequency $\tilde{\omega}_{\mathrm{q}}$, and α_{q} is again the qubit anharmonicity. Due to the nonlinearity of the qubit circuit and the linear, transversal coupling, the resonator mode inherits a nonlinearity itself, captured by the resonator anharmonicty α_{r}. In most cases, this nonlinearity is small compared to the linewidth of the resonator, yielding a completely different response as discussed in Sec. 1.3.4. Conclusively, in this quantum optics picture, the dispersive interaction is a cross-Kerr interaction, an important concept revisited in the context of low-loss amplification with superconducting circuits.

1.2 Superconducting quantum circuits for hybrid architectures

The idea behind hybrid architectures is to combine different types of quantum degrees of freedom, for instance superconducting quantum circuits, spin and molecular qubits, and magnons, to achieve an operational performance of the combined system that couldn't be reached by the individual systems [232].

Preserving quantum coherence

In every quantum system discussed in the context of quantum computing, an optimal compromise between deliberate exchange of information and the preservation of the logical quantum state stored in the system has to be found [197]. At the end, what matters is the number of possible operations. The nuclear spin of atoms is an example for a quantum system which can be well isolated from its environment, and preserves the initialized quantum state for seconds [162] and even hours [239], outperforming most other qubit candidates. However, the high degree of isolation exacerbates the fast manipulation of the quantum state and the implementation of fast two qubit gates, which are technological prerequisites for quantum information processing. Therefore, systems allowing for the possibility to switch interactions on and off with high contrast deliberately, are of great value.

Boosting interactions with superconductors

Superconducting quantum circuits are particularly interesting for hybrid systems as they offer a high degree of control over the circuit parameters. Since the circulating currents and voltages give rise to electric and magnetic fields, their capabilities of combining them with other quantum systems are manifold. Moreover, the dissipationless energy transport provided by superconductors reduces local heating significantly.

Another practically unique property of superconductors is the kinetic inductance, an inductive contribution arising from the motion of the Cooper pairs, which can exceed the geometric inductance by orders of magnitude. Due to the kinetic inductance, the impedance of a superconducting circuit is not limited by the vacuum impedance, and the interaction between light and matter is not limited by the fine-structure constant [197]. Recently, high impedance superconducting resonators have been used to implement quantum buses between spin qubits in semi-conductor heterostructures [125, 154].

Demands on superconductors

In many hybrid systems, the application of strong, external magnetic fields is required for the control of at least one of the quantum systems [232]. Although the superconducting state is weakened by the presence of magnetic fields in most cases, as I will briefly discuss in the following sections, there are superconducting materials sufficiently resilient against magentic fields. Conventionally, the magnetic field resilience of a superconductor is expressed in a critical magnetic field B_c, which usually depends on the orientation of the field direction with respect to the plane of the superconducting thin film [214].

Another aspect is the operational temperature of the systems. In conventional (metallic) superconductors, the formation of Cooper pairs is linked to a characteristic energy scale. As a consequence, the superconducting state prevails only at temperatures below a critical temperature T_c. Additionally, even at electronic temperatures below the critical temperature normal-conducting excitations out of the superconducting ground state, the quasiparticles, are present, and although superconductors carry direct currents dissipationless, at finite frequencies, the excitation of quasiparticles adds dissipation to the circuit [93, 169, 220, 227].

In the following sections, I will briefly discuss the main requirements on superconductors in more detail: the effect of external magnetic fields on superconductors and the resulting consequences for quantum circuits, as well as the kinetic inductance naturally arising from the superconducting condensate. Finally, I will discuss the properties of a promising material: superconducting granular aluminum.

1.2.1 Superconductors in finite magnetic fields

For the operation of a superconducting quantum circuit in external magnetic fields, several effects have to be considered that can influence the performance of the circuit: the suppression of the superconducting gap and the critical temperature, the penetration of the thin film by Abrikosov vortices [4], and interference effects inside a Josephson tunnel junction [214].

Suppression of the gap parameter

In all superconductors, the application of an external magnetic field destroys the superconducting state eventually. The presence of a magnetic field breaks the time-reversal symmetry and lifts the energy degeneracy between electrons with opposite spin and momentum, which are predominantly involved in the formation of Cooper pairs. While the Zeeman splitting of the electron spin is independent of the field orientation with respect to the film plane, the effect on the orbital motion of the electrons is usually different for fields applied parallel and perpendicular [214].

In the Abrikosov Gor'kov theory, the strength of an external perturbation on the superconducting condensate is specified by the energy difference it causes between time-reversed electrons [214], and is referred to as the pair breaking strength $2\alpha_{\mathrm{PB}}$. If the pair breaking strength equals the BCS gap $\mathit{\Delta}_{00}$ in zero magnetic field and temperature, the superconducting state finally vanishes.

The characteristic parameters of a superconductor are the critical temperature T_{c}, the gap parameter $\mathit{\Delta}$, which is a measure of the pair correlation of two electrons, and the energy gap $\mathit{\Omega}_{\mathrm{G}}$ in the quasiparticle excitation spectrum. In zero magnetic field the gap parameter and the energy gap are not only identical and commonly referred to as the superconducting gap, but also related to the critical temperature according to the BCS theory [10]

$$\mathit{\Delta}_{\mathrm{BCS}}(T=0, B=0) = \mathit{\Delta}_{00} = 1.76 k_{\mathrm{B}} T_{\mathrm{c}}. \tag{1.45}$$

Although this relation does not strictly hold in the presence of external magnetic fields [208], it is used to approximate the dependence of the superconducting gap on the pair breaking strength from the behavior of the critical temperature. By applying a two-fluid model similar to the calculation of the kinetic inductance discussed in more detail in Sec. 1.2.2, the dependence

$$\frac{\mathit{\Delta}(\alpha_{\mathrm{PB}})}{\mathit{\Delta}_{00}} = \sqrt{\frac{1-2\alpha_{\mathrm{PB}}/\mathit{\Delta}_{00}}{1+2\alpha_{\mathrm{PB}}/\mathit{\Delta}_{00}}} \tag{1.46}$$

is found [214]. The pair breaking strength entering the equation depends on the physical origin of the external perturbation. For instance, the action of an external magnetic field applied in-plane with respect to a superconducting thin film is described by a quadratic relation between the pair breaking strength and the applied magnetic field $\alpha_{\mathrm{PB}} \propto B^2$, while it is a linear dependence $\alpha_{\mathrm{PB}} \propto B$ for out-of-plane fields [214]. Assuming that the superconductivity is destroyed above a critical magnetic field B_c, the dependence of the superconducting gap on the in-plane magnetic field is

$$\frac{\Delta(B)}{\Delta_{00}} = \sqrt{\frac{1-(B/B_\mathrm{c})^2}{1+(B/B_\mathrm{c})^2}}. \tag{1.47}$$

Magnetic field penetration

The response of superconductors towards external magnetic fields is generally divided into two different categories or types [214]: Superconductors of type-I expel the magnetic field from the inner volume of the superconductor, and remain in the so-called Meissner phase up to the point the superconducting state vanishes at the critical magnetic field B_c. To the contrary, type-II superconductors expel the magnetic field only up to a first critical field $B_{\mathrm{c},1}$, above which the superconductor enters an intermediate phase and is partially penetrated by the magnetic field in form of Abrikosov vortices, until the superconductivity is destroyed above the second critical field $B_{\mathrm{c},2}$.

In the Meissner phase, external magnetic fields are expelled by the induction of screening currents in a narrow region below the surface [151]. The thickness of this region is determined by the penetration depth λ. Provided the magnetic fields are homogeneous on the length scale of the BCS coherence length ξ_0, which is the characteristic length scale on which the pair correlation between two electrons with opposite spin and momentum decays, the penetration depth derived from BCS theory approaches the value found in the classical London theory [138].

The London theory is phenomenological and local, and assumes that the magnetic field exponentially decreases on the length scale of the London penetration depth λ_L. At zero-temperature, the London penetration depth is [214]

$$\lambda_\mathrm{L}(T=0) = \left(\frac{2m_\mathrm{e}}{\mu_0 n_\mathrm{s}(2e)^2}\right)^{1/2}. \tag{1.48}$$

Here, m_e is the electron mass, e is the elementary charge, μ_0 is the vacuum permeability, and n_s is the Cooper pair density.

Disordered superconductors

In superconducting materials with a short mean free path l of the electrons, the coherence length of the superconducting condensate is reduced and the ability of the condensate in screening external magnetic fields is weakened. This circumstance is captured by an effective penetration depth λ_{eff} [214]

$$\lambda_{\text{eff}} \approx \lambda_{\text{L}}(T) \left(1 + \frac{\xi_0}{l}\right)^{1/2} , \tag{1.49}$$

which is always larger than the London penetration depth. As a side note, for completeness, the coherence length ξ_0 entering the expression for the effective penetration depth can deviate from the BCS coherence length [214].

Vortex state

According to the phenomenological Ginzburg-Landau theory, the two types of superconductors are distinguished by their surface energy arising at interfaces between superconducting and normal-conducting regions. The sign of the surface energy depends on the ratio of the penetration depth and the coherence length. For a type-II superconductor, the penetration depth is much larger than the coherence length and the surface energy is negative, favoring the formation of normal-conducting regions separated from the superconducting regions by a circulating screening current, referred to as Abrikosov vortices. Each vortex carries a single magnetic flux quantum $\Phi_0 = h/(2e)$.

In thin films of superconductors, for which the penetration depth is comparable to the film thickness, the screening potential of the condensate is usually reduced additionally, as the mean free path is smaller due to scattering at the film boundaries. As a consequence, superconductors that are of type-I in bulk can become type-II superconductors in thin films. Although magnetic vortices constitute regions of reduced superconducting gap, acting as sinks or traps for quasiparticles, the uncontrolled motion of vortices can induce noise to a quantum circuit [211].

Interference effects in Josephson junctions

Similar to the flux quantization in superconducting loops and Abrikosov vortices, the magnetic flux Φ enclosed in a JJ perpendicular to the tunnel contact is quantized in multiples of the magnetic flux quantum Φ_0. The area A considered in the case of a JJ, the equivalent to the loop area in a SQUID, is determined by the width b of the JJ, the thickness of the insulating barrier d, and the penetration depth λ, as illustrated in Fig. 1.13a. As long as the inductance of the superconducting electrodes is small, screening effects are negligible, and the enclosed flux is equal to the external flux Φ_{ext}.

If the applied external flux deviates from integer multiples of the magnetic flux quantum, the supercurrent density $J(x)$ across the JJ oscillates sinusoidally as a function of the position coordinate x. As a consequence, the net supercurrent I across the JJ becomes a function of the external magnetic flux. For JJs with a rectangular shape, and assuming a homogeneous external magnetic field B_{ext} and critical current density j_{c}, the dependence of the maximal supercurrent on the external magnetic flux is [214]

$$I(\Phi_{\mathrm{ext}}) = I_{\mathrm{c}} \left| \frac{\sin(\pi\Phi_{\mathrm{ext}}/\Phi_0)}{\pi\Phi_{\mathrm{ext}}/\Phi_0} \right| . \tag{1.50}$$

As shown in Fig. 1.13b, the obtained supercurrent beyond the central maximum is significantly smaller than in zero-field even if the condition for constructive interference is met. In case the JJ is embedded in a tank circuit, the suppression of the critical current caused by a destructive interference lowers the transition frequency of the circuit significantly [196].

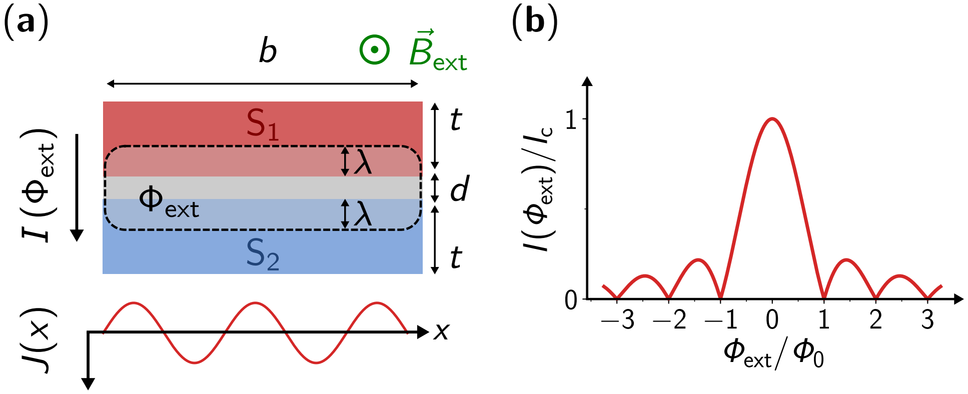

Figure 1.13: Josephson tunnel junction: Interference effects. a) Cross section of a conventional JJ sandwich structure composed of two superconducting electrodes of thickness t, denoted S_1 (red) and S_2 (blue), separated by a thin insulating layer (grey) of thickness d. Similar to a superconducting loop, the magnetic flux Φ_{ext} enclosed in the area around the tunnel contact determined by the penetration depth λ and indicated by the black dashed line, is quantized and an integer multiple of the magnetic flux quantum Φ_0. In the presence of an external magnetic field $\vec{B}_{\mathrm{ext}}$ (green) oriented in parallel to the plane of the JJ, the supercurrent density $J(x)$ oscillates sinusoidally along the JJ. As a consequence, the maximal net supercurrent $I(\Phi_{\mathrm{ext}})$ across the JJ becomes a function of the external magnetic field. **b)** Characteristic oscillation of the maximal supercurrent, normalized by the critical current in zero-field I_{c}. At integer multiples of the magnetic flux quantum, except at zero-field, the supercurrent is completely suppressed.

In practical terms, for a magnetic field applied in-plane, the relation between the enclosed magnetic flux Φ_{ext} and the external magnetic field B_{ext} is

$$\Phi_{\mathrm{ext}} = B_{\mathrm{ext}} b \left(d + 2\lambda \right) . \tag{1.51}$$

Hence, the modulation period of the critical current depends on the physical dimension of the JJ: assuming a vertical expanse of $d + 2\lambda = 40\,\mathrm{nm}$, a $b = 50\,\mathrm{nm}$ wide JJ would be suppressed at 1 T, and already significantly limited in its applicability at much smaller fields. As a side note, the obtained result is only valid if the width of the JJ is significantly smaller than the Josephson penetration depth [216].

1.2.2 Kinetic inductance in superconductors

Any wire made from a conductive material gives rise to a linear geometric inductance which creates a magnetic field surrounding the wire according to Maxwell's equations if a current flows through it. Although the magnitude of the geometric inductance generally depends on the dimension and shape of the wire, it is usually on the order of a few tens of pH/µm. In a superconductor, another inductive contribution arises from the kinetic motion of the Cooper pairs. Due to scattering effects of the electrons, the Cooper pairs inside a superconductor experience a finite inertia against the acceleration caused by an alternating electric field. The effect of the inertia on the response of the system, i.e. the current, is similar to the delay observed in an inductor, and is referred to as the kinetic inductance. In contrast to the geometric inductance, it depends on the microscopic properties of the superconducting material, and is not associated with an external magnetic field surrounding the wire, but rather a magnetic flux inside the wire. In pure superconductors, for instance aluminum, the magnitude of the kinetic inductance is usually only a fraction of the geometric inductance, but can be orders of magnitude larger in disordered or granular superconductors, reaching values up to $\sim$ nH/µm.

Complex conductivity

The response of a superconductor to an alternating electric field is described by the electrical conductivity σ, which is generally frequency dependent and relates the current density $\vec{J}$ with the electric field $\vec{E}$. For a one-dimensional wire, the relation is [214]

$$J = \left(\sigma_1(\omega) + i\sigma_2(\omega) \right) E. \tag{1.52}$$

While the real part $\sigma_1(\omega)$ accounts for energy loss in the material, the imaginary part $\sigma_2(\omega)$ is a measure of the charge carriers inertia, and will be related to the kinetic inductance. Although the energy dissipation in a superconductor is zero for constant fields, it is generally non-zero at finite frequencies due to the presence of normal-conducting excitations of the superconducting ground state, the quasiparticles.

Even for excitation frequencies well below the superconducting gap ($\omega \ll 2\Delta/\hbar$) and temperatures well below the critical temperature ($T \ll T_{\mathrm{c}}$), non-equilibrium quasiparticles can be present in a superconductor [57, 107, 229]. Hence, in the *two-fluid model*[214], the response of a superconductor is described by a combination of a non-interacting superconducting, and a normal-conducting fluid.

At finite excitation frequencies $\omega \geq 0$, the real part of the total conductivity is dominated by the quasiparticles (index n), and the imaginary part is dominated by the condensate (index s)

$$\sigma(\omega) = \sigma_{1,\mathrm{n}}(\omega) - i\sigma_{2,\mathrm{s}}(\omega). \tag{1.53}$$

The physical implications of the complex conductivity for superconducting quantum circuitry can be better understood by translating Eq. 1.53 into the language of electrical engineering. In electrical circuits, the complex conductance plays the role of an admittance, which is the inverse of the impedance Z. In the spirit of the two-fluid model, the impedance of the superconductor is modeled with a parallel circuit consisting of a resistor R and an inductor L_{k}

$$\frac{1}{Z} = \frac{1}{R} - \frac{1}{i\omega L_{\mathrm{k}}} = \frac{A_{\mathrm{s}}}{l_{\mathrm{s}}}\sigma(\omega). \tag{1.54}$$

Here, l_{s} and A_{s} are the length and the cross section of the considered superconducting wire, respectively. The comparison between the terms on both sides of Eq. 1.54 yields an expression for the resistance R

$$R = \frac{l_{\mathrm{s}}}{A_{\mathrm{s}}}\frac{1}{\sigma_{1,\mathrm{n}}} = N_{\square}R_{\square}, \tag{1.55}$$

and an expression for the kinetic inductance L_{k}

$$L_{\mathrm{k}} = N_{\square}\frac{1}{t\omega\sigma_{2,\mathrm{s}}}, \tag{1.56}$$

where $N_{\square}$ is the number of squares of the wire, t is the film thickness, and $R_{\square} = 1/(\sigma_{1,n}t)$ is the sheet resistance. The interpretation of the obtained result is, that at finite excitation frequencies ω, the intrinsic inertia of the condensate gives rise to an reactive impedance, and, therefore is not a perfect shunt for the dissipative quasiparticle branch. Hence, the impedance of the circuit is enhanced due to the kinetic inductance of the condensate, but the presence of quasiparticles will introduce finite losses.

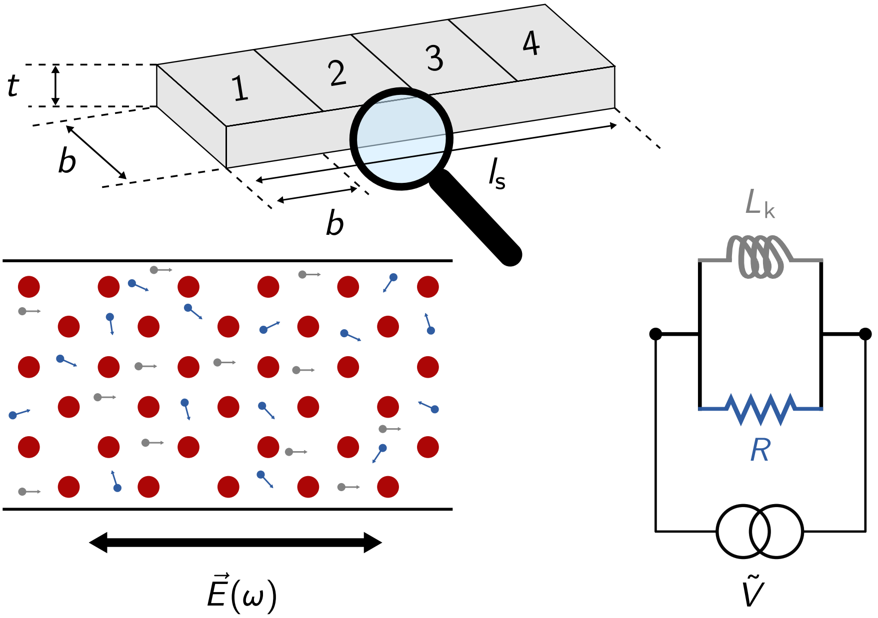

Figure 1.14: Kinetic inductance in superconductors. The grey cuboid illustrates a superconducting wire of width b and length l_s, patterned from a superconducting thin film of thickness t. The geometry of the wire, as seen from a top view, can be sectioned into squares. In many cases, the properties of the wire can be derived from the total number of squares or sheets $N_\square$ arising from the geometry, and the system parameters specified per sheet, for instance the sheet resistance $R_\square = \rho_\mathrm{n}/t$, where ρ_n is the normal-state resistivity of the material, or the sheet inductance $L_\square$. In a superconductor, the sheet inductance is generally a combination of a geometric contribution related to the wire geometry, and a kinetic contribution arising from the kinetic motion of the Cooper pairs. Since normal-conducting quasiparticles are usually present, the response of a superconductor towards an alternating electrical field $\vec{E}(\omega)$ is commonly described by a two-fluid model, as illustrated in the bottom left panel. While the quasiparticles (blue) are prone to inelastic scattering, for instance at the wire boundaries or impurities in the crystal lattice (red circles), adding dissipation to the system, the Cooper pairs (grey) propagate dissipationless but inherit a finite inertia, causing a time delay. Therefore, neglecting the geometric inductance, the electrical response of a superconducting wire can be mapped onto a parallel circuit composed of a resistive branch representing the quasiparticle, and an inductive branch representing the condensate. At finite excitation frequencies, the condensate is not a perfect shunt for the quasiparticle branch, and the presence of quasiparticles is dissipative. In disordered superconductors, the kinetic inductance can exceed the geometric inductance by orders of magnitude.

Mattis-Bardeen theory

An expression for the imaginary part of the conductivity in the superconducting state is found in the Mattis-Bardeen-theory (MBT) on the anomalous skin effect in normal and superconducting metals [150]. In the local ($l \ll \lambda_L$) and dirty limit ($l \ll \xi_0$), where l is the mean-free path of the electrons, the imaginary part of the superfluid conductivity $\sigma_{2,s}$ is related to the resistivity in the normal-conducting state ρ_n, and the kinetic inductance associated with the condensate is

$$L_\mathrm{k} = N_\square \underbrace{\frac{R_\square h}{2\pi^2 \mathit{\Delta}} \frac{1}{\tanh\left(\frac{\mathit{\Delta}}{2k_B T}\right)}}_{L_\square} . \qquad (1.57)$$

Here, T is the electronic temperature, $\mathit{\Delta}$ is the gap parameter, $R_\square = \rho_\mathrm{n}/t$ is the normal-state sheet resistance or resistance per square, and $L_\square$ is the sheet inductance. At temperatures well below the critical temperature ($T \ll T_\mathrm{c}$), the expression for the sheet inductance reduces to

$$L_\square = \frac{R_\square h}{2\pi^2 \mathit{\Delta}}. \qquad (1.58)$$

Based on these simple relations, provided the energy gap $\mathit{\Delta}$ or the critical temperature T_c are known, an estimate of the kinetic inductance emerging in the superconducting state is possible for a given geometry, by measuring the normal-state sheet resistance of the material at room temperature and extracting the total number of sheets from the circuit design. However in general, for distributed devices with a non-uniform current distribution along the superconductor, the energy participation of each part has to be taken into account in addition.

1.2.3 Superconducting granular aluminum

Superconducting granular aluminum (grAl) is a promising candidate for the application in hybrid architectures owing to its tunable and intrinsically nonlinear kinetic inductance [144, 198, 230], the large critical magnetic in-plane field [29, 43, 47], and low losses in the microwave regime [90, 91, 217, 230].

As its name indicates, the grAl microstructure is composed of crystalline aluminum (Al) grains embedded in an insulating, non-stoichiometric AlO_x matrix, which grows when Al is evaporated in an oxygen atmosphere. Even for a small amount of oxygen, separated Al grains form. The typical diameters are (3 ± 1) nm [54], but the grain size generally depends on the substrate temperature during the film deposition [3].

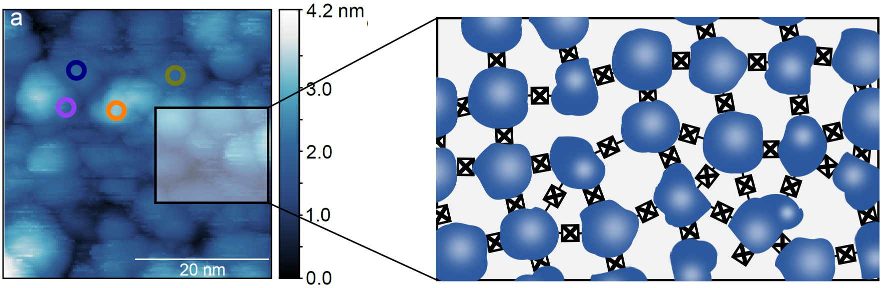

Figure 1.15: Granular aluminum microstructure. Scanning tunneling microscopy image (left-hand panel) of a granular aluminum (grAl) thin film, adapted from Ref. [234]. The microstructure of grAl consists of crystalline Al grains with diameters on the order of a few nanometer, which are embedded in an insulating, non-stoichiometric aluminum-oxide (AlO_x) matrix. Since the tunneling of Cooper pairs between neighboring grains gives rise to a nonlinear kinetic inductance similar to conventional JJs, the electrodynamics of grAl thin films are modeled as networks of JJs.

Similar to conventional JJ, the transparency of the insulating barrier separating neighboring grains allows for an inter-grain coupling via the Josephson effect, constituting the source of kinetic inductance and nonlinearity of superconducting grAl. Taking the results of the MBT for disordered superconductors summarized in Eq. 1.58 as a basis, the magnitude of the kinetic inductance is controlled by the normal-state resistivity ρ_n and the sheet resistance $R_\square = \rho_\mathrm{n}/t$ of the film. For grAl, the resistivity is controlled by the partial oxygen pressure in the evaporation chamber p_{O_2} and the Al evaporation rate r_Al, as shown in Fig. 1.16b.

The obtained sheet inductance in grAl thin films can be varied over three orders of magnitude reaching values up to nH/□ for films of $t = 10 - 20\,\mathrm{nm}$ thickness [90, 238]. So far, the kinetic inductance of grAl has been successfully used for the implementation of linear superinductors [91], promising circuit elements for new qubit concepts, and particle detectors [217]. However, the nonlinearity stemming from the grAl microstructure has not yet drawn much attention in the context of superconducting quantum circuits.

Another consequence of the grAl microstructure is a dome-shaped phase-diagram of the critical temperature T_c and the superconducting gap Δ_grAl observed in grAl thin films as a function of the normal-state resistivity ρ_n, with a maximum occuring between $\rho_\mathrm{n} = 100 - 1000\,\mu\Omega\,\mathrm{cm}$ [133, 181] (see Fig. 1.16a). While films evaporated on cold substrates $T \leq 100\,\mathrm{K}$ reach values up to $T_\mathrm{c} \geq 3\,\mathrm{K}$ [181], films evaporated on room-temperature substrates are limited to $T_\mathrm{c} \approx 2.2\,\mathrm{K}$ [133]. Despite numerous

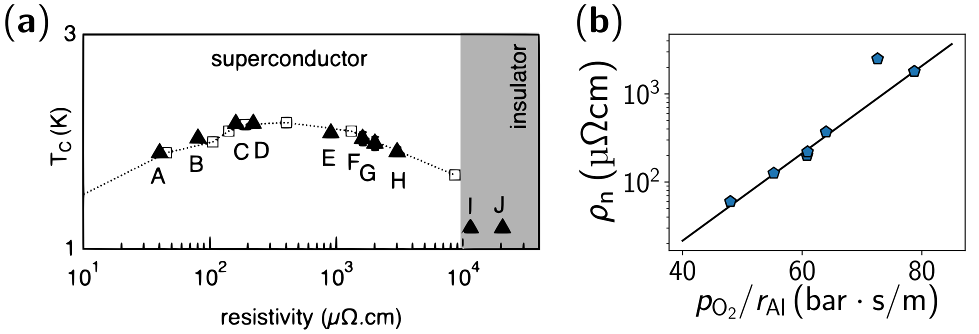

Figure 1.16: grAl: phase-diagram. a) Critical temperature T_c of grAl thin films as a function of the normal-state resistivity ρ_n constituting the grAl phase diagram. Adapted from Ref. [133]. The behavior observed for the superconducting gap Δ_{grAl} is similar. With increasing resistivity, the critical temperature increases until it reaches a maximum value, which depends on the substrate temperature during evaporation. Above a certain resistivity, the films do not become superconducting on a macroscopic scale and enter an insulating regime. **b)** Normal-state resistivity of grAl thin films measured at room temperature, plotted as a function of the ratio between the partial oxygen pressure in the evaporation chamber p_{O_2} and the Al evaporation rate r_{Al}. Notably, the evaporation rates are mean values, calculated from the film thickness and the duration of the evaporation. The black solid line indicates an exponential fit passing through the coordinate origin, excluding the outlier.

experimental investigations [9,47,54,133,181], an unambiguous physical explanation for the enhanced critical temperature is still missing.

Among the discussed explanations for the dome-shape is the competition between finite size effects in the Al grains enhancing the critical temperature [173], and an increase in the phase fluctuations of the superconducting order parameter with increasing normal-state resistivity, which eventually suppresses superconductivity on a macroscopic scale eventually [52]. Evidence obtained by optical spectroscopy measurements suggests a Mott-type superconductor-to-insulator transition driven by the increasing decoupling between the grains and an increasing electrostatic charging energy [160], supporting the notion of well separated grains rather than disorder on the atomic scale. A comprehensive overview on superconducting grAl in the literature is given in Ref. [89].

Quantum electrodynamics

Motivated by the grAl microstructure, the quantum electrodynamics of grAl thin films can be modeled with the aid of effective arrays of JJs. For geometries favoring a unidirectional current along the film, for instance rectangular-shaped stripline

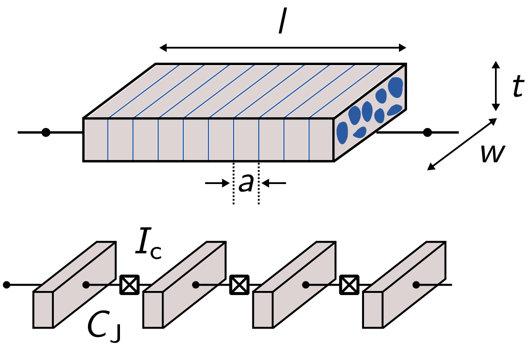

Figure 1.17: grAl: effective circuit model. Graphical illustration of a rectangular-shaped grAl strip with volume $V_{\mathrm{grAl}} = l \times w \times t$. For the prediction of the cQED properties, the film is divided into equally sized segments of length a, which are thought of being separated by insulating barriers, forming a one-dimensional array of effective JJs. The critical current I_{c} associated to each effective JJ is determined by the critical current density j_{c}, an intrinsic property of the film, and the cross section of the segment $A = w \times t$, a property of the geometry: $I_{\mathrm{c}} = j_{\mathrm{c}}/(w \times t)$. The effective junction capacitance C_{J} is expected to be large, but determining a value experimentally is generally difficult.

resonators or more generally geometries with a large aspect ratio, the dimensions of the effective array can be reduced to one [144].

In the one-dimensional limit, the total grAl volume V_{grAl} is divided into segments of volume $a \times w \times t$, where a is the length of an effective junction, and w and t are the width and the thickness of the film, respectively, as shown in Fig. 1.17. Therefore, the total number of effective junctions of a rectangular strip is $N = l/a$, which is also the total number of degrees of freedom considered in the model.

Provided the zero-point fluctuations of the phase difference between neighboring grains are small, the nonlinearity emerging from the inter-grain coupling can be treated perturbatively, similar to the transmon qubit [116] (see also Sec. 1.1.3). The corresponding quantum optics Hamiltonian of such a weakly nonlinear multi-mode system is

$$\hat{H} = \sum_{m=0}^{N-1} \hbar\omega_m \hat{a}_m^\dagger \hat{a}_m + \underbrace{\frac{\hbar}{2} K_{m,m} \omega_m \hat{a}_m^\dagger \hat{a}_m \hat{a}_m^\dagger \hat{a}_m}_{\mathrm{self-Kerr}} + \underbrace{\sum_{m,k=0}^{N-1} \frac{\hbar}{2} K_{m,k} \omega_m \hat{a}_m^\dagger \hat{a}_m \hat{a}_k^\dagger \hat{a}_k}_{\mathrm{cross-Kerr}}, \qquad (1.59)$$

where ω_m are the N eigenmodes of the model, and $K_{m,m}$ and $K_{m,k}$ are the self-Kerr and cross-Kerr coefficients, respectively. The model prediction for the self-Kerr coefficient of the fundamental mode K_{11} is

$$K_{11} = -\mathcal{C}\pi e a \frac{\omega_1^2}{j_\mathrm{c} V_\mathrm{grAl}}, \tag{1.60}$$

where $\mathcal{C}$ is a numerical factor close to unity, generally depending on the standing-wave pattern of the current, and e is the electron charge [144]. Consequently, for a given frequency ω_1, the implementation with the smallest volume and lowest critical current density j_c offers the largest nonlinearity.

Critical current density

Besides the resonance frequency and the grAl volume, the prediction of the expected self- and cross-Kerr coefficients requires the knowledge of the critical current density j_c in grAl films. Similar to conventional JJ, the critical current density is a measure of how much dissipationless supercurrent the film can sustain per unit area, and is expected to decrease with increasing normal-state resistivity, i.e. decreasing inter-grain coupling.

In order to determine the critical current density j_c, switching current measurements of grAl direct current superconducting quantum interference devices (dc SQUIDs) were performed [78]. Similar to a single JJ, a dc SQUID switches into the resistive state above a certain bias current, denoted the switching current I_sw, as discussed in App. D. Since a dc SQUID is composed of two JJ embedded in a superconducting loop, the switching current modulates with the flux enclosed in its loop (see App. E). For the investigated grAl SQUIDs, the two JJs are defined by geometric constrictions in the loop wire, forming regions of reduced critical current and therefore higher switching probability. Even though the film geometry is continuous, suggesting a superconducting weak link behavior [134], the switching dynamics are dominated by the inter-grain coupling, as a result of the grAl microstructure and the short grAl coherence length [78].

Generally speaking, the switching into the resistive state is a probabilistic process, and reflects the interplay between the energy potential defined by the SQUID in the presence of a finite bias current, and the properties of the condensate [15]. The switching behavior can be described by the motion of an effective phase particle in the two-dimensional SQUID potential under the action of gravity and friction [214]. If a supercurrent is sustained by the SQUID, the phase particle is trapped in a local minimum, but as soon as it escapes, it enters the so-called running state in which a finite voltage drop occurs according to the second Josephson equation

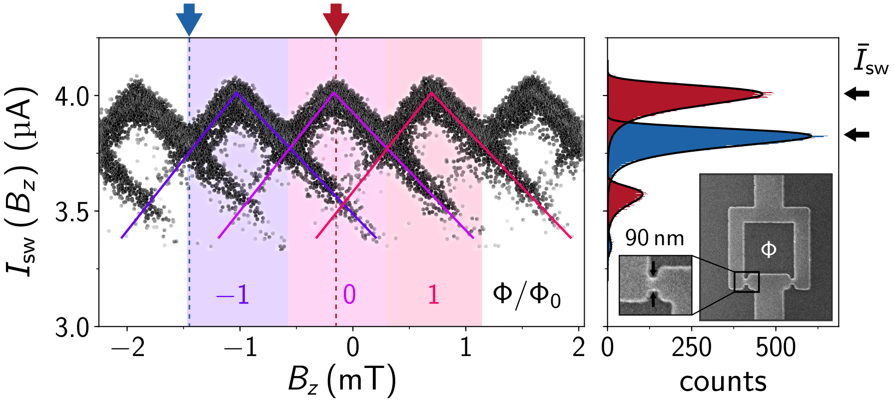

Figure 1.18: grAl dc SQUID: switching current measuerments. Switching current I_{sw} of a dc SQUID patterned from a single grAl thin film with normal state resistivity $\rho_{\mathrm{n}} = 1520\,\mu\Omega\,\mathrm{cm}$, measured as a function of the external field B_z applied perpendicular to the SQUID loop. The SQUID design contains two identical geometric constrictions of width $w = 90\,\mathrm{nm}$ constituting regions of reduced critical current and therefore elevated switching probability. The critical current density is calculated from the maximal switching current in zero-field and the cross section of the geometric constriction $j_{\mathrm{c}} = \bar{I}_{\mathrm{sw}}(0)/(tw)$. Due to the large loop inductance, the magnetic flux modulation of the switching current is highly suppressed, including the observation of excited flux states, as indicated by the colored lines [129]. The right-hand panel shows two switching current histograms measured at zero (red) and maximal (blue) SQUID frustration, with the black lines indicating fits to the obtained distributions.

(see Sec. 1.1.2). Although the escape mechanism is generally complex, including a possible retrapping of the particle after an escape has occurred, an important consequence of the dynamical process is that the measured switching current is not necessarily even close to the critical current of the device. Premature switching caused by thermal activation [34, 120] and macroscopic quantum tunneling [60], especially in devices with small Josephson energy, can cause significant deviations. However, by implication, the measured switching current approaches the critical current with increasing Josephson energy (see App. D).

Figure 1.18 depicts the periodic modulation of the measured switching current with the magnetic field B_z applied perpendicular to the SQUID loop. The triangular shape can be explained by the large loop inductance, which suppresses not only the modulation amplitude, but also allows for excited fluxon states, i.e. different numbers of flux quanta trapped in the SQUID loop [129]. As shown in the right-hand panel, for each bias field, the switching current follows a characteristic distribution from which the value $\bar{I}_{\mathrm{sw}}$ with highest probability can be extracted [122]. Additional information about the switching process is contained in the distribution width [78].

For the presented device, the obtained switching current is $\bar{I}_{\mathrm{sw}} \approx 4\,\mu\mathrm{A}$, and the corresponding Josephson energy is well above the ambient thermal energy at cryogenic temperatures $E_\mathrm{J}/k_\mathrm{B} \gg 1\,\mathrm{K}$, i.e. the influence of thermally activated premature switching is small. Therefore, the critical current density is calculated from the measured switching current in zero-field $\bar{I}_{\mathrm{sw}}(0)$ and the combined cross sections of the two constrictions

$$j_\mathrm{c} = \frac{\bar{I}_{\mathrm{sw}}(0)}{2t(w_1 + w_2)}, \tag{1.61}$$

where w_1 and w_2 are the widths of the two geometric constrictions, and t is the film thickness. For the device shown in Fig. 1.18, the thickness and widths are $t = 20\,\mathrm{nm}$ and $w_1 = w_2 = 90\,\mathrm{nm}$, respectively, yielding a critical current density $j_\mathrm{c}(1520\,\mu\Omega\,\mathrm{cm}) = 1.1\,\mathrm{mA}/\mu\mathrm{m}^2$.

From similar switching current measurements performed on devices with a similar SQUID geometry but fabricated from different grAl thin films, the relation between the critical current density and the normal-state resistivity was deduced, with the results shown in Fig. 1.19. As expected, the critical current density decreases with increasing normal-state resistivity, and is found to follow a power-law $j_\mathrm{c} \propto \rho_\mathrm{n}^{-1.3}$. More information on the devices is given in App. D.

A more detailed report on the switching current experiments performed on grAl SQUIDs is found in Ref. [78], including a discussion about the observed diffusive motion of the effective phase particle.

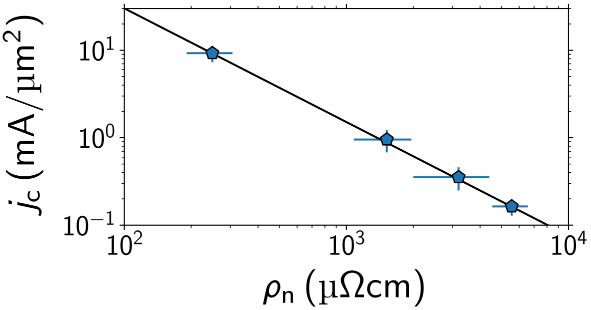

Figure 1.19: grAl: critical current density. Critical current density j_c of various superconducting grAl thin films with different normal-state resistivity ρ_n. The critical current densities are calculated according to Eq. 1.61 from the zero-field switching current $\bar{I}_{\mathrm{sw}}(0)$ measured in dc SQUIDs, similar to the device shown in Fig. 1.18, and the cross-section of the geometric constrictions extracted from scanning-electron-microscopy images. With increasing normal-state resistivity ρ_n, the critical current density decreases with a power law $j_\mathrm{c} \propto \rho_\mathrm{n}^{-1.3}$ as indicated by the black solid line.

1.3 Quantum-limited amplification

For the operation of superconducting quantum circuits, a low ambient temperature well below the critical temperature T_c of the superconducting material is required, mainly to prevent the thermal excitation of quasiparticles. Since the critical temperature is on the order of a few kelvin for the most commonly used superconducting materials, such as thin film aluminum ($T_\mathrm{c} \approx 1.4\,\mathrm{K}$) [111] and the niobium compounds ($T_\mathrm{c} \geq 8\,\mathrm{K}$) [118], but also in more recently applied materials like granular aluminum ($T_\mathrm{c} \geq 1.4\,\mathrm{K}$) [91, 133, 181, 238] and tantalum ($T_\mathrm{c} = 4.3\,\mathrm{K}$) [177], the devices are mounted in a cryogenic experimental setup operated at a few tens of millikelvin. Although the devices have to be thermally isolated from the environment outside the measurement setup, until today the signal processing is still carried out at room temperature, imposing an exceptional importance to the connection between the device and the signal detector.

In the early years, the pioneers of cQED dreamed of a QND readout with a signal-to-noise ratio (SNR) sufficient to detect the qubit state within an integration time on a par with the coherence time of the circuit, enabled by the strength of the readout signal [24]. However, the experimental observation is a renormalization of the qubit lifetime with increasing signal strength [155], i.e. the occupation of the readout resonator, and a non-QND behavior of the readout [209]. Although the breakdown of the dispersive approximation above a critical occupation number, accompanied by the breakdown of the QND property of the readout was known from the beginning [24], the origin of the much more pronounced lifetime renormalization is still under strong debate [145, 174]. A consequence of the experimentally encountered limit on the signal strength was the improvement of the SNR by reducing the noise in the measurement chain.

In cQED experiments, the energy scale of the signal photons carrying information about the qubit's quantum state is in the range of a few gigahertz. Guided through coaxial cables, the electrical field of the propagating photons can be linked to a voltage which is detected at room temperature. Since the equivalent voltage of a microwave photon in a $50\,\Omega$ environment is extremely small compared to the thermal voltage fluctuations at room temperature, the signal has to be amplified by several orders of magnitude. Although every amplifier adds noise to the signal and degrades the SNR inherently [40, 98], in a chain of amplifiers, the SNR is determined by the first amplifier stage provided its power gain, the ratio between the outgoing to the incident power in a linear amplifier, is sufficient to saturate the noise of the following amplifier stage(s). Consequently, the first amplifier stage should be the amplifier with the best noise performance.

The amount of added noise depends strongly on the implementation of the amplifier, and is conventionally referred back to the input port of the amplifier. In this way, the quoted added noise is independent of the amplification, and is therefore comparable between different amplifiers. Fundamentally, there is a lower bound on the precision with which two conjugate variables can be measured at the same time, denoted the quantum limit [46]. For a bosonic amplifier, the quantum limit is half a photon of added noise per unit time and bandwidth [40], which is significantly lower than the added noise of common commercial amplifiers, for instance state-of-the-art high-electron-mobility-transistor (HEMT) amplifiers [140]. With the advent of SQCs twenty years ago, a type of bosonic amplifier has gained renewed interest, and, since then, has repeatedly proven to reach the quantum limit: the superconducting parametric amplifier.

Besides the noise performance, there are other properties essential for the operation of an amplifier, which are briefly introduced in the following Sec. 1.3.1. After a basic understanding of amplifiers is established, the noise performance of an amplifier chain is discussed in Sec. 1.3.2, followed by a brief discussion about the working principle of parametric amplifiers in Sec. 1.3.3 and Sec. 1.3.4, and a summary of common amplifier terminology and the classification of parametric amplifiers in Sec. 1.3.5.

1.3.1 Basics of amplification

Independent of the physical implementation, there are several figures of merit consulted to assess the performance of an amplifier. Conceptually, an amplifier is a two-port device that receives a signal through its input port, and sends out an amplified version through its output port, as illustrated in Fig. 1.20. Notably, the input and output port can be located at the same physical port. In the simplest form, the outgoing power P_{out} is linearly related to the incident power P_{in},

$$P_{\text{out}} = G(\omega) P_{\text{in}}, \tag{1.62}$$

where $G(\omega) = P_{\text{out,on}}/P_{\text{out,off}}$ is the frequency dependent *power gain*, the ratio between the output power with (on) and without (off) the amplifier being operated. Amplifiers that fulfill this criterion are denoted *linear amplifiers*.

For most linear amplifiers, the linear regime of operation is only a part of the full range of operation, and eventually, the power gain will start to become nonlinear with increasing incident power. The signal power range in which the linearity of amplification prevails, is referred to as the *dynamic range* of the amplifier. Closely related to the dynamic range is the *saturation power*: amplification requires the

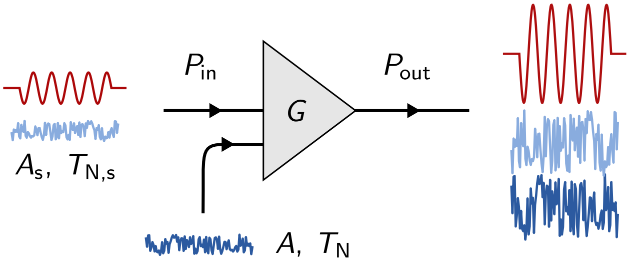

Figure 1.20: Schematic representation of an amplifier. The amplifier (triangle) has a conceptual input and output port, which, however, can be the same physical port. The periodic signal (red) and the noise incident to the input port of the amplifier (light blue) are amplified. For a linear amplifier, the relation between incident and outgoing power is linear $P_{\text{out}} = G(\omega)P_{\text{in}}$, where the power gain $G(\omega)$ is the magnitude of amplification. The noise added by the amplifier (dark blue) is usually referred back to its input port, and accounted for by introducing a second, artificial noise port. The amount of added noise is quantified by an added noise number A or alternatively by a noise temperature T_N, with similar quantities A_s and $T_{\text{N,s}}$ defined for the noise already carried by the signal.

transfer of energy from an energy reservoir onto the signal, but for every amplifier, the utilized physical process is usually limited to a certain input power, above which the power gain starts to diminish. Conventionally, the saturation power in parametric amplifiers is defined as the 1 dB compression point, the signal power P_{in} at which the maximal power gain G_0 is reduced by 1 dB.

$$P_{1\,\text{dB}} = P_{\text{in}}\big|_{G=G_0-1\,\text{dB}} \tag{1.63}$$

Another important characteristic of an amplifier is the *instantaneous bandwidth* B, the frequency domain in which amplification occurs. As mentioned above, the power gain is a function of frequency, and the instantaneous bandwidth is defined as the frequency domain in which the power gain is not lower than 3 dB compared to the maximal power gain G_0 (see Fig. 1.21). In the context of cQED, the required instantaneous bandwidth is at the minimum the linewidth of the readout resonator, which is typically on the order of a few megahertz.

In addition to the constraints on the instantaneous bandwidth, the amplifier's range of operation has to be aligned with the signal frequency at the same time. Therefore, the center of the power gain has to be frequency tunable in case the instantaneous bandwidth is not significantly larger than the linewidth of a readout resonator. The maximal tunability of the power gain is referred to as the *bandwidth* of the amplifier, and, the larger the bandwidth is, the more versatile the amplifier is. For cQED experiments, the signal frequency is usually in the range $1-10\,\text{GHz}$. In the ideal case, a single amplifier covers the whole frequency domain.

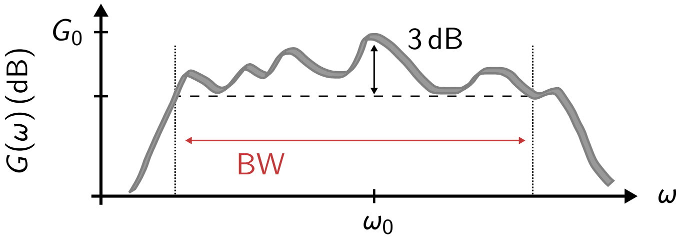

Figure 1.21: Power gain and instantaneous bandwidth. Power gain G in decibel as a function of the incident signal frequency ω. In general, the instantaneous bandwidth of an amplifier is defined as the frequency domain in which the supplied power gain is not more than 3 dB lower than the maximal power gain G_0.

Based on the figures of merit discussed in this section, there are many different types of amplifiers that outperform superconducting parametric amplifiers by far, despite the enormous effort spent during the last decades. Until today, the ideal superconducting amplifier is not yet found. However, the general performance of an amplifier becomes peripheral in case the amplifier adds too much noise to the signal, since the only purpose of parametric amplifiers in the context of cQED is the improvement in SNR compared to commercial alternatives.

1.3.2 The measurement efficiency

The quantum or measurement efficiency η of an experiment determines how close the measurement apparatus approaches the quantum limit — the lower bound on the measurement accuracy determined by the principles of quantum mechanics [46] — which can be inferred from the noise in the detected signal [97]. In general, the detected noise is a combination of the intrinsic noise carried by the signal itself, and the inevitable noise added by the amplifier stages of the experimental apparatus. Circuit QED experiments are performed with bosonic signals, and the measurement observables are related to the quadrature operators

$$\hat{I} = \frac{1}{2}(\hat{a}^\dagger + \hat{a}) \qquad \hat{Q} = \frac{i}{2}(\hat{a}^\dagger - \hat{a}), \tag{1.64}$$

which constitute the real and imaginary part of the field amplitudes and obey a non-zero commutation relation $[\hat{I}, \hat{Q}] = i/2$. Similar to the position and momentum of a quantum particle, the commutation relation causes a lower bound on their combined variances $\Delta I \Delta Q \geq 1/4$ (see App. B.1). In other words, the readout signal contains at least noise in form of quantum fluctuations.

The uncertainty can be translated into a number of noise photons $A_\mathrm{s} \geq 1/2$ carried by the signal per unit time and bandwidth, where the lower bound corresponds to the vacuum fluctuations already encountered as the ground state fluctuations in the quantum harmonic oscillator (see Sec. 1.1.1). Coherent states are an example of bosonic states satisfying the lower bound independent of their amplitude, with noise equally distributed in both quadratures $\Delta I = \Delta Q$ (see Fig. 1.22 and App. B.1). Although not further pursued in the scope of my thesis, there are so-called squeezed states of light for which the uncertainty is distributed non-uniformly [225].

In addition to the intrinsic uncertainty of the observables, typical cQED experiments involve several amplifier stages, whereof all degrade the SNR by adding noise to the signal. In a chain of amplifiers without losses between the individual stages (see Fig. 1.22), the total added noise number A_meas per unit time and bandwidth, referred back to the input port of the first amplifier stage, is

$$A_\mathrm{meas} = A_\mathrm{s} + A_1 + \frac{A_2}{G_1} + \frac{A_3}{G_1 G_2} + ..., \tag{1.65}$$

where A_i and G_i are the added noise number and power gain of the i th amplifier stage [37]. Provided the power gain of the first amplifier stage is large compared to the noise added by the second amplifier stage ($G_1 \gg A_2$), the added noise of the measurement setup is dominated by the first amplifier stage. Notably, another way of expressing the noise performance is the noise temperature, an effective temperature derived from the energy associated with the noise photons [40]. Although the noise temperature is commonly quoted for commercial amplifiers, I find it less intuitive since the temperature associated with the quantum limit is frequency dependent.

For a linear bosonic and phase-preserving amplifier, i.e. a device amplifying both signal quadratures by the same amount, the quantum limit of added noise A is found to originate from quantum fluctuations. According to the Haus-Caves theorem [40, 98], the added noise number is

$$A = \frac{1}{2}\left|1 - \frac{1}{G}\right|, \tag{1.66}$$

constituting the lower bound on the noise added by the experimental apparatus.

Figure 1.22 illustrates the amplification process in a setup containing three amplifier stages. Incident to the input port of the amplifier chain is a coherent state with amplitude $|\langle \hat{a}_\mathrm{in} \rangle|$ and (arbitrary) phase ϕ, represented in the quadrature plane and in the rotating-frame of the carrier frequency ω. The noise is normally distributed in both quadratures, with the corresponding standard deviations around the expectation value of the signal denoted σ_I and σ_Q. The outgoing signal has an increased amplitude,

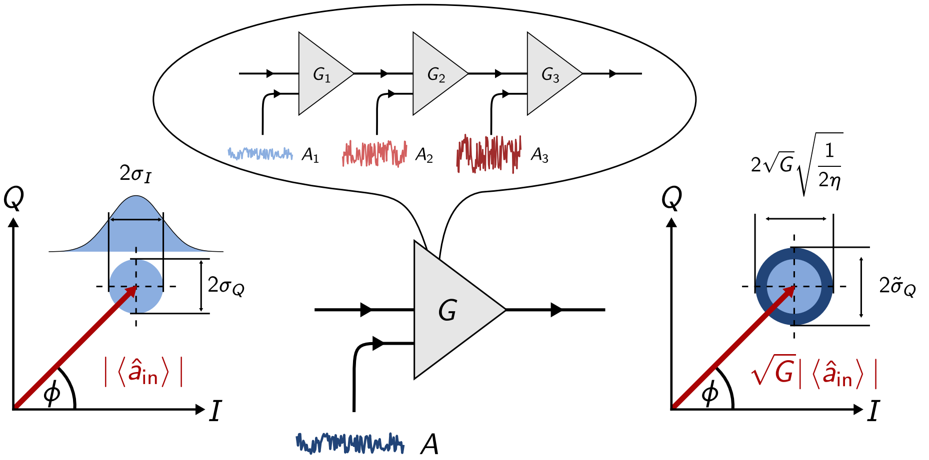

Figure 1.22: Measurement efficiency of an amplifier chain. The action of an amplifier chain composed of three individual amplifiers can be mapped onto a single device, with power gain $G = G_1G_2G_3$ and effective added noise number A (Eq. 1.65). The signal incident to the amplifier chain is a single coherent state (red) with amplitude $|\langle\hat{a}_{\text{in}}\rangle|$ and (arbitrary) phase ϕ, and is illustrated in the complex or quadrature plane spanned by I and Q. In the rotating frame of its carrier frequency ω, the phase is time-independent. The noise (light blue) is phase-insensitive and equally distributed in both quadratures. After the amplification, the signal amplitude is increased by a factor $\sqrt{G}$. Besides the amplified signal noise (light blue), the total noise in the output mode contains an additional contribution owing to the noise added by the amplifier chain (dark blue). The measurement efficiency $0 \leq \eta \leq 1$ determines how close the measurement setup approaches the quantum limit.

scaled by the square root of the total power gain $\sqrt{G}$, and carries additional noise due to the noise added by the amplifier chain.

The measurement efficiency can be defined as the ratio between the lowest achievable variance σ^2_{ideal} and the actually measured variance σ^2 in the outgoing field:

$$\eta = \frac{\sigma^2_{\text{ideal}}}{\sigma^2}. \tag{1.67}$$

For a coherent state prepared in the readout resonator of a cQED experiment, and a quantum-limited, phase-preserving amplification chain, the ideal variance is $\sigma^2_{\text{ideal}} = \sigma^2_I = \sigma^2_Q = 1/2$, i.e. a total of one noise photon per unit time and bandwidth in both quadratures combined. A description on how to determine the measurement efficiency is given in Ref. [97] and Ref. [220], and experimentally demonstrated in Sec. 3.8 with a superconducting parametric amplifier.

1.3.3 The principle of parametric amplification

In a parametric amplifier (paramp), a weak signal is amplified by the periodic modulation of one of the system parameters with time, which can be the refractive index in an optical medium [48, 75], or the resonance frequency of a mechanical oscillator [192] or an electrical circuit [103].

The working principle of a paramp can be understood under the classical considerations of a simple harmonic oscillator formed by a parallel circuit of a capacitor and an inductor. The charge residing on the capacitor plates oscillates at the natural resonance frequency $\omega_0 = 1/\sqrt{LC}$ of the circuit between the values $+|Q|$ and $-|Q|$. The oscillating current through the inductor lacks behind by a quarter period. If either the capacitance or the inductance is modulated with time, energy can be transferred to the system, or pulled out of it, depending on the frequency and the phase of the modulation.

More precisely, assuming the capacitor plates are movable and are pulled apart against the Coulomb force every time the capacitor is charged, followed by a restoration of the initial configuration when the voltage across the capacitor is zero, mechanical energy is parametrically converted into electrical energy, alongside with an increase of the oscillating charge amplitude $|Q|$. If the external modulation is carried out in the exact opposite order, equivalent to a phase shift of π, energy is drawn off the resonance. The same operational principle is realized by increasing and decreasing the inductance periodically. Independent of which circuit element is modulated with time, the modulation has to take place at twice the resonance frequency for the given system.

Historically, the first parametric amplifiers based on electrical circuits exploited the nonlinear capacitance of varactor diodes [103]. In superconducting paramps, the modulation of the resonance frequency is enabled by the nonlinear inductance arising in superconducting thin films or JJs [189], i.e. the oscillating current itself modulates the resonance frequency of the system.

1.3.4 Josephson parametric amplifiers

The simplest implementation of a parametric amplifier with superconducting circuits, a Josephson parametric amplifier (JPA), is composed of a single JJ with critical current I_c and Josephson energy $E_J = \Phi_0 I_c/(2\pi)$, shunted by a capacitor C. Similar to the transmon qubit [116], JPAs are operated in the limit $E_J \gg E_c$ of the charge qubit Hamiltonian [30, 166, 206], and, thus the nonlinearity is treated perturbatively [168]. The corresponding quantum optics Hamiltonian is

$$\hat{H}_{\mathrm{JPA}} = \hbar\omega_0 \hat{a}^\dagger \hat{a} + \hbar \frac{K}{2} \hat{a}^\dagger \hat{a}^\dagger \hat{a}\hat{a}, \tag{1.68}$$

where $\hat{a}^\dagger$ and $\hat{a}$ are the bosonic single-mode creation and annihilation operators for the intra-cavity field, respectively, ω_0 is the resonance frequency, and K is the self-Kerr coefficient. In comparison to the transmon qubit, a JPA is operated in the limit $K \ll \kappa$, meaning that the frequency shift per photon is much smaller than the linewidth of the mode. Therefore, driving the JPA results in a continuous shift of the resonance frequency with power rather than in a spectrum composed of discrete energy levels.

For the operation of the single mode or degenerate JPA, a strong classical pump tone is applied close to resonance to drive the circuit into a nonlinear regime in which the response of the JPA around a classical steady-state is highly susceptible to small perturbations, for instance caused by the weak quantum signal. Following Ref. [68], a brief discussion about the operational principle and the main features of a JPA is given based on the input-output formalism [80]. A more detailed version is found in App. B.3.

Classical steady-state

The average number of photons circulating inside a degenerate JPA under continuous pumping is determined by a dimensionless, nonlinear equation [68]

$$\left(\delta^2 + \frac{1}{4}\right)\bar{n} - 2\delta\xi\bar{n}^2 + \xi^2\bar{n}^3 = 1, \tag{1.69}$$

where

$$\delta = \frac{\omega_{\mathrm{p}} - \omega_0}{\kappa + \gamma}, \qquad \bar{n} = \frac{|\alpha|^2}{|\tilde{\beta}_{\mathrm{in}}|^2}, \qquad \tilde{\beta}_{\mathrm{in}} = \frac{\sqrt{\kappa}\beta_{\mathrm{in}}}{\kappa + \gamma}, \qquad \xi = \frac{K|\tilde{\beta}_{\mathrm{in}}|^2}{\kappa + \gamma}. \tag{1.70}$$

The first quantity δ is the frequency detuning between the pump frequency ω_{p} and the bare resonance frequency ω_0 of the JPA, scaled by the total linewidth $\kappa + \gamma$, which itself is determined by the coupling rate to the input port κ and the rate γ at which energy is lost to uncontrolled degrees of freedom. The second quantity $\bar{n}$ represents the mean number of photons inside the cavity $|\alpha|^2$ normalized by the number of incident pump photons. The dimensionless drive amplitude $\tilde{\beta}_{\mathrm{in}}$ is related to the pump power applied at the input port via the absolute drive amplitude

$\beta_{\text{in}} = \sqrt{P_\text{p}/(\hbar\omega_\text{p})}$. Finally, the effective drive strength ξ is determined by the product of pump power and the self-Kerr coefficient K.

The reflection coefficient of the driven JPA is derived from the input-output boundary condition [46, 80], which relates the outgoing field with the incident and the intra-cavity field (see App. B):

$$S_{11} = 1 - \frac{\kappa}{\kappa+\gamma}\frac{1}{\frac{1}{2} - i\delta + i\xi\bar{n}}. \tag{1.71}$$

In contrast to a linear cavity, the reflection coefficient depends on the average photon number inside the cavity, and, therefore on the drive power applied with the pump tone.

Figure 1.23 depicts the power dependence of the amplitude and the phase of the complex reflection coefficient, $|S_{11}|$ and $\arg(S_{11})$, respectively, numerically calculated as a function of the scale invariant pump-cavity detuning δ for different effective drive strengths ξ. At the critical drive strength $\xi_{\text{crit}} = -1/\sqrt{27}$ [68], the solution for the amplitude of the coherent state in the cavity becomes multivalued, and the system bifurcates. For a cavity with negative Kerr coefficient, the bifurcation occurs at the critical detuning $\delta_{\text{crit}} = -\sqrt{3}/2$. Since only two out of three solutions are stable, there are two stable branches the cavity can occupy. Experimentally, which stable branch the cavity occupies depends on the direction of the frequency sweep, as indicated by the solid and the dashed lines. Notably, under non-classical squeezed drives even superposition states of these two stable branches, so-called bosonic Schrödinger Cat-states, are possible [85, 219].

The dimensionless critical drive strength ξ_{crit} can be translated into a critical photon number n_{crit} incident to the cavity at which the bifurcation occurs:

$$n_{\text{crit}} = \frac{(\kappa+\gamma)^3}{\sqrt{27}\kappa|K|}, \tag{1.72}$$

Since the JPA is pumped close to the point of bifurcation for the operation as an amplifier, a large critical photon number is desired to suppress the effect of the signal on the point of operation.

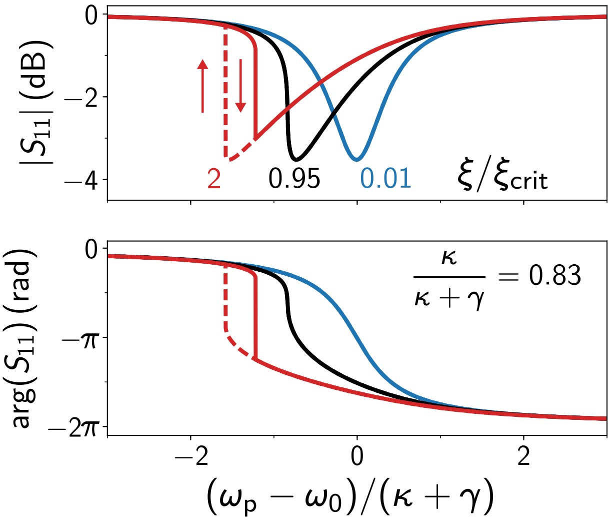

Figure 1.23: JPA: reflection coefficient. Amplitude $|S_{11}|$ (top panel) and phase $\arg(S_{11})$ (bottom panel) of the complex reflection coefficient of a nonlinear cavity with negative Kerr coefficient, numerically calculated as a function of the scale invariant pump-cavity detuning $\delta = (\omega_{\rm p} - \omega_0)/(\kappa+\gamma)$, and for an increasing effective drive strength ξ. At the critical drive strength $\xi_{\rm crit}$, the equation determining the intra-cavity photon number $\bar{n}$ (see Eq. 99) exhibits multiple (three) solutions. While two solutions are stable, the third is unstable, and, thus the system bifurcates. Experimentally, depending on the direction of the pump frequency sweep, either upwards (solid lines) or downwars (dashed lines), the response of the cavity follows different stable branches, and the response becomes hysteretic. In Josephson parametric amplifiers, the system is pumped close to the point of bifurcation, since the response of the system becomes increasingly sensitive to small perturbations in this region.

Power gain:

For a linear and degenerate bosonic amplifier, there is a simple relation between the incident and the (amplified) outgoing signal field amplitudes, $\hat{b}_{\rm in}$ and $\hat{b}_{\rm out}$, respectively, which can be represented in matrix form [68]

$$\begin{pmatrix} \hat{b}_{\rm out,\Delta} \\ \hat{b}^{\dagger}_{\rm out,-\Delta} \end{pmatrix} = \begin{pmatrix} g_{\rm s,\Delta} & g_{\rm i,\Delta} \\ g^{\star}_{\rm i,-\Delta} & g^{\star}_{\rm s,-\Delta} \end{pmatrix} \begin{pmatrix} \hat{b}_{\rm in,\Delta} \\ \hat{b}^{\dagger}_{\rm in,-\Delta} \end{pmatrix}, \tag{1.73}$$

revealing that the outgoing field at positive detuning $\Delta = (\omega_{\rm s} - \omega_{\rm p})/(\kappa+\gamma)$ depends also on the incident modes at negative detuning $-\Delta$. Since there are at least quantum fluctuations present at this frequency, these additional contributions are referred to as the idler tone. The coefficients in front of the incident modes determine the magnitude of amplification and are referred to as the signal and the idler gain-factors, $g_{\mathrm{s},\Delta}$ and $g_{\mathrm{i},\Delta}$, respectively,

$$g_{\mathrm{s},\Delta} = -1 + \frac{\kappa}{\kappa+\gamma}\frac{i(\delta - 2\xi\bar{n} - \Delta) + \frac{1}{2}}{(i\Delta - \lambda_-)(i\Delta - \lambda_+)} \tag{1.74}$$

and

$$g_{\mathrm{i},\Delta} = \frac{\kappa}{\kappa+\gamma}\frac{-i\xi\bar{n}e^{2i\phi_\mathrm{P}}}{(i\Delta - \lambda_-)(i\Delta - \lambda_+)}, \tag{1.75}$$

where ϕ_P is the relative phase between the incident pump and the intra-cavity field, and the terms in the denominator are defined as

$$\lambda_\pm = \frac{1}{2} \pm \sqrt{(\xi\bar{n})^2 - (\delta - 2\xi\bar{n})^2}. \tag{1.76}$$

If the external decay rate is much larger than the internal decay rate ($\kappa \gg \gamma$), the gain factors satisfy

$$G_\Delta = |g_{\mathrm{s},\Delta}|^2 = |g_{\mathrm{i},\Delta}|^2 + 1, \tag{1.77}$$

where G_Δ is the power gain of the amplifier at the signal frequency detuning Δ. In the high gain limit $|g_{\mathrm{s},\Delta}|^2, |g_{\mathrm{i},\Delta}|^2 \gg 1$, the signal incident at the idler frequency is almost equally amplified as the signal. Since there are always at least quantum fluctuations present at every frequency, the simultaneous amplification of contributions from different frequencies causes the additional noise added by the amplifier. Hence, if the input port is cold ($k_\mathrm{B}T \ll \hbar\omega_\mathrm{s}$), the presented implementation of a parametric amplifier reaches the quantum-limit of added noise.

Figure 1.24a depicts the maximal power gain G_0 according to Eq. 1.77, which is observed at zero pump-signal detuning ($\Delta = 0$), calculated as a function of the pump-cavity detuning δ and the effective drive strength ξ/ξ_crit. Again, the critical drive strength ξ_crit determines the lowest drive amplitude at which the system bifurcates. Notably, a JPA is operated below the critical value. For every given drive strength, there is an optimal detuning δ, at which the observed power gain is maximal. Since the self-Kerr coefficient is negative for a JPA, the cavity frequency is shifted to lower values with increasing average population $\bar{n}$, and with that, also the optimal detuning. Close to the point of bifurcation ($\delta_\mathrm{crit}, \xi_\mathrm{crit}$), the observed power gain increases rapidly, as indicated by the transition from a light blue tone into a dark red, and by the horizontal slices shown in Figure 1.24b. The black markers indicate the maximal power gain observed at the ideal pump detuning for five drive strengths investigated.

Gain-bandwidth compromise:

The ideal pump condition in terms of detuning and drive strength (δ, ξ) is the desired configuration of operation, since it minimizes the required pump power for a given

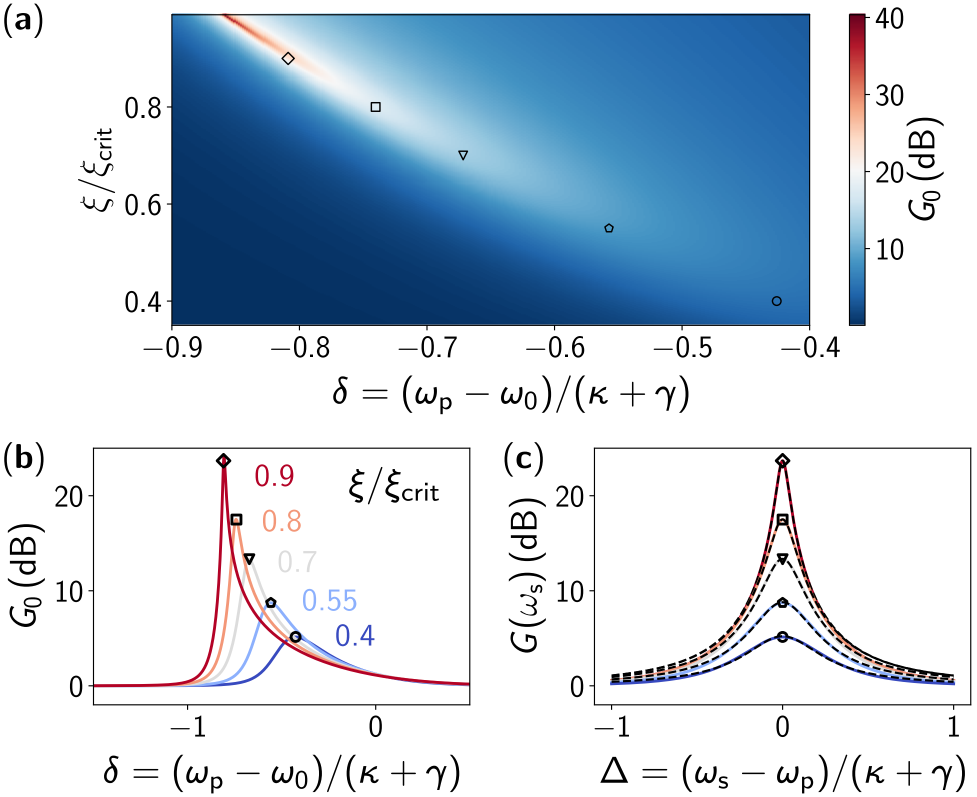

Figure 1.24: JPA: power gain. a) Maximal linear power gain G_0 in decibel, assuming a weak (quantum) signal reflects off the actively pumped cavity, numerically calculated according to Eq. 1.77 as a function of the dimensionless pump-cavity detuning δ, and the effective pump drive strength ξ/ξ_{crit}, where the critical drive strength ξ_{crit} defines the value at which the cavity bifurcates. The detuning between the pump and the signal is zero ($\omega_s - \omega_p = 0$). For every given drive strength ξ, there is an ideal detuning δ at which the maximum power gain G_0 reaches the highest possible value. Since the self-Kerr coefficient is negative and the cavity resonance frequency shifts to lower values with increasing population, the optimal detuning does so, too. The closer the cavity is pumped to the point of bifurcation, the larger the accessible overall maximal power gain. **b)** Maximal power gain G_0 at zero pump-signal detuning ($\Delta = 0$), as a function of the pump-cavity detuning δ for different drive strengths ξ. Each curve corresponds to a horizontal cut through the 2D plot shown in panel a. **c)** Power gain $G(\Delta)$ as a function of the detuning Δ between signal and pump. The shape of the curves is very similar to a Lorentzian, which is indicated by the black dashed lines. The maximal power gain G_0 is observed at zero detuning $\Delta = 0$. The corresponding pump-cavity detunings δ are indicated in panels a and b.

power gain G_0. However, operating the JPA away from the ideal conditions allows for a fine tuning of the operational frequency. Figure 1.24c shows the power gain G in decibel, calculated under optimal pumping as a function of the frequency detuning Δ between signal and pump. The maximal power gain is observed at zero detuning ($\Delta = 0$), indicated by the open black markers. The shape of the gain curves is in good agreement with a Lorentzian, as it is indicated by the black dashed lines. Therefore, the instantaneous bandwidth B of the amplifier is defined as the full width at half maximum (FWHM). As becomes apparent, the bandwidth decreases with increasing maximal power gain G_0, which is referred to as the gain-bandwidth compromise, and expressed in a constant gain-bandwidth product:

$$\sqrt{G_0}B \underset{\gamma \to 0}{\approx} \kappa. \tag{1.78}$$

Overcoming this limitation of standing-wave JPAs is achieved by enhancing the coupling rate with impedance transformers [165, 191], or by using more complex pumping schemes [41, 153].

Saturation power:

For JPAs based on weakly nonlinear cavities with finite fourth order (Kerr) nonlinearity, the dynamic range is suspected to be limited mainly by two mechanisms: pump depletion [2, 190] and a signal induced ac Stark shift of the cavity frequency [31, 136]. While the first effect describes the reduction of the pump tone strength caused by the amplification process, the second ascribes the output power saturation to a detuning from the optimal pump condition.

Following the procedure discussed in Ref. [68] and Ref. [178], both effects can be incorporated into the same framework used to predict the power gain, by introducing an effective drive strength associated with the input signal into Eq. 99 (see App. B.3). Figure 1.25a depicts the calculated power gain G_0 at zero pump-signal detuning $\Delta = 0$ for two cavities with self-Kerr coefficients $|K|/(2\pi) = 1\,\mathrm{kHz}$ (red) and $|K|/(2\pi) = 1024\,\mathrm{kHz}$ (blue) as a function of the input signal power P_s. Above a certain input power, the power gain of the amplifier starts to decrease. The value of the input power at which the decrease starts to become significant depends on the pump power, i.e. the small signal power gain G_0, and the magnitude of the nonlinearity $|K|$. Conventionally, the saturation power is defined as the 1 dB compression point (black markers), the power at which the initial power gain decreased by 1 dB.

In Fig. 1.25b, the saturation power is plotted against $|K|$, for an initial weak-signal power gain of $G_0 \approx 20\,\mathrm{dB}$. Evidently, a small nonlinearity is desired to enhance the saturation power, or more precisely, the ratio of cavity linewidth and nonlinearity

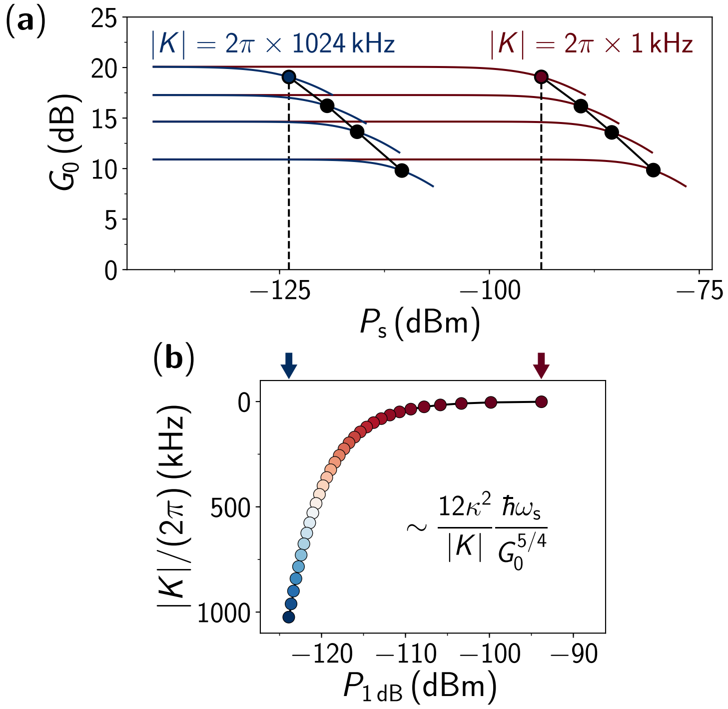

Figure 1.25: JPA: power gain saturation. a) Maximal power gain $G_0 = G(\varDelta = 0)$ as a function of the signal input power P_s, numerically calculated for two sets of nonlinear cavities with self-Kerr coefficients $K/(2\pi) = 1\,\mathrm{kHz}$ (red) and $K/(2\pi) = 1024\,\mathrm{kHz}$ (blue). The calculations consider the signal-induced ac Stark shift of the cavity [178]. For comparison reasons, the power gain is calculated for four different pump conditions $(P_\mathrm{p}, \omega_\mathrm{p})$ for each cavity. The power gain starts to drop at a certain input power, which depends on the magnitude of the nonlinearity $|K|$ and the pump power. The black markers indicate the 1dB compression point, the input power at which the power gain decreased by 1 dB compared to the inital value. The parameters of the cavity are $\omega_0/(2\pi) = 7\,\mathrm{GHz}$, $\kappa/(2\pi) = 350\,\mathrm{MHz}$ and $\gamma/(2\pi) = 0$. **b)** Saturation power determined as the 1dB compression point, numerically calculated as a function of the self-Kerr coefficient $|K|$ for an initial power gain $G_0 = 20\,\mathrm{dB}$. The magnitude of the nonlinearity is reflected by the color of each marker. With decreasing nonlinearity, the saturation power rapidly increases. The black line indicates the expected scaling [76]. In order to obtain a large saturation power, a large ratio $\kappa/|K|$ is beneficial.

$\kappa/|K|$ should be as large as possible [117]. However, at the same time the quality factor $Q = \omega_0/\kappa$ has to be large enough to ensure a stable behavior close to the point of bifurcation, summarized by the constraint $pQ \geq 1$, where p is the kinetic inductance participation ratio [147] (which is $p = 1$ in the discussed scenario). The scaling of the saturation power is given by [76]

$$P_{1\,\mathrm{dB}} \sim \frac{12\kappa^2}{|K|} \frac{\hbar\omega_\mathrm{s}}{G_0^{5/4}}, \tag{1.79}$$

which, indicated by the black solid line, is in good agreement with the calculated saturation powers.

As a side note, the effect of input signal induced ac Stark shifts can be reduced significantly by employing nonlinear elements with intrinsically reduced fourth order nonlinearity, for instance the superconducting nonlinear asymmetric inductive element (SNAIL) [77].

1.3.5 Amplifier classification

In the context of parametric amplification with superconducting quantum circuits, several technical terms exist to distinguish between the different types of amplifiers emerged during the last decades [189]. While all amplifiers share the same conceptual idea — the transfer of energy from a single (or multiple) strong pump tone(s) onto a weak quantum signal using the nonlinearity of JJs or superconducting wires — the various circuit implementations can differ significantly.

As discussed in the previous sections, the parametric amplification process contains at least three tones: a *pump* (ω_p), a *signal* (ω_s), and an *idler* (ω_i), an inevitable mirror tone created during the amplification process. The corresponding frequencies and photon energies of those three tones are imperatively related, depending on the symmetry of the underlying potential. In a *three-wave mixing* process, a single pump photon is converted into a signal and an idler photon, yielding the relation

$$\omega_\mathrm{p} = \omega_\mathrm{s} + \omega_\mathrm{i}, \tag{1.80}$$

while in a *four-wave mixing* process two pump photons are converted at the same time

$$2\omega_\mathrm{p} = \omega_\mathrm{s} + \omega_\mathrm{i}, \tag{1.81}$$

as illustrated in Fig. 1.26.

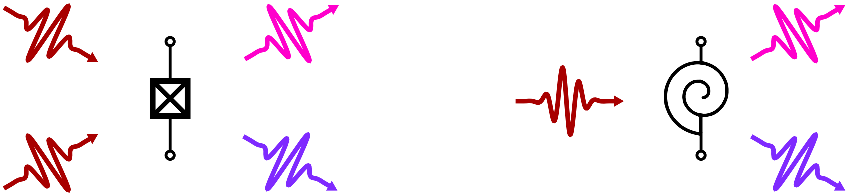

Figure 1.26: Mixing-process. Schematic illustration of a four-wave mixing process (left-hand panel), in which two pump photons (red) are converted into a signal (purple) and an idler photon (pink). The quartic nonlinearity (Φ^4) required for such a mixing process — a Kerr-type nonlinearity — is provided by current biased single JJs, dc SQUIDs, and the kinetic inductance inherent to superconductors. In a three-wave mixing process (right-hand panel), a single pump photon is converted into a signal and an idler photon, which requires a cubic nonlinearity (Φ^3). An example for such an asymmetric circuit element is the SNAIL [77].

The main consequence and difference is the frequency detuning between the three signals, in particular between the pump and the signal, which is significantly larger in devices utilizing a three-wave mixing process, for instance the Josephson parametric converter [19]. As discussed in Sec. 1.1.2, the energy potential of a single JJ or a dc SQUID is symmetric and, thus does not support a three-wave mixing process induced by a current pumping. Circuit elements supporting three-wave mixing are the Josephson ring modulator [20], the SNAIL [77] and the rf SQUID [240] in current bias, as well as the flux pumped dc SQUID operated beyond the flux sweet spot [233].

In case the signal and the idler frequencies are identical ($\omega_\mathrm{s} = \omega_\mathrm{i}$), the amplification process is *phase-sensitive*, which means that one quadrature is amplified, while the other quadrature is deamplified, resulting in a squeezed state of light [235, 236]. Which quadrature is amplified depends on the relative phase between the signal and the pump tone. Additionally, the noise in the outgoing mode is also squeezed, which can be used to operate an amplifier chain beyond the standard quantum limit caused by photon shot noise [127]. If the signal and idler do not share the same frequency, the process is *phase-preserving*, and both quadratures are amplified at the same time.

The energy conversion from the pump to the signal can be obtained by simultaneously confining the tones in resonant systems, so-called *standing-wave parametric amplifiers* [39, 189, 233, 235], or during the simultaneous propagation through a nonlinear medium, so-called *travelling wave parametric amplifiers* [27, 71, 143, 179, 240]. Besides the directionality, travelling-wave amplifiers offer a much larger bandwidth, but are generally more complicated to fabricate due to the greater complexity, and still suffer from unintended internal reflections. Despite a few exceptions [41, 126, 127], most standing-wave amplifiers are operated in reflection and require the use of non-reciprocal elements to separate the incident from the amplified outgoing signal.

Standing-wave amplifiers implemented with a single mode in space or frequency are referred to as *degenerate* amplifiers, while amplifiers utilizing several modes are labeled *non-degenerate*. Notably, both implementations can be operated in the phase-sensitive and the phase-preserving mode of operation.

2 The granular aluminum transmon qubit

The granular aluminum transmon is a superconducting charge qubit in which, instead of a conventional SIS Josephson junction, a small volume of superconducting granular aluminum is shunted by a large capacitor, which serves as the inductance and the source of nonlinearity of the circuit. In comparison to conventional JJ technology, interference patterns have not yet been observed in grAl films in external magnetic fields, i.e. the films are primarily affected by the suppression of the superconducting gap parameter Δ_{grAl}. The main question is: how much nonlinearity does such an grAl element provide and how coherent is it? A summary of the presented results can be found in Ref. [230].

2.1 Multi-junction transmon qubit

Recalling the results obtained in the discussion of the superconducting charge qubit in Sec. 1.1.3, in the transmon limit $E_\mathrm{J} \gg E_\mathrm{c}$, the anharmonicity of the charge qubit spectrum is approximately given by the charging energy E_c and, thus independent of the Josephson energy E_J [116]. Owing to the microstructure of granular aluminum, it is very likely that even relatively small volumes of grAl contain multiple effective JJs. The scaling of the anharmonicity for several JJ in series can be estimated by substituting the Josephson potential of the single JJ in the charge qubit Hamiltonian (see Eq. 1.18) with that of an array — a standard procedure in the context of Josephson parametric amplifiers [68].

For N identically sized JJs in series, and assuming a homogeneous current distribution along the JJs, the phase drop across each element is $\varphi_\mathrm{J} = \varphi/N$, where φ is the total phase drop across the array. The Josephson potential associated to the array is

$$E_\mathrm{J} \cos(\hat{\varphi}) \qquad \rightarrow \qquad N \underbrace{N E_\mathrm{J}}_{E'_\mathrm{J}} \cos(\hat{\varphi}/N), \tag{2.1}$$

where E'_J is the Josephson energy of each individual JJ, which is N times larger to ensure that the inductance of the array is identical to the inductance in the single JJ implementation, i.e. the fundamental transition frequency is kept fixed [68]. As a consequence, the charging energy and the zero-point fluctuations of the superconducting phase φ_{ZPF} (across the array) remain unchanged.

Similar to the single JJ case, the Kerr coefficient K_{array} for the array is determined by the coefficient in front of the quartic term of the Taylor expansion of the Josephson potential:

$$\hbar K_{\mathrm{array}} = -\frac{NE'_J}{2}\left(\frac{\varphi_{\mathrm{ZPF}}}{N}\right)^4 = -\frac{E_J}{2}\frac{\varphi_{\mathrm{ZPF}}^4}{N^2} = \frac{\hbar K}{N^2}. \tag{2.2}$$

According to Eq. 2.2, the anharmonicity of a multi-junction transmon qubit scales with N^{-2} compared to the conventional transmon.

In the more general case of unequal JJs, the Kerr coefficient K of the fundamental mode can be derived from the energy participation ratio p_j of the j th JJ to the mode [156]:

$$K_{\mathrm{array}} = -\frac{1}{2}\sum_j \frac{\omega_1^2}{4E_{J,j}} p_j^2. \tag{2.3}$$

Provided the wavelength is significantly larger than the physical length of the JJ array, the energy participation ratio of each element can be inferred from the ratio of its Josepshon inductance $L_{J,j}$ and the total inductance L in the circuit: $p_j = \frac{L_{J,j}}{L}$. In this way, not only the effect of differently sized JJs can be considered, but also the influence of additional linear (geometric) inductances, which contribute to the total inductance of the circuit, but do not give rise to a Kerr nonlinearity.

2.2 Design

The constraints on the design of the grAl transmon are in some aspects similar to the constraints on a conventional transmon [116]. Like other superconducting quantum circuits, the typical operation frequency of transmon qubits is below 10 GHz. In order to suppress the charge dispersion sufficiently, typically a ratio $E_J/E_c = r \geq 50$ is desired.

In the transmon regime, the approximation for the fundamental transition frequency $\omega_1 \approx \sqrt{8E_J E_c}$ yields a relation between the Josephson energy of the JJ and the transition frequency of the transmon $E_J \approx \sqrt{r/8}\hbar\omega_1$. Fixing a transition frequency determines the Josephson energy and the corresponding Josephson inductance, as well as the charging energy and the size of the shunt capacitor. For a typical transmon, the charging energy is therefore around $E_c/h = 2\pi \times 100 - 300\,\mathrm{MHz}$.

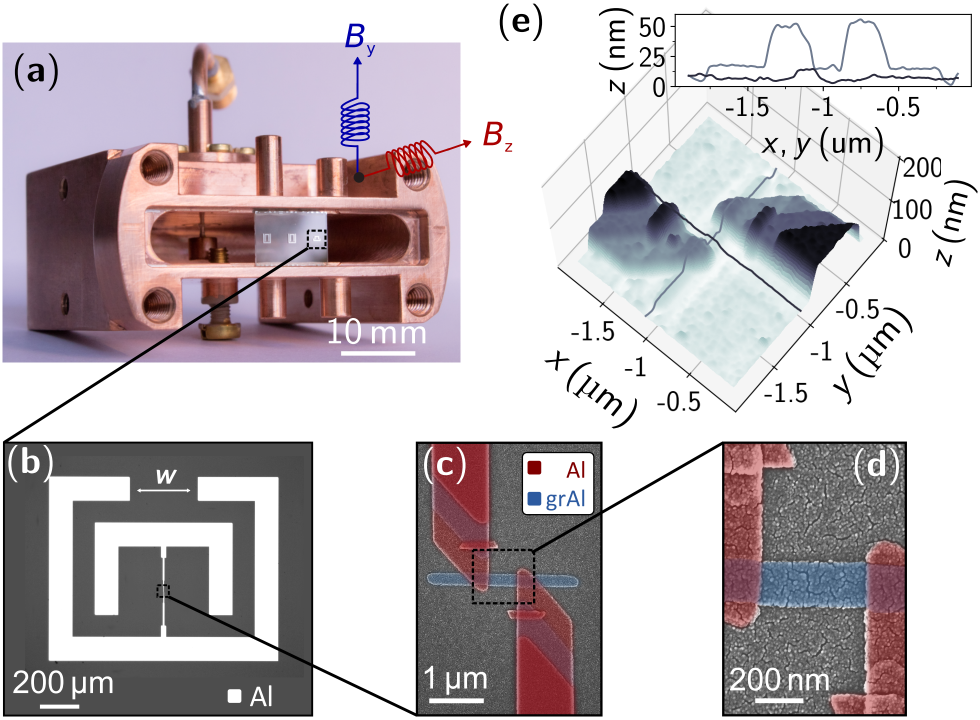

Figure 2.1: grAl Transmon: Circuit design. a) Photograph of a copper-waveguide sample holder equipped with a microwave port similar to Ref. [119], and, optionally, with a 2D vector magnet (see App. C.6). The vector magnet is schematically represented by the blue and red coils, oriented along the y and z directions. The sample is positioned in the center of the waveguide and couples to its electric field at a rate κ. **b)** Optical microscopy image of the qubit sample, consisting of two Al pads forming a capacitor $C_s \approx 137\,\mathrm{fF}$, connected by a grAl inductor $L_{K,\mathrm{grAl}} \approx 2.65\,\mathrm{nH}$. The coupling rate κ is adjusted by changing the gap w (see App. C.4). **c) and d)** Scanning electron microscope (SEM) image of a grAl inductor (false-colored in blue) with volume $V_{\mathrm{grAl}} = 10 \times 200 \times 500\,\mathrm{nm}^3$, together with the pure Al leads (false-colored in red) connecting it to the capacitor electrodes. The grainy surface structure is due to an antistatic Au layer used for imaging. The circuit is obtained in a single lithography step by performing a three-angle shadow evaporation. The Al layer shunts the grAl film in all areas, except for the volume V_{grAl} in the center, which constitutes the source of non-linearity for the qubit [144]. The geometric inductance is $L_s = 0.45\,\mathrm{nH}$, and the contacts contribute to the kinetic inductance with 0.13 nH (see App. C.5). **e)** Atomic force microscope image of the film height z in the area around the grAl inductor, measured on a sample from the same wafer as the sample discussed in the main text. The inset shows the cross section along x (black) and y (grey), as indicated by the arrows and overlay lines in the 3D plot. The cross section along the grAl inductor (grey) confirms the $t_{\mathrm{grAl}} = 10\,\mathrm{nm}$ grAl thickness and $t_{\mathrm{Al}} = 40\,\mathrm{nm}$ for each Al layer.

Table 2.1: grAl transmon: Circuit parameters. The circuit parameters correspond to an effective circuit model composed of an inductance L in parallel with a shunt capacitance C_s. The total inductance arises from the contribution of three inductive elements in series: the geometric stray inductance L_s of the Al leads, the kinetic inductance $L_\mathrm{K,Al}$ of the Al leads including the contact junctions to the grAl volume, and the kinetic inductance $L_\mathrm{K,grAl}$ of the grAl volume. The value quoted for total inductance and the grAl inductance is for a fundamental transition frequency of $f_1 = 7.4887\,\mathrm{GHz}$.

shunt capacitance	total inductance	stray inductance	kinetic inductance (Al)	kinetic inductance (grAl)
C_s	L	L_s	$L_\mathrm{K,Al}$	$L_\mathrm{K,grAl}$
137 fF	3300 pH	450 pH	200 pH	2650 pH

In the grAl transmon, the inductance is provided by the kinetic inductance of the grAl film. Neglecting spurious geometric contributions, the total kinetic inductance of a grAl volume with length l and width b is $L_\mathrm{k} = N_\square L_\square$, where $N_\square = l/b$ is the total number of squares, and $L_\square$ is the kinetic sheet inductance. Recalling the results of Sec. 1.2.2, the sheet inductance of a dirty superconductor is proportional to the sheet resistance $R_\square$. In the case of grAl, the sheet resistance $R_\square$ is controlled by the partial oxygen pressure during evaporation.

Another constraint on the grAl film geometry arises from the total number of junctions inside the grAl volume $N = l/a$, where a is the effective size of a single JJ, which is not necessarily identical to the grain diameter [234]. Since the expected nonlinearity scales with N^2 (see Eq. 2.2), a small volume of grAl with high resistivity and low critical current density is desired in order to provide enough kinetic inductance to meet the criterion on the transition frequency, and to maximize the anharmonicity of the grAl transmon at the same time. At this point I would like to mention, that for small volumes of grAl, the prediction of the kinetic sheet inductance based on the Mattis-Bardeen theory is potentially unprecise, for instance caused by charging effects in the most outer grains residing close at the film surface.

Figure 2.1 shows a typical copper waveguide sample holder used for readout, together with the circuit design of the grAl transmon, consisting of a grAl thin film shunted by an Al capacitor. The shunt capacitance $C_\mathrm{s} \approx 137\,\mathrm{fF}$ is determined from FEM simulations, together with the geometric stray inductance $L_\mathrm{s} \approx 0.45\,\mathrm{nH}$ arising from the pure Al electrodes connecting the grAl volume (see App. C.4). The choice of using Al as a shunting layer was motivated by its low intrinsic kinetic inductance, ensuring an energy participation of the grAl inductance close to unity, as well as the ease of fabrication. The Purcell rate or external coupling rate κ, i.e. the rate at which the qubit spontaneously decays into the waveguide, is controlled by the gap w in the

Table 2.2: grAl transmon: parameters of the grAl thin film. The properties of the grAl volume $V_{\mathrm{grAl}} = 10 \times 200 \times 500\,\mathrm{nm}^3$ are related to the parameters of the grAl thin film. The normal-state resistivity ρ_{n} was measured at room-temperature, and the value of the sheet inductance corresponds to the prediction of the Mattis-Bardeen theory for superconductors in the local and dirty limit (see. Sec. 1.2.2).

normal-state resistivity	sheet resistance	sheet inductance (MBT)	number of squares	critical current density
ρ_{n}	$R_{\square} = \rho_{\mathrm{n}}/t$	$L_{\mathrm{K},\square}$	$N_{\square}$	j_{c}
$(1800 \pm 200)\,\mu\Omega\,\mathrm{cm}$	$(1800 \pm 200)\,\frac{\Omega}{\square}$	$(1.3 \pm 0.1)\,\frac{\mathrm{nH}}{\square}$	2.5	$0.4\,\frac{\mathrm{mA}}{\mu\mathrm{m}^2}$

outer electrode (see. Fig. 2.1b). Notably, in the direct readout of a qubit, it is this rate at which information about the qubit state is collected.

The presented sample was fabricated on a sapphire wafer in a single-step lithography by performing a three-angle shadow evaporation. First, a 10 nm thick grAl layer with room-temperature normal-state resistivity $\rho_{\mathrm{n}} = 1800 \pm 200\,\mu\Omega\,\mathrm{cm}$ and corresponding critical temperature $T_{\mathrm{c}} = 1.9\,\mathrm{K}$ was deposited at zero-angle, followed by two 40 nm thick Al layers evaporated at $\pm 35°$. Thanks to this procedure, only a small grAl volume $V_{\mathrm{grAl}} = 10 \times 200 \times 500\,\mathrm{nm}^3$, highlighted in blue in Fig. 2.1 (panel c and d), remains unshunted by the pure Al layers and participates in the electromagnetic mode with a kinetic inductance $L_{\mathrm{K,grAl}} = 2.65\,\mathrm{nH}$, constituting 80 % of the total inductance, as further discussed in Sec. 2.6. The total number of squares $N_{\square} \approx 2.5$ estimated from the grAl inductance and the kinetic sheet inductance calculated according to Eq. 1.58 is in agreement with the geometric dimensions of the grAl volume. The parameters of the grAl film are summarized in Tab. 2.2, and more details on the fabrication recipe are provided in App. C.9.

2.3 Resonance fluorescence readout

In the resonance fluorescence readout of a superconducting qubit [7], the dynamics of the qubit are directly observed by monitoring the coherent scattering of a probe tone from the qubit. As discussed in Sec. 1.1.4, the application of a microwave tone in close vicinity to the transition frequency ω_{q} of the qubit induces Rabi oscillations between the qubits ground and first excited state, which is reflected in a change of the scattering behavior. For a coherent drive with amplitude $\langle \hat{B}_{\mathrm{in}} \rangle = \beta_{\mathrm{in}}$, the corresponding Rabi frequency Ω_{R} on resonance is [49]

$$\Omega_{\mathrm{R}} = 2\sqrt{\kappa}\beta_{\mathrm{in}}, \tag{2.4}$$

where κ is again the coupling rate between the qubit and the input port, i.e. the waveguide sample holder. As a side note, determining the Rabi frequency enables the calibration of the incident drive power $P_{\mathrm{in}} = \hbar\omega|\beta_{\mathrm{in}}|^2$, and the total attenuation between the microwave source and the qubit.

Provided the Rabi frequency is significantly smaller than the anharmonicity of the qubit $\Omega_{\mathrm{R}} \ll \alpha$ (see Sec. 1.1.4), the response of an anharmonic circuit with a multi-level energy spectrum can be mapped onto the dynamics expected from a two-level system. Using the input-output boundary condition between the incident and the outgoing field [80], the reflection coefficient S_{11} of a two-level system is [7, 49]

$$S_{11} = 1 - \sqrt{\kappa}\frac{\langle\hat{\sigma}_-\rangle}{\langle\hat{B}_{\mathrm{in}}\rangle}, \tag{2.5}$$

where $\hat{\sigma}_-$ is the Pauli lowering operator, which plays the equivalent role of the annihilation operator for bosonic fields. Notably, I would like to mention that there are different forms found for the reflection coefficient in literature, which differ by a complex phase factor in front of the second term.

In general, the observed response evolves over time, until the system has reached its equilibrium or steady-state. The characteristic time scale for this so-called ring-up is determined by the energy relaxation rate Γ_1 and the pure dephasing rate Γ_ϕ. Measurements studying the steady-state behavior are usually referred to as *spectroscopy* measurements, while measurements detecting the time evolution of the system are denoted *time-domain* measurements. Both types of measurements are complementary for the characterization of a qubit, as is demonstrated in the following sections.

Spectroscopy

The frequency dependence of the steady-state ($t \to \infty$) reflection coefficient of a two-level system, measured with a single microwave tone, is [49]

$$S_{11}(\Delta_{\mathrm{q}}) = 1 - \kappa\frac{\Gamma_1\Gamma_2^* - i\Gamma_1\Delta_{\mathrm{q}}}{\Gamma_1(\Gamma_2^{*2} + \Delta_{\mathrm{q}}^2) + \Gamma_2^*\Omega_{\mathrm{R}}}, \tag{2.6}$$

where $\Delta_{\mathrm{q}} = \omega_{\mathrm{q}} - \omega$ is the frequency detuning between the drive tone frequency ω and the qubit frequency ω_{q}, Γ_1 is the energy relaxation rate, Γ_2^* is the dephasing rate, κ is the coupling rate to the drive port, and i is the unit imaginary number. The energy relaxation rate is a combination of spontaneous emission into the input port at a rate κ and into uncontrolled degrees of freedom at a rate γ.

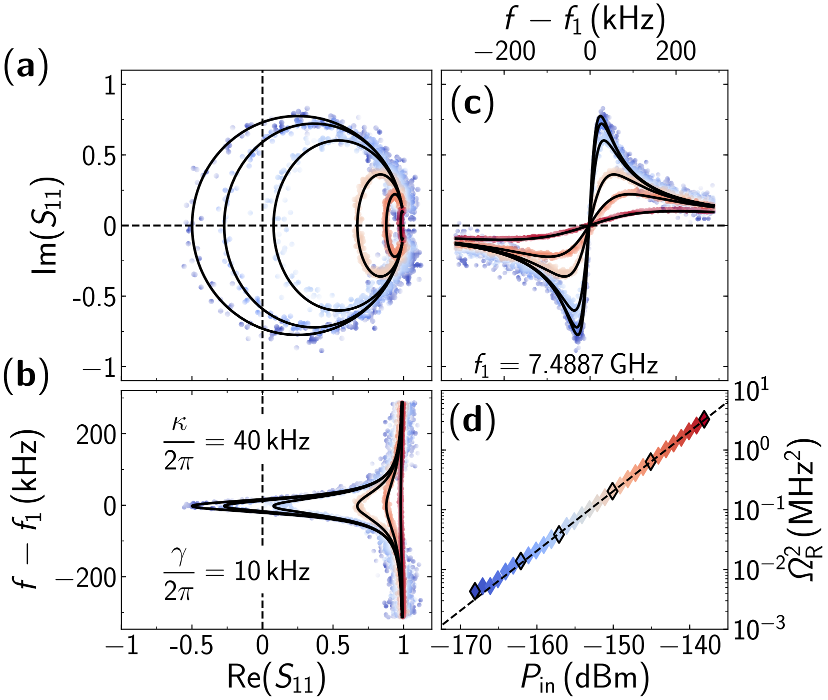

Figure 2.2: grAl Transmon: resonance fluorescence (spectroscopy). a) Single-port reflection coefficient $S_{11}(\omega)$ measured around the fundamental transition frequency $\omega_1 = 2\pi \times 7.4887\,\mathrm{GHz}$ of the grAl transmon. For probe powers P_{in} well below the single-photon regime ($\bar{n} \ll 1$), S_{11} closely resembles a circle in the complex plane (dark blue markers), from which, using Eq. 2.7, the external and internal decay rates $\kappa = 2\pi \times 40\,\mathrm{kHz}$ and $\gamma = 2\pi \times 10\,\mathrm{kHz}$, respectively, are extracted. In **b)** and **c)**, the real and imaginary part of the reflection coefficient $\mathrm{Re}(S_{11})$ and $\mathrm{Im}(S_{11})$, respectively, are plotted as a function of the detuning between the probe frequency f and the qubit frequency f_1. When increasing the probe power P_{in}, the response becomes elliptic in the complex plane, which is the signature of resonance fluorescence of a two-level-system [7, 49]. The black lines indicate fits to the experimental data according to Eq. 2.7. The only fitting parameter is the Rabi-frequency Ω_{R}; κ and γ are fixed by the fit to the low power response. In **d)** the squared Rabi-frequencies Ω_{R}^2 are plotted as a function of the incident power P_{in} seen by the qubit. For a two-level system, given by the limit $\Omega_{\mathrm{R}} \ll \alpha$, the Rabi-frequency is expected to increase linearly with the drive amplitude, as confirmed by the black dashed line passing through the coordinate origin.

In case the decoherence rate is dominated by the energy relaxation $\Gamma_2^* \approx \Gamma_1/2$, the reflection coefficient simplifies to

$$S_{11}(\Delta_\mathrm{q}) = 1 - \frac{2\kappa}{\Gamma_1} \frac{1 + i2\Delta_\mathrm{q}/\Gamma_1}{1 + (2\Delta_\mathrm{q}/\Gamma_1)^2 + 2(\Omega_\mathrm{R}/\Gamma_1)^2}. \tag{2.7}$$

According to Eq. 2.6 and Eq. 2.7, all essential qubit parameters can be extracted from the frequency dependence of the reflection coefficient.

Figure 2.2 depicts the complex reflection coefficient S_{11} measured with a commercial vector network analyzer (VNA) in close vicinity to the fundamental transition frequency $\omega_\mathrm{q} = \omega_1 = 2\pi \times 7.4887\,\mathrm{GHz}$ of the grAl transmon shown in Fig. 2.1, plotted as a function of the probe frequency $f = \omega/(2\pi)$ and the calibrated probe power P_in seen by the qubit.

For an effective two-level system, the reflection coefficient resembles a circle in the complex plane only for low probe powers, i.e. small Rabi-frequencies ($\Omega_\mathrm{R} \ll \kappa, \gamma$), similar to the response of a harmonic system, but becomes increasingly elliptic when the probe power is enhanced (panel a). The deviation from the circular shape is caused by the saturation of the qubit population owing to the anharmonicity of the energy spectrum. Descriptively, the radius of the circle is a measure for the ratio between internal losses, i.e. losses into uncontrolled degrees of freedom, and external losses into the input port, while the eccentricity of the ellipse determines the Rabi frequency.

The qubit parameters $\omega_\mathrm{q}, \kappa, \gamma$ and Ω_R are extracted by fitting the measured data with the expected response in the T_1 limit, given in Eq.2.7, with the resulting fits indicated by the black solid lines. The internal and external decay rates are extracted at low probe powers (dark blue markers) $\gamma = 2\pi \times 10\,\mathrm{kHz}$ and $\kappa = 2\pi \times 40\,\mathrm{kHz}$, respectively, corresponding to characteristic time scales $T_{1,\gamma} \approx 16\,\mu\mathrm{s}$ and $T_{1,\kappa} \approx 4\,\mu\mathrm{s}$. Since both parameters do not change with power in the investigated range, the Rabi frequency remains the only fitting parameter for the measurements at higher probe powers, to enhance the fitting accuracy.

Table 2.3: grAl transmon: spectroscopy. Qubit parameters extracted for the grAl transmon from the resonance fluorescence spectroscopy measurements shown in Fig. 2.2.

resonance frequency $\omega_1/(2\pi)$	external decay rate $\kappa/(2\pi)$	external energy relaxation $T_{1,\kappa} = \kappa^{-1}$	internal decay rate $\gamma/(2\pi)$	internal energy relaxation $T_{1,\gamma} = \gamma^{-1}$
7.4887 GHz	40 kHz	4 µs	10 kHz	16 µs

The dependence of the extracted squared Rabi frequencies Ω_R^2 on the input power is shown in panel d, with the expected linear relation predicted by Eq. 2.4 indicated by the black dashed line. From the drive powers set at room temperature and the corresponding (measured) Rabi frequencies, the total attenuation $A = 103\,\mathrm{dB}$ between the source and the qubit was calibrated.

Time-domain

For the time-domain characterization of the grAl transmon, a microwave pulse with Gaussian envelope and varying amplitude and frequency was applied to manipulate the qubit state, followed by a readout pulse with rectangular envelope applied on resonance with the fundamental transition frequency ω_1. The pulse sequence is illustrated in Fig. 2.3a. The Gaussian envelope of the manipulation pulse reduces the excitation of higher states due to its sharper Fourier spectrum. Since the application of a microwave drive close to resonance induces Rabi oscillations, varying the amplitude β_in and the duration τ_m of the manipulation pulse prepares a different initial qubit state $\Psi(\beta_\mathrm{in}, \tau_\mathrm{m})$, before the readout pulse is applied, which is reflected in the measurement outcome. The readout pulse is integrated and decomposed into the I and Q quadrature at room temperature using a custom-made microwave interferometer (see App. G.9). For an improved SNR of the measurement setup, a dimer Josephson junction array (DJJAA) amplifier has been added to the microwave output line (see Sec. 3).

Figure 2.3b depicts Rabi oscillations of the grAl transmon as a function of the manipulation pulse duration τ_m and the average drive power $P_\mathrm{m} = \hbar\omega_1\Omega_\mathrm{R}^2/(4\kappa)$, which is calibrated from the measured oscillation frequencies Ω_R and related to the drive amplitude β_in. As expected, the Rabi frequency increases with increasing drive power. The right-hand panel shows a single trace for $P_\mathrm{m} = -124.7\,\mathrm{dBm}$. Due to energy relaxation and dephasing, the contrast of the Rabi oscillations decreases over time, i.e. with increasing length of the pulse duration, as indicated by the exponential envelopes (black dashed lines). From the measured curves, the duration τ_π of a π-pulse is calibrated for each drive power, which corresponds to the combination of pulse duration and amplitude required to invert the qubit state. As it is shown in Fig. 2.3c, the Rabi frequencies extracted from the spectroscopy and the time-domain measurements are in good agreement.

The generalized Rabi frequency depends not only on the drive amplitude, but also on the detuning between the drive and the qubit transition frequency Δ_q (see Sec. 1.1.4). Figure 2.3d shows the response of the grAl transmon for manipulation pulses with a fixed amplitude, but with varying pulse duration τ_m and drive frequency f_d, revealing the characteristic Chevron pattern (see Sec. 1.1.4). With increasing

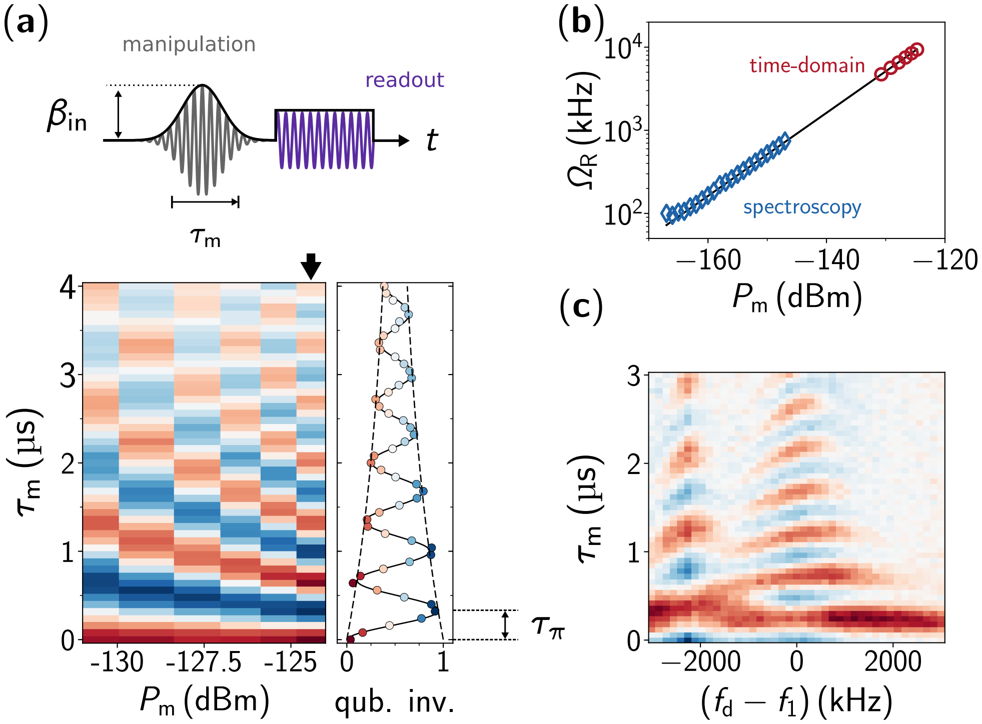

Figure 2.3: grAl transmon: resonance fluorescence (time-domain). a) Pulse sequence applied to perform a Rabi measurement. First, a Gaussian-shaped pulse of duration τ_{m} and amplitude β_{in} is applied at a frequency ω_{d} to manipulate the qubit state. Subsequently, for the readout, a rectangular-shaped pulse of 3.2 µs is applied on resonance, from which the second half is integrated. Measured Rabi-oscillations between the qubit's ground $|0\rangle$ and first excited state $|1\rangle$ as a function of the average drive power of the manipulation pulse P_{m}, and its duration τ_{m}. The color scale represents the qubit population inversion from equilibrium (red) to fully inverted (blue). With increasing drive power, the Rabi-frequency increases as expected. The right-hand panel shows the Rabi-oscillation for $P_{\mathrm{m}} = -124.7\,\mathrm{dBm}$, highlighted in the 2D plot by a black arrow. For a given Rabi frequency, the corresponding pulse duration to invert the qubit is τ_π. The black dashed lines indicate an exponentially decaying envelope. **b)** Comparison between the Rabi-frequencies extracted from spectroscopy (blue markers) and the time-domain measurements (red makers) shown in panel a. The black line indicates the expectation $\Omega_{\mathrm{R}} = \sqrt{4\kappa P_{\mathrm{m}}/(\hbar\omega_1)}$ from which the manipulation powers P_{m} are also calibrated in panel a. **c)** Rabi oscillations for a fixed manipulation power $P_{\mathrm{m}} = -121.9\,\mathrm{dBm}$, but different pulse durations τ_{m} and drive frequencies f_{d}. With increasing detuning from the fundamental transition frequency, the Rabi frequency increases, while the contrast of the oscillations decreases. For negative detunings, a two-photon transition into the second excited state occurs with roughly half the Rabi frequency as in the on-resonance case. From the frequency detuning, the anharmonicity of the energy spectrum is quantified to $\alpha \approx 2\pi \times 4.5\,\mathrm{MHz}$.

Table 2.4: grAl transmon: time-domain. Qubit parameters extracted for the grAl transmon from resonance fluorescence time-domain measurements shown in Fig. 2.4. The pure dephasing time T_ϕ is calculated from the energy relaxation time T_1 and the dephasing time T_2 obtained in the Ramsey and Hahn echo experiment using $T_\phi = T_2/(1 - \frac{T_2}{2T_1})$.

resonance frequency $\omega_1/(2\pi)$	energy relaxation T_1	ext. energy relaxation $T_{1,\kappa}$	int. energy relaxation $T_{1,\gamma}$	dephasing (Ramsey) T_2^* (T_ϕ)	dephasing (echo) T_2 (T_ϕ)
7.4749 GHz	2.8 µs	3.1 µs	20^{+22}_{-6} µs	4.7 µs (28 µs)	5.1 µs (46 µs)

detuning, the observed Rabi oscillations increase in frequency, while the contrast of the measurement, the Rabi oscillation amplitude, decreases at the same time. At drive frequencies below the transition frequency, a second transition occurs, with Rabi oscillations that are roughly a factor $\sqrt{2}$ slower in frequency, suggesting a two-photon transition from the ground state into the second excited state.

Starting from the precise calibration of the π-pulse duration for a given drive amplitude by measuring the Rabi oscillations, the qubit coherence is extracted from a set of three measurements: the energy relaxation measurement, the Ramsey-fringes [186] and the Hahn-echo experiment [94].

In order to determine the energy relaxation time T_1, the qubit state is inverted by applying a 723 ns long π-pulse at an average manipulation power of $P_\mathrm{m} = -131.4$ dBm. With increasing waiting time τ between the end of the manipulation pulse and the beginning of the readout pulse, the population of the excited state decreases exponentially on a characteristic time scale $T_1 = 2.8$ µs, as shown in Fig. 2.4a.

For the Ramsey-fringes measurement, the qubit is prepared in a superposition state on the equator of the Bloch-sphere using a $\pi/2$-pulse, and projected back onto the z-axis with a similar pulse after a waiting time τ. The observed frequency of the Ramsey-fringes is caused by the detuning of the π-pulse frequency $\Delta_\mathrm{m} \approx 2\pi \times 300$ kHz from the qubit frequency. From the exponential envelope, the coherence time $T_2^* = 4.7$ µs is extracted, which is almost twice the energy relaxation time. In the Hahn-echo experiment, an additional π-pulse is applied in-between the $\pi/2$-pulses, reducing the effect of low-frequency noise, yielding $T_2 = 5.1$ µs. From both measurements, the pure dephasing times $T_\phi = 28$ µs and $T_\phi = 46$ µs are calculated using Eq. 1.34, revealing energy relaxation as the main source of decoherence.

In Fig. 2.4b, the fluctuations of the energy relaxation time (grey triangles) and the qubit frequency, both continuously monitored over 15 h are shown. Each marker

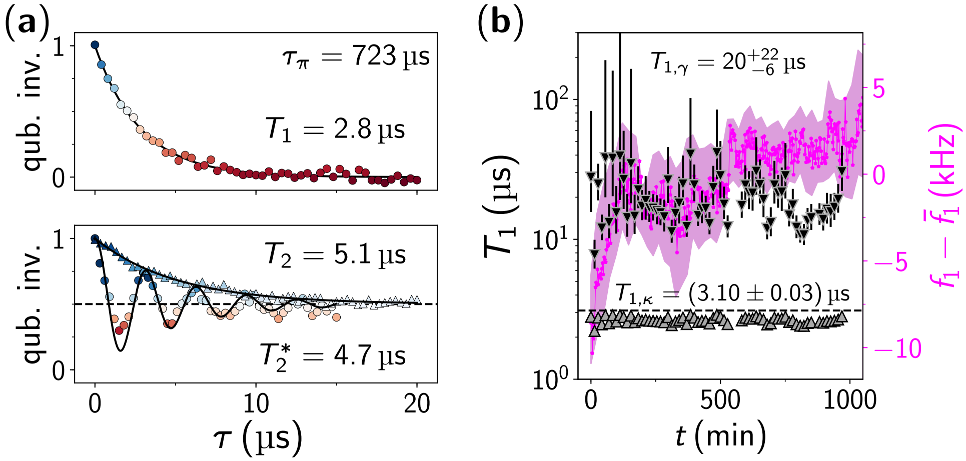

Figure 2.4: grAl transmon: resonance fluorescence (time-domain). a) Measurement of the grAl transmon coherence times. The duration of the π-pulse is 723 ns at an average manipulation power $P_\mathrm{m} = -131.4\,\mathrm{dBm}$. The markers in the top panel show the measured population inversion at a time τ after the π-pulse, and the black line indicates an exponential fit with a characteristic energy relaxation time $T_1 = 2.8\,\mu\mathrm{s}$. The bottom panel shows the results of a Ramsey-fringes (circles) and a Hahn-echo (triangles) measurement. The observed frequency of the Ramsey fringes agrees within 5% with the frequency detuning $\Delta_\mathrm{m} = 2\pi \times 300\,\mathrm{kHz}$ of the π-pulse. From the fits indicated by solid lines, coherence times $T_2^* = 4.7\,\mu\mathrm{s}$ and $T_2 = 5.1\,\mu\mathrm{s}$, as well as the corresponding pure dephasing times $T_\phi = 28\,\mu\mathrm{s}$ and $T_\phi = 46\,\mu\mathrm{s}$, respectively, are extracted. **b)** Time stability of the energy relaxation time (grey triangles) and the deviation $f_1 - \bar{f}_1$ of the qubit transition frequency from its average value $\bar{f}_1$ (pink markers corresponding to the right-hand axis). The pink shaded area is the uncertainty of the qubit frequency measurement. The inverted black triangles show the intrinsic energy relaxation time $T_{1,\gamma} = T_1 T_{1,\kappa}/(T_{1,\kappa} - T_1)$, where $T_{1,\kappa} = 3.1\,\mu\mathrm{s}$ (dashed line) is the limit due to spontaneous emission into the waveguide. Notably, the T_1 and frequency stability data were taken in different cool downs.

represents an average obtained by integrating over 15 min. Although the energy relaxation is limited by spontaneous emission into the waveguide sample holder, limiting the T_1 to $T_{1,\kappa} = 3.1\,\mu\mathrm{s}$ (black dashed line), the relaxation time $T_{1,\gamma}$ due to intrinsic energy decay is inferred using

$$T_{1,\gamma} = T_1 T_{1,\kappa}/(T_{1,\kappa} - T_1). \tag{2.8}$$

The obtained average intrinsic decay time $T_{1,\gamma} = 20^{+22}_{-6}\,\mu\mathrm{s}$ is in agreement with the value obtained from spectroscopy, and on par with other unconventional transmon qubits [141].

The pink markers indicate the detuning of the qubit frequency f_1 from its time average value $\bar{f}_1$, measured in a different measurement run and with higher time resolution. The observed total change is only on the order of the intrinsic linewidth γ, in conformity with the obtained pure dephasing times. Notably, the indicated uncertainty (pink shaded area) is due to the averaging over multiple measurements implemented for the sake of clarity, and does not reflect the intrinsic accuracy of the measurement.

2.4 Two-tone spectroscopy

In a two-tone spectroscopy, two tones are applied at the same time: a weak probe tone to measure the response of the system and an additional drive tone to induce changes in the system. For a qubit, the application of a drive applied close to the transition frequency dresses the bare energy eigenstates of the system (see Sec. 1.1.4), which is the ac equivalent to the Stark effect, very similar to the coupling between a resonator and a qubit. Figure 2.5a depicts the change in the energy spectrum in the presence of such an additional drive tone, including a potential third energy level. In the dressed spectrum, the two lowest energy eigenstates split into two states each, which are separated by the Rabi frequency Ω_R induced by the drive. Consequently, three distinct transitions emerge at frequencies ω_1 and $\omega_1 \pm \Omega_\mathrm{R}$ [7, 13, 215], indicated by the black and purple arrows. In atomic physics, the corresponding fluorescence spectrum is referred to as the Mollow-triplet [158].

For a multi-level system (qudit), the presence of higher energy eigenstates, which remain undressed by the drive as a result of the finite detuning caused by the anharmonicity of the energy spectrum, results in only two distinct transitions between the first and the second excited state, referred to as the Autler-Townes doublet [8, 13]. Since only the excited state splits, the frequency detuning between the two transitions directly reflects the generalized Rabi frequency Ω_R.

Figure 2.5b shows a two-tone spectroscopy performed with the grAl transmon in close vicinity of its fundamental transition frequency f_1. A fixed frequency drive tone was applied at $\Delta_\mathrm{drive} = 2\pi \times 200\,\mathrm{kHz}$ above f_1 with increasing drive power P_drive. Simultaneously, the reflection coefficient S_{11} was measured with a weak probe tone at varying frequency f and constant power $P_\mathrm{in} = -160\,\mathrm{dBm}$ using a commercial VNA.

For small drive powers, only a single resonance is visible in the phase of the reflection coefficient $\arg(S_{11})$ shown in Fig. 2.5b. With increasing drive power, the occupation of the first excited state $|1\rangle$ increases and a second feature becomes visible, 3.9 MHz below the qubit frequency, corresponding to the single-photon transition between the first and the second excited state $|1\rangle \rightarrow |2\rangle$. The frequency detuning between

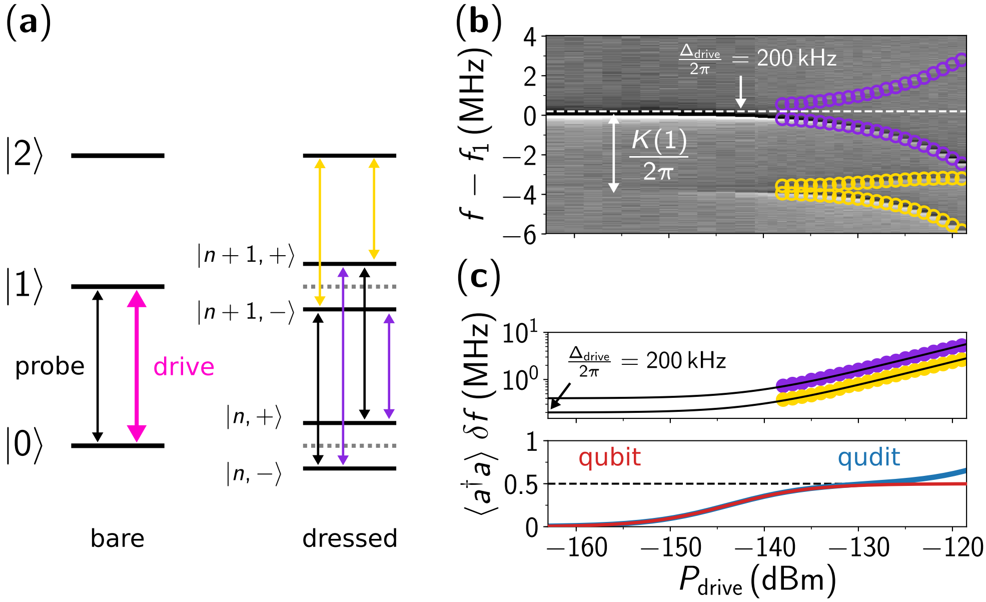

Figure 2.5: grAl transmon: two-tone spectroscopy. a) Energy spectrum of a three-level system (qutrit) in the abscence (bare) and the presence of a strong microwave drive (dressed). During a two-tone spectroscopy, two drives are applied, a weak probe tone (black) and a usually stronger drive tone (pink). The drive splits the two lowest bare energy levels by the Rabi frequency $\Omega_{\rm R}$, inducing three distinct transitions between the dressed ground and the dressed excited state (Mollow triplet, black and purple arrows). As the third energy level remains unaffected, there are only two transition between the dressed excited and the undressed second excited state (Autler-Townes doublet), indicated by yellow arrows. **b)** Phase of the reflection coefficient $\arg(S_{11})$ measured with a weak probe tone of constant power $P_{\rm in} = -160\,$dBm in the vicinity of the qubit frequency f_1, while an additional microwave drive is applied at $\Delta_{\rm drive}/2\pi = f_{\rm drive} - f_1 = 200\,$kHz detuning, indicated by the dashed white line. With increasing drive power $P_{\rm drive}$, the fundamental transition splits into two distinct transitions, corresponding to the side-bands of the Mollow-triplet [158], appearing at frequencies $f_\pm = f_1 \pm \Omega_{\rm R}/(2\pi)$ [7, 13]. Since the population of the first excited state increases with drive power, at $P_{\rm drive} \geq -150\,$dBm a second transition becomes visible 3.9 MHz below f_1, corresponding to the $|1\rangle \rightarrow |2\rangle$ transition. The measured anharmonicity $\alpha = 2\pi \times 3.9\,$MHz, as well as the qubit frequency $f_1 = 7.6790\,$GHz are slightly different than the values reported for the spectroscopy, due to the fact that the measurements were taken in different measurement runs (see App. C.8). Similar to the fundamental transition, the second transition also splits with increasing $P_{\rm drive}$ [13]. **c)** Extracted frequency splittings $\delta f = f_+ - f_-$ for the first two transitions (top panel). The black lines correspond to the theoretical predictions $2\Omega_{\rm R}$ (fundamental transition, purple markers) and $\Omega_{\rm R}$ (second transition, yellow markers), respectively, with $\Omega_{\rm R} = \sqrt{\Delta_{\rm drive}^2 + \Omega^2}$ and $\Omega = \sqrt{4\kappa P_{\rm drive}/hf_{\rm drive}}$. The bottom panel shows the expectation value for the photon number operator $\langle a^\dagger a \rangle$ as a function of the drive power $P_{\rm drive}$ numerically calculated for a qubit (red line) and for an anharmonic multi-level oscillator (see App. C.2).

the two transitions quantifies the qubit anharmonicity α. Notably, the measured anharmonicity $\alpha = 2\pi \times 3.9\,\mathrm{MHz}$ as well as the fundamental transition frequency $f_1 = 7.6790\,\mathrm{GHz}$ were slightly different compared to the values reported for the spectroscopy and time-domain measurements. Since the measurements were taken in different measurement runs, the sample parameters have changed in-between the runs. An overview on the various experiments is found in App. C.8.

With increasing driver power P_{drive}, both transitions $|0\rangle \rightarrow |1\rangle$ and $|1\rangle \rightarrow |2\rangle$ split into two distinct transitions each, as expected from the dressed energy spectrum shown in Fig. 2.5a. Furthermore, the observed frequency splitting is in quantitative agreement with the theoretical modelling of a driven three-level system [7, 13], as illustrated by the black solid lines in Fig.2.5c (top panel).

Since the qubit anharmonicity is on the order of a few megahertz, deviations in the system response from the qubit approximation are expected at higher drive powers. To illustrate this circumstance, the expectation value of the photon number operator $\langle a^\dagger a \rangle$ is shown in Fig. 2.5c (bottom panel), numerically calculated for a two-level (qubit, red) and a multi-level system (qudit, blue) with self-Kerr coefficient $K = \alpha$ (see App. C.2). For a qubit, the steady state occupation number versus drive power saturates at 0.5 as a result of the competition between qubit excitation and stimulated emission. In contrast, above a certain drive power, which depends on the relative size of the induced Rabi frequency and the spectral anharmonicity, the higher dimensionality of the multi-level Hilbert space manifests in an increase of the average photon number. Notably, the numerical calculations are based on a time-independent Hamiltonian, i.e. under the assumption of rectangular-envelope pulses. However, there are more elegant pulse forms and sequences which reduce leakage into higher energy eigenstates significantly, even for Rabi frequencies exceeding the qubit anharmonicity [161].

2.5 Energy spectrum

The multi-dimensionaility of the grAl transmon Hilbert space observed in the two-tone spectroscopy was also confirmed in the resonance fluorescence spectrum. For drive powers $P_{\mathrm{in}} > -138\,\mathrm{dBm}$ beyond the range covered in Fig. 2.2, additional features emerge in the reflection coefficient S_{11} at frequencies f_n below the qubit frequency f_1 (see. Fig. 2.6 left-hand panel). Similar to the high power spectroscopy of JJ transmon qubits [32, 202], these features are multi-photon transitions into higher energy eigenstates E_n starting from the ground state E_0. The transitions are observed at frequencies $f_n = (E_n - E_0)/(nh)$, where n is the level number, and the multi-photon origin is confirmed by the two-tone spectroscopy and the time-domain

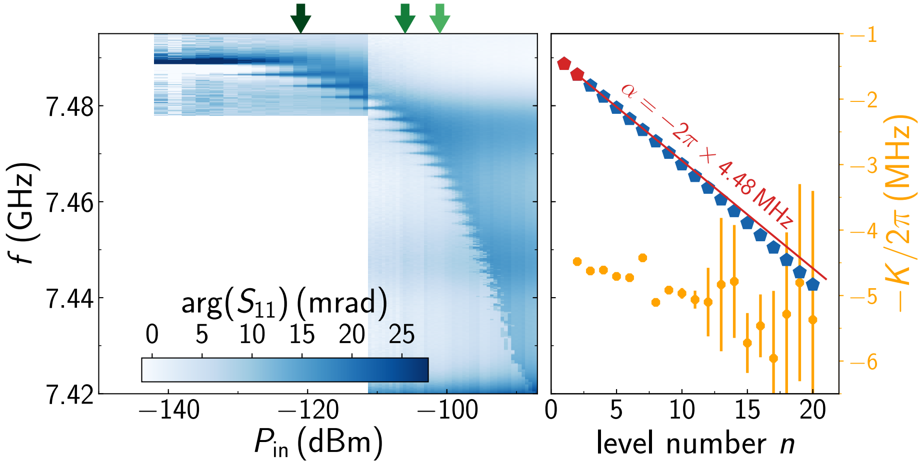

Figure 2.6: grAl Transmon: Energy spectrum. Phase of the measured reflection coefficient $\arg(S_{11})$ as a function of probe frequency f and incident on-chip power P_{in} (left panel). With increasing probe power multi-photon transitions are observed at frequencies f_n, labeled $(|0\rangle \rightarrow |n\rangle)/n$ where n denotes the level number, which are almost equidistant in frequency, as plotted in the right hand panel. From the first two points in the right hand panel (highlighted in red) a qubit anharmonicity $\alpha = K(1) = 2\pi \times 4.48\,\mathrm{MHz}$ is extracted, much larger than the spectral linewidth $\kappa + \gamma = 2\pi \times 50\,\mathrm{kHz}$ (cf. Fig. 2.2). To highlight the change in $K(n)$ with increasing level number n, the red line shows a linear extrapolation from the first two points. The extracted values $K(n)$ are plotted in orange using the right hand axis. The green-colored arrows indicate the power values at which the individual traces shown in Fig 2.7 were measured.

measurements. From the frequency detuning between the first two transitions (red markers in Fig. 2.6 right-hand panel), a qubit anharmonicity $\alpha = 2\pi \times 4.48\,\mathrm{MHz}$ is extracted.

Following the discussion in Sec. 2.1, for a conventional JJ transmon the anharmonicity is given by the charging energy $E_{\mathrm{c,s}} = e^2/2C_{\mathrm{s}}$ of the shunt capacitance [116], which is $E_{\mathrm{c,s}}/\hbar = 2\pi \times 141\,\mathrm{MHz}$ for the geometry presented in Fig. 2.1. Since the anharmonicity is reduced by N^2 for an array of identical JJ, the obtained value for the anharmonicity implies $N = \sqrt{E_{\mathrm{c,s}}/\hbar\alpha} \approx 6$ effective JJ inside the grAl volume. The corresponding effective junctions are therefore separated by $\sim 80\,\mathrm{nm}$, spanning approximately ten grains. This result is in agreement with recent scanning tunneling microscopy measurements performed on similar grAl films, which evidenced the collective charging of clusters of grains [234].

From the measured multi-photon transition frequencies f_n, the frequency shift per photon is calculated according to

$$\hbar K(n) = (E_n - E_{n-1}) - (E_{n+1} - E_n), \tag{2.9}$$

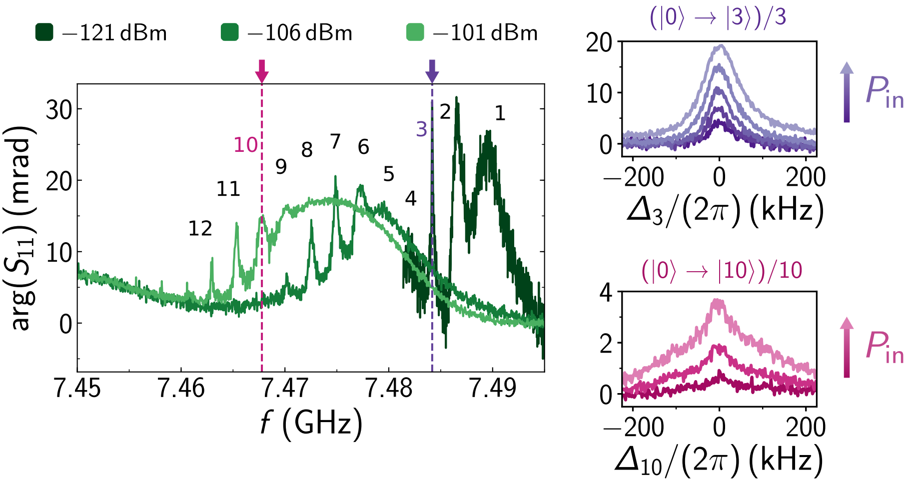

Figure 2.7: grAl Transmon: Energy spectrum. Three individual measurements (left-hand panel) performed at different probe powers ($P_{\mathrm{in}} = -121, -106$ and -101 dBm), as indicated by the equally colored arrows in the 2D plot in Fig. 2.6. Several multi-photon transitions are visible as peaks in the phase response. With increasing power, the linewidth of these transitions broadens, as shown in the right-hand panels for $n = 3$ (top panel, $P_{\mathrm{in}} = -127$ to -123 dBm) and $n = 10$ (bottom panel, $P_{\mathrm{in}} = -105.75$ to -104.75 dBm). Here, $\Delta_n = \omega - \omega_n$, is the frequency detuning between the drive and the respective multi-photon transition frequency, with $\omega_3 = 2\pi \times 7.4842$ GHz and $\omega_{10} = 2\pi \times 7.4678$ GHz, as indicated by the arrows and the vertical dashed lines in the left-hand panel.

with $E_n/h = nf_n$. As shown in the right-hand panel of Fig. 2.6 (right-hand axis), the energy difference between subsequent energy levels $K(n)$ monotonically increases with the level index n, likely due to the contribution of higher order terms arising from the expansion of the Josephson potential, not included in the consideration. A similar decrease in the transition frequency between higher energy eigenstates is also observed in conventional transmon qubits [116].

In the left-hand panel of Fig. 2.7, three measurements are shown which were performed at different drive powers $P_{\mathrm{in}} = -121, -106$ and -101 dBm. At any drive power in this range several multi-photon peaks are visible. The linewidth of each transition broadens with power, as exemplarily illustrated in the right-hand panels of Fig. 2.7 for the 3 rd and the 10 th multi-photon transition. The visibility of the peaks and the background response of the phase is in remarkable agreement with the master-equation simulation presented in App. C.2. The broadening of the $n = 10$ transition compared to $n = 3$ can be explained by the offset charge dispersion present in superconducting charge qubits. Although exponentially suppressed with E_J/E_C for the fundamental transition, the offset charge dispersion increases with a power law in n for higher energy eigenstates [116].

2.6 Magnetic field dependence

For the operation in external magnetic fields, the sample holder is equipped with a 2D-vector magnet, with the two field components graphically indicated by the red and blue coils in Fig. 2.1a. A more detailed description of the sample holder and the vector magnet are found in App. C.3 and App. C.6, respectively. In general, the application of an external magnetic field is expected to reduce the superconducting gap of the pure Al layer $\mathit{\Delta}_{\mathrm{Al}}$, as well as of the grAl layer $\mathit{\Delta}_{\mathrm{grAl}}$, causing an increase of the kinetic inductance associated with both films (see Sec. 1.2.1 and Sec. 1.2.2). Since the effect of magnetic fields applied out-of-plane is usually much stronger, owing to the large aspect ratio between the lateral dimensions of the thin film and the film thickness, the field orientation is aligned with the film plane using both coils simultaneously (see App. C.7).

As a side note, during the resonance fluorescence characterization of the qubit discussed in previous sections, the qubit was protected from external magnetic fields by a combination of cylindrical shields surrounding the waveguide sample holder, constructed of different materials. The most inner layer is a copper shield, followed by a superconducting aluminum and an outer µ-metal shield. For the application of magnetic fields, the µ-metal shield was removed for all measurements.

By applying a magnetic field B_y, aligned in-plane with the sample, a continuous decrease of the qubit frequency $f_1(B_{\mathrm{y}})$ was observed, as plotted in Fig. 2.8a. The measurements were performed in two separate measurement runs, with (filled crosses) and without (open pentagons) an outer superconducting Al shield. When employing the shield, the maximal field was limited to $\sim 70\,\mathrm{mT}$, after which the shield was affected by the field coils and introduced distortions in the field alignment resulting in a sudden decrease of the qubit frequency.

The expected in-plane magnetic field dependence of the qubit transition frequency $f_1(B_{\mathrm{y}})$ is derived by mapping the qubit onto a linearized, lumped-element circuit model consisting of three inductive contributions in series, altogether shunted by a capacitance $C_{\mathrm{s}} = 137\,\mathrm{fF}$. The inductive contributions arise from a field-independent geometric inductance $L_{\mathrm{s}} = 0.45\,\mathrm{nH}$, and two field-dependent kinetic inductances associated with the pure Al and grAl thin films, $L_{\mathrm{k,Al}}(B)$ and $L_{\mathrm{k,grAL}}(B)$, respectively. The lumped-element model transition frequency is

$$f_1(B_{\mathrm{y}}) = \frac{1}{2\pi\sqrt{C_{\mathrm{s}}\left(L_{\mathrm{k,Al}}(B_{\mathrm{y}}) + L_{\mathrm{k,grAl}}(B_{\mathrm{y}}) + L_{\mathrm{s}}\right)}}. \tag{2.10}$$

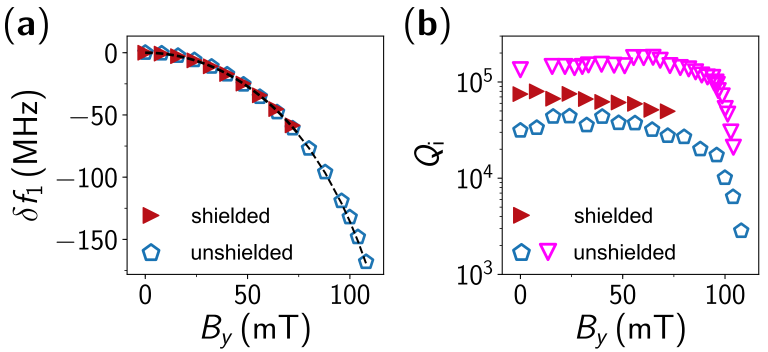

Figure 2.8: Magnetic field dependence. a) Relative change in qubit frequency $\delta f_1 = f_1(B_y) - f_1$ as a function of the applied in-plane magnetic field B_y. The experimental data was measured in two separate measurement runs: with (filled triangles) and without (open pentagons) an outer superconducting Al shield. The field dependence can be fitted to an effective circuit model (see Eq. 2.10), indicated by the black dashed line, from which the critical flux density $B_{\mathrm{c,Al}} = 150 \pm 5\,\mathrm{mT}$ of the Al film was extracted, in agreement with Ref. [152]. Notably, the observed change in the transition frequency was caused by the increasing kinetic inductance in the Al wires. **b)** Internal quality factor $Q_{\mathrm{i}} = \omega_1/\gamma$ for the shielded (filled triangles) and unshielded (open pentagons and triangles) case, both plotted versus the in-plane magnetic field B_y. For moderate fields, the quality factor slowly decreases with increasing field, followed by a sudden decrease above $B \geq 100\,\mathrm{mT}$. A possible explanation is the excitation of quasiparticles due to the suppression of the Al gap.

By describing both superconductors within a two-fluid model [214] (see Sec. 1.2.2), the field dependence of the gap parameter translates into a field dependence of the kinetic inductance

$$L_{\mathrm{k,i}}(B_{\mathrm{y}}) = L_{\mathrm{k,i}}(0)\sqrt{\frac{1 + (B_{\mathrm{y}}/B_{\mathrm{c,i}})^2}{1 - (B_{\mathrm{y}}/B_{\mathrm{c,i}})^2}}, \tag{2.11}$$

where the index $i \in \{\mathrm{Al},\ \mathrm{grAl}\}$ indicates the superconducting material, and $L_{\mathrm{k,i}}(0)$ is the inductance in zero-field. I would like to mention that there are different expressions for the field dependence of the superconducting gap, for instance reported in Ref. [64], which, however, result in a qualitatively very similar prediction.

Due to the large critical magnetic in-plane field of grAl $B_{\mathrm{c,grAl}} \geq 5\,\mathrm{T}$, both, reported in literature in Ref. [47] and more recently observed in grAl microstrip resonators using the same waveguide sample holder [29], the observed change in frequency is primarily due to the lowering of the Al gap Δ_{Al}, which leads to an increase of the kinetic inductance of the Al wires connecting the capacitor electrodes with the grAl volume. From the fit to the data according to Eq. 2.10, the contribution of the Al layer

Table 2.5: grAl transmon: magnetic field performance. Fit parameters according to Eq. 2.10, extracted from the magnetic field dependence of the fundamental transition frequency shown in Fig. 2.8a. The shunt capacitance $C_s = 137\,\mathrm{fF}$, as well as the stray inductance $L_s = 450\,\mathrm{pH}$ remained constant for the fitting procedure.

kinetic inductance (Al)	critical magnetic field	kinetic inductance (grAl)	critical magnetic field
$L_{\mathrm{K,Al}}$	$B_{\mathrm{c,Al}}$	$L_{\mathrm{K,grAl}}$	$B_{\mathrm{c,grAl}}$
200 pH	$150 \pm 5\,\mathrm{mT}$	2650 pH	$> 1\,\mathrm{T}$

to the total inductance is found to be $L_{\mathrm{K,Al}} = 200 \pm 5\,\mathrm{pH}$, and the corresponding critical magnetic field is $B_{\mathrm{c,Al}} = 150 \pm 5\,\mathrm{mT}$, in agreement with Ref. [152] for a film with 80 nm thickness. Furthermore, the obtained value for the contribution of the Al layer sets an upper bound on the contribution of the contact junctions formed by the overlap between the Al and the grAl film, as discussed in App. C.5. The accuracy on the critical field of the grAl is rather small, and the quoted value should be understood as an order of magnitude only.

Besides the increase in kinetic inductance and the consequential change in the transition frequency, the decrease in the superconducting gap and the presence of magnetic fields in general can have detrimental effects on the coherence of a quantum circuit. Figure 2.8b depicts the internal quality factor $Q_{\mathrm{i}} = \omega_1/\gamma$ as a function of the in-plane magnetic field B_{y} measured with (filled triangles) and without (open pentagons and triangles) an outer Al shield. The quoted quality factors are extracted from a fit to the resonance fluorescence response of the qubit (see Fig. 2.2).

In comparison to the data depicted in Fig. 2.2, the overall lower internal quality factor in these three measurement runs observed even in zero-field can be attributed to the removal of the μ-metal shield, which likely results in an increase of the (stray) B_z field oriented perpendicular to the film plane. In the presented grAl transmon design, the Al pads are the most field susceptible components, rendering the qubit frequency and internal quality factor particularly sensitive to out-of-plane magnetic fields, as illustrated by the factor of three difference in Q_{i} values in the unshielded case for nominally identical setups. Moreover, since the time-domain measurements were performed after these three measurement runs, aging effects can be excluded as an explanation for the observed reduction in Q_{i}.

Increasing the in-plane magnetic field results in a slow decrease of the internal quality factor. Above $B_y \geq 100\,\mathrm{mT}$, a sudden decrease in Q_i was observed, potentially caused by the excitation of quasiparticles due to the suppression of the Al gap, or the increasing number of magnetic vortices penetrating the Al thin film.

Finally, it is important to note that the absolute value of the non-linear frequency shift K is not expected to change in magnetic field, because the expression for K in the grAl transmon is independent of the grAl superconducting gap. The only change expected is due to a change in the kinetic inductance participation ratio of the grAl volume, which could also explain the different values for the qubit anharmonicity obtained in different measurement runs.

3 Dimer Josephson Junction Array Amplifier (DJJAA)

The Dimer Josephson junction array amplifier, in short DJJAA, is a non-degenerate, standing-wave parametric amplifier operated in reflection, which is based on the dispersion relation engineering of long arrays of SQUID junctions. A detailed summary of the DJJAA concept can be found in Ref. [231].

The main idea of the DJJAA is to provide a userfriendly working horse for experiments in the framework of cQED and related, by offering the following attributes in a single device:

- Low-noise performance down to the quantum limit
- High dynamic range and saturation power
- Protection of the qubit from pump leakage
- Large effective bandwidth realized by a multi-mode approach.

The DJJAA concept is based on the usage of long, one-dimensional arrays of Josephson elements, in particular dc SQUIDs, resulting in several eigenmodes in the frequency domain between 1 and 10 gigahertz utilized for parametric amplification. Moreover, due to the total length of the arrays, experimentally demonstrated up to $N = 1800$ SQUIDs, the magnitude of the Kerr coefficients is small compared to the linewidth of the modes, which is an important prerequisite for a high dynamic range, as explained in Sec. 1.3.4.

In analogy to the other weakly nonlinear systems, the DJJAA can be described by a quantum optics Hamiltonian of the form

$$\mathbf{H} = \sum_{m=0}^{N-1} \hbar\omega_m \hat{a}_m^\dagger \hat{a}_m + \underbrace{\frac{\hbar}{2} K_{m,m} \omega_m \hat{a}_m^\dagger \hat{a}_m \hat{a}_m^\dagger \hat{a}_m}_{\mathrm{self-Kerr}} + \underbrace{\sum_{m,k=0}^{N-1} \frac{\hbar}{2} K_{m,k} \omega_m \hat{a}_m^\dagger \hat{a}_m \hat{a}_k^\dagger \hat{a}_k}_{\mathrm{cross-Kerr}}, \tag{3.1}$$

where ω_m are the eigenmodes of the DJJAA, and $K_{m,m}$ and $K_{m,k}$ are the self-Kerr and cross-Kerr coefficients, respectively. In particular the cross-Kerr terms are used to enable non-degenerate parametric amplification with pairs of modes.

In order to optimize the non-degenerate operation, the regular dispersion relation of Josephson junction arrays (JJA) is engineered to form pairs of modes, denoted dimers, separated by only a few hundreds of megahertz. For the operation as an amplifier, a strong pump tone is applied in-between two dimer modes, giving rise to a four-wave mixing conversion process and a power gain profile composed of two overlapping curves with Lorentzian spectral line shape, one containing the signal response, the other containing the idler. The obtained detuning between pump and signal frequency protects the measured system, for instance a qubit, from pump leakage.

3.1 Multi-mode parametric amplifiers

Multi-mode parametric amplifiers constitute a class of JPAs utilizing several eigenmodes of the same device for parametric amplification in different frequency domains, such that the overall bandwidth of the amplifier is enhanced [207, 231]. Ideally, a parametric amplifier covers the whole range between $1 - 10\,\mathrm{GHz}$ typically used for cQED experiments.

In standard degenerate and non-degenerate JPAs, the operational bandwidth of the device is enhanced by employing flux tunable junctions, for instance dc SQUIDs or SNAILs [77], with flux dependent critical current and Josephson energy, as shown in Fig. 3.1 (left-hand panel). At least in principle, the obtainable bandwidth is on the order of several gigahertz, but in reality, the power gain tunability of such devices is limited to a smaller range.

By lowering the Josephson energy with flux, the nonlinearity of the modes increases with respect to the resonance frequency, while the effect of higher order nonlinear contributions arising from the Josephson potential are more likely to influence the performance of the amplifier at the same time [31]. As a consequence, the observed saturation power decreases. Moreover, the effect of flux noise in the SQUID loop is proportional to the flux derivative of the frequency dependence on field $\sim \partial\omega/\partial\Phi_{\mathrm{ext}}$, which steadily increases away from effective zero-field, the so-called flux sweet spot.

In a multi-mode amplifier, these limitations are mitigated by using several eigenmodes. A single device can cover a large bandwidth if the maximal flux tunability of

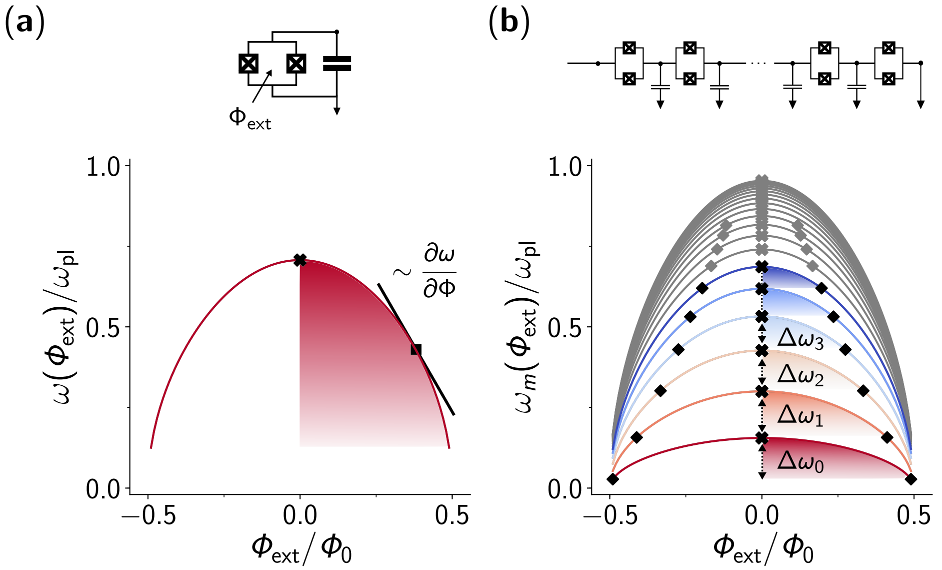

Figure 3.1: Multimode amplifiers: Concept. a) Resonance frequency ω of a JPA circuit containing a single (symmetric) SQUID junction, normalized by the plasma frequency ω_{pl} of the SQUID and calculated as a function of the normalized external magnetic flux $\Phi_{\mathrm{ext}}/\Phi_0$ enclosed in the SQUID loop. The total shunt capacitance of the SQUID is $C = 2C_{\mathrm{J}}$. The bandwidth of the device is given by the frequency tunability of the mode (red area). The black solid line indicates the slope at the indicated flux point (black square) to emphasize the increase in flux noise away from the flux sweet spot (black cross). **b)** Normalized, flux dependent dispersion relation of a long JJA consisting of $N = 1000$ SQUID junctions. The ratio between SQUID capacitance and capacitance to ground is $C_{\mathrm{J}}/C_0 = 2500$. Due to the large number of degrees of freedom, the mode density in the frequency domain is enhanced, with the modes close to the plasma frequency being greyed out. In order to cover a similar bandwidth (colored areas), each eigenmode $m+1$ has to be flux tuned to the next lower frequency m at the flux sweet spot (black crosses) only. The required minimal external flux is indicated for each mode by the black diamonds. Notably, the slope at these points is almost independent of the mode number m.

each mode is larger than the frequency detuning of neighboring eigenmodes in zero field:

$$\underbrace{\omega_{m+1}(0) - \omega_m(0)}_{\Delta\omega_m} \leq \omega_{m+1}(0) - \omega_{m+1}(\Phi_{\mathrm{max}}) \tag{3.2}$$

Here, $\Phi_{\mathrm{max}} \leq 0.5\Phi_0$ is the maximal external magnetic flux at which the device is still operable as an amplifier with sufficient power gain and reasonable saturation power well above the single photon regime.

Josephson junction arrays

For devices with several eigenmodes, the dispersion relation of the system is the dependence of the eigenfrequencies on the mode number. In a long Josephson junction array containing $N \gg 1$ elements, the obtained dispersion relation is composed of a linear regime in which the frequency detuning between neighboring eigenmodes is almost equidistant, and a dense regime close to the plasma frequency ω_{pl} of the JJs (see Fig. 3.1b)

The frequency detuning between the eigenmodes in the linear regime is controlled by the length of the array N, and the ratio of junction capacitance C_{J} and capacitance to ground C_0 [228]:

$$\begin{aligned} \Delta\omega &\sim \frac{1}{N} \\ \Delta\omega &\sim \frac{C_{\mathrm{J}}}{C_0} \end{aligned} \tag{3.3}$$

Since the expected Kerr nonlinearity decreases also with the number of elements, as discussed in Sec. 2.1, using long JJAs is generally benificial. A more detailed discussion about JJA is found in App. F.

Figure 3.1 summarizes the conceptual idea of a multi-mode parametric amplifier by comparing the (ideal) flux modulation of the resonance frequency of a JPA with a single SQUID junction, with the flux dependent dispersion relation of a JJA. As indicated by the colored areas, the flux modulation of each mode required to cover an overall similar bandwidth is highly reduced in the case of the JJA.

3.2 Circuit model

Besides a low number of added noise, a large bandwidth and high dynamic range, the protection of the device under test (DUT) from the influence of the strong pump tone is very crucial for a plug-and-play device. While asymmetric nonlinear elements like the SNAIL [77] enable parametric amplification in a three-wave-mixing process, in which the signal and the pump tone are naturally far detuned, the DJJAA concept follows a different path based on a four-wave-mixing process: the dispersion relation of a JJA is engineered in such a way that it exhibits pairs of modes, denoted dimers, which are used for non-degenerate parametric amplification. With the pump tone applied in-between the two dimer modes, the signal, idler and pump tone frequencies are detuned by up to hundreds of megahertz.

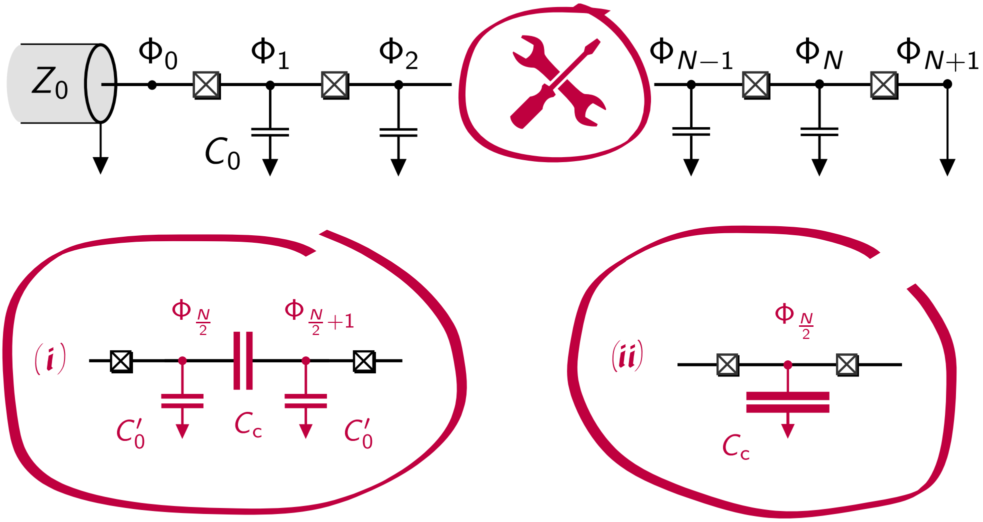

Figure 3.2: DJJAA: dispersion engineering. The effective circuit model of the DJJAA consists of a one-dimensional network of N identical SQUID junctions(crossed boxes), with flux dependent critical current $I_c(\Phi_{ext})$ and junction capacitance C_J, which are separated by superconducting islands contributing with a capacitance to ground C_0. The engineering of the dispersion relation is implemented by either interrupting the array with a large in-plane capacitor (i), or by introducing a large capacitance to ground (ii) in the center of the array. In the first case, the capacitance to ground on the neighboring nodes ($N/2$ and $N/2+1$), is assumed to be enhanced, too, which is captured by the parameter C_0'.

Dispersion relation

The dispersion relation of a single JJA is engineered to allow for non-degenerate parametric amplification by placing a capacitance in the center of the array, either in series to the junction capacitance, or to ground. Figure 3.2 depicts the effective circuit model for both cases. The Josephson elements are indicated by crossed boxes, surrogating a SQUID junction with flux dependent critical current $I_c(\Phi_{ext})$, shunted by its junction capacitance C_J. The superconducting islands inbetween the Josephson elements contribute with a capacitance to ground C_0. The additional circuit elements associated to the center capacitance with size C_c are highlighted in ruby. If the capacitor interrupts the array, as shown in (i), the capacitance to ground on the neighboring islands, denoted C_0', is assumed to be enhanced to account for the physical size of the capacitor plates. The dispersion relation of the DJJAA is derived from the linearized Lagrangian of the effective circuit model [228].

In the case of a galvanically coupled DJJAA device, and provided the center capacitance C_c is in series with the junction capacitance, the corresponding Lagrangian is

$$\begin{aligned}\mathcal{L} = &\sum_{i=1}^{N/2-1} \frac{C_0}{2}\dot{\Phi}_i^2 + \sum_{i=\frac{N}{2}+2}^{N} \frac{C_0}{2}\dot{\Phi}_i^2 \\ &+ \frac{C_0'}{2}\left(\dot{\Phi}_{N/2}^2 + \dot{\Phi}_{N/2+1}^2\right) + \frac{C_\mathrm{c}}{2}\left(\dot{\Phi}_{N/2+1} - \dot{\Phi}_{N/2}\right)^2 \\ &+ \sum_{i=0}^{N/2-1} \frac{C_\mathrm{J}}{2}\left(\dot{\Phi}_{i+1} - \dot{\Phi}_i\right)^2 + \sum_{i=N/2+1}^{N} \frac{C_\mathrm{J}}{2}\left(\dot{\Phi}_{i+1} - \dot{\Phi}_i\right)^2 \\ &- \sum_{i=0}^{N/2-1} E_\mathrm{J}\cos(\varphi_{i+1} - \varphi_i) - \sum_{i=N/2+1}^{N} E_\mathrm{J}\cos(\varphi_{i+1} - \varphi_i),\end{aligned} \tag{3.4}$$

where $\Phi_i = \Phi_0\varphi_i/(2\pi)$ is the node flux on the i th node, and φ_i is the superconducting phase. For clarity, terms arising from similar circuit elements are grouped together in rows. Accordingly, the first row contains the terms arising from the superconducting islands in-between the Josephson elements, while the second row contains the terms that are related to the additional capacitance in the center. Here, the coefficient C_0' is the capacitance to ground attributed to the two nodes to the left and the right of the center capacitor. In a realistic physical implementation, the additional capacitance to ground is likely to be much bigger than the capacitance to ground due to the small superconducting islands in-between the Josephson elements $C_0' \gg C_0$. Finally, the third and the fourth row contain the terms associated with the Josephson elements. Notably, due to the additional lattice site introduced by the center capacitance, the final value of the indices is $N + 1$.

In the limit of small circulating currents with respect to the critical current of the junctions $I \ll I_\mathrm{c}$, the phase drop $\varphi_{i+1} - \varphi_i$ across each junction becomes small even in regions of maximal current, and the Lagrangian is linearized by approximating the nonlinear cosine potentials with harmonic potentials. The corresponding coefficients are the linear Josephson inductances L_J introduced in Sec. 1.1.2.

By introducing the node flux vector $\vec{\Phi} = (\Phi_0, ..., \Phi_N)$, the linear Lagrangian is expressed in a more compact matrix representation

$$\mathcal{L} = \frac{1}{2}\dot{\vec{\Phi}}^\mathrm{T}\tilde{C}\dot{\vec{\Phi}} - \frac{1}{2}\vec{\Phi}^\mathrm{T}\tilde{L}^{-1}\vec{\Phi}, \tag{3.5}$$

where $\tilde{C}$ and $\tilde{L}^{-1}$ are the capacitance and the inverse inductance matrices, respectively (see App. G.1). The matrices contain the information about the distribution of the circuit parameters along the array.

The frequencies ω_m of the eigenmodes and the corresponding standing-wave pattern of the node flux $\vec{\Phi}_m$ along the array are calculated by solving the eigenvalue problem

$$\tilde{C}^{-1/2}\tilde{L}^{-1}\tilde{C}^{-1/2}\vec{\Psi}_m = \omega_m^2\vec{\Psi}_m \tag{3.6}$$

numerically [228].

Figure 3.3a depicts the flux dependent dispersion relation of a DJJAA under the assumption that the SQUID junctions are symmetric and the loop inductance is negligible (see App. E). For the given set of circuit parameters listed in Tab. 3.1, the device exhibits several dimers for which the frequency detuning is significantly smaller compared to a standard JJA. The circular markers indicate the eigenfrequencies at the flux sweet spot, which are compared to the case of a JJA with the exact same parameters in Fig. 3.3b. Each dimer is suitable for nondegenerate parametric amplification, as exemplarily shown for the second dimer in the inset.

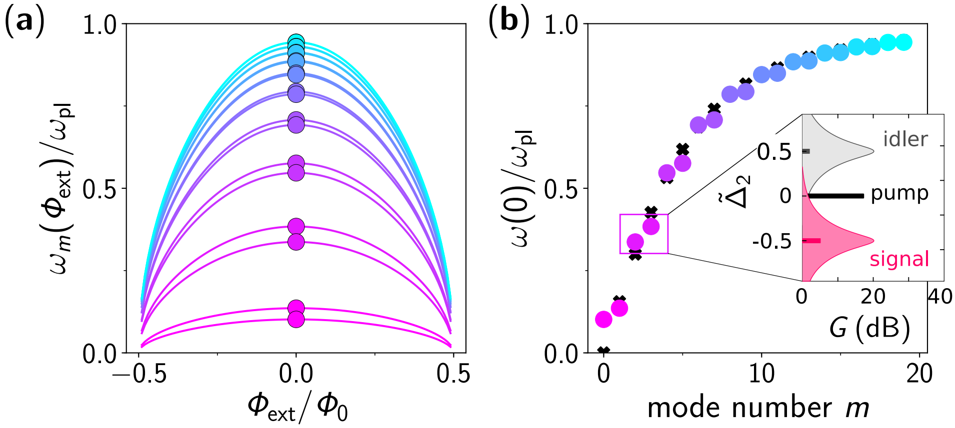

Figure 3.3: DJJAA: Dispersion relation. a) Eigenfrequencies of a DJJAA, normalized by the single junction plasma frequency ω_{pl}, and calculated according to Eq. 3.6 as a function of the normalized external magnetic flux $\Phi_{\mathrm{ext}}/\Phi_0$ enclosed in each SQUID loop. Due to the center capacitance, the DJJAA's dispersion relation exhibits pairs of modes, denoted dimers, which are close in frequency and highlighted in the same color. The circuit parameters used for the calculation are $N = 1000$, $I_{\mathrm{c}}(0) = 6\,\mu\mathrm{A}$, $C_{\mathrm{J}} = 1000\,\mathrm{fF}$, $C_{\mathrm{c}} = 45\,\mathrm{fF}$, $C_0' = 30\,\mathrm{fF}$ and $C_0 = C_{\mathrm{J}}/2500$. **b)** Dispersion relation in zero-field of a single JJA (black crosses) and a DJJAA (colored circles) calculated for the same circuit parameters. As indicated by the inset, each dimer is suitable for nondegenerate parametric amplification, which detunes the pump tone from the signal frequency by a few hundreds of megahertz.

Table 3.1: DJJAA: Circuit parameters. Values for the circuit parameters of the linear model of the DJJAA, as shown in Fig. 3.2, used for the numerical calculation of the flux dependent dispersion relation shown in Fig. 3.3. The zero-field critical current $I_\mathrm{c}(0)$ and the Josephson inductance L_J, as well as junction capacitance are for a single SQUID.

Length	critical current	Josephson inductance	junction capacitance	capacitance to ground	center capacitance	center cap. to ground
N	$I_\mathrm{c}(0)$	$L_\mathrm{J}(0)$	C_J	C_0	C_c	C_0'
1000	6 µA	55 pH	1 pF	1/2500 pF	45 fF	30 fF

Kerr-nonlinearity:

The self-Kerr and cross-Kerr coefficients $K_{m,m}$ and $K_{m,k}$ are obtained by expanding the cosine potentials in the Lagrangian up to the quartic order, and are given by [228]

$$K_{m,m} = -\frac{2\hbar\pi^4 E_\mathrm{J}\eta_{mmmm}}{\Phi_0^4 C_\mathrm{J}^2 \omega_m^2}, \tag{3.7}$$

and

$$K_{m,k} = -\frac{4\hbar\pi^4 E_\mathrm{J}\eta_{mmkk}}{\Phi_0^4 C_\mathrm{J}^2 \omega_m \omega_k}. \tag{3.8}$$

Here, η_{mmkk} is a numerical factor that takes the standing-wave pattern of each mode into account, and is defined as

$$\begin{aligned}\eta_{mmkk} =& C_\mathrm{J}^2 \sum_{i=1}^{N} \left[\left(\sum_{j=0}^{N} \left(\tilde{C}_{i,j}^{-1/2} - \tilde{C}_{i-1,j}^{-1/2} \right) \Psi_{j,m} \right)^2 \right. \\ & \left. \times \left(\sum_{j=0}^{N} \left(\tilde{C}_{i,j}^{-1/2} - \tilde{C}_{i-1,j}^{-1/2} \right) \Psi_{j,k} \right)^2 \right], \end{aligned} \tag{3.9}$$

where $\Psi_{j,m}$ is the j th entry of the m th eigenvector $\vec{\Psi}_m$, and $\tilde{C}_{i,j}^{-1/2}$ is the entry in the i th row and the j th column of the square root of the inverse capacitance matrix.

Although less intuitive as for the transmon qubit, generally speaking, the Kerr coefficients increase with increasing mode number m, but saturate as soon as the dispersion relation approaches the plasma frequency. For the applied circuit model, the standing-wave pattern of the node flux $\vec{\Phi}_m$ is related to the eigenvectors $\vec{\Psi}_m$ [228]:

$$\vec{\Phi}_m = \sqrt{\frac{\hbar}{2\omega_m}} \tilde{C}^{-1/2} \vec{\Psi}_m, \tag{3.10}$$

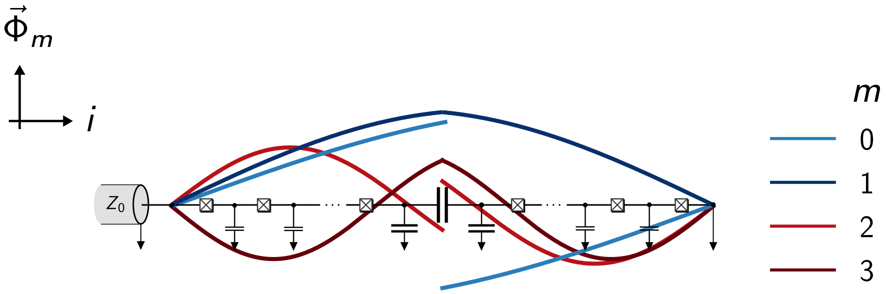

Figure 3.4: DJJAA: Standing-wave pattern. The standing-wave pattern of the node flux eigenvectors $\vec{\Phi}_m$ for the first four eigenmodes $m \in \{0,1,2,3\}$ of a typical DJJAA device with an in-plane center capacitance. The two modes forming a dimer have a similar distribution along the array, with the mode lower in frequency being antisymmetric, or out-of-phase, and the other mode being symmetric, or in-phase, on both sides of the capacitor. Since the current across each element is given by the difference in flux on the neighboring nodes, the distribution reveals that the current is maximal on both ends of the array for all modes, and at the roots of the distribution.

Figure 3.4 depicts the standing-wave patterns of the first four eigenstates, corresponding to the circuit parameters used in Fig. 3.3. In the presented case of an in-plane capacitor, the two modes forming a dimer are symmetric and antisymmetric pairs with respect to the center capacitance.

3.3 Design and fabrication

The DJJAA samples implemented and investigated in the scope of my thesis consist of arrays of optically fabricated SQUID junctions, and are interrupted by an interdigital in-plane capacitor in the center, as shown in Fig. 3.5. The size of center capacitance is controlled by the length and the number of the fingers, while keeping a constant gap, and, as a rule of thumb, is adjusted linearly to the length of the array N.

On the left-hand side, the array is galvanically connected to a microwave input port formed by a 50 Ω on-chip transmission line, and is galvanically grounded on the other end. The JJA is designed in a meander structure, with a total of twelve SQUIDs per meander, with the aim to reduce the physical length of the device and the impact of magnetic field gradients.

The samples are fabricated on double polished sapphire substrates with the aid of a two-step optical-lithography fabrication process. First, the majority of structures including the center capacitor, the on-chip transmission line and most parts of the

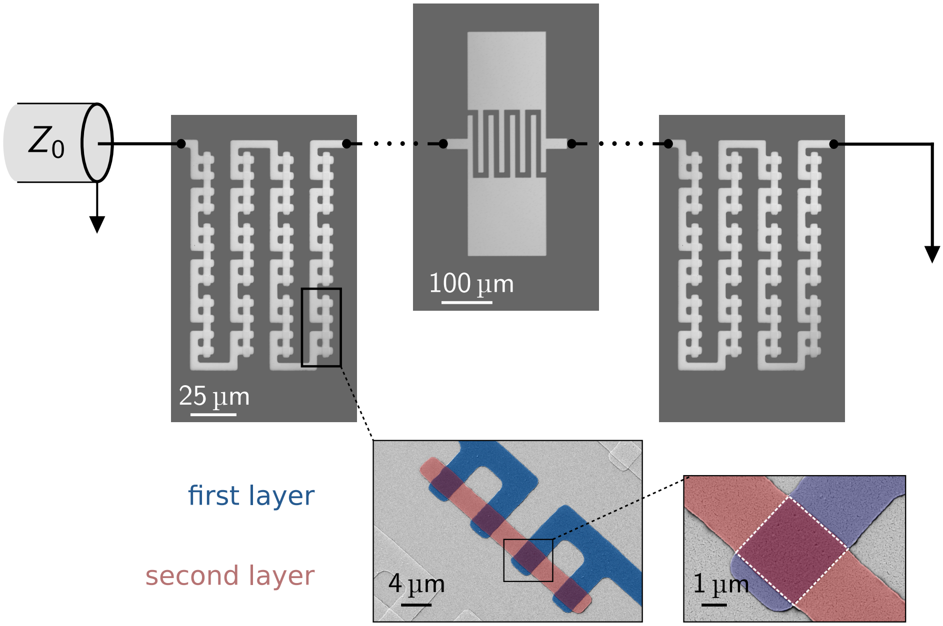

Figure 3.5: DJJAA: sample design. Optical microscopy images of several parts of a DJJAA implementation. The JJA to the left and the right of the interdigital in-plane capacitor in the center is comprised of a meander structur of symmetric dc SQUIDs, with twelve SQUIDs per meander. The left-hand end of the array is galvanically connected to an on-chip transmission line with characteristic impedance $Z_0 \approx 50\,\Omega$, while the right-hand end is grounded. The inset shows a scanning electron microscopy image of two SQUIDs, in which the aluminum thin films are false-color coded to illustrate the fabrication procedure. All structures are patterned on sapphire substrates based on an optical-lithography fabrication process. The overlap areas between the first (blue) and the second layer (red) forming the JJs are $A \approx 10 - 12\mu\text{m}^2$, giving rise to a substantial junction capacitance C_J.

array are patterned, followed by a zero-angle evaporation of 30 nm Al. The magnified region around two SQUIDs, as shown in the scanning electron microscopy images in Fig. 3.5, reveals the parts of the first layer by a blue color. Right before the first Al layer is evaporated, a physical and chemical cleaning procedure is performed to minimize the detrimental effect of resist residuals on the aging of the JJs.

For the precise control of the critical current density j_c of the JJs, the native oxide, which grows naturally when Al is exposed to oxygen, is removed from the first layer with the aid of an argon milling process [92]. Subsequently, the Al film is oxidized statically for a time $t_\text{ox} = 2 - 7$ min in a controlled oxygen atmosphere with constant partial pressure $p_\text{ox} \approx 10$ mbar, followed by a zero-angle evaporation of 40 nm Al (light red). The overlap area between the first and the second layer, highlighted by the white dashed rectangle, forms the JJs.

In order to provide a low loss ground reference, a $200 - 300\,\mathrm{nm}$ platinum layer is evaporated onto the backside of the wafer. As a sticking layer, a $10\,\mathrm{nm}$ layer of titanium is used. More details on the individual fabrication steps are given in App.G.13.

3.4 Dimerization

The dimerization of the array modes is demonstrated for three samples in the top panels in Fig. 3.6a), b), and c), which show the phase of the complex reflection coefficient $\arg(S_{11})$ as a function of probe frequency f and external flux bias Φ_{ext}. The three samples are composed of a different total number of SQUIDs, $N = 1200, 1600$ and 1800, and furthermore differ in the critical current per SQUID $I_{\mathrm{c}} = 7.0\,\mu\mathrm{A}, 3.5\,\mu\mathrm{A}$ and $2.7\,\mu\mathrm{A}$. The corresponding Josephson inductances are $L_{\mathrm{J}} = 47\,\mathrm{pH},\ 94\,\mathrm{pH}$ and $123\,\mathrm{pH}$. Due to the sweep in design parameters, a single dimer in (a), three dimers in (b) and four dimers in (c) were observed.

With increasing external flux, the frequencies of the dimers decrease, as expected from the increase in the SQUID inductance and in agreement with Fig. 3.3. The maximal SQUID frustration, i.e. the maximal kinetic inductance, occurs at $|\Phi_{\mathrm{ext}}/\Phi_0| \approx 0.5$, which is used to calibrate the external magnetic flux. From the obtained modulation amplitude, a high SQUID symmetry in terms of the critical currents of the JJs can

Table 3.2: DJJAA: Circuit parameters (samples). Values for the circuit parameters entering the linearized DJJAA model for the three samples A, B and C shown in Fig. 3.6, used to calculate the corresponding dispersion relations shown in Fig. 3.7. With the aid of sample D, the gain-tunability is demonstrated (see Fig. 3.8). For all samples, the value assumed for the capacitance to ground of the center capacitance is $C_0' = 33\,\mathrm{fF}$.

	array length N	critical current $I_{\mathrm{c}}(0)$	Josephson inductance $L_{\mathrm{J}}(0)$	junction capacitance C_{J}	capacitance to ground C_0	center capacitance C_{c}
sample A	1200	7 µA	47 pH	1225 fF	0.45 pF	30 fF
sample B	1600	3.5 µA	94 pH	1225 fF	0.45 pF	40 fF
sample C	1800	2.7 µA	123 pH	1225 fF	0.45 pF	45 fF
sample D	1300	6.2 µA	53 pH	1225 fF	0.45 pF	32.5 fF

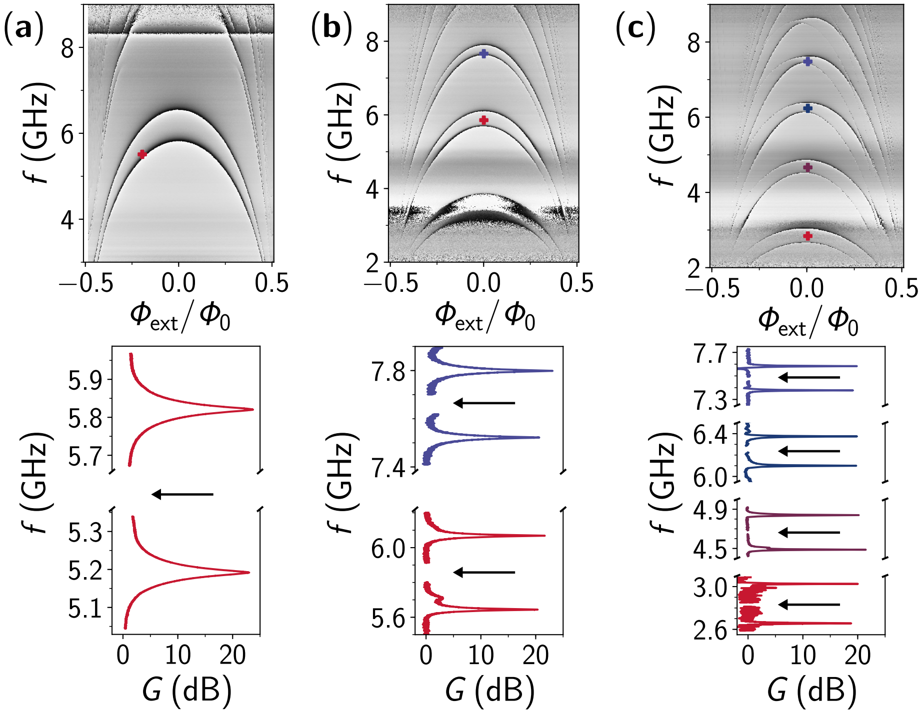

Figure 3.6: Phase response of the complex reflection coefficient $\arg(S_{11})$ **measured as a function of externally applied flux** Φ_{ext} **for three dispersion engineered JJ arrays: a)** $N = 1200$ JJs, $I_c \approx 7.0\,\mu\mathrm{A}$, $C_c = 30\,\mathrm{fF}$, **b)** $N = 1600$ JJs, $I_c \approx 3.5\,\mu\mathrm{A}$, $C_c = 40\,\mathrm{fF}$, **c)** $N = 1800$ JJs, $I_c \approx 2.7\,\mu\mathrm{A}$, $C_c = 45\,\mathrm{fF}$. The dispersion relation is dimerized by introducing C_c in series with the junction capacitance C_J in the center of the array. As expected, the number of modes within the given frequency range (here $2-9\,\mathrm{GHz}$) increases with increasing N and decreasing I_c. By applying a strong pump tone in-between two hybridized modes, non-degenerate power gain exceeding $G_0 = 20\,\mathrm{dB}$ is observed for up to four pairs of modes in a single device, as shown in panel c). The arrow and cross symbols in each panel indicate the external flux bias and pump frequency, color-coded for each dimer. The horizontal features visible in the vicinity of 4 and 8 GHz correspond to the frequency band of the circulator attached to the DJJAA input port.

be inferred, as well as a negligible contribution of the SQUID loop inductance (see App. E).

From the measured spectra, the frequencies ω_m of the eigenmodes are determined, and compared to the prediction of the circuit model, as shown in Fig. 3.7. The circuit parameters corresponding to the individual spectra are listed in Tab. 3.2. Since most circuit parameters entering the model, in particular L_J, C_J, C_c and C_0', are estimated from complementary room-temperature transport measurements and finite element method simulations, the capacitance to ground C_0 per island remains the only real free parameter. A detailed discussion can be found in App. G.4. For all three devices, the same value for the capacitance to ground $C_0 = 0.45\,\mathrm{fF}$ was used to calculate the dispersion relations, as the amplifier packaging and the design are conceptually identical.

Although the agreement between the model prediction and the obtained frequencies is generally satisfying, the agreement is noticeably better for the devices with larger kinetic inductance per SQUID, since the circuit model does not account for additional linear inductances arising from the islands connecting the SQUIDs (see App. G.4).

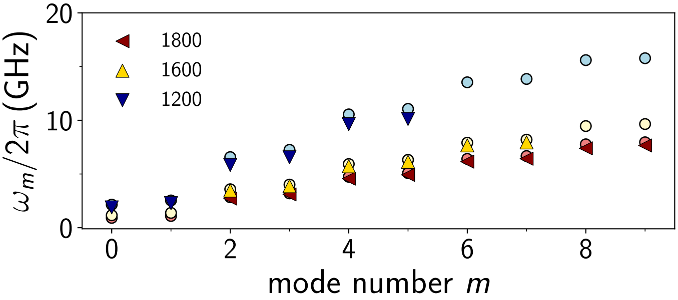

Figure 3.7: DJJAA: dispersion relation at the flux sweet spot. Measured (triangles) and numerically calculated (circles) dispersion relation of the three DJJAA devices A, B, and C shown in Fig. 3.6. The circuit parameters L_J, C_J, C_c and C_0' are estimated from room temperature transport measurements and FEM simulations, and remain fixed, leaving the capacitance to ground C_0 the only free parameter (see App. G.4). For all three samples, the same value $C_0 = 0.45\,\mathrm{fF}$ was used for the calculation. All parameters are listed in Tab. 3.2. Noticeably, the agreement between the model prediction and the measurement is better for the longer arrays, which is not due to the length but rather because of the larger kinetic inductance per SQUID, and the smaller contribution of the stray inductance, which is not included into the model.

3.5 Multi-mode power gain

The power gain $G = P_{\mathrm{out,on}}/P_{\mathrm{out,off}}$ is defined as the ratio between the received power with and without the pump tone applied. Since the response of the system is deduced from the reflection coefficient, which is a ratio of voltages, the power gain is determined as the ratio of the squared amplitudes of the reflection coefficient measured in both cases $G(\omega) = |S_{11,\mathrm{on}}|^2/|S_{11,\mathrm{off}}|^2$. Owing to this normalization, finite losses in the amplifier modes appear as artificial gain in the measurement.

The bottom panels in Fig. 3.6a, b and c depict the power gain G in decibel as a function of probe frequency f when an additional pump tone of power P_{p} and frequency f_{p} is applied in-between two dimerized modes at a time. The black arrows and cross symbols, color-coded individually for each dimer, indicate the external bias flux Φ_{ext} and pump frequency used in each experiment. For most dimers, the pump frequency appears off-centered with respect to the low probe power response shown in the top panels, since the mode population $\bar{n}_m$ caused by the strong pump tone lowers the dimer modes in frequency up to several hundreds of megahertz.

For the DJJAA, the observed power gain is composed of two overlapping Lorentzian curves, symmetrically emerging below and above the pump tone frequency. In general, the frequency detuning between the two maxima can be fine-tuned by the pump power and the pump frequency, similar to Ref. [67]. The maximal power gain G_0 exceeds 20 dB, which is a typical value required to saturate the classical noise added by higher temperature amplifier stages with the amplified quantum noise. For the sample shown in Fig. 3.6c, four dimers were used to obtain parametric amplification, epitomizing the potential of the DJJAA concept. Notably, due to a finite magnetic field gradient along the device, the flux modulation is asymmetric, as discussed in App. G.7, limiting the achievable flux tunability of the device. Such detrimental effects on the performance are mitigated with a dedicated magnetic shielding.

Gain tunability

The flux tunability of the different modes, in particular the achievable tunability of the power gain, is an important figure of merit for the implementation of a multi-mode amplifier. Figure 3.8 depicts the power gain measured in three different dimers in a single device composed of $N = 1300$ JJs. The device is from the same batch as sample a in Fig. 3.6, and has therefore similar circuit parameters.

The frequency tunability of all three modes exceeds 1.5 GHz and, thus the total bandwidth of the device is ≥ 4.5 GHz. Due to the design parameters, the frequency splitting between neighboring dimers is roughly a factor of two larger than the achieved gain tunability. By increasing the number of JJs or the capacitance to ground, a smaller frequency detuning could be achieved.

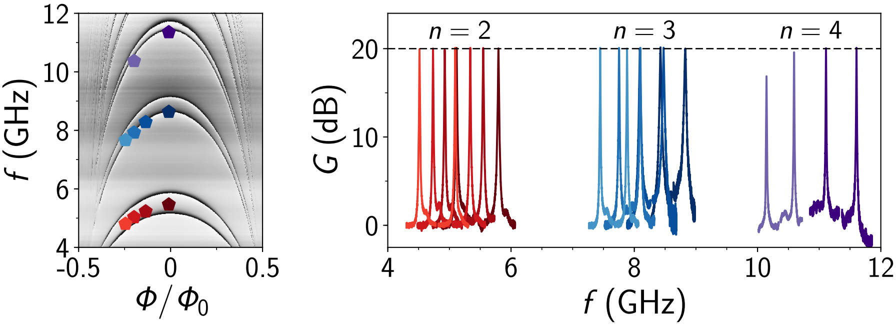

Figure 3.8: Gain flux tunability. Phase of the complex reflection coefficient $\arg(S_{11})$ (left-hand panel), measured for a DJJAA with $N = 1300$ SQUIDs as a function of the probe frequency f and external bias flux Φ/Φ_0, similar to Fig. 3.6. The grey scale covers again the range from $-\pi$ (black) to π (white). The main features in the given frequency range are the second ($n = 2$), third ($n = 3$) and fourth ($n = 4$) dimer of the device. The pentagons highlight the bias flux and pump frequency used to measure the power gain close to the dimer modes. The corresponding power gain G is shown in the right-hand panel as a function of the probe frequency f. The tunable bandwidth of this device measured from the lowest frequency to the highest frequency of each dimer at which $G = 20\,\mathrm{dB}$ was reached exceeds 1.5 GHz for all three dimers.

3.6 Gain-bandwidth product

As mentioned in Sec. 1.3.4, the achieved maximal power gain G_0 (linear units) and the instantaneous bandwidth B of each dimer are related by the external coupling rate of the respective modes, known as the gain-bandwidth compromise. For a non-degenerate parametric amplifier utilizing two modes at a time, the product of gain and bandwidth is limited by both decay rates [46, 67]

$$\sqrt{G_0}B = \underbrace{\frac{2\kappa_{n,+}\kappa_{n,-}}{\kappa_{n,+} + \kappa_{n,-}}}_{\bar{\kappa}_n}, \tag{3.11}$$

where $\kappa_{n,+}$ and $\kappa_{n,-}$ are the external decay rates of the two modes of the n th dimer, and $\bar{\kappa}_n$ is the effective linewidth.

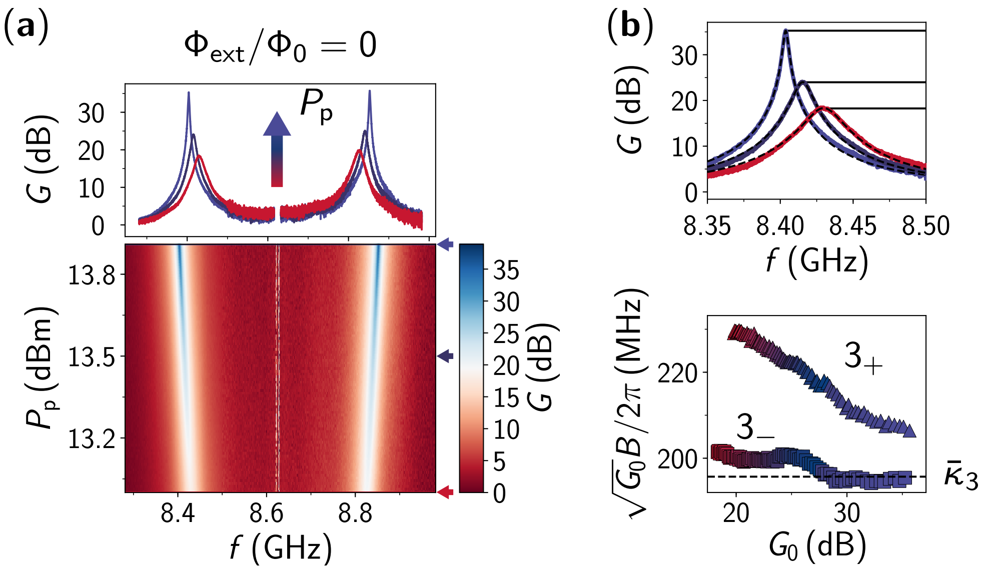

Figure 3.9: Power gain. a) Power gain G in decibel for different pump powers P_p (room-temperature values) and a fixed pump frequency $\omega_p = 2\pi \times 8.622\,\text{GHz}$, measured at the flux sweet spot of the third dimer $n = 3$ (cf. Fig. 3.8) as a function of the frequency f of a low power ($P_s \ll P_p$) probe tone (bottom panel). With increasing pump power, the observed maximal power gain increases, as indicated by the color scale, while the obtained bandwidth decreases. The top panel shows three gain curves for three different pump powers, which are indicated by the equally colored arrows, and reveals the double Lorentzian gain profile. Notably, the sudden increase in noise at probe frequencies above 8.5 GHz is an artefact caused by the commercial vector network analyzer. For clarity, the features associated to the pump tone have been removed from the plot, explaining the small gap in the center (top panel).**b)** In order to extract the maximal power gain G_0 and the bandwidth B of the amplifier, Lorentzian fits are performed for both modes individually, as demonstrated for the lower mode 3_- (top panel). The bottom panel compares the extracted gain-bandwidth product $\sqrt{G_0}B$ of both modes with the expected value $\bar{\kappa}_3$ (black dashed line).

The maximal power gain G_0 of the DJJAA is adjusted by the pump conditions, the combination of pump frequency ω_p and pump power P_p. In general, the pump frequency is set to a frequency in-between two dimerized modes. However, due to the finite Kerr nonlinearity of both modes, the resonance frequencies of the dimer modes shift downwards in frequency with increasing mode population and pump power, as theoretically demonstrated for a degenerate amplifier (see Fig. 1.23). As a consequence, there are ideal pump conditions for which the required pump power is minimized.

Figure 3.9a depicts the power gain G obtained for the third dimer of the sample D (see Fig. 3.8), measured as a function of the probe frequency f for a steadily increasing pump power. The pump frequency remained fixed at $\omega_p = 2\pi \times 8.622\,\text{GHz}$ during the measurement. Under the given conditions, not only the maximal power gain increases, but also the detuning between the two points at which the maximal power gain occurs in frequency increases.

The instantaneous bandwidth B and the maximal power gain G_0 are extracted by fitting individual Lorentzian curves to the frequency dependence of the (linear) power gain profiles:

$$G(\omega) = \frac{G_0\,(B/2)^2}{(\omega - \omega_0)^2 + (B/2)^2} + G_{\text{offset}}, \tag{3.12}$$

as demonstrated in Fig. 3.9b. Here, G_{offset} is a finite offset value and ω_0 is the frequency at which the maximal power gain occurs.

The gain-bandwidth product extracted for both modes is plotted in Fig. 3.9b (bottom panel), and compared to the theoretical value $\bar{\kappa}_3 = 196\,\text{MHz}$, which has been deduced from the low probe power reflection coefficient of the amplifier for each dimer individually. While the obtained gain-bandwidth product of the lower mode agrees well with the prediction, the upper mode exhibits generally larger values and a moderate decrease with increasing power gain.

For the sample shown in Fig. 3.6a, the obtained gain-bandwidth product $\sqrt{G_0}B \approx 170\,\text{MHz}$ is also in good agreement with the average of the two measured linewidths $\bar{\kappa}/2\pi = 172\,\text{MHz}$ (not shown). Since the inductance per SQUID is significantly larger for samples B and C, the obtained bandwidth is considerably smaller for these samples.

Flux tunability

For the same device, the dependence of the gain-bandwidth product with the applied flux bias was investigated for two dimers. Figure 3.10 depicts the comparison between the theoretical prediction $\bar{\kappa}_n$ and the gain-bandwidth product obtained from the power gain measurements shown in Fig. 3.8 (right-hand panel) for the second ($n = 2$) and the third ($n = 3$) dimer.

Since the inductance of the SQUIDs is enhanced with increasing flux Φ_{ext}, the characteristic impedance of the amplifier increases at the same time, which lowers the effective linewidth of the modes (black solid lines). The triangle and the square markers indicate the gain-bandwidth products for the upper and lower frequency mode of each dimer, respectively, which are generally in good agreement with the prediction.

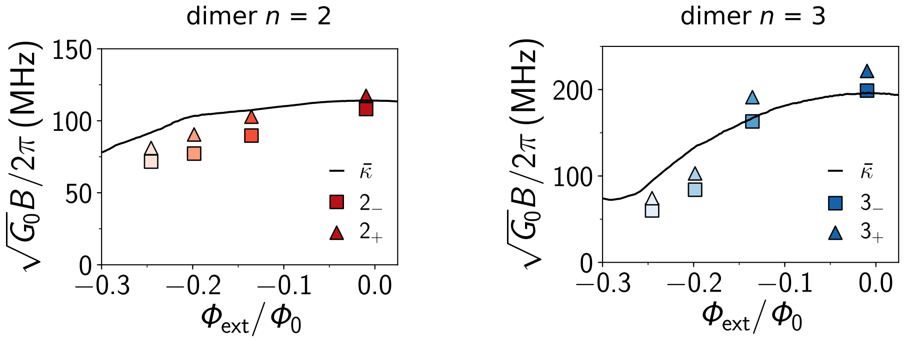

Figure 3.10: Gain-bandwidth product. Product of the linear power gain G_0 and the amplifier bandwidth B for the second and third dimer of sample D shown in Fig. 3.8, measured at different values for the external magnetic flux Φ_{ext} inside the SQUID loops. The black solid line indicates the expected value determined by the effective linewidth $\bar{\kappa}_n = 2\kappa_{n,+}\kappa_{n,-}/(\kappa_{n,+} + \kappa_{n,-})$. The triangles and squares indicate the measured gain-bandwidth products for the upper and lower frequency mode, respectively. The color code is identical to the gain measurements in Fig. 3.8.

3.7 Saturation power

The saturation power of an amplifier is conventionally determined by the 1 dB compression point, the input power at which the power gain has been reduced by 1 dB compared to the low signal power value. Figure 3.11 depicts a representative saturation power measurement, performed with the upper mode of the third dimer in sample D (see Fig. 3.8)

The initial power gain G_0 for small signal powers P_s is determined by the pump conditions (ω_p, P_p), which are adjusted such that the ideal conditions are closely met for four different power gain values. In case the pump frequency ω_p is slightly lower compared to the ideal detuning, the increase in signal power shifts the amplifier modes closer towards the optimal condition due to the signal induced ac Stark effect, resulting in a slight increase in the observed power gain. The measured curves show only a slight increase, before the power gain starts to steadily decrease. As expected, the corresponding 1 dB compression points, indicated by the black markers, are observed at higher signal powers for lower power gain values, in agreement with Fig. 1.25. Since the total attenuation of the input line was not calibrated in the same measurement run, the quoted signal power values are accurate within an order of magnitude.

At the flux sweet spot (left-hand panel) and at even higher signal powers well beyond the saturation power, the power gain abruptly disappears, with the origin of this behavior remaining unresolved. A similar behavior is not observed in the measurement away from the sweet spot (right-hand panel), but has been observed in other devices, too.

Another aspect revealed by the measurements, in particular by the light grey curves, is the increase in flux noise with increasing power gain owing to the smaller amplifier bandwidth. In addition, the observed flux noise increases with increasing detuning away from the flux sweet spot, caused by the steeper slope $\partial\omega_m/\partial\Phi_{\text{ext}}$ (see App. G.7).

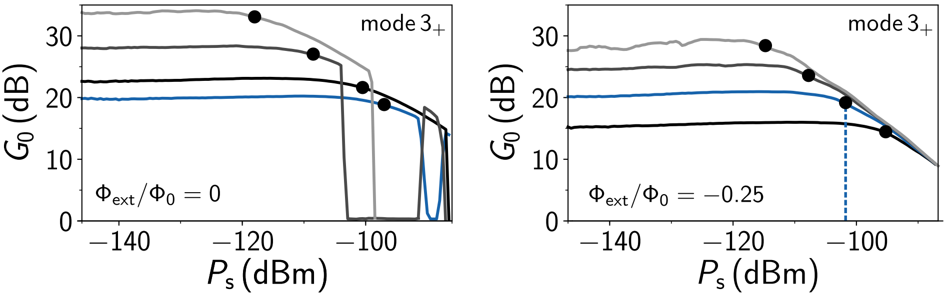

Figure 3.11: Saturation power measurement. Maximal power gain G_0 as a function of the incident signal power P_s, measured for the upper mode of the third dimer in the sample shown in Fig. 3.8. The two panels depict the results obtained for four different pump conditions at two different flux bias points, $\Phi_{\text{ext}}/\Phi_0 = 0$ (left-hand panel) and $\Phi_{\text{ext}}/\Phi_0 = -0.25$ (right-hand panel). With increasing signal power, the power gain starts to decrease, with the 1 dB compression points indicated by the black markers. The blue line highlights the curve with an initial power gain of 20 dB. At the flux sweet spot, the power gain suddenly breaks down, which has been observed in other samples, too, but does not occur in the right-hand panel. The origin of this phenomenon remains unresolved. Notably, the quoted signal power was not calibrated, but is only roughly determined using an estimate of the total attenuation $A = 76$ dB in the input line, which has been measured in a different cool down using the Rabi frequency of the grAl transmon (see Fig. 2.3) at a comparable frequency. Therefore, the results should be considered rather qualitatively.

3.8 Noise performance

The calibration of the noise performance of a DJJAA requires a calibrated power source used to determine the power incident to its input port. If the power gain of the DJJAA is sufficiently high $(G \geq 100)$ to saturate the noise added by subsequent amplifier stages, the SNR of the whole measurement setup is dominated by the SNR in front of the DJJAA, and the noise can be deduced in absolute values from the calibrated signal strength.

Such a calibrated power source can be build from a superconducting qubit dispersively coupled to a dedicated readout resonator. As discussed in App. B.2, the power reflected from the readout resonator is related to the mean photon number $\bar{n}_\mathrm{r}$ inside the resonator, which in turn can be determined from the transition frequency of the qubit and the dispersive shift χ_qr (see Sec. 1.1.6).

Measurement photon number

In a reflection measurement, the amplitude of the frequency dependent reflection coefficient can be normalized to unity using the off-resonant response of the system, independent of the total attenuation and power gain in the measurement setup, as shown in Fig. 1.11. For the measurement of the readout resonator, a pulse or continuous tone is applied at a fixed frequency in close vicinity to its resonance frequency f_r. The signal received at room temperature is downconverted to an intermediate (IF) frequency, before it is digitized. By comparing the signal with a reference from the same microwave source, the signal can be decomposed into the quadratures I and Q. Using the calibrated signal strength, the measured quadratures can be expressed in the measurement photon amplitude $\sqrt{n_\mathrm{meas}}$ [97, 220], with $I^2 + Q^2 = n_\mathrm{meas}$. The scaling accounts for the improvement of the SNR due to the signal strength ($\propto \sqrt{\bar{n}_\mathrm{r}}$), the measurement rate $\left(\propto \sqrt{\kappa_\mathrm{r}}\right)$, and the integration time ($\sqrt{T_\mathrm{m}}$), and enables to determine the noise in the received signal in numbers of photons per unit time and bandwidth.

In a continuous single-port reflection measurement performed on resonance, and neglecting the internal losses of the readout resonator, the measurement photon number is

$$n_\mathrm{meas} \underset{\gamma_\mathrm{r}\to 0}{=} \bar{n}_\mathrm{r} \frac{\kappa_\mathrm{r}}{4} T_\mathrm{m}, \tag{3.13}$$

where T_m is the measurement integration time, and γ_r and κ_r are the resonator's internal and external decay rates, respectively.

The mean circulating number of photons inside the resonator $\bar{n}_\mathrm{r}$ is calibrated by measuring the qubit's fundamental transition frequency f_q in a sequence of Ramsey fringes experiments [186]. The frequency f_R of the Ramsey oscillations is given by the drive detuning from the qubit's transition frequency $f_\mathrm{R} = |f_\mathrm{d} - f_\mathrm{q}|$, which is chosen to be comparable to the frequency shift induced by the population of the readout resonator $\Delta f_\mathrm{q} = \bar{n}_\mathrm{r} 2\chi_\mathrm{qr}$, where $2\chi_\mathrm{qr} = -2\pi \times 480\,\mathrm{kHz}$ is the qubit dispersive shift [24]. The resonator is populated with $\bar{n}_\mathrm{r}$ photons by simultaneously applying

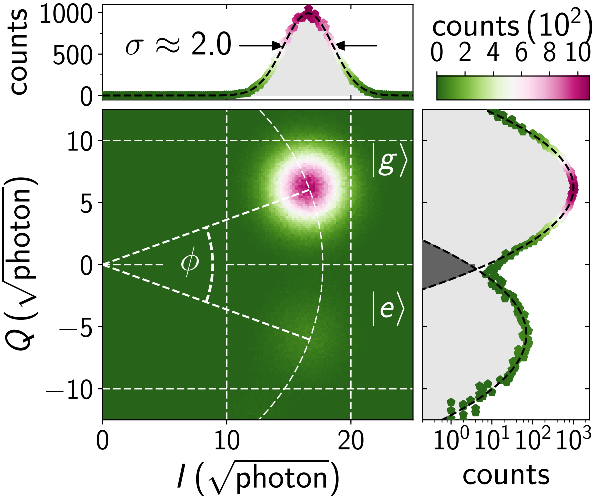

Figure 3.12: Quadrature histogram) 2D-histogram of measured I and Q quadratures of the readout resonator at $f_\mathrm{r} = 5.8224\,\mathrm{GHz}$. The I and Q values are reported in units of square root of measurement photons $\sqrt{\bar{n}_\mathrm{r}\kappa_\mathrm{r}T_\mathrm{m}/4}$, where $\bar{n}_\mathrm{r} \approx 150$, $\kappa_\mathrm{r}/2\pi = 2.7\,\mathrm{MHz}$ and $T_\mathrm{m} = 500\,\mathrm{ns}$, for a total of 6×10^5 counts. We observe two peaks in the $IQ-$plane, a larger one corresponding to the qubit ground state $|g\rangle$, and an approximately ten times smaller peak corresponding to the first excited state $|e\rangle$. The qubit temperature calculated from the observed populations is $T_\mathrm{q} = 87\,\mathrm{mK}$, in agreement with the base plate temperature of the dilution refrigerator of 80 mK, which was raised to activate thermal excitations of the qubit. The distribution plots along I (top panel) and Q (right panel) are plotted for slices centered on the ground state peak. From a Gaussian-fit we extract a standard deviation $\sigma = 2.0\,\sqrt{\text{photon}}$.

a constant tone to the readout resonator at frequency f_r (see App. G.12 for more details).

Figure 3.12 shows a histogram of measured signal quadratures $I(t)$ and $Q(t)$ expressed in units of the measurement photon amplitude $\sqrt{n_\mathrm{meas}}$, for $\bar{n}_\mathrm{r} \approx 150$ and an integration time $T_\mathrm{m} = 500\,\mathrm{ns}$. The resonator linewidth is $\kappa_\mathrm{r} = 2\pi \times 2.7\,\mathrm{MHz}$. A detailed description of the measurement setup and the microwave interferometer used to decompose the readout signal into the quadratures I and Q is found in App. G.8 and App. G.9. The qubit's ground state $|g\rangle$ and first excited state $|e\rangle$ are visible as two circles with Gaussian profile, as expected for a coherent state prepared in the resonator. For clarity, the IQ-plane is rotated such that the information about the qubit state is encoded entirely in the Q-quadrature, as shown by the slices through the histogram along I (top panel) and Q (right-hand panel). The angle between the ground and first excited state is $\phi = 4\arctan\left(|\chi_\mathrm{qr}|/\kappa\right) \approx 40°$.

Measurement efficiency

The measurement efficiency $\eta = 0.13$ at the resonance frequency of the readout resonator is calculated by comparing the measured standard deviation $\sigma = 2.0\,\sqrt{\text{photon}}$ of the ground state distribution in the histogram shown in Fig. 3.12, with the ideal case, which is $\sigma_{\text{ideal}} = 1/\sqrt{2}\,\sqrt{\text{photon}}$ for a coherent state [40].

The reduction in measurement efficiency can be attributed to known and expected losses between the readout resonator and the parametric amplifier. Since a commercial power combiner was used to feed in the pump tone, the power incident to the DJJAA was lowered by at least a factor of two compared to the calibrated value. Additionally, the sample holder was separated from the amplifier by several microwave components, such as circulators and various co-axial cables, which further add dissipation at the readout frequency. Therefore, a conservative upper bound on the measurement efficiency determined by losses is $\eta_{\text{L}} \leq 0.5$, which implies a conservative bound on the quantum efficiency $\eta_{\text{DJJAA}} = \eta/\eta_{\text{L}} \geq 0.26$ for the DJJAA.

Noise visibility

Another contribution of the noise observed at room temperature can be caused by the amplifiers in the output line of the measurement setup operated at higher temperature stages. A way to estimate the saturation of the noise added by these additional amplifier stages with amplified quantum noise incident to the DJJAA, is the noise visibility measurement, as shown in Fig. 3.13. The measurement is performed by comparing the noise power detected with a spetrum analyzer at room temperature, when the DJJAA is on and off. In the frequency region in which the power gain of the DJJAA is large $(G \gg 1)$, the measured noise power is increased and resembles the characteristic Lorentzian line shape of the DJJAA gain profile.

Assuming a frequency independent noise incident to the DJJAA, the maximal noise visibility ΔP is measured at the frequency at which the DJJAA supplies the largest power gain G_0, as indicated by the coincidence with the gain profile, which has been obtained in a separate measurement. From the measured increase in output power, the contribution of the other amplifier stages, primarily the HEMT, can be expressed in an upper bound for the measurement efficiency [97]

$$\eta_{\text{HEMT}} = 1 - 10^{-\Delta P/10}. \tag{3.14}$$

From the maximal value measured $\Delta P = 13.2\,\text{dB}$, an upper bound $\eta_{\text{HEMT}} = 0.95$ is deduced. Notably, the noise visibility measurement alone is not sufficient to

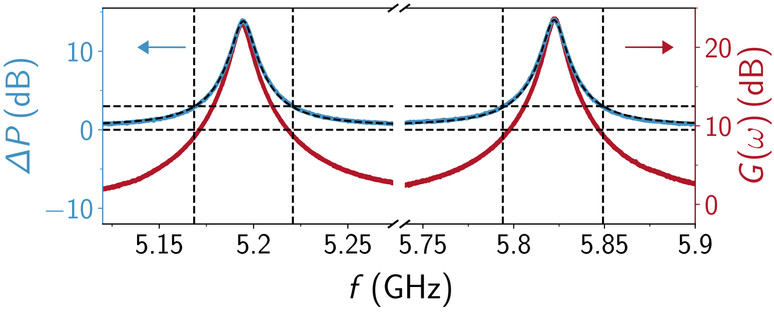

Figure 3.13: Noise visibility. Increase in the measured power at room temperature ΔP (blue curve) due to the amplified quantum noise incident to the DJJAA. For the measurement, only a pump tone is applied to operate the DJJAA with a maximal power gain of $G_0 = 23.2\,\mathrm{dB}$ (red curves), while the power is detected with a commercial spectrum analyzer. In the frequency region in which the power gain of the DJJAA is large ($G \gg 1$), the noise incident to the amplifier, at least quantum fluctuations at the signal and idler frequencies, is amplified and causes an increased noise power at room temperature. The noise floor in this measurement is determined by the noise added by subsequent amplifier stages, for the most part the noise added by a high-electron-mobility transistor amplifier. The black dashed line indicates a Lorentzian fit to the noise visibility.

calibrate the noise performance of the DJJAA, as the losses between the DJJAA and the HEMT are generally unknown, unless they have been calibrated. As an example, a quantum limited first amplifier stage with no attenuation in the line connecting it to the HEMT would show the same noise visibility as a device with a much higher added noise number, but also more attenuation in the line.

3.9 Quantum jumps of a transmon qubit

The increase in measurement efficiency and SNR by operating the DJJAA enabled to trace the state of the transmon qubit on a time scale an order of magnitude faster than its energy relaxation time. From such quantum jump traces, valuable information can be extracted, for instance the statistics of the duration the qubit spends in each state, from which the decay rate $\Gamma_{\downarrow}$ and the excitation rate $\Gamma_{\uparrow}$ can be deduced individually, i.e. the effective qubit temperature.

An exemplary quantum jump trace is depicted in Fig. 3.14 (left-hand panel) for the same integration time $T_\mathrm{m} = 500\,\mathrm{ns}$ and readout strength used in Fig. 3.12. For the detection of the qubit state, highlighted by the solid red line, a multi-point filter is used [220]. The filter declares a jump, when the detected Q-value falls into a range

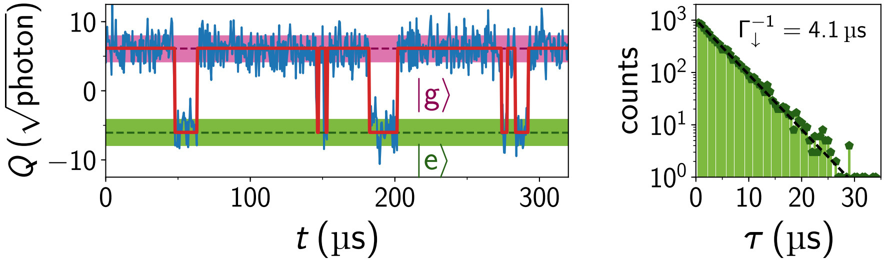

Figure 3.14: Quantum jumps. Typical example of a measured quantum jump trace corresponding to the time evolution of the Q quadrature for the same experiment shown in a). The red solid line indicates the qubit state given by a two point latching filter. The colored areas around the Q values corresponding to $|g\rangle$ (pink) and $|e\rangle$ (green) represent one standard deviation σ, which is the value used for the latching filter.

of $\pm\sigma$ around the mean values $\bar{Q}_m$ $(m \in \mathrm{g, e, f, h})$ associated with the first four qubit states. For the ground and first excited state, the filter-range is color coded by the pink and green areas around the mean values $\bar{Q}_0$ and $\bar{Q}_1$, respectively, which are in turn indicated by the dashed lines.

By compiling a histogram of the duration τ the qubit remains in the excited state, the decay rate $\Gamma_\downarrow^{-1} = 4.1$ µs into the ground state can be extracted from the measured quantum jump traces. Figure 3.14 (right-hand panel) depicts the corresponding histogram together with the exponential fit (black dashed line) from which the decay rate is determined.

Moreover, for uncorrelated quantum jumps, the probability distribution $p(\tau)$ of the times τ follows a Poisson distribution $p(\tau) = \frac{1}{\bar{\tau}} e^{-\tau/\bar{\tau}}$ around a mean value $\bar{\tau}$. Following the analysis reported in Ref. [220], the statistics of the dwelling times extracted from the quantum jumps are expressed in the form $\tau p(\tau) = \frac{\tau}{\bar{\tau}} e^{-\tau/\bar{\tau}}$ for enhanced visibility.

Figure 3.15 depicts the statistics of the quantum jumps corresponding to the histogram in Fig. 3.12, for the ground (pink) and the first excited state (green). For the binning, a constant bin size Δ_b in units of $\log(\tau)$ is used. Both distributions are in excellent agreement with the prediction of uncorrelated quantum jumps, indicated by the black dashed lines, which are of the form [220]

$$\frac{\sum \Delta_\mathrm{b}}{\bar{\tau}} \log(10) \tau \frac{\tau}{\bar{\tau}} e^{-\frac{\tau}{\bar{\tau}}}. \tag{3.15}$$

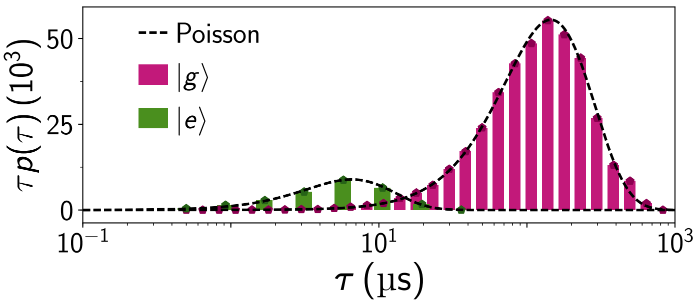

Figure 3.15: Quantum jumps statistics. Histograms of the time τ the transmon spent in the ground (pink) and first excited state (green), weighted by its probability $p(\tau)$. The black dashed lines indicate the expected statistics assuming uncorrelated quantum jumps between the two states following a Poisson distribution.

Here, $\sum$ is the total sum of the histogram values, and the term in front of the Poisson distribution ensures that the integral coincides with the total number of measurements stored in the bins.

As expected, the qubit spent significantly more time in the ground state than in the first excited state, or in other words, the contribution of the excitation rate to the energy relaxation rate is negligible $\Gamma_\downarrow \gg \Gamma_\uparrow$.

Qubit temperature

Owing to the interaction between the transmon qubit and its environment, the excitation rate $\Gamma_\uparrow$ out of the ground state is non-zero, as discussed in the previous section, causing a finite equilibrium occupation of the excited state. The extent of such excitations can be expressed in an effective qubit temperature, calculated from the relative population of the qubit states. For a transmon qubit, the occupation in the energy eigenstates beyond the computational basis ($|0\rangle$ and $|1\rangle$) can be included into the analysis.

For a qubit in thermal equilibrium with its environment, the occupation probability p_m of the m th energy eigenstate follows a Boltzmann distribution

$$p_m \propto e^{-\frac{E_m}{k_\mathrm{B} T_\mathrm{q}}}, \tag{3.16}$$

where k_B is the Boltzmann constant, and T_q is the effective qubit temperature. Similar to the Boltzmann statistics of a multi-particle system, the occupation probability of each qubit state observed in a time ensemble is calculated from the number of

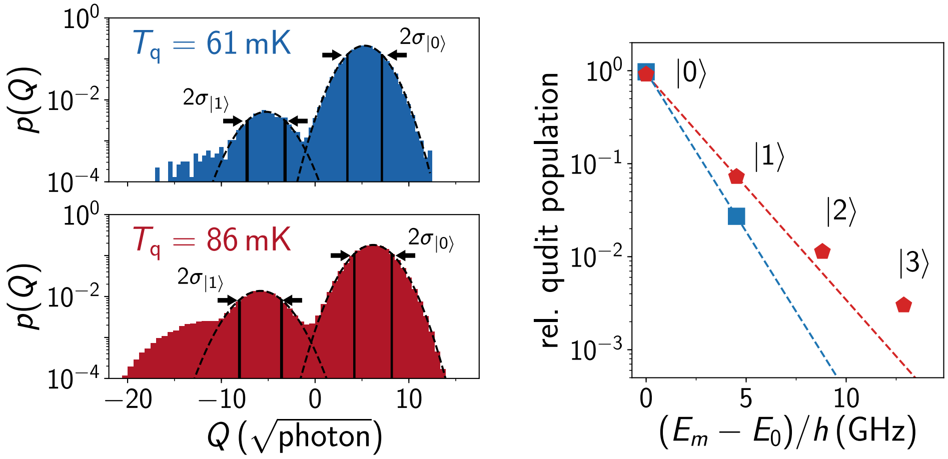

Figure 3.16: Transmon temperature. Histograms of the probability $p(Q)$ for finding the measurement outcome Q within regions of bin size $\Delta Q = 0.6\,\sqrt{\mathrm{photon}}$. Similar to Fig. 3.12, the information about the qubit states is projected onto the Q quadrature. The black dashed lines indicate Gaussian fits, from which the mean values $\bar{Q}_m$ and the standard deviations σ_m are extracted for the ground and first excited states. The area below the curves within one standard deviation is used to calculate the relative population of the qubit states. For a qubit in thermal equilibrium, the relative population follows a Boltzmann distribution $\propto e^{-E_\mathrm{m}/(k_\mathrm{b}T_\mathrm{q})}$ (dashed lines), from which the qubit temperature is deduced, yielding $T_\mathrm{q} = 61\,\mathrm{mK}$ and $T_\mathrm{q} = 87\,\mathrm{mK}$.

measurements N_m the qubit has been found in the respective state m, divided by the total number of measurements $N = \sum N_m$:

$$p_m = \frac{N_m}{N} \tag{3.17}$$

The corresponding numbers N_m are extracted from the IQ-histogram, either from the maximal number of counts associated to each state, or the integrated counts within one standard deviation σ. Hence, the effective qubit temperature is calculated from the Boltzmann factor of the first two eigenstates

$$T_\mathrm{q} = \frac{E_1 - E_0}{k_\mathrm{B} \ln(N_0/N_1)}, \tag{3.18}$$

if not more qubit states can be distinguished, or by fitting a Boltzmann distribution to the relative occupation

$$N_m(\epsilon_m)/N = n_0 e^{-\frac{\epsilon_m}{k_\mathrm{B}T_\mathrm{q}}}. \tag{3.19}$$

Here, the parameter $\epsilon_m = (E_m - E_0)$ is the energy difference between the m th energy eigenstate to the ground state energy E_0, and n_0 is the relative ground state occupation. The energy eigenstates are determined from the qubit spectrum (see App. G.10).

Figure 3.16 compares the probability histogram p(Q) of measuring a value along the Q quadrature for a cryostat base temperature $T_{\mathrm{base}} = 30\,\mathrm{mK}$ (top panel) with the outcome of an experiment operated at $T_{\mathrm{base}} = 80\,\mathrm{mK}$. In both cases, the first two states of the transmon are clearly distinguishable, while the higher energy eigenstates accumulate at the left-hand edge of the distribution. However, from the continuous quantum jump traces similar to Fig. 3.14, the third and the fourth eigenstate are still distinguishable.

The relative population of the qubit states $N_m(\epsilon)/N$ is extracted from the probability of measuring a Q quadrature value within one standard deviation around the mean value $\bar{Q}_m$ associated to each transmon state. For the measurements taken at a lower base temperature, the qubit temperature saturates at a constant value $T_{\mathrm{q}} \approx 61\,\mathrm{mK}$, which is an indication for non-thermal processes that increase the excited state population beyond thermal equilibrium. At the elevated base temperature, the qubit temperature of $T_{\mathrm{q}} = 87\,\mathrm{mK}$ approaches the physical temperature of the cryostat base plate.

4 Conclusion & outlook

In the scope of my thesis, I investigated the applicability of superconducting granular aluminum for the implementation of nonlinear inductances designated for the use in hybrid architectures, i.e. systems dedicated to combine the advantages of superconducting quantum circuits with other quantum degrees of freedom. For this purpose, the properties of grAl thin films were examined with the aid of transport measurements, as well as in form of a dispersive measurement technique, realized by embedding a grAl inductor into a resonant circuit to build a superconducting transmon qubit. Besides the determination of the quantum coherence of the grAl transmon, the investigation was targeted to assess the performance of the material in external magnetic fields, an important prerequisite for the usage in many hybrid systems. In order to decrease the required measurement time, a non-degenerate parametric amplifier was developed in addition.

Nonlinear granular aluminum inductors

The investigated grAl thin films were deposited in a standard electron beam evaporator by evaporating pure aluminum in a low-pressure oxygen atmosphere ($\sim 10^{-5}$ mbar). As demonstrated, the normal-state resistivity of the fabricated films is controlled by the ratio of the partial oxygen pressure inside the evaporation chamber and the pure aluminum evaporation rate, and can be varied over three orders of magnitude. Since the kinetic sheet inductance of disordered superconductors is proportional to the sheet resistance according to the Mattis-Bardeen theory, the control of the film resistivity enables the implementation of physically small inductors offering a large kinetic inductance at eye level with conventional Josephson junction technology [91].

The nonlinearity of such inductive elements stems from the grAl microstructure, which is composed of separate and crystalline aluminum grains embedded in a non-stoichiometic AlO_x matrix [234]. The thin, insulating barrier between neighboring grains enables a finite Josephson coupling for film resistivities $\rho_\mathrm{n} \leq 10^4\ \mu\Omega\,\mathrm{cm}$, above which granular aluminum enters an insulating regime [133]. Similar to conventional JJ, the nonlinearity is determined by the phase fluctuations across the inter-grain boundaries. Owing to the grAl microstructure, the quantum electrodynamics of grAl resonators can be mapped onto an array of effective JJs, which links the self-Kerr coefficient of the fundamental mode of a rectangular-shaped stripline resonator to the critical current density j_c and the volume V_{grAl} of the grAl film: $K_{11} \propto j_c^{-1}$ and $K_{11} \propto V_{\mathrm{grAl}}^{-1}$ [144].

The critical current density j_c of superconducting grAl films was determined with the aid of switching current experiments of micro-SQUIDs patterned from single grAl layers. In the used design, the SQUID loop was narrowed down in two regions to form short, geometric constrictions of widths $\leq 100\,\mathrm{nm}$ and lengths $\leq 300\,\mathrm{nm}$. Due to the short coherence length of superconducting grAl compared to the geometric dimension of the constrictions, the switching into the normal state in such constrictions is expected to be local and determined by the Josephson coupling between the Al grains [78]. In this notion, the switching is more likely to take place inside the constriction merely due to the reduced critical current of the film in these regions. The obtained critical current density was found to decrease with increasing normal-state resistivity following a power law $j_c \propto \rho_n^{-1.3}$. Moreover, the analysis of the switching current distributions have revealed a diffusive motion of the effective phase particle inside the two-dimensional sQUID potential, as reported in Ref. [78].

In order to further investigate the applicability of grAl elements for hybrid systems, a grAl transmon qubit was fabricated by shunting a small volume of granular aluminum $V_{\mathrm{grAl}} = 500 \times 200 \times 10\,\mathrm{nm}^3$, constituting the nonlinear inductance of the circuit, with a pure aluminum in-plane capacitor. The used fabrication process was based on an in-situ three-angle shadow evaporation technique [128], demonstrating the integrability of the grAl fabrication with standard Josephson junction technology.

The coherence of the grAl transmon qubit was directly determined from resonance fluorescence measurements of the fundamental transition, in spectroscopy, i.e. with a continuous microwave drive, and in time domain, i.e. with pulsed signals. The energy relaxation time was found to be limited by the Purcell decay into the waveguide sample holder to $T_{1,\kappa} = 3.1\,\mu\mathrm{s}$, while the internal decay time due to uncontrolled degrees of freedom was found to be $T_{1,\gamma} = 20^{+22}_{-6}\,\mu\mathrm{s}$. Complementary Ramsey-fringes [186] and Hahn-echo [94] experiments further portend pure dephasing times $T_\phi = 28\,\mu\mathrm{s}$ and $T_\phi = 46\,\mu\mathrm{s}$, respectively, indicative for a stable qubit transition frequency and on par with state-of-the art superconducting qubit implementations.

By directly tracing the fundamental transition frequency over the duration of 15 h using spectroscopy techniques, a total change on the order of 10 kHz was observed, reinforcing the results of the time domain measurements. However, the mean value of the fundamental transition frequency was prone to changes between consecutive cool downs, with spreads on the order of several hundred megahertz. Although the exact origin remained unresolved, a potential explanation are changes in the configuration of the grAl volume, supported by the concomitant change in the obtained anharmonicity of the grAl transmon.

From resonance fluorescence measurements performed at higher readout power and additional two-tone spectroscopy measurements, the anharmonicity of the qubit was determined to $\alpha = 2\pi \times 4.48\,\mathrm{MHz}$ at a fundamental transition frequency of $f_1 = 7.4887\,\mathrm{GHz}$. By comparing the obtained value with the expected anharmonicity of a conventional transmon $\alpha \approx E_\mathrm{c}/\hbar$ [116], which is determined by the charging energy E_c of the shunt capacitance, the result suggests $N = 6$ effective junctions inside the grAl volume, and, hence an effective junction length of $a = 80\,\mathrm{nm}$. Although the deduced size is an order of magnitude larger than the grain size, it is in agreement with scanning-tunneling microscopy measurements, which revealed the simultaneous charging of clusters of grains, indicative for a locally high barrier transparency [234].

Eventually, the grAl transmon was measured in external magnetic fields, which were applied with a specifically developed 2D vector magnet integrated into a 3D waveguide sample holder, capable of creating in-plane fields on the order of several hundred millitesla. The measurements showed that the investigated grAl transmon implementation was limited by the low impedance shunting layers made from pure aluminum. However, a reasonable coherence time was sustained up to fields reaching 100 mT, which is already in the range required for the operation of semiconducting spin [154, 194] and molecular qubits [22, 23, 83]. Moreover, although the transition frequency was lowered by over 200 MHz due to the suppression of the gap parameter of the pure aluminum film, a high resolution measurement of the transition frequency did not reveal any anticrossings with other mesoscopic systems, a typical observation in conventional transmon qubits [114, 131, 135, 195].

In conclusion, the results reported on the grAl transmon have demonstrated that nonlinear inductances made from small volumes of granular aluminum are promising candidates for the application in hybrid systems, as they offer low microwave losses, sufficient nonlinearity to build a qubit, and resilience against external magnetic fields.

In future experiments, the limit on the energy relaxation time caused by the spontaneous emission into the input port could be mitigated by implementing a dispersive readout scheme for the qubit. Moreover, by using smaller volumes of granular aluminum, the anharmonicity of the grAl transmon could be enhanced compared to the presented implementation. However, even the presented value renders the grAl transmon a potential candidate for the application in bosonic codes for quantum information processing [87, 99, 113, 157, 219]. For the extended application in hybrid systems, the aluminum shunting layer could be exchanged by superconducting materials with larger critical magnetic fields, for instance niobium compounds [123, 167, 193]. Alternatively, implementations of other qubit designs which do not require large shunting capacitors, for instance the fluxonium qubit [91, 148], could be entirely fabricated from a single granular aluminum layer.

The DJJAA

In order to improve the signal-to-noise ratio of the measurement setup, a non-degenerate parametric amplifier was developed based on the dispersion engineering of long Josephson junction arrays, referred to as the dimer Josephson junction array amplifier, in short DJJAA. By placing a capacitance in the center of the array, the DJJAA exhibits pairs of modes, denoted dimers, coupled by a cross-Kerr interaction.

The main idea behind the DJJAA concept is to cover a large frequency band utilizing several eigenmodes of the same device in different frequency domains and, thus lowering the required frequency tunability of each mode. The usage of multiple dimers for non-degenerate amplification was demonstrated with up to four modes in a single device containing $N = 1800$ JJs. Since the DJJAA devices were fabricated based on a simple and cheap optical-lithography process demonstrates that the DJJAA concept is robust and affordable for a large variety of groups working on superconducting quantum circuits. In combination with the potentially large bandwidth, DJJAAs could be used in cryogenic setups as ordinary as commercial amplifiers.

The noise performance of a typical DJJAA was determined using a cQED experiment composed of a conventional transmon qubit dispersively coupled to a dedicated readout resonator. The cQED system was used as a calibrated power source to determine the power incident to the DJJAA. The measurement efficiency of the DJJAA was found to be $\eta_{\mathrm{DJJAA}} \geq 0.26$, i.e. reaching 26% of the quantum limit on par with other superconducting parametric amplifiers [97, 143, 220], with remaining uncertainties caused by unknown and unaccounted microwave losses stemming from the components connecting the transmon to the amplifier.

Due to the enhanced signal-to-noise ratio enabled by the DJJAA, the state of the transmon was continuously traced using an integration time of $T_{\mathrm{m}} = 500\,\mathrm{ns}$, roughly an order of magnitude faster than the energy relaxation time of the qubit. From the statistics of the amount of time the qubit spent in the ground and the first excited state, the energy relaxation time as well as the effective temperature of the qubit were determined, revealing the saturation of the qubit temperature to $T_{\mathrm{q}} = 60\,\mathrm{mK}$, well above the operational temperature of the dilution refridgerator: A well-known but yet unresolved issue reported in other articles [107, 204], but only detectable due to the low noise performance offered by the DJJAA.

In conclusion, the DJJAA concept was successfully implemented using different total numbers of JJs and circuit parameters. The obtained results were in good agreement with the predictions deduced from effective circuit models, indicative for the high degree of control on the amplifier parameters.

Potential improvements in future designs are the usage of a large capacitance to ground to realize the dimerization of the dispersion relation, as it reduces the negative effect of variations in the critical currents of the JJs and magnetic gradients along the device. Moreover, it is yet to be demonstrated to build a single device that covers the whole frequency band between $1 - 10\,\mathrm{GHz}$.

Bibliography

1. Abbott, B. P., Abbott, R., Abbott, T. D., Abernathy, M. R., Acernese, F., *et al.: Observation of Gravitational Waves from a Binary Black Hole Merger*. Phys. Rev. Lett. **116**, 061102 (2016) (cit. on p. 1).
2. Abdo, B., Kamal, A. & Devoret, M.: *Nondegenerate three-wave mixing with the Josephson ring modulator*. Phys. Rev. B **87**, 014508 (2013) (cit. on p. 58).
3. Abeles, B., Cohen, R. W. & Cullen, G. W.: *Enhancement of Superconductivity in Metal Films*. Phys. Rev. Lett. **17**, 632–634 (1966) (cit. on p. 39).
4. Abrikosov, A. A.: *On the magnetic properties of superconductors of the second group*. Sov. Phys. JETP **5**, 1174–1182 (1957) (cit. on p. 32).
5. Ardavan, A., Rival, O., Morton, J. J. L., Blundell, S. J., Tyryshkin, A. M., Timco, G. A. & Winpenny, R. E. P.: *Will Spin-Relaxation Times in Molecular Magnets Permit Quantum Information Processing?* Phys. Rev. Lett. **98**, 057201 (2007) (cit. on p. 1).
6. Arute, F., Arya, K., Babbush, R., Bacon, D., Bardin, J. C., *et al.: Quantum supremacy using a programmable superconducting processor*. Nature **574**, 505–510 (2019) (cit. on pp. 2, 19).
7. Astafiev, O., Zagoskin, A. M., Abdumalikov, A. A., Pashkin, Y. A., Yamamoto, T., Inomata, K., Nakamura, Y. & Tsai, J. S.: *Resonance Fluorescence of a Single Artificial Atom*. Science **327**, 840–843 (2010) (cit. on pp. 67–69, 75–77).
8. Autler, S. H. & Townes, C. H.: *Stark Effect in Rapidly Varying Fields*. Phys. Rev. **100**, 703–722 (1955) (cit. on p. 75).
9. Bachar, N., Pracht, U. S., Farber, E., Dressel, M., Deutscher, G. & Scheffler, M.: *Signatures of Unconventional Superconductivity in Granular Aluminum*. Journal of Low Temperature Physics **179**, 83–89 (2015) (cit. on p. 41).
10. Bardeen, J., Cooper, L. N. & Schrieffer, J. R.: *Microscopic Theory of Superconductivity*. Phys. Rev. **106**, 162–164 (1957) (cit. on pp. 5, 32).
11. Barends, R., Kelly, J., Megrant, A., Sank, D., Jeffrey, E., *et al.: Coherent Josephson Qubit Suitable for Scalable Quantum Integrated Circuits*. Phys. Rev. Lett. **111**, 080502 (2013) (cit. on p. 25).

12. Barends, R., Kelly, J., Megrant, A., Veitia, A., Sank, D., *et al.: Superconducting quantum circuits at the surface code threshold for fault tolerance*. Nature **508**, 500–503 (2014) (cit. on p. 3).
13. Baur, M., Filipp, S., Bianchetti, R., Fink, J. M., Göppl, M., Steffen, L., Leek, P. J., Blais, A. & Wallraff, A.: *Measurement of Autler-Townes and Mollow Transitions in a Strongly Driven Superconducting Qubit*. Phys. Rev. Lett. **102**, 243602 (2009) (cit. on pp. 75–77).
14. Bell, J. S.: *On the Einstein Podolsky Rosen paradox*. Physics Physique Fizika **1**, 195–200 (1964) (cit. on p. 1).
15. Ben-Jacob, E., Bergman, D. J., Imry, Y., Matkowsky, B. J. & Schuss, Z.: *Thermal activation from the fluxoid and the voltage states of dc SQUIDs*. Journal of Applied Physics **54**, 6533–6542 (1983) (cit. on p. 43).
16. Benhelm, J., Kirchmair, G., Roos, C. F. & Blatt, R.: *Towards fault-tolerant quantum computing with trapped ions*. Nature Physics **4**, 463–466 (2008) (cit. on p. 1).
17. Benioff, P.: *The computer as a physical system: A microscopic quantum mechanical Hamiltonian model of computers as represented by Turing machines*. Journal of Statistical Physics **22**, 563–591 (1980) (cit. on p. 1).
18. Bennett, C. H. & Brassard, G.: *Quantum cryptography: Public key distribution and coin tossing*. Theoretical Computer Science **560**. Theoretical Aspects of Quantum Cryptography – celebrating 30 years of BB84, 7–11 (2014) (cit. on p. 1).
19. Bergeal, N., Schackert, F., Metcalfe, M., Vijay, R., Manucharyan, V. E., Frunzio, L., Prober, D. E., Schoelkopf, R. J., Girvin, S. M. & Devoret, M. H.: *Phase-preserving amplification near the quantum limit with a Josephson ring modulator*. Nature **465** (2010) (cit. on p. 61).
20. Bergeal, N., Vijay, R., Manucharyan, V. E., Siddiqi, I., Schoelkopf, R. J., Girvin, S. M. & Devoret, M. H.: *Analog information processing at the quantum limit with a Josephson ring modulator*. Nature Physics **6**, 296–302 (2010) (cit. on p. 61).
21. Bethe, H. A.: *The Electromagnetic Shift of Energy Levels*. Phys. Rev. **72**, 339–341 (1947) (cit. on p. 29).
22. Bienfait, A., Pla, J. J., Kubo, Y., Stern, M., Zhou, X., *et al.: Reaching the quantum limit of sensitivity in electron spin resonance*. Nature Nanotechnology **11**, 253–257 (2016) (cit. on pp. 3, 115).
23. Bienfait, A., Pla, J. J., Kubo, Y., Zhou, X., Stern, M., *et al.: Controlling spin relaxation with a cavity*. Nature **531**, 74–77 (2016) (cit. on pp. 3, 115).
24. Blais, A., Huang, R.-S., Wallraff, A., Girvin, S. M. & Schoelkopf, R. J.: *Cavity quantum electrodynamics for superconducting electrical circuits: An architecture for quantum computation*. Phys. Rev. A **69**, 062320 (2004) (cit. on pp. 25–27, 46, 104).

25. Blatt, R. & Roos, C. F.: *Quantum simulations with trapped ions*. Nature Physics **8**, 277–284 (2012) (cit. on p. 1).

26. Blatt, R. & Wineland, D.: *Entangled states of trapped atomic ions*. Nature **453**, 1008–1015 (2008) (cit. on p. 1).

27. Bockstiegel, C., Gao, J., Vissers, M. R., Sandberg, M., Chaudhuri, S., Sanders, A., Vale, L. R., Irwin, K. D. & Pappas, D. P.: *Development of a Broadband NbTiN Traveling Wave Parametric Amplifier for MKID Readout*. Journal of Low Temperature Physics **176**, 476–482 (2014) (cit. on p. 61).

28. Bogani, L. & Wernsdorfer, W.: *Molecular spintronics using single-molecule magnets*. Nature Materials **7**, 179–186 (2008) (cit. on p. 1).

29. Borisov, K., Rieger, D., Winkel, P., Hernandez, F., Valenti, F., *et al.: Superconducting granular aluminum resonators resilient to magnetic fields up to 1 Tesla* (2020) (cit. on pp. 4, 39, 81).

30. Bouchiat, V., Vion, D., Joyez, P., Esteve, D. & Devoret, M. H.: *Quantum Coherence with a Single Cooper Pair*. Physica Scripta **T76**, 165 (1998) (cit. on pp. 15, 53).

31. Boutin, S., Toyli, D. M., Venkatramani, A. V., Eddins, A. W., Siddiqi, I. & Blais, A.: *Effect of Higher-Order Nonlinearities on Amplification and Squeezing in Josephson Parametric Amplifiers*. Phys. Rev. Applied **8**, 054030 (2017) (cit. on pp. 58, 86).

32. Braumüller, J., Cramer, J., Schlör, S., Rotzinger, H., Radtke, L., *et al.: Multiphoton dressing of an anharmonic superconducting many-level quantum circuit*. Phys. Rev. B **91**, 054523 (2015) (cit. on p. 77).

33. Braumüller, J., Sandberg, M., Vissers, M. R., Schneider, A., Schlör, S., *et al.: Concentric transmon qubit featuring fast tunability and an anisotropic magnetic dipole moment*. Applied Physics Letters **108** (2016) (cit. on p. 25).

34. Büttiker, M., Harris, E. P. & Landauer, R.: *Thermal activation in extremely underdamped Josephson-junction circuits*. Phys. Rev. B **28**, 1268–1275 (1983) (cit. on p. 44).

35. Caldeira, A. O. & Leggett, A. J.: *Influence of Dissipation on Quantum Tunneling in Macroscopic Systems*. Phys. Rev. Lett. **46**, 211–214 (1981) (cit. on p. 1).

36. Campagne-Ibarcq, P., Eickbusch, A., Touzard, S., Zalys-Geller, E., Frattini, N. E., *et al.: Quantum error correction of a qubit encoded in grid states of an oscillator* (2019) (cit. on pp. 3, 19).

37. Castellanos-Beltran, M. A.: *Development of a Josephson parametric amplifier for the preparation and detection of nonclassical states of microwave fields* (University of Colorado, 2010) (cit. on p. 50).

38. Castellanos-Beltran, M. A., Irwin, K. D., Hilton, G. C., Vale, L. R. & Lehnert, K. W.: *Amplification and squeezing of quantum noise with a tunable Josephson metamaterial*. Nature Physics **4**, 929–931 (2008) (cit. on p. 2).
39. Castellanos-Beltran, M. & Lehnert, K.: *Widely tunable parametric amplifier based on a superconducting quantum interference device array resonator*. Applied Physics Letters **91**, 083509 (2007) (cit. on p. 61).
40. Caves, C. M.: *Quantum limits on noise in linear amplifiers*. Phys. Rev. D **26**, 1817–1839 (1982) (cit. on pp. 4, 46, 47, 50, 106).
41. Chien, T.-C., Lanes, O., Liu, C., Cao, X., Lu, P., Motz, S., Liu, G., Pekker, D. & Hatridge, M.: *Multiparametric amplification and qubit measurement with a Kerr-free Josephson ring modulator*. Phys. Rev. A **101**, 042336 (2020) (cit. on pp. 58, 62).
42. Chiorescu, I., Nakamura, Y., Harmans, C. J. P. M. & Mooij, J. E.: *Coherent Quantum Dynamics of a Superconducting Flux Qubit*. Science **299**, 1869–1871 (2003) (cit. on p. 1).
43. Chui, T., Lindenfeld, P., McLean, W. L. & Mui, K.: *Coupling and isolation: Critical field and transition temperature of superconducting granular aluminum*. Phys. Rev. B **24**, 6728–6731 (1981) (cit. on pp. 4, 39).
44. Cirac, J. I. & Zoller, P.: *Quantum Computations with Cold Trapped Ions*. Phys. Rev. Lett. **74**, 4091–4094 (1995) (cit. on p. 1).
45. Clarke, J. & Wilhelm, F. K.: *Superconducting quantum bits*. Nature **453**, 1031–1042 (2008) (cit. on p. 2).
46. Clerk, A. A., Devoret, M. H., Girvin, S. M., Marquardt, F. & Schoelkopf, R. J.: *Introduction to quantum noise, measurement, and amplification*. Rev. Mod. Phys. **82**, 1155–1208 (2010) (cit. on pp. 47, 49, 54, 99).
47. Cohen, R. W. & Abeles, B.: *Superconductivity in Granular Aluminum Films*. Phys. Rev. **168**, 444–450 (1968) (cit. on pp. 4, 39, 41, 81).
48. Collett, M. J. & Gardiner, C. W.: *Squeezing of intracavity and traveling-wave light fields produced in parametric amplification*. Phys. Rev. A **30**, 1386–1391 (1984) (cit. on p. 52).
49. Cottet, N.: *Energy and information in fluorescence with superconducting circuits*. PhD thesis (PSL Research University, Ecole Normale Superieure, 2018) (cit. on pp. 67–69).
50. Day, P. K., LeDuc, H. G., Mazin, B. A., Vayonakis, A. & Zmuidzinas, J.: *A broadband superconducting detector suitable for use in large arrays*. Nature **425**, 817–821 (2003) (cit. on p. 2).

51. De Graaf, S. E., Faoro, L., Burnett, J., Adamyan, A. A., Tzalenchuk, A. Y., Kubatkin, S. E., LindstrÃ¶m, T. & Danilov, A. V.: *Suppression of low-frequency charge noise in superconducting resonators by surface spin desorption*. Nature Communications **9**, 1143 (2018) (cit. on p. 3).
52. Deutscher, G.: *Critical fluctuations in granular superconductors*. Physics Letters A **35**, 28–29 (1971) (cit. on p. 41).
53. Deutscher, G. & Dodds, S. A.: *Critical-field anisotropy and fluctuation conductivity in granular aluminum films*. Phys. Rev. B **16**, 3936–3942 (1977) (cit. on p. 4).
54. Deutscher, G., Fenichel, H., Gershenson, M., Grünbaum, E. & Ovadyahu, Z.: *Transition to zero dimensionality in granular aluminum superconducting films*. Journal of Low Temperature Physics **10**, 231–243 (1973) (cit. on pp. 4, 39, 41).
55. Deutscher, G., Gershenson, M., Grünbaum, E. & Imry, Y.: *Granular Superconducting Films*. Journal of Vacuum Science and Technology **10**, 697–701 (1973) (cit. on p. 4).
56. De Visser, P. J., Baselmans, J. J. A., Diener, P., Yates, S. J. C., Endo, A. & Klapwijk, T. M.: *Number Fluctuations of Sparse Quasiparticles in a Superconductor*. Phys. Rev. Lett. **106**, 167004 (2011) (cit. on p. 3).
57. De Visser, P. J., Goldie, D. J., Diener, P., Withington, S., Baselmans, J. J. A. & Klapwijk, T. M.: *Evidence of a Nonequilibrium Distribution of Quasiparticles in the Microwave Response of a Superconducting Aluminum Resonator*. Phys. Rev. Lett. **112**, 047004 (2014) (cit. on p. 37).
58. Devoret, M. H. & Martinis, J. M.: *Implementing qubits with superconducting integrated circuits*. Quantum Inf. Process. **3**, 163 (2004) (cit. on p. 2).
59. Devoret, M. H. & Schoelkopf, R. J.: *Superconducting Circuits for Quantum Information: An Outlook*. Science **339**, 1169–1174 (2013) (cit. on p. 2).
60. Devoret, M. H., Martinis, J. M. & Clarke, J.: *Measurements of Macroscopic Quantum Tunneling out of the Zero-Voltage State of a Current-Biased Josephson Junction*. Phys. Rev. Lett. **55**, 1908–1911 (1985) (cit. on p. 44).
61. DiCarlo, L., Chow, J. M., Gambetta, J. M., Bishop, L. S., Johnson, B. R., *et al.*: *Demonstration of two-qubit algorithms with a superconducting quantum processor*. Nature **460**, 240–244 (2009) (cit. on p. 19).
62. Didier, N., Bourassa, J. & Blais, A.: *Fast Quantum Nondemolition Readout by Parametric Modulation of Longitudinal Qubit-Oscillator Interaction*. Phys. Rev. Lett. **115**, 203601 (2015) (cit. on p. 26).
63. Dirac, P. A. M.: *The principles of quantum mechanics* **27** (Oxford university press, 1981) (cit. on p. 1).

64. Douglass, D. H.: *Magnetic Field Dependence of the Superconducting Energy Gap*. Phys. Rev. Lett. **6**, 346–348 (1961) (cit. on p. 81).
65. Duan, L.-M., Lukin, M. D., Cirac, J. I. & Zoller, P.: *Long-distance quantum communication with atomic ensembles and linear optics*. Nature **414**, 413–418 (2001) (cit. on p. 1).
66. Dutt, M. V. G., Childress, L., Jiang, L., Togan, E., Maze, J., Jelezko, F., Zibrov, A. S., Hemmer, P. R. & Lukin, M. D.: *Quantum Register Based on Individual Electronic and Nuclear Spin Qubits in Diamond*. Science **316**, 1312–1316 (2007) (cit. on p. 1).
67. Eichler, C., Salathe, Y., Mlynek, J., Schmidt, S. & Wallraff, A.: *Quantum-Limited Amplification and Entanglement in Coupled Nonlinear Resonators*. Phys. Rev. Lett. **113**, 110502 (2014) (cit. on pp. 98, 99).
68. Eichler, C. & Wallraff, A.: *Controlling the dynamic range of a Josephson parametric amplifier*. EPJ Quantum Technology **1**, 1–19 (2014) (cit. on pp. 53–55, 58, 63, 64).
69. Ekert, A. K.: *Quantum cryptography based on Bell's theorem*. Phys. Rev. Lett. **67**, 661–663 (1991) (cit. on p. 1).
70. Englund, D., Fattal, D., Waks, E., Solomon, G., Zhang, B., Nakaoka, T., Arakawa, Y., Yamamoto, Y. & Vučkovć, J.: *Controlling the Spontaneous Emission Rate of Single Quantum Dots in a Two-Dimensional Photonic Crystal*. Phys. Rev. Lett. **95**, 013904 (2005) (cit. on p. 1).
71. Eom, B. H., Day, P. K., LeDuc, H. G. & Zmuidzinas, J.: *A wideband, low noise superconducting amplifier with high dynamic range*. Nature Physics **8**, 623–627 (2012) (cit. on p. 61).
72. Essen, L. & Parry, J. V. L.: *An Atomic Standard of Frequency and Time Interval: A Cæsium Resonator*. Nature **176**, 280–282 (1955) (cit. on p. 1).
73. Feynman, R. P.: *Simulating physics with computers*. International Journal of Theoretical Physics **21**, 467–488 (1982) (cit. on p. 1).
74. Fragner, A., Göppl, M., Fink, J. M., Baur, M., Bianchetti, R., Leek, P. J., Blais, A. & Wallraff, A.: *Resolving Vacuum Fluctuations in an Electrical Circuit by Measuring the Lamb Shift*. Science **322**, 1357–1360 (2008) (cit. on p. 29).
75. Franken, P. A., Hill, A. E., Peters, C. W. & Weinreich, G.: *Generation of Optical Harmonics*. Phys. Rev. Lett. **7**, 118–119 (1961) (cit. on p. 52).
76. Frattini, N. E., Sivak, V. V., Lingenfelter, A., Shankar, S. & Devoret, M. H.: *Optimizing the Nonlinearity and Dissipation of a SNAIL Parametric Amplifier for Dynamic Range*. Phys. Rev. Applied **10**, 054020 (2018) (cit. on pp. 59, 60).

77. Frattini, N., Vool, U., Shankar, S., Narla, A., Sliwa, K. & Devoret, M.: *3-wave mixing Josephson dipole element*. Applied Physics Letters **110**, 222603 (2017) (cit. on pp. 60, 61, 86, 88).

78. Friedrich, F., Winkel, P., Borisov, K., Seeger, H., Sürgers, C., Pop, I. M. & Wernsdorfer, W.: *Onset of phase diffusion in high kinetic inductance granular aluminum micro-SQUIDs*. Superconductor Science and Technology **32**, 125008 (2019) (cit. on pp. 43–45, 114).

79. Gambetta, J., Blais, A., Schuster, D. I., Wallraff, A., Frunzio, L., Majer, J., Devoret, M. H., Girvin, S. M. & Schoelkopf, R. J.: *Qubit-photon interactions in a cavity: Measurement-induced dephasing and number splitting*. Phys. Rev. A **74**, 042318 (2006) (cit. on p. 28).

80. Gardiner, C. W. & Collett, M. J.: *Input and output in damped quantum systems: Quantum stochastic differential equations and the master equation*. Phys. Rev. A **31**, 3761–3774 (1985) (cit. on pp. 53, 54, 68).

81. Gely, M. F., Steele, G. A. & Bothner, D.: *Nature of the Lamb shift in weakly anharmonic atoms: From normal-mode splitting to quantum fluctuations*. Phys. Rev. A **98**, 053808 (2018) (cit. on p. 29).

82. Gisin, N. & Thew, R.: *Quantum communication*. Nature Photonics **1**, 165–171 (2007) (cit. on p. 1).

83. Godfrin, C., Ferhat, A., Ballou, R., Klyatskaya, S., Ruben, M., Wernsdorfer, W. & Balestro, F.: *Operating Quantum States in Single Magnetic Molecules: Implementation of Grover's Quantum Algorithm*. Phys. Rev. Lett. **119**, 187702 (2017) (cit. on pp. 1, 3, 115).

84. Goldman, L. & Rockwell, R. J.: *Lasers in medicine* (Gordon and Breach, New York, 1971) (cit. on p. 1).

85. Goto, H.: *Bifurcation-based adiabatic quantum computation with a nonlinear oscillator network*. Scientific Reports **6**, 21686 (2016) (cit. on p. 54).

86. Gottesman, D., Kitaev, A. & Preskill, J.: *Encoding a qubit in an oscillator*. Phys. Rev. A **64**, 012310 (2001) (cit. on p. 11).

87. Grimm, A., Frattini, N. E., Puri, S., Mundhada, S. O., Touzard, S., Mirrahimi, M., Girvin, S. M., Shankar, S. & Devoret, M. H.: *The Kerr-Cat Qubit: Stabilization, Readout, and Gates* (2019) (cit. on p. 115).

88. Gross, C. & Bloch, I.: *Quantum simulations with ultracold atoms in optical lattices*. Science **357**, 995–1001 (2017) (cit. on p. 1).

89. Grünhaupt, L.: *Granular aluminium superinductors* (KIT Scientific Publishing, 2019) (cit. on p. 41).

90. Grünhaupt, L., Maleeva, N., Skacel, S. T., Calvo, M., Levy-Bertrand, F., Ustinov, A. V., Rotzinger, H., Monfardini, A., Catelani, G. & Pop, I. M.: *Loss Mechanisms and Quasiparticle Dynamics in Superconducting Microwave Resonators Made of Thin-Film Granular Aluminum*. Phys. Rev. Lett. **121**, 117001 (2018) (cit. on pp. 39, 40).
91. Grünhaupt, L., Spiecker, M., Gusenkova, D., Maleeva, N., Skacel, S. T., *et al.: Granular aluminum as a superconducting material for high-impedance quantum circuits*. Nature Materials **18**, 816–819 (2019) (cit. on pp. 3, 39, 40, 46, 113, 116).
92. Grünhaupt, L., von Lüpke, U., Gusenkova, D., Skacel, S. T., Maleeva, N., *et al.: An argon ion beam milling process for native AlOx layers enabling coherent superconducting contacts*. Applied Physics Letters **111**, 072601 (2017) (cit. on p. 94).
93. Gustavsson, S., Yan, F., Catelani, G., Bylander, J., Kamal, A., *et al.: Suppressing relaxation in superconducting qubits by quasiparticle pumping*. Science **354**, 1573–1577 (2016) (cit. on p. 31).
94. Hahn, E. L.: *Spin Echoes*. Phys. Rev. **80**, 580–594 (1950) (cit. on pp. 24, 73, 114).
95. Hanson, R., Gywat, O. & Awschalom, D. D.: *Room-temperature manipulation and decoherence of a single spin in diamond*. Phys. Rev. B **74**, 161203 (2006) (cit. on p. 1).
96. Hanson, R., Kouwenhoven, L. P., Petta, J. R., Tarucha, S. & Vandersypen, L. M. K.: *Spins in few-electron quantum dots*. Rev. Mod. Phys. **79**, 1217–1265 (2007) (cit. on p. 1).
97. Hatridge, M., Shankar, S., Mirrahimi, M., Schackert, F., Geerlings, K., *et al.: Quantum Back-Action of an Individual Variable-Strength Measurement*. Science **339**, 178–181 (2013) (cit. on pp. 49, 51, 104, 106, 116).
98. Haus, H. A. & Mullen, J. A.: *Quantum Noise in Linear Amplifiers*. Phys. Rev. **128**, 2407–2413 (1962) (cit. on pp. 46, 50).
99. Heeres, R. W., Reinhold, P., Ofek, N., Frunzio, L., Jiang, L., Devoret, M. H. & Schoelkopf, R. J.: *Implementing a universal gate set on a logical qubit encoded in an oscillator*. Nature Communications **8**, 94 (2017) (cit. on pp. 28, 115).
100. Hensen, B., Bernien, H., Dréau, A. E., Reiserer, A., Kalb, N., *et al.: Loophole-free Bell inequality violation using electron spins separated by 1.3 kilometres*. Nature **526**, 682–686 (2015) (cit. on p. 1).
101. Hood, C. J., Lynn, T. W., Doherty, A. C., Parkins, A. S. & Kimble, H. J.: *The Atom-Cavity Microscope: Single Atoms Bound in Orbit by Single Photons*. Science **287**, 1447–1453 (2000) (cit. on p. 26).
102. Horodecki, R., Horodecki, P., Horodecki, M. & Horodecki, K.: *Quantum entanglement*. Rev. Mod. Phys. **81**, 865–942 (2009) (cit. on p. 1).

103. Hyde, F.: *Varactor-diode parametric amplifiers*. Proceedings of the Institution of Electrical Engineers **111**, 1080–1087(7) (1964) (cit. on p. 52).

104. Imamoglu, A., Awschalom, D. D., Burkard, G., DiVincenzo, D. P., Loss, D., Sherwin, M. & Small, A.: *Quantum Information Processing Using Quantum Dot Spins and Cavity QED*. Phys. Rev. Lett. **83**, 4204–4207 (1999) (cit. on p. 1).

105. Ithier, G., Collin, E., Joyez, P., Meeson, P. J., Vion, D., *et al.: Decoherence in a superconducting quantum bit circuit*. Phys. Rev. B **72**, 134519 (2005) (cit. on p. 18).

106. Jaynes, E. T. & Cummings, F. W.: *Comparison of quantum and semiclassical radiation theories with application to the beam maser*. Proceedings of the IEEE **51**, 89–109 (1963) (cit. on p. 26).

107. Jin, X. Y., Kamal, A., Sears, A. P., Gudmundsen, T., Hover, D., *et al.: Thermal and Residual Excited-State Population in a 3D Transmon Qubit*. Phys. Rev. Lett. **114**, 240501 (2015) (cit. on pp. 37, 117).

108. Josephson, B.: *Possible new effects in superconductive tunnelling*. Physics Letters **1**, 251–253 (1962) (cit. on pp. 3, 12).

109. Kane, B. E.: *A silicon-based nuclear spin quantum computer*. Nature **393**, 133–137 (1998) (cit. on p. 1).

110. Kelly, J., Barends, R., Fowler, A. G., Megrant, A., Jeffrey, E., *et al.: State preservation by repetitive error detection in a superconducting quantum circuit*. Nature **519**, 66–69 (2015) (cit. on p. 3).

111. Khukhareva, I.: *The superconducting properties of thin aluminum films*. Soviet Physics JETP **16**, 828–832 (1963) (cit. on p. 46).

112. Kimble, H. J.: *The quantum internet*. Nature **453**, 1023–1030 (2008) (cit. on p. 1).

113. Kirchmair, G., Vlastakis, B., Leghtas, Z., Nigg, S. E., Paik, H., Ginossar, E., Mirrahimi, M., Frunzio, L., Girvin, S. M. & Schoelkopf, R. J.: *Observation of quantum state collapse and revival due to the single-photon Kerr effect*. Nature **495**, 205–209 (2013) (cit. on p. 115).

114. Klimov, P. V., Kelly, J., Chen, Z., Neeley, M., Megrant, A., *et al.: Fluctuations of Energy-Relaxation Times in Superconducting Qubits*. Phys. Rev. Lett. **121**, 090502 (2018) (cit. on pp. 3, 115).

115. Knill, E., Laflamme, R. & Milburn, G. J.: *A scheme for efficient quantum computation with linear optics*. Nature **409**, 46–52 (2001) (cit. on p. 1).

116. Koch, J., Yu, T. M., Gambetta, J., Houck, A. A., Schuster, D. I., Majer, J., Blais, A., Devoret, M. H., Girvin, S. M. & Schoelkopf, R. J.: *Charge-insensitive qubit design derived from the Cooper pair box*. Phys. Rev. A **76**, 042319 (2007) (cit. on pp. 1, 4, 15, 18, 29, 42, 52, 63, 64, 78, 79, 115).

117. Kochetov, B. A. & Fedorov, A.: *Higher-order nonlinear effects in a Josephson parametric amplifier*. Phys. Rev. B **92**, 224304 (2015) (cit. on p. 59).

118. Kodama, J.-I., Itoh, M. & Hirai, H.: *Superconducting transition temperature versus thickness of Nb film on various substrates*. Journal of Applied Physics **54**, 4050–4054 (1983) (cit. on p. 46).

119. Kou, A., Smith, W. C., Vool, U., Pop, I. M., Sliwa, K. M., Hatridge, M., Frunzio, L. & Devoret, M. H.: *Simultaneous Monitoring of Fluxonium Qubits in a Waveguide*. Phys. Rev. Applied **9**, 064022 (2018) (cit. on p. 65).

120. Kramers, H.: *Brownian motion in a field of force and the diffusion model of chemical reactions*. Physica **7**, 284–304 (1940) (cit. on p. 44).

121. Krantz, P., Kjaergaard, M., Yan, F., Orlando, T. P., Gustavsson, S. & Oliver, W. D.: *A quantum engineer's guide to superconducting qubits*. Applied Physics Reviews **6**, 021318 (2019) (cit. on p. 2).

122. Kurkijärvi, J.: *Intrinsic Fluctuations in a Superconducting Ring Closed with a Josephson Junction*. Phys. Rev. B **6**, 832–835 (1972) (cit. on p. 44).

123. Kwon, S., Fadavi Roudsari, A., Benningshof, O. W. B., Tang, Y.-C., Mohebbi, H. R., *et al.*: *Magnetic field dependent microwave losses in superconducting niobium microstrip resonators*. Journal of Applied Physics **124**, 033903 (2018) (cit. on p. 116).

124. Lamb, W. E. & Retherford, R. C.: *Fine Structure of the Hydrogen Atom by a Microwave Method*. Phys. Rev. **72**, 241–243 (1947) (cit. on p. 29).

125. Landig, A. J., Koski, J. V., Scarlino, P., Mendes, U. C., Blais, A., Reichl, C., Wegscheider, W., Wallraff, A., Ensslin, K. & Ihn, T.: *Coherent spin-photon coupling using a resonant exchange qubit*. Nature **560**, 179–184 (2018) (cit. on p. 31).

126. Lecocq, F., Ranzani, L., Peterson, G. A., Cicak, K., Simmonds, R. W., Teufel, J. D. & Aumentado, J.: *Nonreciprocal Microwave Signal Processing with a Field-Programmable Josephson Amplifier*. Phys. Rev. Applied **7**, 024028 (2017) (cit. on p. 62).

127. Lecocq, F., Ranzani, L., Peterson, G., Cicak, K., Metelmann, A., Kotler, S., Simmonds, R., Teufel, J. & Aumentado, J.: *Microwave Measurement beyond the Quantum Limit with a Nonreciprocal Amplifier*. Phys. Rev. Applied **13**, 044005 (2020) (cit. on pp. 61, 62).

128. Lecocq, F., Pop, I. M., Peng, Z., Matei, I., Crozes, T., Fournier, T., Naud, C., Guichard, W. & Buisson, O.: *Junction fabrication by shadow evaporation without a suspended bridge*. Nanotechnology **22**, 315302 (2011) (cit. on p. 114).

129. Lefevre-Seguin, V., Turlot, E., Urbina, C., Esteve, D. & Devoret, M. H.: *Thermal activation of a hysteretic dc superconducting quantum interference device from its different zero-voltage states*. Phys. Rev. B **46**, 5507–5522 (1992) (cit. on p. 44).

130. Leibfried, D., Blatt, R., Monroe, C. & Wineland, D.: *Quantum dynamics of single trapped ions*. Rev. Mod. Phys. **75**, 281–324 (2003) (cit. on p. 1).
131. Le Sueur, H., Svilans, A., Bourlet, N., Murani, A., Berge, L., Dumoulin, L. & Joyez, P.: *Microscopic charged fluctuators as a limit to the coherence of disordered superconductor devices*. arXiv (2018) (cit. on pp. 3, 115).
132. Leuenberger, M. N. & Loss, D.: *Quantum computing in molecular magnets*. Nature **410**, 789–793 (2001) (cit. on p. 1).
133. Levy-Bertrand, F., Klein, T., Grenet, T., Dupré, O., Benoıt, A., *et al.: Electrodynamics of granular aluminum from superconductor to insulator: Observation of collective superconducting modes*. Phys. Rev. B **99**, 094506 (2019) (cit. on pp. 4, 40, 41, 46, 113).
134. Likharev, K. K.: *Superconducting weak links*. Rev. Mod. Phys. **51**, 101–159 (1979) (cit. on pp. 11, 12, 43).
135. Lisenfeld, J., Bilmes, A., Megrant, A., Barends, R., Kelly, J., Klimov, P., Weiss, G., Martinis, J. M. & Ustinov, A. V.: *Electric field spectroscopy of material defects in transmon qubits*. npj Quantum Information **5**, 105 (2019) (cit. on pp. 3, 115).
136. Liu, G., Chien, T.-C., Cao, X., Lanes, O., Alpern, E., Pekker, D. & Hatridge, M.: *Josephson parametric converter saturation and higher order effects*. Applied Physics Letters **111**, 202603 (2017) (cit. on p. 58).
137. Lloyd, S.: *Universal Quantum Simulators*. Science **273**. Full publication date: Aug. 23, 1996, 1073–1078 (1996) (cit. on p. 1).
138. London, F. & London, H.: *The electromagnetic equations of the supraconductor*. Proceedings of the Royal Society of London. Series A-Mathematical and Physical Sciences **149**, 71–88 (1935) (cit. on p. 33).
139. Loss, D. & DiVincenzo, D. P.: *Quantum computation with quantum dots*. Phys. Rev. A **57**, 120–126 (1998) (cit. on p. 1).
140. Low noise factory: *LNF-LNC0.3 14A* (cit. on p. 47).
141. Luthi, F., Stavenga, T., Enzing, O. W., Bruno, A., Dickel, C., *et al.: Evolution of Nanowire Transmon Qubits and Their Coherence in a Magnetic Field*. Phys. Rev. Lett. **120**, 100502 (2018) (cit. on p. 74).
142. Mabuchi, H. & Doherty, A. C.: *Cavity Quantum Electrodynamics: Coherence in Context*. Science **298**, 1372–1377 (2002) (cit. on pp. 25, 26).
143. Macklin, C., O'Brien, K., Hover, D., Schwartz, M. E., Bolkhovsky, V., Zhang, X., Oliver, W. D. & Siddiqi, I.: *A near–quantum-limited Josephson traveling-wave parametric amplifier*. Science **350**, 307–310 (2015) (cit. on pp. 61, 116).

144. Maleeva, N., Grünhaupt, L., Klein, T., Levy-Bertrand, F., Dupre, O., *et al.: Circuit quantum electrodynamics of granular aluminum resonators*. Nature Communications **9**, 3889 (2018) (cit. on pp. 4, 39, 42, 43, 65, 114).

145. Malekakhlagh, M., Petrescu, A. & Türeci, H. E.: *Lifetime renormalization of weakly anharmonic superconducting qubits. I. Role of number nonconserving terms*. Phys. Rev. B **101**, 134509 (2020) (cit. on p. 46).

146. Mandelstam, L. & Leontowitsch, M.: *Zur Theorie der Schrödingerschen Gleichung*. Zeitschrift für Physik **47**, 131–136 (1928) (cit. on p. 1).

147. Manucharyan, V. E., Boaknin, E., Metcalfe, M., Vijay, R., Siddiqi, I. & Devoret, M.: *Microwave bifurcation of a Josephson junction: Embedding-circuit requirements*. Phys. Rev. B **76**, 014524 (2007) (cit. on p. 60).

148. Manucharyan, V. E., Koch, J., Glazman, L. I. & Devoret, M. H.: *Fluxonium: Single Cooper-Pair Circuit Free of Charge Offsets*. Science **326**, 113–116 (2009) (cit. on pp. 1, 3, 116).

149. Martinis, J. M., Nam, S., Aumentado, J. & Urbina, C.: *Rabi Oscillations in a Large Josephson-Junction Qubit*. Phys. Rev. Lett. **89**, 117901 (2002) (cit. on p. 1).

150. Mattis, D. C. & Bardeen, J.: *Theory of the Anomalous Skin Effect in Normal and Superconducting Metals*. Phys. Rev. **111**, 412–417 (1958) (cit. on p. 39).

151. Meissner, W. & Ochsenfeld, R.: *Ein neuer Effekt bei Eintritt der Supraleitfähigkeit*. Naturwissenschaften **21**, 787–788 (1933) (cit. on p. 33).

152. Meservey, R. & Tedrow, P. M.: *Properties of Very Thin Aluminum Films*. Journal of Applied Physics **42**, 51–53 (1971) (cit. on pp. 81, 82).

153. Metelmann, A. & Clerk, A. A.: *Nonreciprocal Photon Transmission and Amplification via Reservoir Engineering*. Phys. Rev. X **5**, 021025 (2015) (cit. on p. 58).

154. Mi, X., Benito, M., Putz, S., Zajac, D. M., Taylor, J. M., Burkard, G. & Petta, J. R.: *A coherent spin-photon interface in silicon*. Nature **555**, 599–603 (2018) (cit. on pp. 3, 31, 115).

155. Minev, Z. K., Mundhada, S. O., Shankar, S., Reinhold, P., Gutiérrez-Jáuregui, R., Schoelkopf, R. J., Mirrahimi, M., Carmichael, H. J. & Devoret, M. H.: *To catch and reverse a quantum jump mid-flight*. Nature **570**, 200–204 (2019) (cit. on pp. 23, 24, 27, 46).

156. Minev, Z. K.: *Catching and Reversing a Quantum Jump Mid-Flight* (2019) (cit. on p. 64).

157. Mirrahimi, M.: *Cat-qubits for quantum computation*. Comptes Rendus Physique **17**. Quantum microwaves / Micro-ondes quantiques, 778–787 (2016) (cit. on p. 115).

158. Mollow, B. R.: *Power Spectrum of Light Scattered by Two-Level Systems*. Phys. Rev. **188**, 1969–1975 (1969) (cit. on pp. 75, 76).
159. Morello, A., Pla, J. J., Zwanenburg, F. A., Chan, K. W., Tan, K. Y., *et al.*: *Single-shot readout of an electron spin in silicon*. Nature **467**, 687–691 (2010) (cit. on p. 1).
160. Moshe, A. G., Farber, E. & Deutscher, G.: *Optical conductivity of granular aluminum films near the Mott metal-to-insulator transition*. Phys. Rev. B **99**, 224503 (2019) (cit. on p. 41).
161. Motzoi, F., Gambetta, J. M., Rebentrost, P. & Wilhelm, F. K.: *Simple Pulses for Elimination of Leakage in Weakly Nonlinear Qubits*. Phys. Rev. Lett. **103**, 110501 (2009) (cit. on pp. 19, 77).
162. Muhonen, J. T., Dehollain, J. P., Laucht, A., Hudson, F. E., Kalra, R., *et al.*: *Storing quantum information for 30 seconds in a nanoelectronic device*. Nature Nanotechnology **9**, 986–991 (2014) (cit. on p. 30).
163. Müller, C., Cole, J. H. & Lisenfeld, J.: *Towards understanding two-level-systems in amorphous solids: insights from quantum circuits*. Reports on Progress in Physics **82**, 124501 (2019) (cit. on p. 3).
164. Murch, K. W., Weber, S. J., Macklin, C. & Siddiqi, I.: *Observing single quantum trajectories of a superconducting quantum bit*. Nature **502**, 211–214 (2013) (cit. on p. 22).
165. Mutus, J. Y., White, T. C., Barends, R., Chen, Y., Chen, Z., *et al.*: *Strong environmental coupling in a Josephson parametric amplifier*. Applied Physics Letters **104** (2014) (cit. on p. 58).
166. Nakamura, Y., Pashkin, Y. A. & Tsai, J. S.: *Coherent control of macroscopic quantum states in a single-Cooper-pair box*. Nature **398**, 786–788 (1999) (cit. on pp. 1, 15, 53).
167. Niepce, D., Burnett, J. & Bylander, J.: *High Kinetic Inductance* NbN *Nanowire Superinductors*. Phys. Rev. Applied **11**, 044014 (2019) (cit. on p. 116).
168. Nigg, S. E., Paik, H., Vlastakis, B., Kirchmair, G., Shankar, S., Frunzio, L., Devoret, M. H., Schoelkopf, R. J. & Girvin, S. M.: *Black-Box Superconducting Circuit Quantization*. Phys. Rev. Lett. **108**, 240502 (2012) (cit. on pp. 29, 53).
169. Nsanzineza, I. & Plourde, B. L. T.: *Trapping a Single Vortex and Reducing Quasiparticles in a Superconducting Resonator*. Phys. Rev. Lett. **113**, 117002 (2014) (cit. on p. 31).
170. Ofek, N., Petrenko, A., Heeres, R., Reinhold, P., Leghtas, Z., *et al.*: *Extending the lifetime of a quantum bit with error correction in superconducting circuits*. Nature **536**, 441–445 (2016) (cit. on p. 3).

171. Paik, H., Schuster, D. I., Bishop, L. S., Kirchmair, G., Catelani, G., *et al.: Observation of High Coherence in Josephson Junction Qubits Measured in a Three-Dimensional Circuit QED Architecture*. Phys. Rev. Lett. **107**, 240501 (2011) (cit. on p. 25).

172. Parmenter, R. H.: *Isospin Formulation of the Theory of a Granular Superconductor*. Phys. Rev. **154**, 353–368 (1967) (cit. on p. 4).

173. Parmenter, R. H.: *Size Effect in a Granular Superconductor*. Phys. Rev. **166**, 392–396 (1968) (cit. on p. 41).

174. Petrescu, A., Malekakhlagh, M. & Türeci, H. E.: *Lifetime renormalization of driven weakly anharmonic superconducting qubits. II. The readout problem*. Phys. Rev. B **101**, 134510 (2020) (cit. on p. 46).

175. Petta, J. R., Johnson, A. C., Taylor, J. M., Laird, E. A., Yacoby, A., Lukin, M. D., Marcus, C. M., Hanson, M. P. & Gossard, A. C.: *Coherent Manipulation of Coupled Electron Spins in Semiconductor Quantum Dots*. Science **309**, 2180–2184 (2005) (cit. on p. 1).

176. Pittman, T. B., Jacobs, B. C. & Franson, J. D.: *Probabilistic quantum logic operations using polarizing beam splitters*. Phys. Rev. A **64**, 062311 (2001) (cit. on p. 1).

177. Place, A. P. M., Rodgers, L. V. H., Mundada, P., Smitham, B. M., Fitzpatrick, M., *et al.: New material platform for superconducting transmon qubits with coherence times exceeding 0.3 milliseconds* (2020) (cit. on p. 46).

178. Planat, L., Dassonneville, R., Martınez, J. P., Foroughi, F., Buisson, O., Hasch-Guichard, W., Naud, C., Vijay, R., Murch, K. & Roch, N.: *Understanding the Saturation Power of Josephson Parametric Amplifiers Made from SQUID Arrays*. Phys. Rev. Applied **11**, 034014 (2019) (cit. on pp. 58, 59).

179. Planat, L., Ranadive, A., Dassonneville, R., Martınez, J. P., Léger, S., Naud, C., Buisson, O., Hasch-Guichard, W., Basko, D. M. & Roch, N.: *A photonic crystal Josephson traveling wave parametric amplifier*. arXiv (2019) (cit. on p. 61).

180. Pop, I. M., Geerlings, K., Catelani, G., Schoelkopf, R. J., Glazman, L. I. & Devoret, M. H.: *Coherent suppression of electromagnetic dissipation due to superconducting quasiparticles*. Nature **508**, 369–372 (2014) (cit. on pp. 3, 25).

181. Pracht, U. S., Bachar, N., Benfatto, L., Deutscher, G., Farber, E., Dressel, M. & Scheffler, M.: *Enhanced Cooper pairing versus suppressed phase coherence shaping the superconducting dome in coupled aluminum nanograins*. Phys. Rev. B **93**, 100503 (2016) (cit. on pp. 4, 40, 41, 46).

182. Quaranta, O., Cecil, T. W., Gades, L., Mazin, B. & Miceli, A.: *X-ray photon detection using superconducting resonators in thermal quasi-equilibrium*. Superconductor Science and Technology **26**, 105021 (2013) (cit. on p. 2).

183. Rabi, I. I.: *On the Process of Space Quantization*. Phys. Rev. **49**, 324–328 (1936) (cit. on p. 25).

184. Rabi, I. I.: *Space Quantization in a Gyrating Magnetic Field*. Phys. Rev. **51**, 652–654 (1937) (cit. on p. 25).

185. Raimond, J. M., Brune, M. & Haroche, S.: *Manipulating quantum entanglement with atoms and photons in a cavity*. Rev. Mod. Phys. **73**, 565–582 (2001) (cit. on pp. 25, 26).

186. Ramsey, N. F.: *A Molecular Beam Resonance Method with Separated Oscillating Fields*. Phys. Rev. **78**, 695–699 (1950) (cit. on pp. 24, 73, 104, 114).

187. Reed, M. D., DiCarlo, L., Nigg, S. E., Sun, L., Frunzio, L., Girvin, S. M. & Schoelkopf, R. J.: *Realization of three-qubit quantum error correction with superconducting circuits*. Nature **482**, 382–385 (2012) (cit. on p. 3).

188. Ristè, D., Bultink, C. C., Tiggelman, M. J., Schouten, R. N., Lehnert, K. W. & DiCarlo, L.: *Millisecond charge-parity fluctuations and induced decoherence in a superconducting transmon qubit*. Nature Communications **4**, 1913 (2013) (cit. on p. 3).

189. Roy, A. & Devoret, M.: *Introduction to parametric amplification of quantum signals with Josephson circuits*. Comptes Rendus Physique **17**. Quantum microwaves / Micro-ondes quantiques, 740–755 (2016) (cit. on pp. 52, 60, 61).

190. Roy, A. & Devoret, M.: *Quantum-limited parametric amplification with Josephson circuits in the regime of pump depletion*. Phys. Rev. B **98**, 045405 (2018) (cit. on p. 58).

191. Roy, T., Kundu, S., Chand, M., Vadiraj, A. M., Ranadive, A., Nehra, N., Patankar, M. P., Aumentado, J., Clerk, A. A. & Vijay, R.: *Broadband parametric amplification with impedance engineering: Beyond the gain-bandwidth product*. Applied Physics Letters **107**, 262601 (2015) (cit. on p. 58).

192. Rugar, D. & Grütter, P.: *Mechanical parametric amplification and thermomechanical noise squeezing*. Phys. Rev. Lett. **67**, 699–702 (1991) (cit. on p. 52).

193. Samkharadze, N., Bruno, A., Scarlino, P., Zheng, G., DiVincenzo, D. P., DiCarlo, L. & Vandersypen, L. M. K.: *High-Kinetic-Inductance Superconducting Nanowire Resonators for Circuit QED in a Magnetic Field*. Phys. Rev. Applied **5**, 044004 (2016) (cit. on p. 116).

194. Samkharadze, N., Zheng, G., Kalhor, N., Brousse, D., Sammak, A., Mendes, U. C., Blais, A., Scappucci, G. & Vandersypen, L. M. K.: *Strong spin-photon coupling in silicon*. Science **359**, 1123–1127 (2018) (cit. on pp. 3, 115).

195. Schlör, S., Lisenfeld, J., Müller, C., Bilmes, A., Schneider, A., Pappas, D. P., Ustinov, A. V. & Weides, M.: *Correlating Decoherence in Transmon Qubits: Low Frequency Noise by Single Fluctuators*. Phys. Rev. Lett. **123**, 190502 (2019) (cit. on pp. 3, 115).

196. Schneider, A., Wolz, T., Pfirrmann, M., Spiecker, M., Rotzinger, H., Ustinov, A. V. & Weides, M.: *Transmon qubit in a magnetic field: Evolution of coherence and transition frequency*. Phys. Rev. Research **1**, 023003 (2019) (cit. on pp. 4, 35).

197. Schoelkopf, R. J. & Girvin, S. M.: *Wiring up quantum systems*. Nature **451**, 664–669 (2008) (cit. on pp. 30, 31).

198. Schön, Y., Voss, J. N., Wildermuth, M., Schneider, A., Skacel, S. T., Weides, M. P., Cole, J. H., Rotzinger, H. & Ustinov, A. V.: *Rabi oscillations in a superconducting nanowire circuit*. npj Quantum Materials **5**, 18 (2020) (cit. on p. 39).

199. Schrödinger, E.: *Die gegenwärtige Situation in der Quantenmechanik*. Naturwissenschaften **23**, 807–812 (1935) (cit. on p. 1).

200. Schrödinger, E.: *Discussion of Probability Relations between Separated Systems*. Mathematical Proceedings of the Cambridge Philosophical Society **31**, 555–563 (1935) (cit. on p. 1).

201. Schuster, D. I., Houck, A. A., Schreier, J. A., Wallraff, A., Gambetta, J. M., *et al.: Resolving photon number states in a superconducting circuit*. Nature **445**, 515–518 (2007) (cit. on p. 28).

202. Schuster, D. I.: *Circuit quantum electrodynamics*. PhD thesis (Yale University, 2007) (cit. on p. 77).

203. Serniak, K., Diamond, S., Hays, M., Fatemi, V., Shankar, S., Frunzio, L., Schoelkopf, R. & Devoret, M.: *Direct Dispersive Monitoring of Charge Parity in Offset-Charge-Sensitive Transmons*. Phys. Rev. Applied **12**, 014052 (2019) (cit. on p. 3).

204. Serniak, K., Hays, M., de Lange, G., Diamond, S., Shankar, S., Burkhart, L. D., Frunzio, L., Houzet, M. & Devoret, M. H.: *Hot Nonequilibrium Quasiparticles in Transmon Qubits*. Phys. Rev. Lett. **121**, 157701 (2018) (cit. on p. 117).

205. Shiddiq, M., Komijani, D., Duan, Y., Gaita-Ari*ño, A*., Coronado, E. & Hill, S.: *Enhancing coherence in molecular spin qubits via atomic clock transitions*. Nature **531**, 348–351 (2016) (cit. on p. 1).

206. Shnirman, A., Schön, G. & Hermon, Z.: *Quantum Manipulations of Small Josephson Junctions*. Phys. Rev. Lett. **79**, 2371–2374 (1997) (cit. on pp. 15, 53).

207. Sivak, V. V., Shankar, S., Liu, G., Aumentado, J. & Devoret, M. H.: *Josephson Array-Mode Parametric Amplifier*. Phys. Rev. Applied **13**, 024014 (2020) (cit. on p. 86).

208. Skalski, S., Betbeder-Matibet, O. & Weiss, P. R.: *Properties of Superconducting Alloys Containing Paramagnetic Impurities*. Phys. Rev. **136**, A1500–A1518 (1964) (cit. on p. 32).

209. Slichter, D. H., Vijay, R., Weber, S. J., Boutin, S., Boissonneault, M., Gambetta, J. M., Blais, A. & Siddiqi, I.: *Measurement-Induced Qubit State Mixing in Circuit QED from Up-Converted Dephasing Noise*. Phys. Rev. Lett. **109**, 153601 (2012) (cit. on p. 46).

210. Smith, W. C., Kou, A., Xiao, X., Vool, U. & Devoret, M. H.: *Superconducting circuit protected by two-Cooper-pair tunneling*. npj Quantum Information **6**, 8 (2020) (cit. on p. 3).

211. Song, C., Heitmann, T. W., DeFeo, M. P., Yu, K., McDermott, R., Neeley, M., Martinis, J. M. & Plourde, B. L. T.: *Microwave response of vortices in superconducting thin films of Re and Al*. Phys. Rev. B **79**, 174512 (2009) (cit. on pp. 3, 34).

212. Taur, Y. & Richards, P. L.: *Parametric amplification and oscillation at 36 GHz using a point-contact Josephson junction*. Journal of Applied Physics **48**, 1321–1326 (1977) (cit. on p. 2).

213. Thiele, S., Balestro, F., Ballou, R., Klyatskaya, S., Ruben, M. & Wernsdorfer, W.: *Electrically driven nuclear spin resonance in single-molecule magnets*. Science **344**, 1135–1138 (2014) (cit. on p. 1).

214. Tinkham, M.: *Introduction to Superconductivity* Second Edition (Dover Publications, 2004) (cit. on pp. 31–37, 43, 81).

215. Toyli, D. M., Eddins, A. W., Boutin, S., Puri, S., Hover, D., Bolkhovsky, V., Oliver, W. D., Blais, A. & Siddiqi, I.: *Resonance Fluorescence from an Artificial Atom in Squeezed Vacuum*. Phys. Rev. X **6**, 031004 (2016) (cit. on p. 75).

216. Ustinov, A. V.: *Solitons in Josephson junctions*. Physica D: Nonlinear Phenomena **123**. Annual International Conference of the Center for Nonlinear Studies, 315–329 (1998) (cit. on p. 36).

217. Valenti, F., Henriques, F., Catelani, G., Maleeva, N., Grünhaupt, L., *et al.*: *Interplay Between Kinetic Inductance, Nonlinearity, and Quasiparticle Dynamics in Granular Aluminum Microwave Kinetic Inductance Detectors*. Phys. Rev. Applied **11**, 054087 (2019) (cit. on pp. 39, 40).

218. Vijay, R., Slichter, D. H. & Siddiqi, I.: *Observation of Quantum Jumps in a Superconducting Artificial Atom*. Phys. Rev. Lett. **106**, 110502 (2011) (cit. on p. 23).

219. Vlastakis, B., Kirchmair, G., Leghtas, Z., Nigg, S. E., Frunzio, L., Girvin, S. M., Mirrahimi, M., Devoret, M. H. & Schoelkopf, R. J.: *Deterministically Encoding Quantum Information Using 100-Photon Schrödinger Cat States*. Science **342**, 607–610 (2013) (cit. on pp. 11, 19, 54, 115).

220. Vool, U., Pop, I. M., Sliwa, K., Abdo, B., Wang, C., *et al.: Non-Poissonian Quantum Jumps of a Fluxonium Qubit due to Quasiparticle Excitations*. Phys. Rev. Lett. **113**, 247001 (2014) (cit. on pp. 31, 51, 104, 107, 108, 116).

221. Vool, U.: *Engineering Synthetic Quantum Operations*. PhD thesis (Yale University, 2017) (cit. on p. 12).

222. Vool, U. & Devoret, M.: *Introduction to quantum electromagnetic circuits*. International Journal of Circuit Theory and Applications **45**, 897–934 (2017) (cit. on p. 9).

223. Vrijen, R., Yablonovitch, E., Wang, K., Jiang, H. W., Balandin, A., Roychowdhury, V., Mor, T. & DiVincenzo, D.: *Electron-spin-resonance transistors for quantum computing in silicon-germanium heterostructures*. Phys. Rev. A **62**, 012306 (2000) (cit. on p. 1).

224. Wallraff, A., Schuster, D. I., Blais, A., Frunzio, L., Huang, R.-S., Majer, J., Kumar, S., Girvin, S. M. & Schoelkopf, R. J.: *Strong coupling of a single photon to a superconducting qubit using circuit quantum electrodynamics*. Nature **431**, 162–167 (2004) (cit. on p. 25).

225. Walls, D. F.: *Squeezed states of light*. Nature **306**, 141–146 (1983) (cit. on p. 50).

226. Walls, D. F.: *Quantum Optics* (Springer-Verlag, 1994) (cit. on p. 26).

227. Wang, C., Gao, Y. Y., Pop, I. M., Vool, U., Axline, C., *et al.: Measurement and control of quasiparticle dynamics in a superconducting qubit*. Nature Communications **5**, 5836 (2014) (cit. on pp. 3, 31).

228. Weißl, T., Küng, B., Dumur, E., Feofanov, A. K., Matei, I., Naud, C., Buisson, O., Hekking, F. W. J. & Guichard, W.: *Kerr coefficients of plasma resonances in Josephson junction chains*. Phys. Rev. B **92**, 104508 (2015) (cit. on pp. 88, 89, 91, 92).

229. Wenner, J., Yin, Y., Lucero, E., Barends, R., Chen, Y., *et al.: Excitation of Superconducting Qubits from Hot Nonequilibrium Quasiparticles*. Phys. Rev. Lett. **110**, 150502 (2013) (cit. on p. 37).

230. Winkel, P., Borisov, K., Gruenhaupt, L., Rieger, D., Spiecker, M., Valenti, F., Ustinov, A. V., Wernsdorfer, W. & Pop, I. M.: *Implementation of a transmon qubit using superconducting granular aluminum*. arXiv (2019) (cit. on pp. 4, 39, 63).

231. Winkel, P., Takmakov, I., Rieger, D., Planat, L., Hasch-Guichard, W., *et al.: Nondegenerate Parametric Amplifiers Based on Dispersion-Engineered Josephson-Junction Arrays*. Phys. Rev. Applied **13**, 024015 (2020) (cit. on pp. 4, 85, 86).

232. Xiang, Z.-L., Ashhab, S., You, J. Q. & Nori, F.: *Hybrid quantum circuits: Superconducting circuits interacting with other quantum systems*. Rev. Mod. Phys. **85**, 623–653 (2013) (cit. on pp. 3, 30, 31).

233. Yamamoto, T., Inomata, K., Watanabe, M., Matsuba, K., Miyazaki, T., Oliver, W. D., Nakamura, Y. & Tsai, J. S.: *Flux-driven Josephson parametric amplifier*. Applied Physics Letters **93** (2008) (cit. on pp. 2, 61).

234. Yang, F., Storbeck, T., Gozlinski, T., Grünhaupt, L., Pop, I. M. & Wulfhekel, W.: *Microscopic charging and in-gap states in superconducting granular aluminum*. arXiv (2019) (cit. on pp. 40, 66, 78, 113, 115).

235. Yurke, B., Corruccini, L. R., Kaminsky, P. G., Rupp, L. W., Smith, A. D., Silver, A. H., Simon, R. W. & Whittaker, E. A.: *Observation of parametric amplification and deamplification in a Josephson parametric amplifier*. Phys. Rev. A **39**, 2519–2533 (1989) (cit. on pp. 2, 61).

236. Yurke, B., Kaminsky, P. G., Miller, R. E., Whittaker, E. A., Smith, A. D., Silver, A. H. & Simon, R. W.: *Observation of 4.2-K equilibrium-noise squeezing via a Josephson-parametric amplifier*. Phys. Rev. Lett. **60**, 764–767 (1988) (cit. on p. 61).

237. Zhang, H., Chakram, S., Roy, T., Earnest Nathan andLu, Y., Huang, Z., Weiss, D., Koch, J. & Schuster, D. I.: *Universal fast flux control of a coherent, low-frequency qubit* (2020) (cit. on p. 2).

238. Zhang, W., Kalashnikov, K., Lu, W.-S., Kamenov, P., DiNapoli, T. & Gershenson, M.: *Microresonators Fabricated from High-Kinetic-Inductance Aluminum Films*. Phys. Rev. Applied **11**, 011003 (2019) (cit. on pp. 40, 46).

239. Zhong, M., Hedges, M. P., Ahlefeldt, R. L., Bartholomew, J. G., Beavan, S. E., Wittig, S. M., Longdell, J. J. & Sellars, M. J.: *Optically addressable nuclear spins in a solid with a six-hour coherence time*. Nature **517**, 177–180 (2015) (cit. on p. 30).

240. Zorin, A. B.: *Josephson Traveling-Wave Parametric Amplifier with Three-Wave Mixing*. Phys. Rev. Applied **6**, 034006 (2016) (cit. on p. 61).

List of publications

42. Borisov, K., Rieger, D., Winkel, P., Hernandez, F., Valenti, F., *et al.*: *Superconducting granular aluminum resonators resilient to magnetic fields up to 1 Tesla* (2020).

121. Friedrich, F., Winkel, P., Borisov, K., Seeger, H., Sürgers, C., Pop, I. M. & Wernsdorfer, W.: *Onset of phase diffusion in high kinetic inductance granular aluminum micro-SQUIDs*. Superconductor Science and Technology **32**, 125008 (2019).

126. Gebauer, R., Karcher, N., Gusenkova, D., Spiecker, M., Grünhaupt, L., *et al.*: *State preparation of a fluxonium qubit with feedback from a custom FPGA-based platform* (2019).

151. Grünhaupt, L., Spiecker, M., Gusenkova, D., Maleeva, N., Skacel, S. T., *et al.*: *Granular aluminum as a superconducting material for high-impedance quantum circuits*. Nature Materials **18**, 816–819 (2019).

236. Maleeva, N., Grünhaupt, L., Klein, T., Levy-Bertrand, F., Dupre, O., *et al.*: *Circuit quantum electrodynamics of granular aluminum resonators*. Nature Communications **9**, 3889 (2018).

364. Valenti, F., Henriques, F., Catelani, G., Maleeva, N., Grünhaupt, L., *et al.*: *Interplay Between Kinetic Inductance, Nonlinearity, and Quasiparticle Dynamics in Granular Aluminum Microwave Kinetic Inductance Detectors*. Phys. Rev. Applied **11**, 054087 (2019).

386. Winkel, P., Borisov, K., Gruenhaupt, L., Rieger, D., Spiecker, M., Valenti, F., Ustinov, A. V., Wernsdorfer, W. & Pop, I. M.: *Implementation of a transmon qubit using superconducting granular aluminum*. arXiv (2019).

387. Winkel, P., Takmakov, I., Rieger, D., Planat, L., Hasch-Guichard, W., *et al.*: *Nondegenerate Parametric Amplifiers Based on Dispersion-Engineered Josephson-Junction Arrays*. Phys. Rev. Applied **13**, 024015 (2020).

Appendix

A Circuit quantization

Quantizing an electrical circuit starts with finding the Hamiltonian of the classical equivalent [62]. In general, an electromagnetic circuit is the connection of individual circuit elements, for instance inductors, capacitors and resistors, to form an electrical network. The arrangment of these elements, referred to as the topology of the circuit, determines the resonant behavior of the system in terms of the distribution of the electrical currents and voltages over the network. Therefore, current and voltage constitute a suitable set of generalized coordinates to describe a linear circuit, with the corresponding time dynamics determined by the Hamilton function, and expressed in form of a set of equations of motion (EOM). Boundary conditions arising from the circuit topology and external biases are considered by applying Kirchhoff's circuit laws. If the network is entirely build from linear circuit elements, a set of independent variables can be found: the circuit's degrees of freedom (DOF). Since the DOF are independent, the Hamiltonian corresponding to the circuit can be expressed as a collection of independent harmonic oscillators, analogously to a linear mechanical system composed of masses and springs. Finding the correct DOF from a given circuit topology is therefore essential for understanding and predicting the behavior of a circuit in terms of its resonant frequencies and corresponding mode distributions. However, if the system contains nonlinear elements, the DOF cannot necessarily be decoupled but influence each other at all times, making an analysis of the circuit significantly more difficult [46, 62].

For a quantum circuit, the same general concepts apply, with the fundamental difference that the primarily classical variables current and voltage are conjugate variables in the quantum mechanical sense, and therefore cannot be measured with infinite precision at the same time. In order to derive the Hamiltonian of a quantum circuit, first the classical Hamiltonian is derived from the Lagrangian of the circuit, before the classical variables are promoted to quantum mechanical operators, referred to as canonical quantization. The independent DOF of the system are either found by diagonalizing the Lagrangian or the Hamiltonian [22]. A detailed and modern description of the technique to find the DOF, specifically applied to superconducting quantum circuits, is found in the work of *U. Vool and M. Devoret* in Ref. [62], from which I will briefly recap the main ideas.

A.1 Finding the classical Hamiltonian

Finding the Lagrangian of a circuit starts by dividing the circuit into two families of elementary building blocks: branches and nodes. The branches represent the dipolar circuit elements, for instance capacitors and inductors, and the nodes mark the connection points between the branches. Each branch is associated with a branch voltage $v_\mathrm{b}(t)$ and branch current $i_\mathrm{b}(t)$, as schematically shown in Fig. 1, which are related to the electrical and the magnetic field of the branch:

$$v_\mathrm{b}(t) = \int_{\text{beginning of b}}^{\text{end of b}} \vec{E}(\vec{r},t) \cdot \mathrm{d}\vec{l} \tag{1}$$

$$i_\mathrm{b}(t) = \frac{1}{\mu_0} \oint_{\text{around b}} \vec{B}(\vec{r},t) \cdot \mathrm{d}\vec{s} \tag{2}$$

The path of integration is chosen such that it includes all field components. Therefore, the dynamics of current and voltage are ultimately governed by Maxwell's equation, and the wires composing the circuit can be seen as auxillaries to guide and direct the electromagnetic fields. This connection constitutes the foundation for the later introduced description of superconducting quantum circuits in the language of quantum optics by the use of bosonic field operators. Notably, the circuit elements shown in Fig. 1 are depicted in the lumped-element representation, which means by definition, that the electromagnetic fields are collimated within the element, and that the elements are connected by perfectly conducting wires. In other words, the time delay due to the propagation of signals at a finite speed is neglected. Mapping a superconducting circuit onto an effective lumped-element model is particularly helpful to describe the behavior of the circuit in a limited frequency range, although it is a simplification in general. The lumped-element inductance of the effective circuit model might represent the total geometric inductance of a distributed superconducting wire, and the lumped-element model does not cover the standing-wave pattern of the current along the wire.

The sign convention for the branch current and voltage, as indicated in Fig. 1, is such that the energy absorbed in the branch becomes

$$E_\mathrm{b}(t) = \int_{-\infty}^{t} v_\mathrm{b}(t')i_\mathrm{b}(t')\mathrm{d}t'. \tag{3}$$

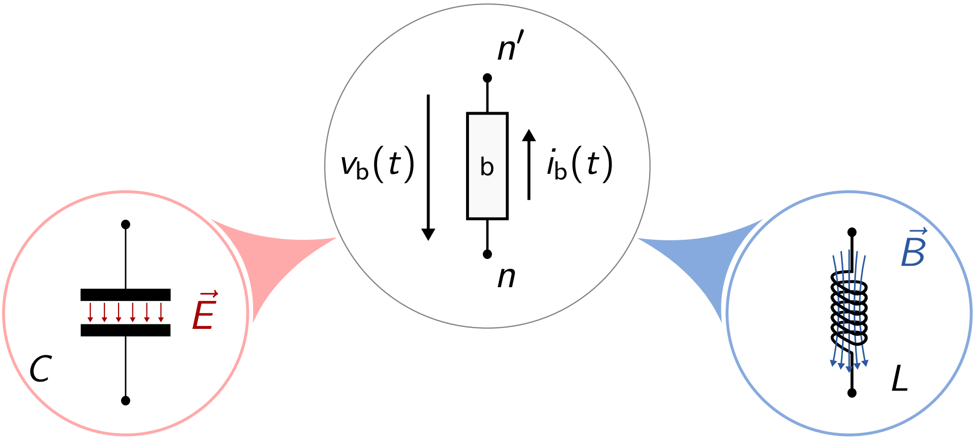

Figure 1: Branch and node representation of dipolar circuit elements. In the center, surrounded by a grey circle, the branch and node representation of a dipolar element is shown. The branch element, indicated by a black rectangle, has two connections, one at the top and one at the bottom, which both lead to a single node each (black markers) with indices n and n'. The electromagnetic properties of the branch element are characterized by a branch voltage v_b and a branch current i_b. The sign convention for the branch current and voltage defines the power absorbed by the branch element to be a positive number. In the red and the blue circle two common examples of linear dipolar elements are given: a capacitor (red) and an inductor (blue). For a capacitor exposed to an external voltage bias, an electrical field emerges (red arrows) between the capacitor plates due to the induced electrical charges with opposite sign. In contrast, a current flowing through an inductor gives rise to a magnetic field (blue arrows). Both circuit elements are depicted as lumped elements, which means that the electronic properties are concentrated in idealized electrical components connected by perfectly conducting wires. Thus, the propagation delay across the element is neglected on the time scale of any signal. Moreover, the electromagnetic fields are assumed to be confined inside the elements.

Instead of current and voltage, a complementary but generally more convenient basis to describe a superconducting circuit is given by the generalized magnetic branch flux and branch charge Φ_b and Q_b, respectively:

$$\Phi_\mathrm{b}(t) = \int_{-\infty}^{t} v_\mathrm{b}(t')\mathrm{d}t' \tag{4}$$

$$Q_\mathrm{b}(t) = \int_{-\infty}^{t} i_\mathrm{b}(t')\mathrm{d}t'. \tag{5}$$

The integration is performed up to the present time t, where the starting point is sufficiently far in the past, where both current and voltage were zero. This set of quantities is particularily suited for superconducting circuits, since, as it turns out, the magnetic flux is related to the macroscopic phase of the superconducting wavefunction, which is the conjugate of the charge. External perturbations in the form of offset magnetic fields inducing currents in loops, or potential offset charges residing on nodes, are considered by Kirchhoff's circuit laws:

$$\sum_{\text{all b around loop } l} \Phi_{\mathrm{b}} = \Phi_{\mathrm{ext},l} \tag{6}$$

$$\sum_{\text{all b arriving at node } n} Q_{\mathrm{b}} = Q_{\mathrm{off},n}. \tag{7}$$

For complicated circuits composed of many branches and nodes, finding the DOS of a network demands a strategic procedure to eliminate redundant variables, as there are generally less DOF than branches and nodes. However, since the circuits discussed in the scope of my thesis are simple with respect to their topology, I will omit a detailed discussion of the procedure described in Ref. [62] in its most general form. At its heart, it provides a guideline to find a convenient set of generalized coordinate variables to begin with, from which the Lagrangian can be readily derived.

In contrast to a mechanical system composed of masses and springs, where the generalized position coordinate and momentum are determined by the position and momentum of the centers of mass, in an electrical circuit, both, the magnetic flux and the charge can be considered as the position or the momentum coordinate. Anticipating the action of a Josephson junction being that of a nonlinear inductor, a convenient choice is to treat the magnetic flux as the position coordinate. The mathematical implementation of this choice is realized by describing the circuit based on a set of node variables. Similar to the flux of a branch, a node flux Φ_n can be defined for each node. Since both sets of variables are complementary, the node and the branch variables can be converted into one another. For instance, in the abscence of external magnetic biases, the branch and node flux are simply related by

$$\Phi_b = \Phi_n - \Phi_{n'}, \tag{8}$$

where n and n' are the nodes on both sides of the respective branch b.

For the purpose of eliminating the redundant variables, first a reference node is chosen for the whole circuit, denoted the ground node, by setting the corresponding node flux to zero. Since the generalized velocity in the node representation is identical to the time derivative of the node flux $\dot{\Phi}_n$, and the difference between the velocities of two neighboring nodes is equal to the voltage across the branch connecting the nodes $v_{\mathrm{b}} = \dot{\Phi}_n - \dot{\Phi}_{n'}$, the kinetic energy associated to a linear capacitive branch becomes

$$E_{\mathrm{kin,b}} = \frac{C}{2}\left(\dot{\Phi}_n - \dot{\Phi}_{n'}\right)^2. \tag{9}$$

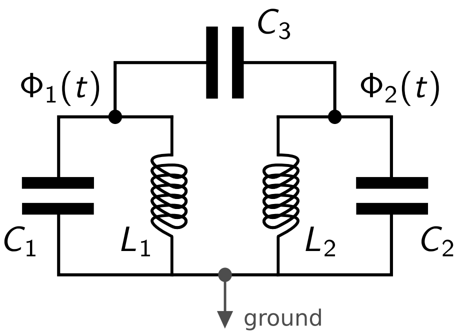

Figure 2: Electromagnetic circuit. Lumped-element electronic schematic of a simple circuit of two LC oscillators with capacitance C_i and inductance L_i, which are capacitively coupled by a third capacitance C_3. The circuit contains three nodes, indicated by black markers, from which the bottom one is assigned the ground (grey), and the other two are the DOF of the circuit. Each node is associated with a node flux Φ_i.

The effective mass is given by the capacitance C. Analogously, the potential energy of a linear inductive branch becomes

$$E_{\text{pot,b}} = \frac{1}{2L}\left(\Phi_n - \Phi_{n'}\right)^2 . \tag{10}$$

Eventually, the Lagrangian of the whole circuit is given by the difference between the kinetic energies of all capacitive branches, and the potential energies of all inductive branches

$$\mathcal{L} = \sum_{\text{b}} E_{\text{kin,b}} - \sum_{\text{b}} E_{\text{pot,b}}. \tag{11}$$

Figure 2 depicts the electronic schematic of an exemplary circuit with three nodes. The circuit consists of three capacitors C_1, C_2, and C_3, and two inductors L_1 and L_2. Since the circuit does not contain any closed loop, external magnetic biases can be neglected. As indicated, the lower node is assigned the ground node, with the corresponding node flux being zero. The Lagrangian of the circuit is

$$\mathcal{L} = \frac{C_1}{2}\dot{\Phi}_1^2 + \frac{C_2}{2}\dot{\Phi}_2^2 + \frac{C_3}{2}\left(\dot{\Phi}_2 - \dot{\Phi}_1\right)^2 - \frac{\Phi_1^2}{2L_1} - \frac{\Phi_2^2}{2L_2}. \tag{12}$$

By introducing the node flux vector $\vec{\Phi} = (\Phi_1, \Phi_2)$, the Lagrangian can be expressed in a more compact form using a matrix representation

$$\mathcal{L} = \frac{1}{2}\dot{\vec{\Phi}}^{\mathrm{T}}\tilde{C}\dot{\vec{\Phi}} - \frac{1}{2}\vec{\Phi}^{\mathrm{T}}\tilde{L}^{-1}\vec{\Phi}, \tag{13}$$

where $\tilde{C}$ and $\tilde{L}^{-1}$ are the generally symmetric capacitance and the inverse inductance matrix, respectively. For the given circuit shown in Fig. 2, the corresponding matrices are

$$\tilde{C} = \begin{pmatrix} C_1 + C_3 & -C_3 \\ -C_3 & C_2 + C_3 \end{pmatrix} \qquad \text{and} \qquad \tilde{L}^{-1} = \begin{pmatrix} \frac{1}{L_1} & 0 \\ 0 & \frac{1}{L_2} \end{pmatrix},$$

revealing that due to the circuit topology and the initial choice of generalized coordinates, the inverse inductance matrix is diagonal while the capacitance matrix is not. Consequently, a linear coordinate transformation is required in order to decouple the coordinates and to find the true DOF.

The EOM for the generalized node fluxes, Φ_1 and Φ_2, are derived from the system Lagrangian using the Euler-Lagrange equation

$$\sum_i \frac{\mathrm{d}}{\mathrm{d}t} \frac{\partial \mathcal{L}}{\partial \dot{\Phi}_i} - \frac{\partial \mathcal{L}}{\partial \Phi_i} = 0. \tag{14}$$

Since the capacitive contributions in the Lagrangian are harmonic, the conjugate momenta have the dimension of a charge

$$Q_i = \frac{\partial \mathcal{L}}{\partial \dot{\Phi}_i}, \tag{15}$$

and, more precisely, represent the charges on each node. In the given example, the node charges are

$$\begin{aligned} Q_1 &= (C_1 + C_3)\dot{\Phi}_1 - C_3\dot{\Phi}_2 \\ Q_2 &= (C_2 + C_3)\dot{\Phi}_2 - C_3\dot{\Phi}_1. \end{aligned}$$

Generally speaking, for a circuit containing only linear capacitors, the relation between the canonical momenta, the node charges Q_i, and the generalized velocities, the derivatives of the node flux $\dot{\Phi}_i$, is determined by the capacitance matrix $\tilde{C}$. Similar to the node flux vector, a node charge vector $\vec{Q} = (Q_1, Q_2)$ can be defined, and the relation becomes

$$\vec{Q} = \tilde{C}\dot{\vec{\Phi}}. \tag{16}$$

Deriving the Hamiltonian of the circuit requires the inversion of this relation, which is equivalent to a variable transformation of the generalized coordinates $(\vec{\Phi}, \dot{\vec{\Phi}})$ into the canonical coordinates $(\vec{\Phi}, \dot{\vec{Q}})$. Mathematically, the change in variables is performed using a Legendre transformation:

$$H = \sum_i \dot{\Phi}_i Q_i - \mathcal{L}. \tag{17}$$

Applying the Legendre transformation onto the given example, yields the classical circuit Hamiltonian

$$H = \frac{1}{C_1C_2 + C_1C_3 + C_2C_3}\left[\frac{(C_2+C_3)Q_1^2}{2} + \frac{(C_1+C_3)Q_2^2}{2} + C_3Q_1Q_2\right] + \frac{\Phi_1^2}{2L_1} + \frac{\Phi_2^2}{2L_2}, \tag{18}$$

which can be represented in a matrix form using the node flux and charge vectors:

$$H = \frac{1}{2}\vec{Q}^{\mathrm{T}}\tilde{C}^{-1}\vec{Q} + \frac{1}{2}\vec{\Phi}^{\mathrm{T}}\tilde{L}^{-1}\vec{\Phi}. \tag{19}$$

Similar to the Lagrangian given in Eq. 12, the Hamilton is not diagonal in the current coordinate basis, as shown by the coupling term $\sim Q_1Q_2$.

Diagonalization

In general, finding the basis that diagonalizes the Hamiltonian can be performed at an early stage by diagonalizing the Lagragian first before deriving the Hamiltonian. Depending on the circuit topology, the prefered coordinate transformation for the Lagrangian has the form

$$\vec{Y} = \tilde{L}^{-1/2}\vec{\Phi} \tag{20}$$

or

$$\vec{Y} = \tilde{C}^{1/2}\vec{\Phi}, \tag{21}$$

where $\tilde{L}^{-1/2}$ and $\tilde{C}^{1/2}$ are the square roots of the inverse inductance and capacitance matrix respectively, defined as $\tilde{L}^{-1/2}\cdot\tilde{L}^{-1/2} = \tilde{L}^{-1}$ and $\tilde{C}^{1/2}\cdot\tilde{C}^{1/2} = \tilde{C}$. Since the inverse inductance matrix is already diagonal in the given example, the more convenient choice is the first transformation, which results in the Lagrangian

$$\mathcal{L} = \frac{1}{2}\dot{\vec{Y}}^{\mathrm{T}}\underbrace{\tilde{L}^{1/2}\cdot\tilde{C}\cdot\tilde{L}^{1/2}}_{\tilde{A}}\dot{\vec{Y}} - \frac{1}{2}\vec{Y}^{\mathrm{T}}\vec{Y}. \tag{22}$$

The eigenvalues and eigenvectors of the Lagrangian are found by diagonalizing the the matrix $\tilde{A}$. For the circuit shown in Fig. 2, the matrix $\tilde{A}$ is

$$\tilde{A} = \begin{pmatrix} L_1(C_1+C_3) & -\sqrt{L_1L_2}C_3 \\ -\sqrt{L_1L_2}C_3 & L_2(C_2+C_3) \end{pmatrix}, \tag{23}$$

which can be rewritten

$$\tilde{A} = \begin{pmatrix} \Omega_1^{-2} & -\frac{\beta}{\Omega_1\Omega_2} \\ -\frac{\beta}{\Omega_1\Omega_2} & \Omega_2^{-2} \end{pmatrix} \tag{24}$$

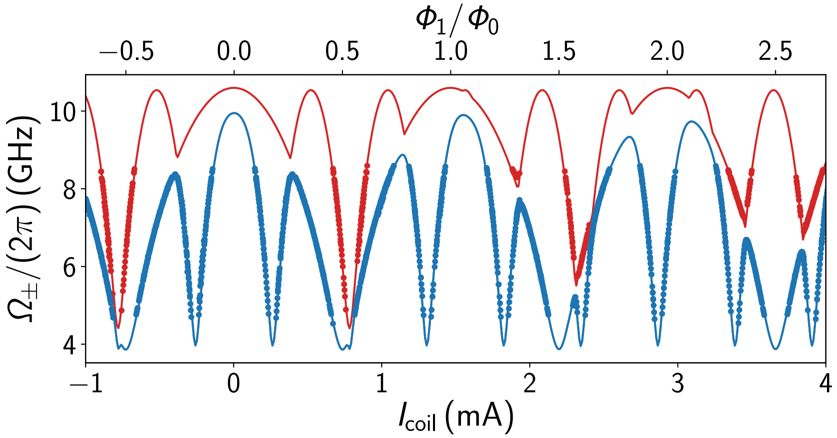

Figure 3: Classical circuit analysis. Measured eigenfrequencies $\Omega_\pm$ (red and blue markers) of two capacitively coupled transmon qubits with flux tunable SQUID junctions. Since the SQUIDs are asymmetric with respect to the critical currents of the individual JJs (see App. E), the observed flux modulation amplitude reaches a lower bound of 4 GHz. Additionally, the SQUID loop areas also differ by design, i.e. the area ratio is 2.811, resulting in a fast oscillation and a slow oscillation with the flux Φ_1 enclosed in the smaller loop. Whenever the two transmons are tuned on resonance, they hybridize, resulting in an avoided level-crossing. Although the transmons are intrinsically nonlinear, the flux modulation can be predicted from the linear circuit model shown in Fig. 2. The red and blue solid lines correspond to the solutions given in Eq. 27.

by introducing the parameters $\Omega_i^{-2} = L_i(C_i + C_3$ and $\beta = C_3/\sqrt{(C_1 + C_3)(C_2 + C_3)}$. Performing an eigendecomposition

$$\tilde{A} = \tilde{S}\tilde{\Lambda}\tilde{S}^{-1}, \tag{25}$$

where $\tilde{S}$ is a matrix of the same size and dimension as $\tilde{A}$, composed of the eigenvectors of $\tilde{A}$, gives the diagonal matrix $\tilde{\Lambda}$

$$\tilde{\Lambda} = \begin{pmatrix} \Omega_+^{-2} & 0 \\ 0 & \Omega_-^{-2} \end{pmatrix}, \tag{26}$$

with the corresponding eigenvalues defined as

$$\Omega_\pm = \left(\frac{2\Omega_1^2\Omega_2^2}{\Omega_1^2 + \Omega_2^2 \pm \left[(\Omega_1^2 - \Omega_2^2)^2 + 4\beta^2\Omega_1^2\Omega_2^2\right]^{1/2}} \right)^{1/2}. \tag{27}$$

It is straight forward to show that the same coordinate transformation also diagonalizes the Hamiltonian.

The presented conceptual procedure is also applicable to more complex circuits with more degrees of freedom, as long as the circuit does not contain any closed loops, which requires the consideration of the external magnetic flux enclosed in the loops. Moreover, in the presence of time-dependent external flux, a consistent procedure becomes even more important [67].

A simplification is possible in the case of dc SQUIDs with negligible loop inductance (see App. E) and assuming a static external flux only. Under these conditions, the lowest energy eigenstates can be calculated by representing the dc SQUID by a linear inductor with flux dependent inductance. Figure 3 depicts the response of two capacitively coupled transmon qubits with asymmetric SQUID junctions. Since the SQUID loop areas differ by almost a factor of three, two distinct modulation periods are observable, resulting in a modulation pattern composed of a fast and a slow oscillation. Whenever the two transmons are tuned on resonance, the hybridization caused by the capacitive coupling manifests in form of avoided level-crossings. The solid red and blue lines illustrate a fit to the measured data according to Eq. 27, for which the flux dependence introduced by the SQUIDs is accounted for using Eq. 159.

So far, the presence of offset charges $Q_{\mathrm{off,n}}$ on the individual nodes has been neglected, since, for a classical circuit, these offset charges only shift the equilibrium point around which the node charges oscillate. However, in a superconducting quantum circuit, the situation can be different, as shown in the context of the superconducting charge qubit in Sec. 1.1.3.

A.2 Canonical quantization

In classical Hamiltonian mechanics, the time evolution of the canonical coordinates is determined by Hamilton's equations. For an electrical circuit discribed in the node variable framework, Hamilton's equations for the node flux and charge variables are

$$\frac{\mathrm{d}\vec{Q}}{\mathrm{d}t} = -\frac{\partial H}{\partial \vec{\Phi}} \qquad \text{and} \qquad \frac{\mathrm{d}\vec{\Phi}}{\mathrm{d}t} = +\frac{\partial H}{\partial \vec{Q}}. \tag{28}$$

Both equations can be expressed in a more general form using the Poisson bracket

$$\frac{\mathrm{d}\vec{Q}}{\mathrm{d}t} = \{\vec{Q}, H\} + \frac{\partial \vec{Q}}{\partial t}, \tag{29}$$

as exemplarily displayed for the node charge $\vec{Q}$. Since the development of quantum mechanics, it is known that the classical behavior of a system is just a manifestation of the underlying quantum behavior, observed for systems involving a large number of particles or high energies, which is referred to as the correspondence principle [3, 12]. In the canonical quantization of a classical system proposed by Paul Dirac [13], the primarily classical canonical coordinates are promoted to quantum mechanical operators, for instance the node flux and charge of an electrical (quantum) circuit

$$\begin{aligned} \vec{\Phi} &\quad\rightarrow\quad \hat{\vec{\Phi}} \\ \vec{Q} &\quad\rightarrow\quad \hat{\vec{Q}} \\ H &\quad\rightarrow\quad \hat{H}, \end{aligned}$$

and the Poisson brakets are substituted with the corresponding commutators

$$\{\vec{Q}, H\} \qquad \rightarrow \qquad \frac{1}{i\hbar}[\hat{\vec{Q}}, \hat{H}]. \tag{30}$$

The quantum operators are indicated by hats. The idea of the canonical quantization is to preserve the form of the Hamilton equations. Hence, in the Heisenberg picture in which the quantum operators are time dependent while the quantum states do not change with time, the time evolution of a quantum operator is determined by

$$\frac{\mathrm{d}\vec{Q}}{\mathrm{d}t} = \frac{1}{i\hbar}[\hat{\vec{Q}}, \hat{H}] + \frac{\partial \vec{Q}}{\partial t}, \tag{31}$$

which is known as the Heisenberg equation of motion.

Another consequence of the canonical quantization is, that conjugate variables obey the canonical commutation relation

$$[\hat{\Phi}, \hat{Q}] = i\hbar. \tag{32}$$

The sign in front of the term on the right-hand side of the equation determines the node flux as the position variable, and the node charge as the conjugate momentum, in agreement with the classical treatment [62]. Since conjugate variables are mathematically defined in such a way that they are Fourier transform duals of one another, they naturally underlie an uncertainty principle. Even in classical mechanics this mathematical definition induces an uncertainty between conjugate pairs, for instance as observed for the frequency and the time duration of a periodic signal.

In the following, I will discuss the quantization of an electrical circuit with the aid of a more simple resonant circuit: The LC-oscillator. The lumped-element circuit representation is schematically depicted in Fig. 4. The circuit has two nodes, from which the lower node is selected to be the ground node, while the top node is associated with the generalized node flux operator Φ, defined as the time integral of the voltage operator V across the capacitor

$$\hat{\Phi}(t) = \int_{-\infty}^{t} \hat{V}(t')\mathrm{d}t'. \tag{33}$$

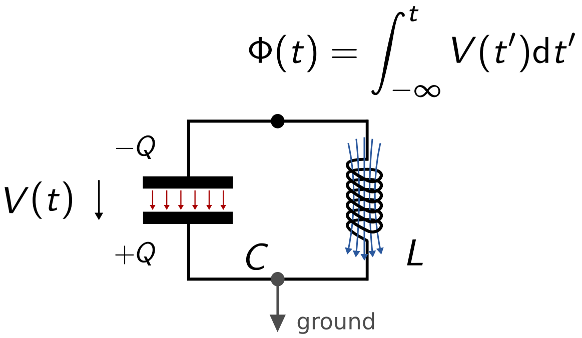

Figure 4: LC-Oscillator. Circuit schematic representation of a parallel LC oscillator. The voltage V across the capacitor C induces the charges $\pm Q$ on the capacitor plates, and is associated to an electrical field (red arrows). The current I through the inductor L gives rise to a magnetic field (blue arrows). The node flux Φ, which is the time integral of the voltage V, is the position coordinate, while the charge Q is the conjugate momentum.

For the quantum harmonic oscillator, following the procedure described in previous sections, the Hamiltonian is

$$H = \frac{\hat{Q}^2}{2C} + \frac{\hat{\Phi}^2}{2L}, \tag{34}$$

where $\hat{Q}$ is the node charge operator. While the spectrum of the node flux is continuous, the spectrum of the charge operator is discrete.

Similar to the mechanical quantum harmonic oscillator, the canonical coordinates are expressed in terms of creation and annihilation operators $\hat{a}^\dagger$ and $\hat{a}$, respectively,

$$\hat{\Phi} = \Phi_{\mathrm{ZPF}} \left(\hat{a} + \hat{a}^\dagger\right) \tag{35}$$

$$\hat{Q} = -iQ_{\mathrm{ZPF}} \left(\hat{a} - \hat{a}^\dagger\right). \tag{36}$$

Here, Φ_{ZPF} and Q_{ZPF} are the zero-point fluctuations of the node flux and the node charge, respectively. By definition, they determine the magnitude of the ground-state fluctuations in both variables in the abscence of excitations, and are the manifestation of the uncertainty principle. In a superconducting circuit, the size of these fluctuations is controlled by the relative size of the circuit elements:

$$\Phi_{\mathrm{ZPF}} = \sqrt{\frac{\hbar Z_0}{2}} \tag{37}$$

$$Q_{\mathrm{ZPF}} = \sqrt{\frac{\hbar}{2Z_0}}, \tag{38}$$

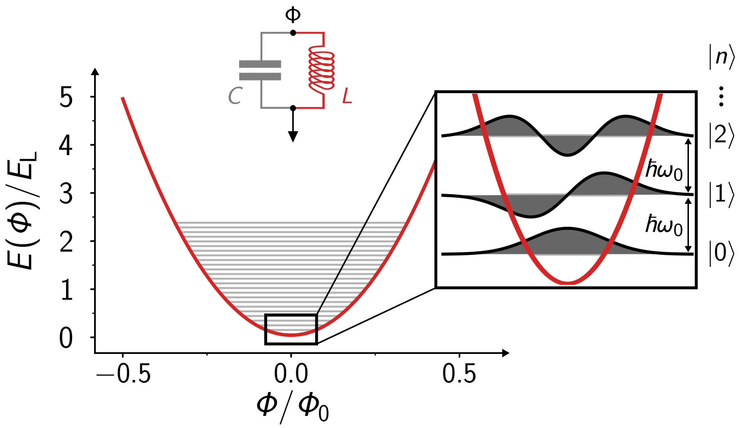

Figure 5: Quantum LC-oscillator. Parabolic energy potential $E = \Phi^2/(2L)$ of the harmonic LC oscillator, plotted as a function of the node flux Φ in numbers of the magnetic flux quantum Φ_0. Since the node flux is chosen to be the canonical position variable, the conjugate momentum is the charge Q on the capacitor. The energy is normalized by the inductive energy $E_\mathrm{L} = \varphi_0^2/L$, and the grey horizontal lines indicate the discrete but infinite set of eigenenergies $E_\mathrm{n} = \hbar\omega_0(n + 1/2)$, where n are the eigenvalues of the photon number operator, and $\omega_0 = 1/\sqrt{LC}$ is the resonance frequency of the LC oscillator. The basis $|n\rangle$ spanned by the eigenvectors of the photon number operator is referred to as the Fock basis. The inset shows the region of the potential around zero flux, including the first three energy eigenstates and the corresponding eigenfunctions $|n\rangle \in \{0, 1, 2\}$. The eigenfunction of the ground state is a Gaussian, and the zero-point fluctuations of the node flux are related to the standard-deviation of the ground state. Obviously, the Fock states are not the eigenstates of the node flux and the current operator. The circuit parameters chosen for the calculation are $C = 200\,\mathrm{fF}$ and $L = 2\,\mathrm{nH}$, resulting in a characteristic impedance $Z_0 = 100\,\Omega$.

where $Z_0 = \sqrt{L/C}$ is the circuit's characteristic impedance. According to the definitions of the zero-point fluctuations, the suppression of the fluctuation in one variable by changing the characteristic impedance of the circuit, enhances the fluctuation in the other variable. For linear circuits with more than one DOF, each eigenmode can be associated with a characteristic impedance.

As mentioned earlier, the node flux and the charge of the harmonic oscillator are ultimatively related to electromagnetic fields created by the current flowing through the inductor and the charges residing on the capacitor plates. For that reason, in the context of superconducting quantum circuits, the creation and annihilation operators correspond to single-mode field amplitude operators, which obey the bosonic commutation relation

$$[\hat{a}, \hat{a}^\dagger] = 1. \tag{39}$$

The quantization of electromagnetic fields is subject of the second quantization. By inserting Eq. 35 and Eq.36 into Eq. 34, yields the Hamiltonian in second quantization

$$\hat{H} = \hbar\omega_0 \left(\hat{a}^\dagger \hat{a} + \frac{1}{2} \right), \tag{40}$$

where $\omega_0 = 1/\sqrt{LC}$ is the resonance frequency of the LC oscillator. The operator $\hat{n} = \hat{a}^\dagger \hat{a}$ is the occupation number operator, which has a discrete eigenbasis, denoted the Fock basis, given by the discrete set of elementary excitations of the electromagnetic field, the photons:

$$\hat{n} \left| n \right\rangle = n \left| n \right\rangle, \tag{41}$$

In the Fock basis spanned by $|n\rangle$, with $n \in \mathcal{Z}^{\geq 0}$, the eigenenergies of the quantum harmonic oscilaltor are

$$E_n = \hbar\omega \left(n + \frac{1}{2} \right), \tag{42}$$

where n is the number of photons inside the oscillator. The energy spacing between consecutive energy levels is detemined by the resonance frequency of the circuit and does not depend on the number of photons inside the oscillator. Figure 5 depicts the quadratic energy potential of the quantum harmonic oscillator $E = \varPhi^2/(2L)$ (red), and the first twenty energy eigenenergies E_n, indicated by the grey horizontal lines. The inset shows the first three eigenenergies E_0, E_1, and E_2, highlighting the equidistance between the energy eigenstates, and the real parts of their corresponding eigenfunctions $\varPsi_0(\varPhi)$, $\varPsi_1(\varPhi)$ and $\varPsi_2(\varPhi)$ in position space.

The general expression of the eigenfunctions in the position space are

$$\varPsi_n(\varPhi) = \langle \varPhi | n \rangle = \frac{1}{\sqrt{2^n n!}} \left(\frac{1}{2\pi \varPhi_{\mathrm{ZPF}}^2} \right)^{\frac{1}{4}} e^{-\varPhi^2/(4\varPhi_{\mathrm{ZPF}}^2)} H_n \left(\frac{1}{\sqrt{2}\varPhi_{\mathrm{ZPF}}} \varPhi \right), \tag{43}$$

where $H_n(z)$ are the Hermite polynomials, $\varPhi$ are the eigenvalues of the flux operator and $|\varPhi\rangle$ the corresponding eigenfunctions satisfying

$$\hat{\varPhi} \left| \varPhi \right\rangle = \varPhi \left| \varPhi \right\rangle. \tag{44}$$

Since the eigenfunctions of observables are interpreted as probability amplitudes in quantum mechanics, the illustration of $\varPsi_n(\varPhi)$ shows that depending on the state, some values of the node flux will be measured with higher probability, while some values, the roots of $\varPsi_n(\varPhi) = 0$, will never be measured. Notably, for all Fock states, the expectation value of the current and voltage is zero. According to Eq. 43, the eigenfunction of the ground state $\varPsi_0$ is a Gaussian, with its standard deviation σ determined by the flux zero-point fluctuations $\sigma = \sqrt{2}\varPhi_{\mathrm{ZPF}}$.

The same procedure can be applied to circuits with a larger number of DOF, where the eigenmodes are independent and therefore described by an individual pair of creation and annihilation operators. In a nonlinear circuit, the decomposition into independent modes is not necessarily possible, but in many applications not desired either.

B Input-output formalism

In the framework of quantum electrodynamics with superconducting circuits, the carriers of signals and information are photons in the microwave regime of the electromagnetic spectrum. For the readout and manipulation of the circuit's quantum state, the photons have to interact with the plasma oscillation in some way, either via the electric or magnetic field. Besides this intentional interaction, in a real system, there are unintentional interactions to uncontrolled degrees of freedom residing in the electromagnetic environment of the circuit. A consequence of these interactions is, that the system cannot be treated as a closed quantum system, but becomes an open quantum system which is subject to energy relaxation and dephasing.

Similar to conventional radio frequency technology, resonant superconducting quantum circuits constitute a hardware interface that transduces the electromagnetic fields of propagating photons into oscillating currents and voltages. The coupling strength between the circuit and the electromagnetic wave can be controlled by the multipole moments of the circuit. A popular example is the coupling via the electric dipole moment of the circuit, arising from its shape in form of a microwave antenna, as demonstrated with the grAl transmon discussed in Ch. 2 and the cQED system discussed in Sec. 1.1.6.

Independent of the obtained coupling strength, the engineered interaction between quantized light and matter in superconducting quantum circuits is conceptually very similar to the rich physics studied in quantum optics, as discussed in Sec. 1.1. A mathematical framework particularly suitable to describe the dynamics of an open quantum system in this context, is the input-output formalism [21]. At its heart, it provides a direct mathematical relation between the incident photons, the photons stored inside the quantum system, and the outgoing photons. The following description of the input-output formalism is deduced from the excellent works of C. W. Gardiner and M. J. Collett [21], A. A. Clerk *et al.* [6], S. Girvin [22], Eichler and Wallraff [15], and U. Vool [61].

Introducing dissipation

Figure 6 depicts the schematic illustration of a cavity, which is coupled to a microwave input port on the left-hand side, and to an artificial loss port on the right-hand side. The cavity is described by the Hamiltonian $\hat{H}_{\mathrm{sys}}$, and is illustrated in the form of an optical cavity composed of two semi-transparent, concave mirrors, that confine the light inside the volume between the mirrors. However, despite the chosen portrayal, the cavity might be in place of a superconducting circuit all the same. While the

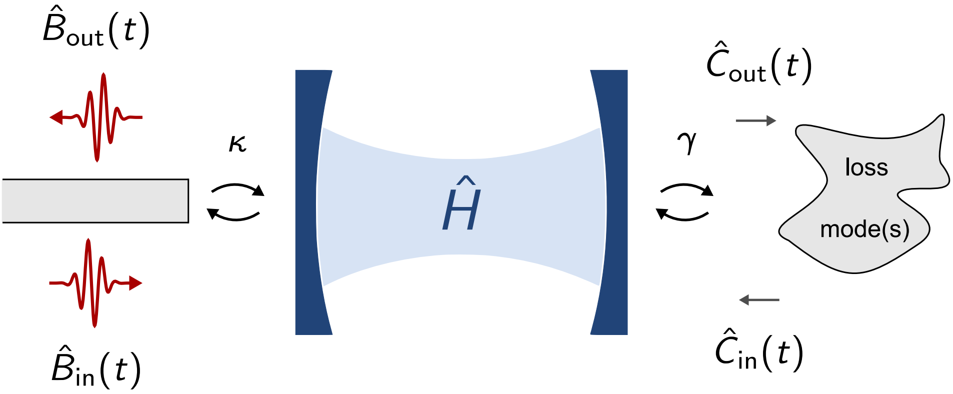

Figure 6: Input-output representation of a single cavity. Schematic representation of a microwave cavity described by the corresponding Hamiltonian $\hat{H}_{\mathrm{sys}}$, which is coupled to a microwave input port on the left-hand side, and to an artificial loss port on the right-hand side. Referring to quantum optics experiments, the cavity is depicted in the form of two semi-transparent, concave mirrors that confine the electromagnetic field inside the cavity. The transparency of the mirrors determines the coupling rates κ and γ to the two microwave ports. For a superconducting circuit, the coupling rate κ to the input port is well controlled by the dipole moment of the circuit, while the coupling rate γ to uncontrolled degrees of freedom is much more difficult to predict and to control. In the vast majority of systems, the ideal case is $\gamma \to 0$. The field confined inside the cavity, and the propagating fields in the microwave ports is described by a set of single-mode field amplitude operators. For the two ports, the incident and outgoing fields are distinguished, and carry a corresponding index.

desired exchange of information is carried out via the input port, the artificial loss port accounts for the system's interaction with uncontrolled degrees of freedom. For that reason, the corresponding coupling rates are referred to as the internal, and external coupling rate, γ and κ, respectively. The two coupling rates determine how fast the field inside the cavity can be excited, and how fast it spontaneously decays into the two ports.

Each part of the system is associated with a set of bosonic field amplitude operators. For a single mode cavity, the stationary field inside the cavity is described by a set of creation and annihilation operators denoted $\hat{A}^{\dagger}$ and $\hat{A}$, respectively, while the fields in the microwave ports $\hat{B}$ and $\hat{C}$ will be separated into incident and outgoing fields, as indicated by the arrows.

The combined Hamiltonian of the whole arrangement, including the two ports and the exchange of excitations, is

$$\hat{H} = \hat{H}_{\mathrm{sys}} + \hat{H}_{\mathrm{input}} + \hat{H}_{\mathrm{bath}} + \hat{H}_{\mathrm{int,input}} + \hat{H}_{\mathrm{int,bath}}, \tag{45}$$

where $\hat{H}_{\mathrm{sys}}$ is the cavity or system Hamiltonian, as it might describe a quantum two-level system, $\hat{H}_{\mathrm{input}}$ and $\hat{H}_{\mathrm{bath}}$ are the Hamiltonians associated with the input and loss port, respectively, and $\hat{H}_{\mathrm{int,input}}$ and $\hat{H}_{\mathrm{int,bath}}$ determine the interaction between the cavity and the input port, and the cavity and the loss modes, respectively.

A convenient and natural choice is to model the input port and the loss port by an infinite set of independent harmonic modes

$$\hat{H}_{\mathrm{input}} = \hbar \int_0^\infty \mathrm{d}\omega \hat{B}^\dagger(\omega)\hat{B}(\omega) \tag{46}$$

and

$$\hat{H}_{\mathrm{bath}} = \hbar \int_0^\infty \mathrm{d}\omega \hat{C}^\dagger(\omega)\hat{C}(\omega) \tag{47}$$

which obey the bosonic commutation relation $[\hat{b}(\omega), \hat{b}^\dagger(\omega')] = \delta(\omega - \omega')$ and $[\hat{c}(\omega), \hat{c}^\dagger(\omega')] = \delta(\omega - \omega')$. Here ω and ω' are the frequencies of the bosonic modes. Within the rotating-wave approximation, the interaction Hamiltonians are

$$\hat{H}_{\mathrm{int,input}} = \frac{\hbar}{\sqrt{2\pi}} \int_0^\infty \mathrm{d}\omega \sqrt{\kappa(\omega)} \left[\hat{A}^\dagger \hat{B}(\omega) + \hat{B}^\dagger(\omega)\hat{A}\right] \tag{48}$$

and

$$\hat{H}_{\mathrm{int,bath}} = \frac{\hbar}{\sqrt{2\pi}} \int_0^\infty \mathrm{d}\omega \sqrt{\gamma(\omega)} \left[\hat{A}^\dagger \hat{C}(\omega) + \hat{C}^\dagger(\omega)\hat{A}\right], \tag{49}$$

which describe the exchange of single photons between the ports and the cavity. For simplicity, two-photon interactions, which can be present in nonlinear cavities [68], are neglected. Referring to superconducting circuits, the given form of the interaction Hamiltonians reminds of a linear coupling between two harmonic oscillators, as discussed in previous sections, induced by a shared capacitance or a shared inductance.

The strength of the interaction is given by the generally complex and frequency dependent coefficients $\kappa(\omega)$ and $\gamma(\omega)$. In the Markov approximation, these coefficients are considered to be constant and independent of frequency, which means that the port modes interact with the system only in close vicinity of its resonance frequency ($\kappa, \gamma \ll \omega_0$), or in other words, that the state of the cavity as seen from the input port does not change significantly within one period. Unlike the intra-cavity field operators, the field operators associated to the ports represent densities of photons per unit bandwidth.

Quantum Langevin equation:

In the Heisenberg picture, the time evolution of the observables, in this case the field amplitude operators, is determined by the Heisenberg equation of motion. For observables without explicit time dependence, the Heisenberg EOM reduces to [8]

$$\dot{\hat{A}}(t) = \frac{1}{i\hbar}[\hat{A}(t), \hat{H}]. \tag{50}$$

Here, the operator $\hat{A}$ represents the intra-cavity field, and a similar expression is found for the port modes $\hat{B}$ and $\hat{C}$. By inserting the Hamiltonian according to Eq. 45, and using the bosonic commutation relation, the EOM of $\hat{A}$ becomes

$$\dot{\hat{A}}(t) = \frac{1}{i\hbar}[\hat{H}_{\text{sys}}, \hat{A}(t)] - \frac{i}{\sqrt{2\pi}} \int_0^\infty \mathrm{d}\omega \sqrt{\kappa} \hat{B}(\omega) - \frac{i}{\sqrt{2\pi}} \int_0^\infty \mathrm{d}\omega \sqrt{\gamma} \hat{C}(\omega) \tag{51}$$

The time evolution of the port modes $\hat{B}$ and $\hat{C}$ is found by solving their corresponding Heisenberg EOM [21], and are of the form

$$\hat{B}(\omega) = e^{-i\omega(t-t_0)} \hat{B}_0(\omega) + \frac{1}{\sqrt{2\pi}} \int_{t_0}^{t} \mathrm{d}t' \sqrt{\kappa} e^{-i\omega(t-t_0)} \hat{A}(t'), \tag{52}$$

where $\hat{B}_0(\omega)$ is the value of the input port mode at time $t_0 < t$. Since t_0 is a moment in the past, $\hat{B}_0(\omega)$ plays the role of an initial value. An equivalent expression is found for the modes of the loss port. Inserting the obtained solutions into Eq. 51 yields

$$\dot{\hat{A}}(t) = \frac{1}{i\hbar}[\hat{H}_{\text{sys}}, \hat{A}(t)] - \frac{\kappa}{2}\hat{A} - \frac{\gamma}{2}\hat{A} - \sqrt{\kappa}\hat{B}_{\text{in}} - \sqrt{\gamma}\hat{C}_{\text{in}}, \tag{53}$$

which is the quantum Langevin equation of the intra-cavity field operator. In the Markov approximation, the interaction with the port manifests in the form of damping terms of the intra-cavity field at rates κ and γ. The incident modes are defined as

$$\hat{B}_{\text{in}}(t) = \frac{i}{\sqrt{2\pi}} \int_0^\omega \mathrm{d}\omega e^{-i\omega(t-t_0)} \hat{B}_0(\omega), \tag{54}$$

and

$$\hat{C}_{\text{in}}(t) = \frac{i}{\sqrt{2\pi}} \int_0^\omega \mathrm{d}\omega e^{-i\omega(t-t_0)} \hat{C}_0(\omega), \tag{55}$$

and are the port modes that interact with the intra-cavity field at time t. A complementary or time-reversed quantum Langevin equation can be derived that relates the time evolution of the intra-cavity field at time t with the solutions of the port modes at future times $t_1 > t$. In analogy to the incident port modes, a set of outgoing modes can be defined similar to Eq. 54 and 55. Comparing the obtained quantum Langevin equations yields the following boundary conditions

$$\hat{B}_{\text{out}} - \hat{B}_{\text{in}} = \sqrt{\kappa}\hat{A} \tag{56}$$

and

$$\hat{C}_{\mathrm{out}} - \hat{C}_{\mathrm{in}} = \sqrt{\gamma}\hat{A}, \tag{57}$$

which relate the incident and outgoing modes with the intra-cavity mode. In most cases, the bath of loss modes is considered to be cold, and the modes incident to the cavity through the loss port are neglected. However, the additional channel increases the energy relaxation rate of the intra-cavity field.

B.1 Optical phase space

A convenient way to illustrate the time evolution of a system is the phase space. In classical and quantum mechanics alike, the phase space is spanned by the conjugate variables of the system, for instance the position and momentum of a mechanical pendulum, or the flux and charge in an electrical circuit. If the system has a single DOF, the phase space is a two-dimensional space similar to the complex plane. For an optical system described by bosonic field operators, a similar representation is available, denoted the optical phase space. Since the bosonic field operators obey the bosonic commutation relation, a set of complementary conjugate variables is defined

$$\hat{I} = \frac{1}{2}(\hat{a}^\dagger + \hat{a}) \tag{58}$$

$$\hat{Q} = \frac{i}{2}(\hat{a}^\dagger - \hat{a}), \tag{59}$$

which are referred to as the quadrature operators, and obey the commutation relation

$$[\hat{I}, \hat{Q}] = \frac{i}{2}. \tag{60}$$

At this point, I would like to emphasize that there are different possibilities for the normalization of the quadrature operators. In the given normalization, the quadrature operators $\hat{I}$ and $\hat{Q}$ represent the real and imaginary part of the field amplitude operator, respectively,

$$\hat{a} = \hat{I} + i\hat{Q}, \tag{61}$$

which is a convenient choice since the corresponding variances are given in number of photons. The normalization affects the result of the commutation relation and the lower bound for the uncertainty in the quadratures

$$\Delta I \Delta Q \geq \frac{1}{4}, \tag{62}$$

where ΔI and ΔQ are the variances. However, independent of the normalization, the fluctuations in the photon number of any bosonic mode are correctly recovered

$$|\Delta A|^2 = (\Delta I)^2 + (\Delta Q)^2 \geq \frac{1}{2}, \tag{63}$$

with the lower bound of half a photon representing the quantum fluctuations, as for instance present in the ground state of the quantum harmonic oscillator.

The Wigner function

In quantum optics, the different states of light are commonly represented with the Wigner function $W(\alpha)$, a quasiprobability distribution that maps the quantum mechanical wavefunction of a state onto a statistical distribution in phase space. Although the Wigner function is real valued and normalized to unity, since it can take on negative values for non-classical states of light — indicating quantum interference — the corresponding distribution represents a quasiprobability only.

Any point α in the two-dimensional optical phase space is determined by its real and imaginary part

$$\alpha = I + iQ. \tag{64}$$

The quantities I and Q are the real valued eigenvalues of the quadrature operators. Following this notation, the Wigner function is defined as [28]

$$W(I,Q) = \frac{1}{\pi}\int_{-\infty}^{\infty} \mathrm{d}u e^{-i2uQ} \langle I + \frac{u}{2}|\rho|I - \frac{u}{2}\rangle \tag{65}$$

where ρ is the density matrix describing the state of light in this context. In general, a quantum system can appear as a statistical ensemble if it is coupled to other systems that are inaccessible for the observer. The density matrix is a classical superposition of pure states $|\Psi_j\rangle$

$$\rho = \sum_j = p_j |\Psi_j\rangle \langle\Psi_j| , \tag{66}$$

where the coefficients p_j are classical probabilities. In this notation, the density matrix corresponding to a pure state, for instance the Fock state $|n\rangle$, is

$$\rho = |n\rangle \langle n| . \tag{67}$$

Figure 7 depicts the Wigner function of the Fock state $|1\rangle$ in a two-dimensional contour plot (left-hand top panel) and in a three-dimensional surface plot (left-hand bottom panel). In both cases, the region in which the Wigner function becomes negative is indicated in pink, while the positive values are highlighted in a purple color tone. Since the Fock state is an eigenstate of the number operator, it is maximally uncertain in the phase, and the Wigner function is symmetric around the origin. Fock states are highly non-classical states of light, and are generally difficult to generate. Simply applying a period and monochromatic drive with harmonic time evolution to a quantum harmonic oscillator, will not create a Fock state, but a particular superposition of Fock states, denoted a coherent state.

Coherent states

A coherent state is a special quantum state of light in an harmonic oscillator, for which the expectation values of the field quadrature operators oscillate periodically with time, similar to the classical solutions. By definition it is an eigenstate of the annihilation operator

$$\hat{A}\left|\alpha\right\rangle = \alpha\left|\alpha\right\rangle, \tag{68}$$

where the corresponding eigenvalue α represents the complex field amplitude of the coherent state. Since the annihilation operator and the number operator do not commute, the coherent state is not an eigenstate of the number operator, but is distributed in the Fock basis

$$\hat{a}\left|\alpha\right\rangle = e^{-\frac{1}{2}|\alpha|^2}\sum_{n=0}^{\infty}\frac{\alpha^n}{\sqrt{n!}}\left|n\right\rangle. \tag{69}$$

The probability of a Fock state being occupied follows a discrete Poisson distribution around the mean value $\bar{n} = |\alpha|^2$, and accordingly, the corresponding standard deviation of the distribution grows with the square root of the mean value $\sigma_n = \sqrt{\bar{n}}$. Despite the increasing uncertainty in the photon number, the uncertainty in the quadratures is independent of α

$$\sigma_I = \sqrt{\langle\alpha|\hat{I}^2|\alpha\rangle - \langle\alpha|\hat{I}|\alpha\rangle^2} = \frac{1}{2} = \sigma_Q, \tag{70}$$

and moreover equal to the vacuum fluctuations. Consequently, in the high amplitude limit, the coherent state approaches the classical limit, and since the time evolution of a coherent state under the action of the quantum harmonic oscillator Hamiltonian resembles that of the classical trajectory, it is oftern referred to as the classical state.

Figure 7 depicts the Wigner function $W(I, Q)$ in the optical phase space of the coherent state $|\alpha\rangle = |\sqrt{2}(1+i)\rangle$ in the two right-hand panels. Since the coherent state is not an eigenstate of the quantum harmonic oscillator, it will rotate around the origin with time at the frequency of the oscillator. In contrast to the solution for the Fock state $|1\rangle$ (left-hand panels), for which the Wigner function becomes negative in some regions, it is never below zero for the coherent state. The cross section of the distribution along the quadratures is a Gaussian, as indicated by the projections.

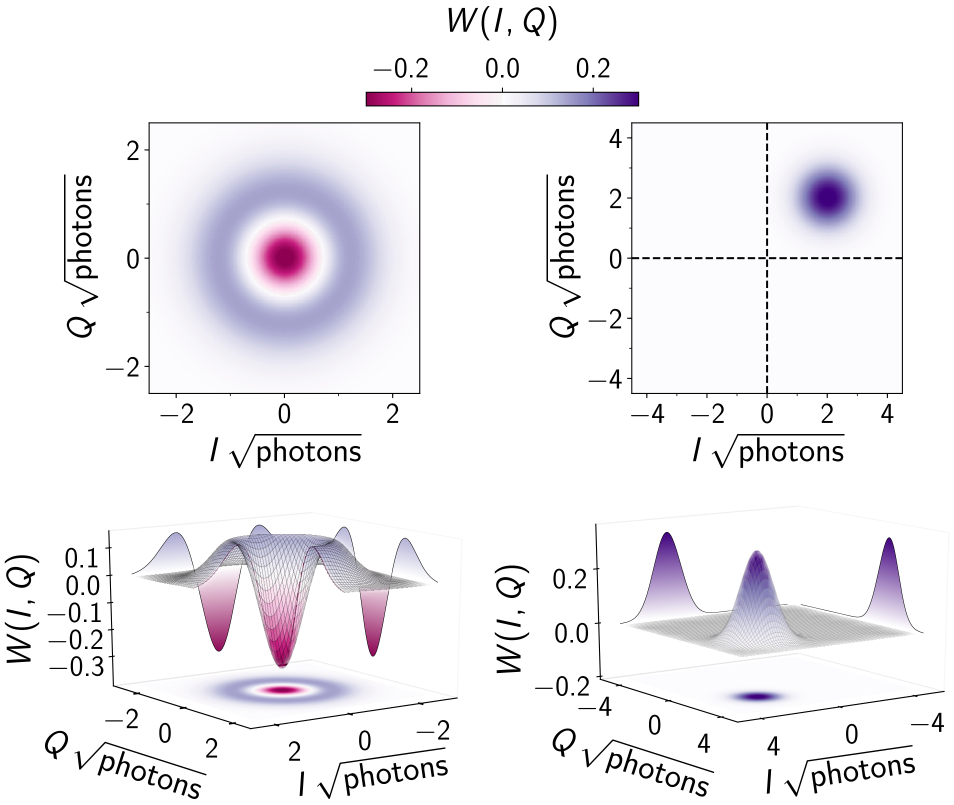

Figure 7: Optical phase space: Wigner function representation of states of light. The two top panels show contour plots of the Wigner function $W(\alpha)$ of the Fock state $|1\rangle$ (left-hand panel) and the coherent state $|\alpha = \sqrt{2}(1+i)\rangle$, plotted in the two-dimensional (optical) phase space. The eigenvalues of the quadrature operators I and Q, spanning the phase space, are of the same dimension as the field amplitudes. For the Fock state, the Wigner function takes on negative values (pink regions), which is the signature of quantum behavior, while the coherent state is always positive (purple regions). Since the Fock state is an eigenstate of the number operator, the number of photons is $n = 1$. In contrast, the coherent state is a superposition of Fock states, with the mean number of photons $\bar{n}$ determined by the distance to the origin $\bar{n} = |\alpha|^2$. An interesting feature of the coherent state is, that the uncertainty in I and Q, indicated by the size of the disc, is independent of the mean number of photons. In order to emphasize the difference between the two states, the two bottom panels show a three-dimensional plot of the corresponding Wigner functions. The projection of the coherent state is a Gaussian.

B.2 The damped and driven harmonic oscillator

The methodology of the input-output formalism and its application to circuit quantum electrodynamics can be demonstrated in many aspects with the aid of the quantum harmonic oscillator. Although the obtained time evolution is that of a linear system, the conceptual treatment is the same as for a nonlinear system, with the main difference, that analytical solutions can be found for the linear system, the description of a nonlinear system might involve numerical calculations.

For the quantum harmonic oscillator, neglecting the constant term due to the zero-point fluctuations, the considered system Hamiltonian is

$$\hat{H}_{\mathrm{sys}} = \hbar\omega_0 \hat{A}^\dagger \hat{A}, \tag{71}$$

and the quantum Langevin equation of the intra-cavity field is

$$\dot{\hat{A}} = -i\omega\hat{A} - \frac{\kappa}{2}\hat{A} - \frac{\gamma}{2}\hat{A} - \sqrt{\kappa}\hat{B}_{\mathrm{in}} - \sqrt{\gamma}\hat{C}_{\mathrm{in}}. \tag{72}$$

The presence of the two ports and their finite coupling to the cavity introduces two damping terms, that cause an exponential decay of the intra-cavity field. In case a strong drive is applied through the input port of the cavity, the corresponding incident fields are decomposed into a classical part representing the drive, and a quantum part representing quantum fluctuations,

$$\hat{B}_{\mathrm{in}}(t) = \hat{b}_{\mathrm{in}}(t) + \beta_{\mathrm{in}}(t) \tag{73}$$

where the classical part is indicated by the Greek letter. A very common drive form is a classical, monochromatic drive with frequency ω_{p},

$$\beta_{\mathrm{in}}(t) = \beta_{\mathrm{in}} \cos\left(\omega_{\mathrm{p}} t + \phi_{\mathrm{p}}\right), \tag{74}$$

where β_{in} is the amplitude of the drive and ϕ_{p} is its phase, which is not of importance for a linear system, but becomes important in the context of phase-sensitive parametric amplification with nonlinear cavities. In most cases, the bath of loss modes is assumed to be cold, and the incident modes $\hat{C}_{\mathrm{in}}$ consisting of quantum fluctuations only, are neglected.

Ring-up and classical steady-state

Similar to the decomposition of the incident field, the response of the intra-cavity to the drive can be separated in a classical part, which describes the generally complex expectation value of the intra-cavity field, and a quantum part, representing the quantum fluctuations around that expectation value:

$$\hat{A}(t) = \hat{a}(t) + \alpha(t) \tag{75}$$

The time evolution of the classical part in a frame rotating with the drive frequency ω_p, is

$$\dot{\alpha}(t) = -i(\omega_0 - \omega_\mathrm{p})\alpha - \frac{\kappa+\gamma}{2}\alpha - \underbrace{\sqrt{\kappa}\beta_\mathrm{in}}_{=\Omega/2}. \tag{76}$$

For a monochromatic drive, the last term is a complex number that determines the effective strength of the drive tone $\Omega = 2\sqrt{\kappa}\beta_\mathrm{in}$, and contains the pump phase.

As soon as a drive is applied to the cavity, the state of the intra-cavity field starts to change. If the drive amplitude is constant, the state of the intra-cavity field will reach an equilibrium state, denoted the steady-state, in which the excitation due to the drive is balanced by the dissipation. However, the change of the intra-cavity field is not instantaneous, but evolves on a characteristic time scale, usually referred to as the ring-up time. The solutions of the quantum Langevin equation are of the form

$$\alpha(t) = \left(\alpha_0 - \frac{\Omega}{i2\Delta - (\kappa+\gamma)}\right) e^{i\Delta t - \frac{\kappa+\gamma}{2}t} + \frac{\Omega}{i2\Delta - (\kappa+\gamma)}, \tag{77}$$

where α_0 is the initial state of the cavity at time $t = 0$, and $\frac{\Omega}{i2\Delta-(\kappa+\gamma)}$ is the equilibrium state, which depends not only on the detuning $\Delta = \omega_\mathrm{p} - \omega_0$ between the drive and resonance frequency of the cavity, but also on the effective drive strength Ω and the decay rates κ and γ.

In some situations, for instance continuous wave measurements for which a monochromatic drive is applied for a duration much longer than the characteristic time scale associated with the ring up, understanding the behavior of the classical steady-state $\dot{\alpha}$ is sufficient to characterize the cavity. For the steady state of a driven, linear cavity, there is always a unique relation between the incident and the intra-cavity field amplitude:

$$\alpha = \frac{\sqrt{\kappa}}{i\Delta - \frac{\kappa+\gamma}{2}}\beta_\mathrm{in} \tag{78}$$

$$= \underbrace{\left(-\sqrt{\kappa}\frac{\frac{\kappa+\gamma}{2} + i\Delta}{\Delta^2 + \left(\frac{\kappa+\gamma}{2}\right)^2}\right)}_{=g(\Delta,\kappa,\gamma)}\beta_\mathrm{in} \tag{79}$$

where $\Delta = \omega_\mathrm{p} - \omega_0$ is the frequency detuning between the drive tone and the resonance frequency of the cavity. In nonlinear cavities, the number of possible solutions for the intra-cavity field depends on the drive strength, with the cavity even entering a deterministically chaotic regime [23]. The derived relation between the intra-cavity field and the incident field is particularly useful to calculate the reflection coefficient using the input-output relation of the classical drive

$$\beta_{\text{out}} = \beta_{\text{in}} + \sqrt{\kappa}\alpha. \tag{80}$$

Reflection coefficient

The reflection coefficient Γ, often labeled S_{11} in reference to the first entry of the scattering matrix used in electrical engineering, is defined as the ratio between the outgoing and the incident field

$$\begin{aligned} \Gamma = S_{11} = \frac{\langle \hat{B}_{\text{out}} \rangle}{\langle \hat{B}_{\text{in}} \rangle} &= \frac{\beta_{\text{out}}}{\beta_{\text{in}}} && (81) \\ &= 1 + \sqrt{\kappa}\frac{\alpha}{\beta_{\text{in}}}. && (82) \end{aligned}$$

Although the measured reflection coefficient is time dependent in general, in continuous wave experiments its steady-state is measured. For a linear cavity, the reflection coefficient is obtained by inserting the steady-state relation between the intra-cavity and the incident field, as given by Eq. 79, into Eq. 82

$$\Gamma = S_{11} = 1 - \kappa \frac{\frac{\kappa+\gamma}{2} + i\Delta}{\Delta^2 + \left(\frac{\kappa+\gamma}{2}\right)^2} \tag{83}$$

Accordingly, the reflection coefficient is a complex number, which can be represented in the complex plane. If the detuning is sweeped from negative to positive values (or vice versa), the reflection coefficient describes a circle in the case of a linear cavity, and the ratio between the coupling rates can be deduced from its radius, see Fig. 9. For a reflection measurement, the circle can always be scaled and oriented using the off-resonant point $(1, 0)$ [20]. In the case $\kappa > \gamma$, usually referred to as the overcoupled regime [51], the reflection coefficient covers all four quadrants of the complex plane, and the corresponding phase, conventionally measured from the positive real axis, performs a full cycle in the range $[-\pi, \pi]$. With increasing losses, less information is encoded in the phase of the reflection coefficient.

Free energy decay

The free energy decay of the intra-cavity field is described by Eq. 77 for $\Omega = 0$. Assuming that the intra-cavity field has been initialized in an arbitrary coherent

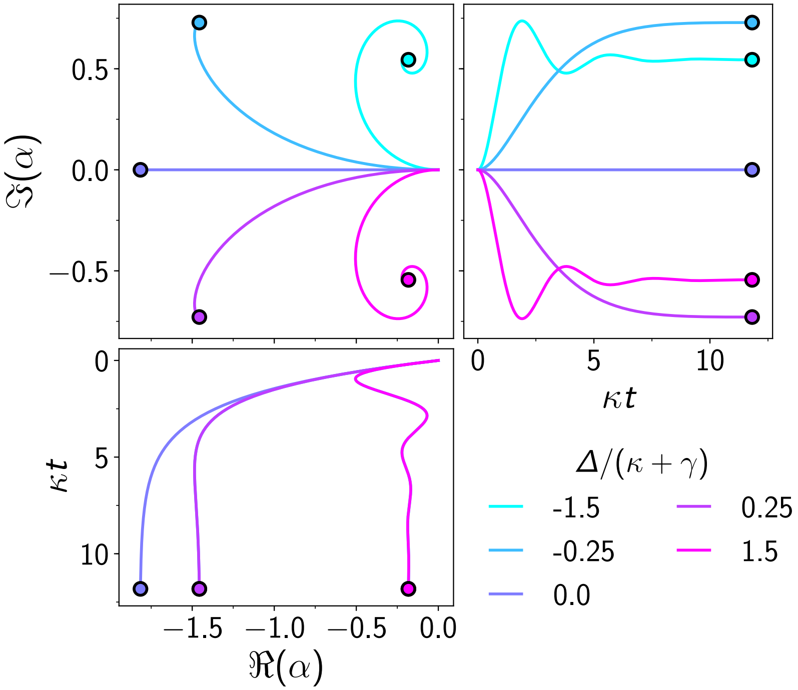

Figure 8: Driven and damped harmonic oscillator: ring-up. Time evolution of the complex expectation value of the intra-cavity field $\alpha = \langle \hat{A} \rangle$ of a harmonic oscillator exposed to a coherent and constant drive, and finite dissipation at a rate $\kappa + \gamma$, calculated according to Eq. 77. The different colors indicate different detunings Δ between the drive frequency ω_p and the resonance frequency ω_0 of the oscillator ($\Delta = \omega_\mathrm{p} - \omega_0$). The constant effective drive strength is $\Omega = 2\sqrt{\kappa}\beta_\mathrm{in}$, which is a combination of the average incident field amplitude β_in, and the coupling rate κ between the input port and the harmonic oscillator. In the presented case, the effective drive strength is $\Omega = 2\kappa$, and the ratio of the coupling rates is $\gamma/\kappa = 0.1$. Depending on the detuning, the intra-cavity field reaches a different steady-state, and follows different trajectories in the optical phase space (top left panel). The corresponding time evolution of the real and imaginary part, the quadratures, is shown in the bottom and right-hand panel. Notably, while the characteristic time scale for the intra-cavity field to reach its steady-state is given by $\sim 1/\kappa$, the drive strength ϵ and the loss rate γ influence the steady-state amplitude only, but not the qualitative shape of the trajectory. The uncertainty of the trajectory and the steady state due to quantum fluctuations is not shown.

state α_0 by the application of a drive, at time $t = 0$, the drive is turned off and the intra-cavity field evolves freely according to the quantum Langevin equation given in Eq. 76. The temperature of the baths in the ports is zero, and the effect of quantum

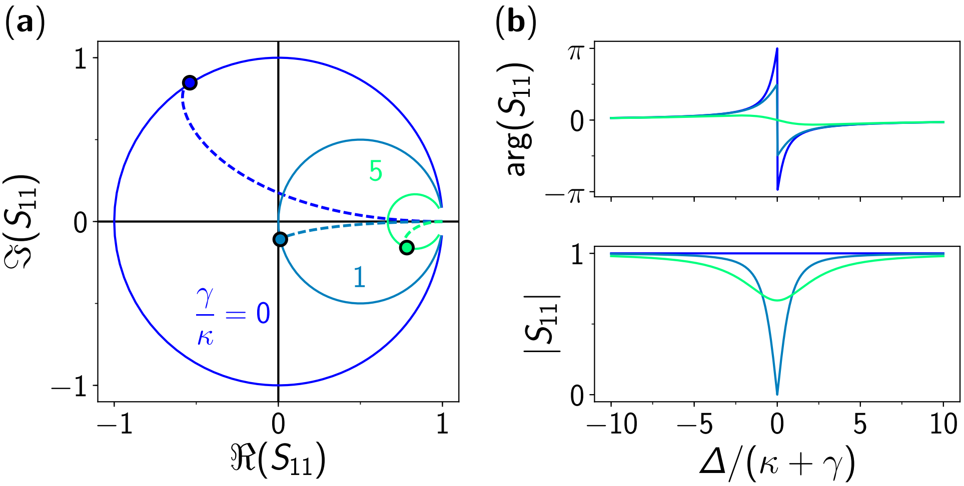

Figure 9: Harmonic oscillator: reflection coefficient. Complex reflection coefficient $\Gamma = S_{11}$ as obtained for a harmonic oscillator in its steady-state, calculated for three different ratios between the external and internal coupling rates κ and γ, respectively. The dashed lines indicate the time evolution of the reflection coefficient for three arbitrarily chosen detunings $\Delta = \omega_\mathrm{p} - \omega_0$, and the round markers represent the corresponding steady-state. By changing the detuning Δ, the reflection coefficient follows a circle in the complex plane. Depending on the ratio between external and internal coupling, the circle covers different quadrants. In general, the ratio κ/γ is encoded in the radius of the circle. The magnitude of the coupling rates is deduced from the frequency dependence of the phase $\arg(S_{11})$ and amplitude $|S_{11}|$, shown in the right-hand panels. Conventionally, the phase is measured from the positive real axis. If $\kappa\rangle\gamma$, the change in phase covers the full range $[-\pi, \pi]$, while it is $[-\pi, \pi]$ for $\kappa \leq \gamma$. Cavities of the first category are denoted overcoupled, while the others are denoted undercoupled. The special case $\kappa = \gamma$ is refered to as critical coupling, for which all incident power is absorbed in the oscillator, as indicated by the amplitude signal.

fluctuations is neglected. The solution for the intra-cavity field amplitude in a frame rotating at a frequency ω_p is of the form

$$\alpha(t) = \alpha_0 e^{-\Delta t} e^{-\frac{\kappa+\gamma}{2}t}, \tag{84}$$

where the second factor describes the oscillation of the field's phase at a frequency determined by the detuning Δ between the frequency of the rotating frame and the resonance frequency of the cavity, and the third factor describes the exponential decay of the field amplitude over time. The characteristic time scale of the exponential decay is $2/(\kappa+\gamma)$. The energy stored inside the cavity is proportional to the mean number of photons $\bar{n} = |\alpha|^2$, and the respective time evolution is

$$\bar{n}(t) = n_0 e^{-(\kappa+\gamma)t}. \tag{85}$$

Therefore, while the field amplitude decays at a rate $(\kappa+\gamma)/2$, the charactersitic time scale for the exponential energy decay is $T_1 = 1/(\kappa+\gamma)$.

Outgoing power

The power in the reflected outgoing mode is

$$P_{\mathrm{out}} = \hbar\omega \left\langle \hat{B}^{\dagger}_{\mathrm{out}} \hat{B}_{\mathrm{out}} \right\rangle , \tag{86}$$

where ω is the drive frequency, and, according to the input-output relation, is a combination of two parts: the incident field directly reflected from the cavity, and the power emitted by the cavity. In the limit of a strong drive, the contribution of the quantum fluctuations are negligible, and the power is determined by the classical field amplitudes

$$P_{\mathrm{out}} \approx \hbar\omega |\beta_{\mathrm{out}}|^2 \tag{87}$$

Using the input-output relation of the classical part given in Eq. 80 and the relation between the intra-cavity field and the incident field accodring to Eq. 79, yields an expression that relates the outgoing power to the incident power

$$\begin{aligned} |\beta_{\mathrm{out}}|^2 &= \left(1 + \kappa|g|^2 + \sqrt{\kappa}(g^\star + g)\right) |\beta_{\mathrm{in}}|^2 \\ &= \left(1 - \frac{\kappa\gamma}{\Delta^2 + \left(\frac{\kappa+\gamma}{2}\right)^2}\right) |\beta_{\mathrm{in}}|^2 \end{aligned} , \tag{88}$$

or to the average number of photons inside the cavity $\bar{n} = |\alpha|^2$

$$|\beta_{\mathrm{out}}|^2 = \left(\frac{\Delta^2 + \left(\frac{\kappa+\gamma}{2}\right)^2 - \gamma\kappa}{\kappa}\right) \bar{n}. \tag{89}$$

Both results show, that if the coupling rates to both ports are identical $\kappa = \gamma$, referred to as a critically coupled cavity in electrical engineering, the outgoing power is zero on resonance $\Delta = 0$. Another rather surprising result is obtained in the limit $\kappa \gg \gamma$, or equivalently $\gamma \to 0$, in which the coupling to the second port is negligible. The outgoing power, again evaluated on resonance ($\Delta = 0$), is

$$P_{\mathrm{out}} \underset{\gamma\to 0}{=} \hbar\omega_0 \frac{\kappa}{4} \bar{n}, \tag{90}$$

which means that, due to the interference between the incident fields arriving at the cavity's input port and the intra-cavity fields leaking out, the observed decay rate in the driven case is $\kappa/4$ instead of κ for the undriven case. This result is crucial for thecalibration of of the measurement efficiency of the experimental setup (see Sec. 3.8).

B.3 The damped and driven anharmonic oscillator

The following sections are an extention of Sec. 1.3.4 and discuss the behavior of a weakly anharmonic oscillator in the limit $\kappa \gg K$, representative for the degenerate Josephson parametric amplifier (JPA).

The EOM for the intra-cavity field of the denegerate JPA is

$$\dot{\hat{A}} = -i\omega_0\hat{A} - iK\hat{A}^\dagger\hat{A}\hat{A} - \frac{\kappa}{2}\hat{A} - \frac{\gamma}{2}\hat{A} - \sqrt{\kappa}\hat{B}_{\mathrm{in}} - \sqrt{\gamma}\hat{c}_{\mathrm{in}}, \tag{91}$$

where $\hat{B}_{\mathrm{in}}(t)$ and $\hat{c}_{\mathrm{in}}$ are the incident signals through the input port and the artificial loss port, respectively. Similar to the quantum harmonic oscillator, there is a boundary condition relating the intra-cavity field with the incident and outgoing fields:

$$\hat{B}_{\mathrm{out}}(t) = \hat{B}_{\mathrm{in}} + \sqrt{\kappa}\hat{A}, \tag{92}$$

and

$$\hat{c}_{\mathrm{out}}(t) = \hat{c}_{\mathrm{in}} + \sqrt{\gamma}\hat{A}. \tag{93}$$

The two rates γ and κ reflect the strength of the coupling between the ports and the JPA, and determine how fast an incident field can drive the intra-cavity field, and, once excited, how fast the intra-cavity field decays into the ports spontaneously. Surprisingly, in the case of a driven cavity measured in reflection, the observed intra-cavity field decay is slower compared to the free decay (see Eq. 90) [22].

For the operation of the system as an amplifier, the energy required to amplify the quantum signal is provided by a strong drive tone, denoted the pump. Since the amplitude of the pump tone is orders of magnitude larger compared to that of the signal, it is treated classically and described by a coherent state with constant amplitude and phase, while the signal is treated quantum mechanically. In the spirit of this distinction, the incident, the outgoing and the intra-cavity fields are decomposed into a classical and a quantum part:

$$\hat{B}_{\mathrm{in}}(t) = \left(\hat{b}_{\mathrm{in}}(t) + \beta_{\mathrm{in}}\right)^{-i\omega_{\mathrm{p}}t}, \tag{94}$$

$$\hat{B}_{\mathrm{out}}(t) = \left(\hat{b}_{\mathrm{out}}(t) + \beta_{\mathrm{out}}\right)^{-i\omega_{\mathrm{p}}t}, \tag{95}$$

$$\hat{A}(t) = \left(\hat{a}(t) + \alpha\right)^{-i\omega_{\mathrm{p}}t}. \tag{96}$$

Accordingly, the classical parts are represented by Greek letters, and the quantum signals are given in Latin letters, with the hat indicating their quantum nature. The time evolution is harmonic and determined by the frequency of the pump ω_{p}, which is equivalent to a frame rotating at the pump frequency. The modes of the loss port are not decomposed, but are treated solely quantum mechanically. This is a valid assumption provided the bath is cold $k_B T_{\mathrm{bath}} \ll \hbar\omega_0$, with the only virtue of the bath being the absorption of excitations from the system, without exciting it.

In order to derive expressions for the amplification of the device as a function of the pump parameters, the pump amplitude and the pump frequency, first, the classical steady state of the cavity is derived, and from that, the reflection of the quantum signal is treated perturbatively.

Classical steady-state:

The steady state of the classical intra-cavity field α, satisfying the condition $\dot{\alpha} = 0$, is calculated by inserting Eq. 94-96 into the EOM defined in Eq. 91, and keeping the classical terms only.

$$i(\omega_0 - \omega_{\mathrm{p}})\alpha + \frac{\kappa + \gamma}{2}\alpha + iK\alpha^\star\alpha^2 = \sqrt{\kappa}\beta_{\mathrm{in}} \tag{97}$$

Notably, the drive amplitude β_{in} and the intra-cavity field amplitude α do not have the same units. By multiplying both sides of the equation with its complex conjugate yields:

$$(\omega_0 - \omega_{\mathrm{p}})^2 + \left(\frac{\kappa + \gamma}{2}\right)^2 |\alpha|^2 + 2K(\omega_0 - \omega_{\mathrm{p}})|\alpha|^4 + K^2|\alpha|^6 = \kappa|\beta_{\mathrm{in}}|^2. \tag{98}$$

For a coherent state, the complex amplitude is proportional to the mean number of photons, in particular $\beta_{\mathrm{in}} = \sqrt{\bar{n}_{\mathrm{in}}}$ and $\alpha = \sqrt{\bar{n}}$. Therefore, the deduced equation relates the mean number of incident photons with the mean number of photons stored in the cavity. Following the procedure of Eichler and Wallraff [15], Eq. 98 can be expressed in scale invariant quantities:

$$\left(\delta^2 + \frac{1}{4}\right)\bar{n} - 2\delta\xi\bar{n}^2 + \xi^2\bar{n}^3 = 1, \tag{99}$$

where

$$\delta = \frac{\omega_{\mathrm{p}} - \omega_0}{\kappa + \gamma}, \qquad \bar{n} = \frac{|\alpha|^2}{|\tilde{\beta}_{\mathrm{in}}|^2}, \qquad \tilde{\beta}_{\mathrm{in}} = \frac{\sqrt{\kappa}\beta_{\mathrm{in}}}{\kappa + \gamma}, \qquad \xi = \frac{K|\tilde{\beta}_{\mathrm{in}}|^2}{\kappa + \gamma}. \tag{100}$$

The first quantity δ is the frequency detuning between the pump and the bare resonance frequency of the cavity, scaled by the total cavity linewidth $\kappa + \gamma$. The second quantity $\bar{n}$ represents the mean number of photons inside the cavity relative to the incident pump power, which is defined via the dimensionless drive amplitude $\tilde{\beta}_{\mathrm{in}}$. Finally, the effective drive strength χ is determined by the product of pump power and nonlinearity.

By inserting the boundary condition for the classical pump applied through the input port, $\beta_{\mathrm{out}} = \beta_{\mathrm{in}} + \sqrt{\kappa}\alpha$, the reflection coefficient becomes:

$$S_{11} = 1 - \frac{\kappa}{\kappa+\gamma}\frac{1}{\frac{1}{2} - i\delta + i\xi\bar{n}}, \tag{101}$$

which is Eq. 101 in the main text.

Power gain:

The power gain of the single-port JPA is calculated by inserting the expression for the field amplitudes, given in Eqs. 94-96, into Eq. 91, the EOM of the intra-cavity field amplitude, and keeping terms only, that are linear in the quantum part $\hat{a}(t)$.

The corresponding quantum Langevin equation describing the time evolution of the quantum part is

$$\dot{\hat{a}}(t) = i(\omega_{\mathrm{p}} - \omega_0 - 2K|\alpha|^2 + i\frac{\kappa+\gamma}{2})\hat{a}(t) - iK\alpha^2\hat{a}^\dagger(t) + \sqrt{\kappa}\hat{B}_{\mathrm{in}}. \tag{102}$$

Although the time evolution of the intra-cavity field is of interest if the device is operated with microwave pulses, first, a better understanding of the behavior of the steady state in the frequency domain is particularly helpful. Since the EOM of the quantum part of the intra-cavity field is linear in $\hat{a}(t)$, it can be solved by decomposing the signal into its Fourier-components [15]:

$$\hat{a}(t) = \sqrt{\frac{\kappa+\gamma}{2\pi}}\int_{-\infty}^{\infty} \mathrm{d}\Delta e^{-i\Delta(\kappa+\gamma)t}\hat{a}_\Delta. \tag{103}$$

Here $\Delta = (\omega_{\mathrm{s}} - \omega_{\mathrm{p}})/(\kappa+\gamma)$ is the dimensionless detuning between the pump frequency ω_{p}, and the frequency of the weak quantum signal ω_{s}. Equivalent expressions are found for the quantum parts of the field amplitudes of the incident modes $\hat{b}_{\mathrm{in}}$ and $\hat{c}_{\mathrm{in}}$. Furthermore, the amplitude of the classical part can be expressed in terms of the mean number of photons inside the cavity $\bar{n}$, defined by Eq. 99, and the pump phase ϕ_{p}: $\alpha = \sqrt{\bar{n}}e^{i\phi_{\mathrm{p}}}$. Hence, the steady state of the quantum part is determined by

$$0 = \left(i(\delta - 2\xi\bar{n} + \Delta) - \frac{1}{2}\right)\hat{a}_\Delta - i\xi\bar{n}e^{2i\phi_{\mathrm{p}}}\hat{a}^\dagger_{-\Delta} + \frac{\sqrt{\kappa}}{\kappa+\gamma}\hat{b}_{\mathrm{in},\Delta} + \frac{\sqrt{\gamma}}{\kappa+\gamma}\hat{c}_{\mathrm{in},\Delta}. \tag{104}$$

Apparently, due to the nonlinearity of the cavity, contributions of the intra-cavity field symmetrically detuned from the pump frequency, with detunings Δ and $-\Delta$, are mixed. The complete relation between the incident and the intra-cavity field is most conveniently formulated in a matrix representation of Eq. 104 and its complex conjugate.

$$\begin{pmatrix} \hat{d}_{\mathrm{in},\Delta} \\ \hat{d}^{\dagger}_{\mathrm{in},-\Delta} \end{pmatrix} = \begin{pmatrix} i(-\delta + 2\xi\bar{n} - \Delta) + \frac{1}{2} & i\xi\bar{n}e^{-i2\phi_\mathrm{p}} \\ -i\xi\bar{n}e^{-2i\phi_\mathrm{p}} & i(\delta - 2\xi\bar{n} - \Delta) + \frac{1}{2} \end{pmatrix} \begin{pmatrix} \hat{a}_{\Delta} \\ \hat{a}^{\dagger}_{-\Delta} \end{pmatrix} \tag{105}$$

Here, the operator $\hat{d}_{\mathrm{in},\Delta} = (\sqrt{\kappa}\hat{b}_{\mathrm{in},\Delta} + \sqrt{\gamma}\hat{c}_{\mathrm{in},\Delta})/(\kappa + \gamma)$ summarizes the modes incident to the cavity. Inverting the matrix yields the relation between the intra-cavity field amplitudes and the new operators $\hat{d}_{\mathrm{in},\Delta}$ introduced for the incident modes

$$\hat{a}_{\Delta} = \frac{i(\delta - 2\xi\bar{n} - \Delta) + \frac{1}{2}}{(i\Delta - \lambda_-)(i\Delta - \lambda_+)}\hat{d}_{\mathrm{in},\Delta} + \frac{-i\xi\bar{n}e^{2i\phi_\mathrm{p}}}{(i\Delta - \lambda_-)(i\Delta - \lambda_+)}\hat{d}^{\dagger}_{\mathrm{in},-\Delta}, \tag{106}$$

where the terms in the denominator are defined as

$$\lambda_{\pm} = \frac{1}{2} \pm \sqrt{(\xi\bar{n})^2 - (\delta - 2\xi\bar{n})^2}. \tag{107}$$

With the aid of the input-output boundary conditions which are defined in Eq. 92 and Eq. 93, a compact relation between the outgoing and the incident field amplitudes is found:

$$\hat{b}_{\mathrm{out},\Delta} = g_{\mathrm{s},\Delta}\hat{b}_{\mathrm{in},\Delta} + g_{\mathrm{i},\Delta}\hat{b}^{\dagger}_{\mathrm{in},-\Delta} + \sqrt{\frac{\gamma}{\kappa}}(g_{\mathrm{s},\Delta} + 1)\hat{c}_{\mathrm{in},\Delta} + \sqrt{\frac{\gamma}{\kappa}}g_{\mathrm{i},\Delta}\hat{c}^{\dagger}_{\mathrm{in},-\Delta} \tag{108}$$

Remarkably, the outgoing signal of the pumped nonlinear cavity at a detuning Δ does not only contain amplified contributions of the incident signal at the same detuning, but also from the mirrored contributions at detuning $-\Delta$. Since there are at least quantum fluctuations present at this frequency, these additional contributions are referred to as the idler tone. The coefficients in front of the incident modes determine the magnitude of amplification and are referred to as the signal and the idler gain-factors, $g_{\mathrm{s},\Delta}$ and $g_{\mathrm{i},\Delta}$, respectively.

$$g_{\mathrm{s},\Delta} = -1 + \frac{\kappa}{\kappa + \gamma}\frac{i(\delta - 2\xi\bar{n} - \Delta) + \frac{1}{2}}{(i\Delta - \lambda_-)(i\Delta - \lambda_+)} \tag{109}$$

and

$$g_{\mathrm{i},\Delta} = \frac{\kappa}{\kappa + \gamma}\frac{-i\xi\bar{n}e^{2i\phi_\mathrm{p}}}{(i\Delta - \lambda_-)(i\Delta - \lambda_+)} \tag{110}$$

If the coupling rate to the input port is much larger than the coupling to the artificial loss port ($\kappa \gg \gamma$), the gain factors satisfy

$$G_{\Delta} = |g_{\mathrm{s},\Delta}|^2 = |g_{\mathrm{i},\Delta}|^2 + 1, \tag{111}$$

where G_{Δ} is the power gain of the amplifier at the signal frequency detuning. In the high gain limit $|g_{\mathrm{s},\Delta}|^2, |g_{\mathrm{i},\Delta}|^2 \gg 1$, the signal incident at the idler frequency is almost equally amplified as the signal. Since there are always at least quantum fluctuations present at every frequency, the simultaneous amplification of contributions from different frequencies causes the additional noise added by the amplifier. Hence, if the input port is cold ($k_\mathrm{B}T \ll \hbar\omega_\mathrm{s}$), the presented implementation of a parametric amplifier reaches the quantum-limit of added noise.

In analogy to the relation between incident and intra-cavity field amplitudes, there is a simple matrix representation summarizing the relation between incident and outgoing signals:

$$\begin{pmatrix} \hat{b}_{\mathrm{out},\Delta} \\ \hat{b}^{\dagger}_{\mathrm{out},-\Delta} \end{pmatrix} = \begin{pmatrix} g_{\mathrm{s},\Delta} & g_{\mathrm{i},\Delta} \\ g^{\star}_{\mathrm{i},-\Delta} & g^{\star}_{\mathrm{s},-\Delta} \end{pmatrix} \begin{pmatrix} \hat{b}_{\mathrm{in},\Delta} \\ \hat{b}^{\dagger}_{\mathrm{in},-\Delta} \end{pmatrix} \tag{112}$$

Saturation power:

The power gain offered by any type of linear amplifier existing is generally limited to a certain range of incident signal power, referred to as the dynamic range of the amplifier, above which the gain either starts to decrease, or the relation between incident and outgoing signal becomes nonlinear. In the first case, due to the compensation of increasing input signal power and decreasing power gain, the signal output power approaches a maximal value and therefore saturates. While the origin of power gain saturation depends on the amplifier's physical implementation, for Josephson parametric amplifiers there are two mechanism suspected to cause the onset of saturation: pump depletion and a signal induced ac Stark shift of the cavity frequency, as discussed in the main text.

For the derivation of the power gain in the previous section, the strength of the pump tone was assumed to be constant, or stiff, as the theory experts say. Provided the incident signal is weak, the amount of pump photons converted into signal photons is negligible compared to the total number of pump photons inside the cavity. However, with increasing signal power, a siginificant number of pump photons is required to generate the output signal, and consequently, the pump tone is depleted. The reduction of the effective pump strength due to the conversion process, and with that, the reduction in power gain is referred to as pump depletion [54]. Another mechanism, which is suspected to be the dominant source of saturation, is the signal induced frequency shift of the cavity frequency [40]. As discussed in the main text, for every pump power below the point of bifurcation, there is an optimal pump frequency at which the observed power gain is maximal. In the presence of a quartic term ($\propto \hat{\Phi}^4$), the resonance frequency depends on the mean number of photons inside the cavity, and for that reason, the optimal pump frequency shifts to lower values with increasing pump power, as shown in Fig. 1.24a. If the signal power increases, the amplifier is shifted away from the ideal pumping condition, and the power gain decreases without an adjustment of the pump parameters.

Both effects are included into the discussion by considering additional terms for the calculation of the mean number of pump photons inside the cavity $\bar{n}$ that are nonlinear in the signal amplitude $\hat{a}$. As discussed in Ref. [15] and Ref. [48], the next higher order terms taken into account are $2iK\left\langle \hat{a}^\dagger \hat{a}\right\rangle \alpha$ and $iK\left\langle \hat{a}^2\right\rangle \alpha^\star$, which are added to Eq. 97. Consequently, the previously rather slim equation determining the mean number of pump photons becomes considerably more extensive:

$$\bar{n}\left[\delta^2+\frac{1}{4}-3\xi_{\hat{a}}\delta+5\xi_{\hat{a}}^2+2\xi_{\hat{a}}^3\right]+\bar{n}^2\left(-2\delta\xi+5\xi\xi_{\hat{a}}\right)+\bar{n}^3\xi^3. \tag{113}$$

The effective drive strength due to the signal photons is captured by $\xi_{\hat{a}}=K\bar{n}_{\hat{a}}/(\kappa+\gamma)$, where $\bar{n}_{\hat{a}}=\langle\hat{a}_\Delta^\dagger\hat{a}_\Delta\rangle+\langle\hat{a}_{-\Delta}^\dagger\hat{a}_{-\Delta}\rangle$ is the mean number of photons inside the cavity, evaluated at the signal (Δ) and the idler ($-\Delta$) frequency. Notably, the effect of the relative phase between pump tone and signal is neglected, synonymous to the assumption that the frequency detuning between pump and signal is (significantly) larger than the intermediate frequency (IF) bandwidth of the measurement setup [48]. The intra-cavity signal photons $\hat{a}_\Delta$ and $\hat{a}_{-\Delta}$ are related to the input field amplitude and the mean number of pump photons according to Eq. 106. However, since the latter depends in turn on the mean number of signal photons, the steady state has to be calculated self-consistently.

In order to calculate the saturation effect with increasing signal power P_s, first the intra-cavity field is calculated according to Eq. 106 for the number of pump photons calculated from Eq. 99 under the optimal pump conditions (ξ,δ), but without considering the signal-induced ac Stark shift. The effective signal input field amplitude is determined by the incident signal power $|\tilde{b}_\mathrm{in}|^2=\kappa P_\mathrm{s}/(\hbar\omega_\mathrm{s}[\kappa+\gamma]^2)$, while the input at the idler frequency is assumed to be zero. Notably, the discussed treatment does not include the effect of quantum fluctuations, which are present at all frequencies. For amplifiers with large saturation power, this simplification introduces minor deviations from the actual situation only. The obtained solutions for the intra-cavity fields $\hat{a}_\Delta$ and $\hat{a}_-\Delta$ are plugged in into Eq. 113, and in turn, the corrected mean number of pump photons $\bar{n}$ is used to calculate the corrected intra-cavity fields. This procedure has to be repeated several times for the result to converge. After the final iteration, the obtained results are used to calculate the power gain $G_0(P_\mathrm{s})$ as a function of the signal power shown in Fig. 1.25.

C grAl transmon: supplementary information

In the following sections, additional information on the grAl transmon discussed in Ch. 2 in the main text are given, including derivations of mathematical formulas used to extract information from measurements, finite-element method simulations of the waveguide sample holder and the grAl transmon circuit design, as well as details on the measurement setup and the operation of the 2D vector magnet. Similar information is provided in the supplementary information found in Ref. [65].

C.1 Resonance fluorescence: reflection coefficient

The reflection coefficient of a qubit given in Eq. 2.7 used to fit the resonance fluorescence spectroscopy measurements (see Fig. 2.2), is derived starting from Eq. 2.5 and following the description in Ref. [9].

First, the expectation value of the lowering operator of the qubit is expressed using the Pauli operators σ_x and σ_y:

$$\langle\hat{\sigma}_-\rangle = (\langle\hat{\sigma}_x\rangle - i\,\langle\hat{\sigma}_y\rangle)/2. \tag{114}$$

The steady state expectation values (time $t \to \infty$) for the Pauli operators $\hat{\sigma}_x, \hat{\sigma}_y, \hat{\sigma}_z$ for a qubit exposed to a continuous drive with amplitude Ω and detuning $\Delta_\mathrm{q} = \omega_\mathrm{q} - \omega$ to the qubit frequency ω_q, and in the presence of energy relaxation at a rate Γ_1 and dephasing at a rate $\Gamma_2^* = \Gamma_1/2 + \Gamma_\varphi$, ($\Gamma_\varphi$: pure dephasing rate) are given by [9]:

$$\langle\hat{\sigma}_x(\Omega,\Delta_\mathrm{q})\rangle = \Gamma_1\Gamma_2^*\Omega\left(\Gamma_1(\Gamma_2^{*2}+\Delta_\mathrm{q}^2)+\Gamma_2^*\Omega^2\right)^{-1} \tag{115}$$

$$\langle\hat{\sigma}_y(\Omega,\Delta_\mathrm{q})\rangle = \Gamma_1\Delta_\mathrm{q}\Omega\left(\Gamma_1(\Gamma_2^{*2}+\Delta_\mathrm{q}^2)+\Gamma_2^*\Omega^2\right)^{-1} \tag{116}$$

$$\langle\hat{\sigma}_z(\Omega,\Delta_\mathrm{q})\rangle = -1+\Gamma_2^*\Omega^2\left(\Gamma_1(\Gamma_2^{*2}+\Delta_\mathrm{q}^2)+\Gamma_2^*\Omega^2\right)^{-1} \tag{117}$$

Using Eq. 115 and Eq. 116, the expectation value of the Pauli lowering operator becomes

$$\langle\hat{\sigma}_-\rangle = \frac{1}{2}\frac{\Gamma_1\Gamma_2^*\Omega - i\Gamma_1\Delta_\mathrm{q}\Omega}{\Gamma_1\left(\Gamma_2^{*2}+\Delta_\mathrm{q}^2\right)+\Gamma_2^*\Omega^2}. \tag{118}$$

By inserting Eq. 118 into the expression for the reflection coefficient given in Eq. 2.5, yields

$$S_{11}(\Delta_\mathrm{q}) = 1 - \frac{\sqrt{\kappa}\Omega_\mathrm{R}}{2\beta_\mathrm{in}}\frac{\Gamma_1\Gamma_2^* - i\Gamma_1\Delta_\mathrm{q}}{\Gamma_1(\Gamma_2^{*2}+\Delta_\mathrm{q}^2)+\Gamma_2^*\Omega_\mathrm{R}}, \tag{119}$$

where $\Omega_\mathrm{R} = \Omega$ is the Rabi frequency on resonance. As discussed in Sec. 1.1.4, the generalized Rabi frequency is equal to the drive amplitude Ω only on resonance, but depends on the detuning between drive and qubit frequency. Although the detuning is swept during the spectroscopy measurement shown in Fig. 2.2, the value extracted from the fits and entering the expression for the reflection coefficient is the Rabi frequency on resonance, i.e. the drive amplitude.

The relation between the Rabi frequency Ω_R and the expectation value of the bosonic field amplitude $\langle B_\mathrm{in}\rangle = \beta_\mathrm{in}$ is

$$\Omega_\mathrm{R} = 2\sqrt{\kappa}\,\langle B_\mathrm{in}\rangle = 2\sqrt{\kappa}\beta_\mathrm{in}. \tag{120}$$

In the limit of negligible pure dephasing $\Gamma_\varphi \ll \Gamma_1$, and using Eq. 120, the reflection coefficient simplifies to

$$S_{11}(\Delta_\mathrm{q}) = 1 - \frac{2\kappa}{\Gamma_1}\frac{1 + i2\Delta_\mathrm{q}/\Gamma_1}{1 + (2\Delta_\mathrm{q}/\Gamma_1)^2 + 2(\Omega_\mathrm{R}/\Gamma_1)^2}, \tag{121}$$

which is Eq. 2.7 in the main text. The factor in front of the second term of Eq. 121 is the coupling efficiency κ/Γ_1, with $\Gamma_1 = \kappa + \gamma$. It is a measure of the relative size of the internal loss rate γ compared to the external coupling rate κ. At low Rabi frequencies, for which mainly the two lowest energy levels are populated and the qubit response closely resembles a circle, the qubit is found in the overcoupled regime for $\kappa > \gamma$ and in the undercoupled regime for $\kappa < \gamma$, similar to the harmonic oscillator (see Fig. 9).

C.2 Numerical calculation of the Kerr Hamiltonian

The observed frequency and power dependence of the grAl transmon reflection coefficient, shown in Fig. 2.6 and Fig. 2.7, is simulated using a Kerr Hamiltonian exposed to a coherent microwave drive. In the rotating frame of the coherent drive, the Hamiltonian is

$$H_\mathrm{Kerr}/\hbar = \Delta_1 a^\dagger a - \frac{K}{2}a^{\dagger 2}a^2 - \frac{\Omega}{2}(a^\dagger + a), \tag{122}$$

where $\Delta_1 = \omega_1 - \omega$ is the detuning between the fundamental transition frequency ω_1 and the drive tone frequency ω, $a^\dagger$ and a are the bosonic single-mode field amplitude creation and annihilation operators of the intra-cavity field, respectively, and Ω is the drive amplitude. The self-Kerr coefficient is $K = 2\pi \times 4.5\,\mathrm{MHz}$, based on the value obtained in the experiment.

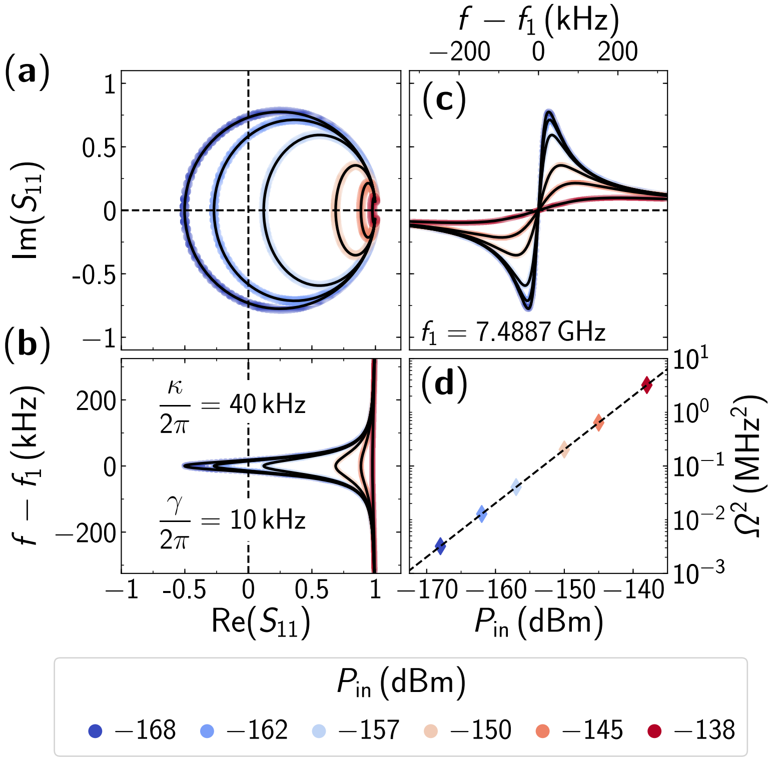

Figure 10: Numerical calculations: resonance fluorescence. Complex reflection coefficient S_{11} plotted in the complex plane **(a)**, together with the frequency dependence of the real part **(b)** and the imaginary part **(c)**, numerically calculated for varying probe frequencies f around the resonance frequency $f_1 = 7.4887\,\text{GHz}$ of the driven Kerr Hamiltonian (see Eq. 122). For comparison reasons, the input drive power P_{in}, the Kerr-coefficient $K = 2\pi \times 4.5\,\text{MHz}$, and the decay rates $\gamma = 2\pi \times 10\,\text{kHz}$ and $\kappa = 2\pi \times 40\,\text{kHz}$, are set to coincide with the experimenal values (see Fig. 2.2). The black lines indicate least-square fits using Eq. 2.7. The only fit parameter is the Rabi-frequency Ω_R reported in d. The linear dependence of the Rabi frequency with drive amplitude and the quantitative agreement with the measured data shown in Fig. 2.2d confirm the validity of the qubit limit and enables the calibration of the input line attenuation $A = 103\,\text{dB}$.

In analogy to the reflection coefficient of the harmonic oscillator defined in Eq. 82, the reflection coefficient of an anharmonic oscillator is [6, 21]

$$S_{11} = 1 + \sqrt{\kappa}\frac{\langle a \rangle}{\beta_{\text{in}}}. \tag{123}$$

The expectation values of the intra-cavity field $\langle a \rangle$ are calculated as a function of the drive detuning Δ_1 and amplitude Ω, by solving the corresponding master equation numerically using Qutip [33, 34]. Notably, in order to align the simulation results

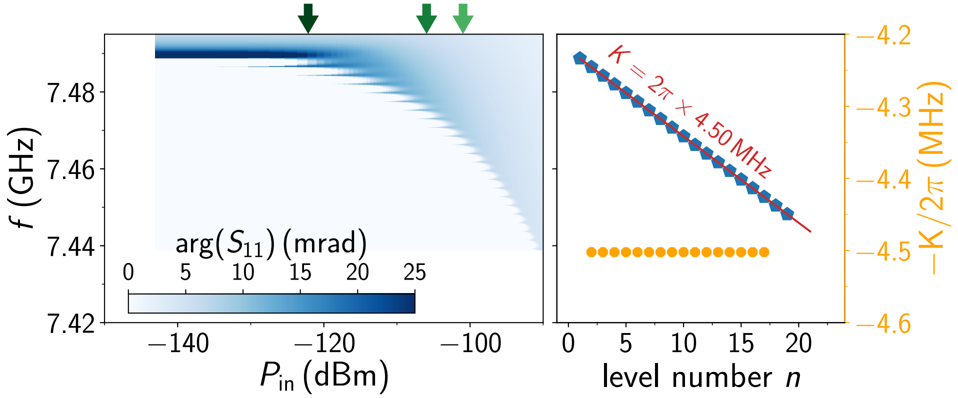

Figure 11: Numerical calculations: energy spectrum. Phase of the numerically calculated reflection coefficient $\arg(S_{11})$ as a function of probe frequency f and probe power P_{in} (left panel), reproducing the measurement results shown in Fig. 2.6. The multi-photon peaks are equally spaced in frequency, with the difference given by $K/2 = 2\pi \times 2.25\,\mathrm{MHz}$ (right-hand panel). In contrast to the experiment, a constant frequency shift K is obtained (orange markers, right hand panel), as expected, because the Kerr Hamiltonian in Eq. 122 only contains terms up to the 4th order. The green markers indicate the probe power values at which the individual traces shown in Fig. 12 are taken.

with the measurements and the analytical reflection coefficient of a qubit in EQ. 119, an additional phase factor $e^{-i\pi/2}$ has to be introduced for the calculated expectation value of the intra-cavity field.

The master equation in Lindblad form in the presence of energy relaxation at a rate Γ_1 is [39]

$$\dot{\rho}_{\mathrm{s}}(t) = -\frac{i}{\hbar}[H_{\mathrm{Kerr}}, \rho_{\mathrm{s}}(t)] + \Gamma_1 \mathcal{D}[a](\rho_{\mathrm{s}}(t)). \tag{124}$$

Here, ρ_{s} is the system's density matrix, H_{Kerr} is the driven Kerr Hamiltonian given in Eq. 122, and $\mathcal{D}[a](\rho)$ is the Lindblad superoperator introducing single-photon dissipation

$$\mathcal{D}[a](\rho_{\mathrm{s}}) = a\rho_{\mathrm{s}}a^{\dagger} - \frac{1}{2}a^{\dagger}a\rho_{\mathrm{s}} - \frac{1}{2}\rho_{\mathrm{s}}a^{\dagger}a. \tag{125}$$

In general, the master equation formalism describes the time evolution of an open quantum system interacting with its environment. The continuously driven system will reach a steady-state for $t \to \infty$, from which the spectroscopy results can be obtained.

For the numerical calculations, the internal and external decay rates $\gamma = 2\pi \times 10\,\mathrm{kHz}$ and $\kappa = 2\pi \times 40\,\mathrm{kHz}$, respectively, are set to the values obtained from the experiment (see Fig. 2.2), constituting a total energy relaxation rate $\Gamma_1 = \kappa + \gamma = 2\pi \times 50\,\mathrm{kHz}$. The

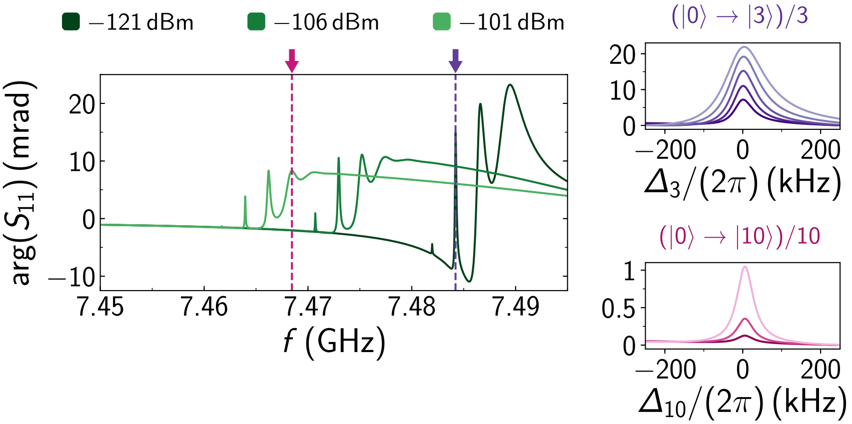

Figure 12: Numerical calculations: energy spectrum. Three individual traces (left-hand panel) calculated at distinct drive powers ($P_{\text{probe}} = -121, -106$ and -101 dBm). Similar to the experimental results shown in Fig. 2.7, several multi-photon transitions are visible at any given drive power in this range. With increasing power, the linewidth of the transitions broadens as depicted by the zoom-ins (right-hand panels) around the 3rd (right, $P_{\text{probe}} = -127$ to -123 dBm) and 10th (left, $P_{\text{probe}} = -105.75$ to -104.75 dBm) multi-photon transition. For a better comparison to the measured data, the phase-offset is removed. Again $\Delta_n = \omega - \omega_n$ is the detuning between the drive and the transition frequency of the n th multi-photon transition. Notably, the sign for Δ_n is different than the sign of the effective transition frequency in the driven Kerr Hamiltonian (see Eq. 122) to ensure that drive frequencies below the respective transition frequency have a negative detuning.

dimension of the Hilbert space is $N_{\text{level}} = 30$. The drive amplitudes $\Omega = 2\sqrt{\kappa}\beta_{\text{in}}$ are chosen to coincide with the values used in the experiment, with $\beta_{\text{in}} = \sqrt{P_{\text{in}}/(\hbar\omega_1)}$. The power values P_{in} are the calibrated values shown in Fig. 2.2d.

Spectroscopy

Figure 10 depicts the numerically calculated reflection coefficient S_{11} and the corresponding least-square fits using Eq. 2.7. The colors are related to the drive power similarly to Fig. 2.2. The linear fit to the extracted Rabi frequencies shown in Fig. 10d confirms that the two-level approximation is valid in the parameter space of the spectroscopy experiment.

Energy spectrum

The experimental results presented in the main text in Fig. 2.6 and Fig. 2.7 are reproduced in the numerical calculation using the same range of probe frequency and power.

Figure 11 depicts the phase of the reflection coefficient $\arg(S_{11})$ as a function of the incident power P_{in} and probe frequency f. Similar to the experiment, multi-photon transitions at frequencies $f_n = (E_n - E_0)/(nh)$ become visible. From a linear fit to the multi-photon frequencies extracted from the 2D plot using the same algorithm as in the main text (see. Fig. 11 right-hand panel), the self-Kerr coefficient $K = 2\pi \times 4.5\,\text{MHz}$ assumed for the calculation is recovered, validating the procedure. Since the Kerr Hamiltonian in Eq. 122 does not contain higher order nonlinear terms, in contrast with the experimental results, the simulated $K(n)$ is independent of the level number n.

For a comparison to Fig. 2.7 shown in the main text, Fig. 12 shows the phase of the calculated reflection coefficient $\arg(S_{11})$ as a function of the probe frequency f for three drive powers $P_{\text{in}} = -121$, -106 and $-101\,\text{dBm}$. The small qualitative difference between simulation and measurement is to some degree caused by the finite frequency dependence of the background phase response in the experiment, attributable to standing-wave resonances in the cryostat wiring. Moreover, the simulation does not account for a finite offset charge dispersion or other effects that potentially broaden the linewidth of the multi-photon transitions.

C.3 3D waveguide sample holder

The same 3D waveguide sample holder design, composed of a hollow copper body with removable lid shown in Fig. 2.1, was used for the readout of the grAl transmon, as well as for the readout of the cQED experiment shown in Fig. 1.10. The height, length and width of the inner volume is 6 mm, 45 mm and 36 mm, respectively, and the wall thickness of the copper body is 2 mm. To simplify the manufacturing process, the edges of the hollow space are round. Due to the large aspect ratio of the waveguide's cross section, the electrical fields in the center of the waveguide, which are oriented in the y-direction according to the coordinate system used for the coils, remain unaffected by the round edges.

The sample readout is performed using a $50\,\Omega$ coaxial microwave port which couples into the volume of the waveguide via the electrical field. The coaxial cable has a center conductor with a diameter of 0.51 mm and an inner shield diameter of 1.68 mm, incasing a teflon dielectric with relative permittivity $\epsilon_{\text{r}} = 2.1$. For

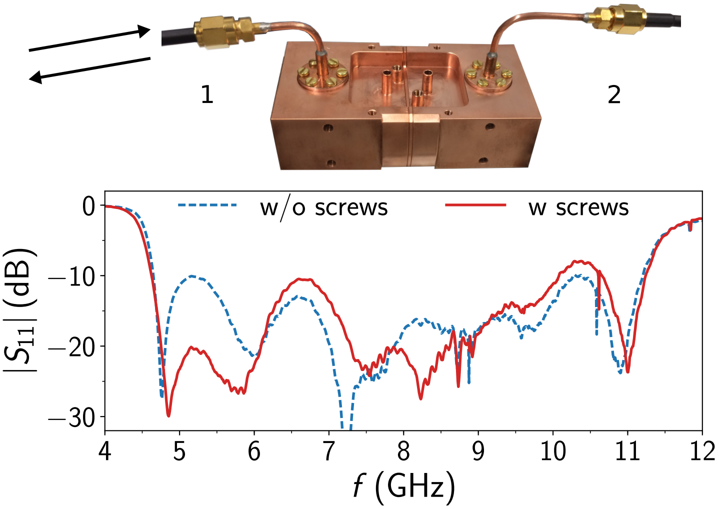

Figure 13: 3D waveguide sample holder. The performance of the microwave ports of two waveguide sample holders can be deduced at room-temperature, by aligning the copper bodies and measuring the reflection coefficient at one port. Since the other port is terminated to 50 Ω, the transmission from one port to the other will appear as losses in the reflection coefficient. Hence, high losses observed in the reflection coefficient are indicative for a good transmission and small internal reflections. As shown in the bottom panel, the observed reflection coefficient is frequency dependent, with a sharp decrease around 4.5 GHz, denoted the cut-off frequency. Due to the adjustment screw incorporated into the bottom of the waveguide (visible in Fig. 2.1), the frequency dependence can be tuned and adapted to the frequency range of the experiment.

impedance transformation, the center conductor ends in a cylinder of radius 2 mm and length 3 mm, with a distance of 1.4 mm to the waveguide ceiling. Additionally, a screw incorporated into the bottom of the waveguide can be used to adjust the impedance matching. At room temperature, the performance of the impedance matching is verified by measuring the reflection coefficient of the input port of one waveguide, when a second waveguide is attached to its body (see Fig. 13).

In the depicted arrangement, signals that couple into the waveguide and are not reflected at the input port, appear as losses in the absolute value of the reflection coefficient $|S_{11}|$. The comparison between the red and the blue curve shows the tunability of the obtained spectrum by changing the position of the screws in both waveguides. After the adjustment was completed for the waveguide used in the experiment, the screws were fixed using silver paste. The band of the waveguide is restricted by a lower cut-off frequency ($\sim$ 4.5 GHz) below which the field is evanescent, and an upper cut-off frequency ($\sim$ 11.5 GHz).

Two copper stubs integrated into the top and bottom of the outer walls, visible in Fig. 13, from which one has a thread, are used to align the Helmholtz coil bodies with the position of the sample.

C.4 FEM simulations

The fundamental transition frequency ω_1 and the external coupling rate κ to the waveguide sample holder are simulated for the circuit geometry (see Fig. 14) using a commercial finite-element method simulator (HFSS - High frequency structure simulator). The inductive contribution of the grAl volume is modeled with a linear lumped-element inductor L_K. Capacitive contributions arising from the grAl microstructure are not considered. In order to extract the shunt capacitance C_s and geometric stray inductance L_s of the grAl transmon circuit design, the transition frequency is simulated for different values of the grAl inductance L_K (see Fig. 15a).

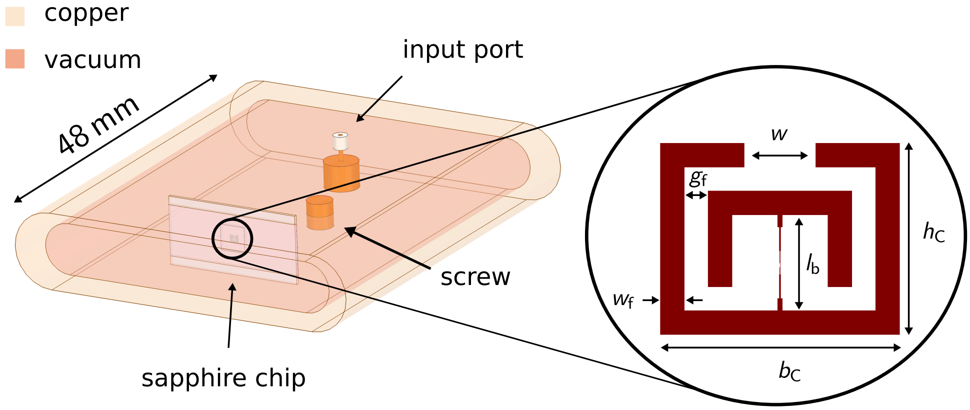

Figure 14: Finite-element method simulation model. For the simulation of the waveguide sample holder and the circuit geometry, the waveguide and the grAl circuit design are translated into effective, three-dimensional models. The waveguide model consists of a copper body (light orange) of similar dimensions as discussed in App. C.3, which is attributed with a perfect conductivity boundary condition and filled with vacuum (light red). The adjustment screw entering through the bottom is considered by a copper rod. The waveguide body hosts a sapphire wafer of thickness 330 μm and relative permittivity $\epsilon_r = 10$ and relative permeability $\mu_r = 1$, on which the circuit is modeled. The capacitor geometry is defined by the width and length of the outer electrode b_C and h_C, respectively, as well as the gap w. The gap between the electrodes is g_f, and the bridge connecting them has a length l_b. The width of the electrode fingers is w_f.

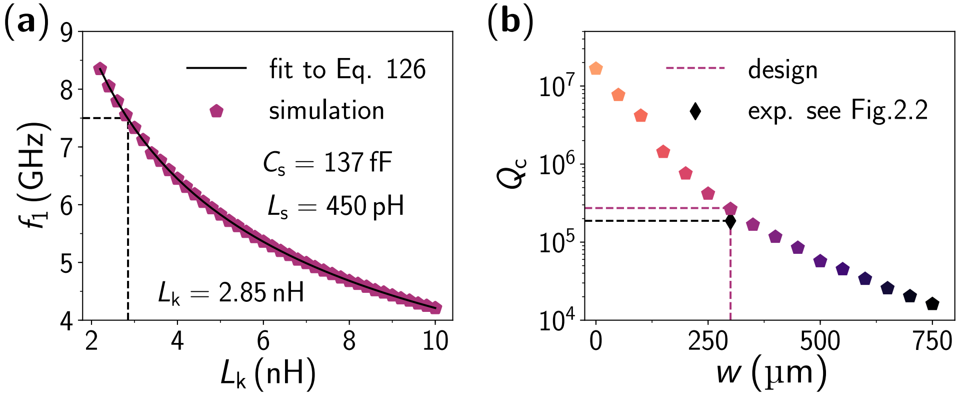

Figure 15: Finite-element method simulations of the linearized circuit. a) Simulated transition frequency f_1 of the linearized circuit obtained using the eigenmode solver of a commercial finite-element method simulator (HFSS), shown in Fig. 14. The grAl volume is substituted with a lumped-element inductance L_k which is swept from 2 nH to 10 nH to extract the shunt capacitance $C_s = 137$ fF and the additional geometric inductance $L_s = 450$ pH arising from the design using Eq. 126. As indicated by the dotted cursors, the measured frequency $f_1 = 7.4887$ GHz corresponds to a value $L_k = 2.85$ nH. **b)** Simulated external quality factor Q_c as a function of the gap w in the outer electrode for $L_k = 2.85$ nH. Similarly to the design of Ref. [53], by closing the gap the external quality factor can be controlled over a range of three orders of magnitude. The colored dashed lines indicate the design value for the experiment and the black marker indicates the measured external quality factor $Q_c = 1.9 \times 10^5$ (see Fig. 2.2).

The physical dimensions of the circuit are listed in Tab. 1. The simulated transition frequencies are fitted to the prediction of an effective lumped-element model

$$f_1(L_K) = \frac{1}{2\pi\sqrt{C_s(L_K + L_s)}}, \tag{126}$$

yielding $C_s = 137$ fF for the shunt capacitance, and $L_s = 450$ pH for the geometric stray inductance (see Fig. 15a).

The external quality factor can be varied over three orders of magnitude by changing the gap w in the outer electrode (see Fig. 2.1b main text and Fig. 15b). Due to the large aspect ratio of the waveguide body, the external quality factor does not change significantly with distance x away from the center of the waveguide as shown in Ref. [65].

Table 1: Geometrical parameters of the grAl transmon design. Width b_C outer capacitor electrode, height h_C outer capacitor electrode, gap in outer electrode w, length of the bridge connecting the capacitor pads l_b, width of capacitor pads w_f, gap between capacitor pads g_f.

b_C	h_C	w	l_b	w_f	g_f
1000 µm	800 µm	300 µm	400 µm	100 µm	100 µm

C.5 Contribution of the contact junctions

The contribution of the contact junctions, which form between the pure Al shunting layer and the grAl thin film, to the kinetic inductance and the measured nonlinearity can be estimated from the fit value for the kinetic inductance of the Al layer $L_\mathrm{K,Al} = 200\,\mathrm{pH}$ extracted from the field dependence of the resonance frequency (see Sec. 2.6). Taking into account the typically 15% kinetic inductance fraction measured in Al thin films [27], and using the geometric stray inductance $L_\mathrm{s} = 450\,\mathrm{pH}$ obtained from FEM simulations (see App. C.4), results in 70 pH intrinsic kinetic inductance and leaves 130 pH to the contact junctions. Hence, according to the energy participation approach for the Kerr coefficient discussed in Sec. 2.1, the contribution of the contact junctions to the anharmonicity of the qubit is negligible.

The critical current for each contact junction is $I_\mathrm{c} = 5\,\mathrm{\mu A}$, corresponding to a critical current density $j_\mathrm{c} = 0.13\,\mathrm{mA/\mu m^2}$. The critical current density of the grAl film can be estimated from the number of effective junctions $N \approx 6$, and the cross section of the film $A_\mathrm{grAl} \approx 10 \times 200\,\mathrm{nm}^2$

$$j_\mathrm{c,grAl} = \frac{\Phi_0}{2\pi}\frac{N}{L_\mathrm{K,grAl}A_\mathrm{gral}} \approx 0.4\,\frac{\mathrm{mA}}{\mathrm{\mu m}^2}, \tag{127}$$

in agreement with the switching current measurements discussed in Sec. 1.2.3 for a film with similar normal-state resistivity.

C.6 2D vector magnet

The waveguide sample holder can be equipped with a 2D vector magnet [65], which consists of a pair of Helmholtz coils (HH) and a solenoid for field alignment, denoted compensation coil (see Fig. 2.1a and Fig. 16) . The field direction of the HH coils is aligned within machining precision with the in-plane direction of the thin films along the y-axis. The compensation coil symmetry axis is oriented in the z direction, perpendicular to the Helmholtz axis and out-of-plane with respect to the sample.

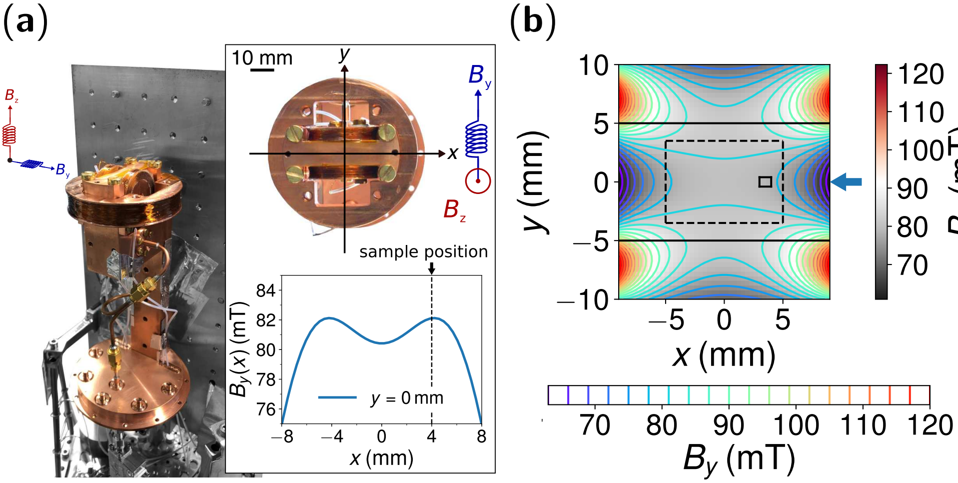

Figure 16: 2D vector magnet a) Photograph of the cryogenic setup used for the magnetic field measurements in Fig. 2.8. The copper waveguide sample holder equipped with the 2D vector magnet (highlighted in color) is mounted at the dilution stage of a table-top *Sionludi* dilution refrigerator (greyscaled), typically operated at a base temperature $T_{\mathrm{base}} \leq 30\,\mathrm{mK}$. The flat copper cylinder visible in the lower part of the image is the lid of the outer shield (not shown), which consists of successive copper (Cu) and aluminum (Al) cylinders, similar to Ref. [27]. The Cu shield was used in all three measurements presented in Fig. 2.8, while the Al shield was only used during the "shielded" cooldown. The inset shows the top view of the copper waveguide sample holder including the 2D vector magnet (top), and the Helmholtz field B_y (bottom) numerically calculated according to Eq. 129 for a bias current $I_{\mathrm{coil}} = 1\,\mathrm{A}$ and as a function of lateral position x. The magnetic field of the two Helmholtz coils is aligned within machining precision with the in-plane direction y of the thin-films. The B_z coil is the compensation coil used to align the in-plane field in-situ. **b)** In-plane field component B_y according to Eq. 129 of the HH coil geometry, calculated as a function of position x and y in the plane of the sample substrate. The horizontal solid black lines indicate the outer dimensions of the waveguide sample holder, defining the spacing between the HH coils, while the black dashed rectangle indicates the substrate dimensions. The sample position is highlighted by the solid black rectangle.

All coils are winded with the same type of NbTi, multifilament superconducting wire with diameter $d = 140\,\mu\mathrm{m}$ (Supercon. Inc. 54S43). The winding parameters - the number of layers n_{L} and the number of windings per layer n_{W}, as well as the physical dimensions of the coils, i.e. the radius R, length l and vertical distance Δy (in the case of the HH coils), are summarized in Tab. 2.

From both coil geometries, the relation between the applied bias current I_{coil} and the magnetic flux density $\vec{B}(\vec{r})$ at position $\vec{r}$ is calculated using the Biot-Savart law. For simplicity, the individual coils are approximated with $n_{\mathrm{L}} \times n_{\mathrm{W}}$ single wire loops. To account for the physical dimension of the coils, the loop radius increases with each added layer $R = R_0 + jd$, where R_0 is the inner radius and j is the number of the layer, and the position along the coils symmetry axis depends on the winding number. In both directions, the step size is given by the wire diameter d. Following the approach of Caparelli *et al.* [4], analytical expression for the magnetic field components $B_r(\vec{r})$ in radial direction (parallel to the loop plane xz), and $B_y(\vec{r})$, oriented perpendicular to the loop plane, are derived from the Biot-Savart law:

$$\begin{aligned} B_r(\vec{r}) = \frac{\mu_0 I_{\text{coil}} R^2}{2} \sum_{k=0}^{\infty} (-1)^{k+1} \frac{k r^{2k-1}}{(2^k k!)^2} y^{-2(k+1)} \\ \Gamma[2(k+1)] {}_2F_1\left(k+1, k+\frac{3}{2}, 2; -\frac{R^2}{y^2}\right) \end{aligned} \tag{128}$$

$$\begin{aligned} B_y(\vec{r}) = \frac{\mu_0 I_{\text{coil}} R^2}{2} \sum_{k=0}^{\infty} (-1)^{k} \frac{(k+1) r^{2k}}{(2^k k!)^2} |y|^{-(2k+3)} \\ \Gamma[2(k+1)] {}_2F_1\left(k+\frac{3}{2}, k+2, 2; -\frac{R^2}{y^2}\right). \end{aligned} \tag{129}$$

Here, ${}_2F_1$ is the hypergeometric function, R is the loop radius, I_{coil} is the bias current magnitude and Γ is the mathematical gamma function (not to be confused with an energy relaxation rate). Notably, the wire loops lie in the xz-plane and the field B_y is perpendicular to this plane. Notably, for the calculation of the field coils, the infinite sum is truncated after 20 terms.

Figure 16a (bottom right) depicts the numerically calculated magnetic flux density of the HH coils as a function of the lateral position x for a bias current $I_\text{b} = 1$ A and

Table 2: 2D vector magnet: coil dimensions and winding parameters. Values for the physical dimension, i.e. the inner coil radius R_0 and length l, and the total number of windings N_w, determined by the number of layers n_L and the number of windings per layer n_w, for the pair of Helmholtz coils and the compensation coil. The lateral separation between the Helmholtz coils is Δy. Numerical calculations based on the coil parameters yield predictions for the flux densities b_y and b_z per ampere at the position of the sample.

	Helmholtz	Compensation
R_0 (mm)	10	30
l (mm)	5	10
Δy (mm)	10	-
n_L	30	32
n_w	35	70
$N_\text{w} = n_\text{L} \times n_\text{w}$	1050	2240
b_y (mA/T)	80	-
b_z (mA/T)	-	50

$y = 0\,\text{mm}$. The center of the waveguide is the origin for x and y as indicated by the black dashed lines (top right panel). Since the magnetic flux density B_y changes by only 3% in the region where the sample chip is mounted ($-5\,\text{mm} \leq x \leq 5\,\text{mm}$), the value $b_y = 80\,\text{mT/A}$ is taken to convert the HH bias current I_coil into a magnetic flux density. For the compensation coil a conversion factor $b_z = 50\,\text{mT/A}$ is found using the same procedure.

Figure 16b depicts the magnetic in-plane field B_y as a function of the position (x, y) in the plane of the sample, numerically calculated for a bias current $I_\text{coil} = 1\,\text{A}$. The horizontal black lines indicate the outer walls of the waveguide sample holder, which define the distance Δy between the HH coils. Moreover, the diced chip containing the sample is indicated by the dashed black rectangle, while the position of the sample itself is indicated by the small black rectangle. The field homogeneity in the area of the sample is emphasized by the uniform grey color scale and the low density of (colored) contour lines.

C.7 Magnetic field alignment

Due to large aspect ratio between the lateral size of the circuit components and the film thickness, the grAl transmon like most other superconducting circuits is significantly more susceptible to out-of-plane components of the magnetic field. As discussed in App. C.6, the magnetic field applied to the sample can be aligned with the in-plane direction by using the compensation field of the 2D vector magnet.

For the alignment of the field, the compensation current is determined for which the transition frequency of the grAl transmon is maximal and the dependence on the compensation field is symmetric around this value. Fig. 17 depicts three measurements performed with a double triangular current bias around different mean values for the compensation field (bottom panels). While the first and the second curves are asymmetric, the symmetry in the third measurement is indicative for a compensation field close to optimum.

Since the behavior of the sample becomes hysteretic in small out-of-plane fields, as exemplarily demonstrated in Fig. 18, the HH current is gradually increased with a step size of $50 - 100\,\text{mA}$, which translates into $4 - 8\,\text{mT}$ using the conversion factor b_y listed in Tab. 2. For each value, the ideal compensation current is determined in the same way as shown in Fig. 17. After the calibration, the currents through the HH and the compensation coil are tuned always at the same time, preventing the application of large out-of-plane fields in the ideal case. Moreover, the sample is reset in a thermal cycle by reaching temperatures well above the critical temperature of the film ($T > T_\text{c} = 1.9\,\text{K}$) after the calibration procedure.

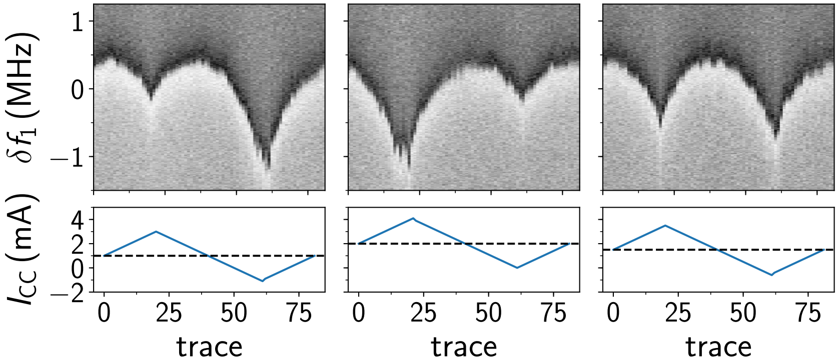

Figure 17: grAl transmon: magnetic field alignment. In order to align the magnetic field in-plane with the grAl transmon, the compensation field B_z is swept in a closed loop around a mean value. From the symmetry of the obtained trajectory of the transition frequency, the ideal compensation field is determined. The top panels show the phase of the reflection coefficient in the range $(-0.3\,\mathrm{rad}, 0.3\,\mathrm{rad})$ represented by the grey scale color map, measured for different compensation currents I_{CC}, as shown in the bottom panels. The mean values for the compensation current are 1 mA, 2 mA, and 1.5 mA, indicated by the black dashed lines. While the first and the second value are too small and too large, respectively, resulting in an asymmetric response, the third value is close to the ideal value.

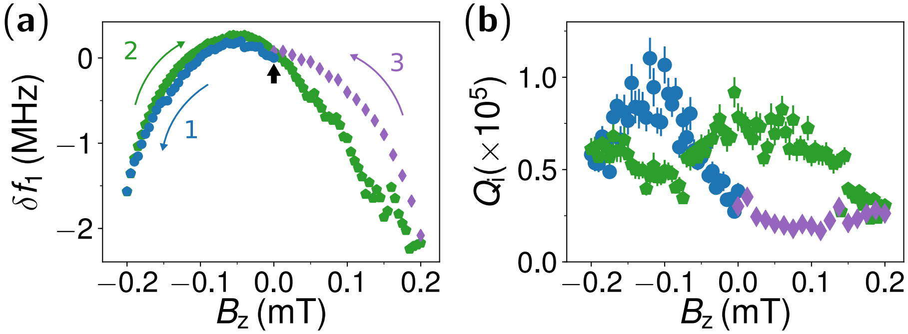

Figure 18: grAl transmon: out-of-plane field dependence a) Fundamental transition frequency and **b)** internal quality factor $Q_i = \omega_1/\gamma$ as a function of the applied out-of-plane magnetic field B_z. Starting from effective zero-field (black arrow), the measurement cycle is indicated by the colored arrows. In both parameters f_1 and Q_i, a hysteretic behavior was observed, which is more pronounced in the frequency domain at positive magnetic fields.

C.8 Overview Measurement runs

The grAl transmon was measured in seven measurement runs, summarized in Tab. 3, which were performed in three different cryogenic setups. The spectroscopy (run #2), time-domain (run #7), and two-tone measurements (run #1) were obtained in two commercial blueFors cryostats of similar type and wiring (see App. G.8). In all three runs, the sample was surrounded by the full outer magnetic shielding. The magnetic field dependence was measured in a custom-made table-top *Sionludi* dilution refrigerator [57], with different configurations for the outer shielding, but always without an outer µ-metal shielding.

The measurement outcomes are illustrated and summarized in Fig. 19 in form of the fundamental transition frequency f_1 as a function of the applied magnetic in-plane field B_y, and the corresponding external quality factor $Q_c = \omega_1/\kappa$ as a function of the transition frequency. Although the external quality factor shows a different frequency dependence than expected from the FEM simulation (black dashed line), the measurement outcomes obtained in different measurement runs align, validating the similarity of the fitting procedure.

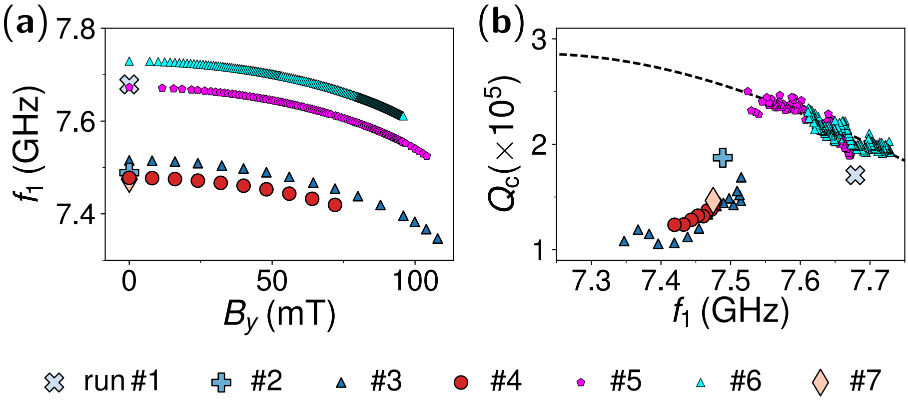

Figure 19: grAl transmon: measurement run overview. The grAl transmon was measured in a total of seven measurement runs, for which the obtained fundamental transition frequencies f_1 are shown in panel **a)** as a function of the applied magnetic in-plane field B_y, and the corresponding external quality factors Q_c in panel **b)** as a function of the transition frequency. In run #1, #2 and #7, no magnetic fields have been applied, and the markers align with zero-field. The black dashed line in panel b indicates the result obtained from the FEM simulations of the sample and the waveguide sample holder (see App. C.4). The deviation from the prediction at frequencies below 7.5 GHz could be explained by standing waves inside the waveguide, caused by imperfections not captured by the simulation, or a different setting for the adjustment screw. As shown in Fig. 13, the coupling into the waveguide does vary with frequency and the position of the screw significantly.

Table 3: Summary of the grAl transmon parameters obtained during different measurement runs: fundamental transition frequency f_1, qubit anharmonicity α, external quality factor (zero-field) Q_c, internal quality factor (zero-field) Q_i, external coupling rate (zero-field) κ, internal decay rate (zero-field) γ, outer shielding configuration.

	run #1	run #2	run #3	run #4	run #5	run #6	run #7
f_1 (GHz)	7.6790	7.4887	7.5156	7.4778	7.672	7.7292	7.4749
$\alpha/2\pi$ (MHz)	3.90	4.48	-	-	-	3.35	4.5
$Q_\mathrm{c}(\times 10^5)$	1.7	1.9	1.8	1.5	1.9	1.9	1.5
$Q_\mathrm{i}(\times 10^3)$	900	750	95	100	130	51	750
$\kappa/2\pi$ (kHz)	45	40	42	50	40	40	51
$\gamma/2\pi$ (kHz)	8.5	10	78	75	58	150	10
Outer shield:							
Cu	yes	yes	yes	yes	yes	yes	yes
Al	yes	yes	no	yes	no	no	yes
µ-metal	yes	yes	no	no	no	no	yes
Magnetic field	no	no	yes	yes	yes	yes	no

C.9 Fabrication recipe

The structures of the grAl transmon are patterned in a resist double-stack composed of two postive direct write electron-beam resists [37]: copolymer PMMA/MAA (El-13), 13% solids dissolved in ethyl lactate and a 950PMMA (A-4), 4% solids dissolved in anisole. Since the resists are spin-coated on an insulating, epipolished sapphire substrate (diameter: 2 inch, thickness: 330 µm), an antistatic Au layer of a few nanometer thickness is evaporated on top of the resist stack. The total resist stack has a height of $\sim 1-1.1$ µm.

After the e-beam write and right before the development, the antistatic gold layer was removed using a Lugol solution, a mixture of potassium iodide and iodine (2:1), dissolved in water. The development was performed by placing the written sample in a mixture of IPA and H_2O (3:1 volume fraction), for about 120 s, while carefully shaking the sample at a frequency of $\sim$ 1 Hz (118 oscillations) using a tweezer. The outcome of the development process was assessed under an optical microscope, as shown in Fig. 20a, with the undercut in the bottom resist visible as bright halo around the main features. The central strip appears connected to the leads due to optical interference effects.

Following the development process, the sample was installed in a commercial *Plassys* e-beam evaporator to perform a three-angle shadow evaporation. The load lock of

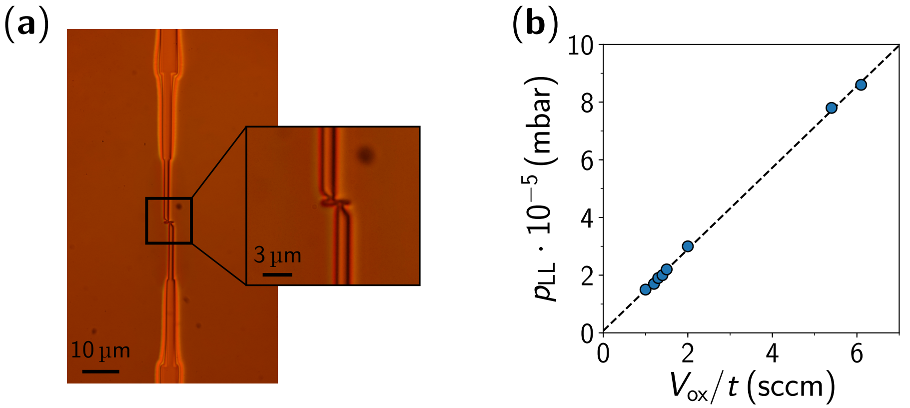

Figure 20: grAl transmon: fabrication. a) Optical microscopy image of the sample after the development. The undercut in the bottom resist is visible as bright halo, while the zoom-in shows the region which later forms the grAl volume. Due to interference effects, the structures appear connected. **b)** Pressure in the load lock p_{LL} of the evaporator as a function of the oxygen mass flow V_{ox}/t in sccm under simultaneous vacuum pumping.

the evaporator was pumped for three hours ($p_{LL} = 1.9 \times 10^{-7}$ mbar). First, resist residuals were removed in a cleaning step for 2 : 30 min using an oxygen/argon (10 sccm/5 sccm) plasma with a beam voltage 200 V and a beam current 10 mA. Subsequently, the pressure in the evaporation chamber was further reduced by employing a Ti gettering to reach 4.9×10^{-8} mbar.

For the metal deposition, first a 10 nm grAl film was evaporated at zero angle. The average aluminum evaporation rate was $r_{Al} = 0.286$ nm/s, calculated from the film thickness, which is confirmed by AFM measurements (see Fig. 2.1), and the duration of the evaporation 35 s. The partial oxygen pressure during the evaporation was $p_{O_2} = 2.25 \times 10^{-5}$ mbar, which is controlled by the injected oxygen mass flow V_{ox}/t and the delivery rate of the turbo pump, as shown in Fig. 20b. Subsequently, an argon milling [27] was used for 10 s, followed by a double-angle evaporation of two 40 nm pure Al thin films under ±35°. However, I would like to point out that the effect of the Ar milling on the contact resistance between the grAl layer and the Al layers was not investigated. An overview on the individual fabrication steps is listed in Tab. 4 and Tab. 5.

Table 4: grAl transmon: electron-beam lithography fabrication recipe – resist application and development.

Resist application	
substrate	C-plane sapphire, double-sided epipolished
1st resist layer	El-13 (thickness: $700 - 800$ nm, positive)
2nd resist layer	A-4 (thickness: ~ 300 nm, positive)
acceleration	1000 rpm/s
spin speed	2000 rpm
spin time	100 s
HP temp	200 °C
HP time	300 s
antistatic layer	Au
e-beam writing	
acceleration voltage	50 kV
Development	
Au remover	Lugol solution
time	$10 - 15$ s
rinse	destilled H_2O
developer	IPA and H_2O (3:1)
time	120 s
rinse	destilled H_2O + N_2 blown-dry

Table 5: grAl transmon: electron-beam lithography fabrication recipe – thin film evaporation.

thin film deposition and lift-off	
cleaning	
mass flows	O_2/Ar (10 sccm/5 sccm)
beam parameters	$U_{\mathrm{beam}} = 200\,\mathrm{V}$, $I_{\mathrm{beam}} = 10\,\mathrm{mA}$
Ti gettering	
duration	2 min (active) and 3 min (passive)
pressure	4.9×10^{-8} mbar
grAl-layer	
thickness	10 nm
rate	0.286 nm/s
O_2 pressure	2.25×10^{-5} mbar
angle	0 °
Ar-milling	
Ar mass flow	4.0 sccm
beam parameters	$U_{\mathrm{beam}} = 400\,\mathrm{V}$, $I_{\mathrm{beam}} = 15\,\mathrm{mA}$
duration	10 s
Al-layers	
thickness	40 nm
rate	1 nm/s
angle	±35 °
lift-off	
solvent	NMP or NEP
time	2.5 h
temperature	90 °C (preheated)
rinse	acetone + ethanol + N_2 blown-dry

D grAl dc SQUIDs: supplementary information

In the following sections, the switching dynamic of an ideal JJ is discussed to provide a basis for the switching current measurements of the grAl SQUIDs.

D.1 The Resistively-Capacitively-Shunted-Junction-model

In the resistively-capacitively-shunted-junction (RCSJ) model, the static and dynamic properties of the gauge-invariant phase difference γ across a Josephson junction is derived from an effective circuit model, that captures the dc transport of a non-resistive supercurrent, as well as the finite dissipation in the presence of quasiparticles.

The circuit diagram of the RCSJ model is depicted in the left-hand panel of Fig. 21a, and consists of a parallel circuit of an ideal JJ (cross symbol), with critical current I_c and sinusoidal current-phase relation, which is shunted by a capacitor with capacitance C, and a resistor with resistance R. The shunt capacitor accounts for the geometric capacitance arising between the electrodes, while the shunt resistor introduces finite dissipation induced by the tunneling of normal-conducting quasiparticles. Although the dynamics of the quasiparticles are generally quite complex, requiring the resistance to be a nonlinear function of the voltage drop V across the junction, it is nevertheless, for the sake of simplicity, considered to be constant.

Provided a finite bias current I, the total current through the effective circuit is the sum of the currents through the three branches

$$I = I_\mathrm{c}\sin(\gamma) + \frac{V}{R} + C\frac{\mathrm{d}V}{\mathrm{d}t}, \tag{130}$$

with an identical voltage drop V across each branch. The voltage V and its time-derivative can be eliminated in favor of the phase difference γ by means of the second Josephson equation, resulting in a second order differential equation in γ

$$\frac{\mathrm{d}^2\gamma}{\mathrm{d}\tau^2} + \frac{1}{Q}\frac{\mathrm{d}\gamma}{\mathrm{d}\tau} + \sin(\gamma) = \frac{I}{I_\mathrm{c}}, \tag{131}$$

where $\tau = \omega_\mathrm{p} t$ is a dimensionless time variable. The frequency ω_p is the plasma frequency of the JJ

$$\omega_\mathrm{p} = \sqrt{\frac{2eI_\mathrm{c}}{\hbar C}}, \tag{132}$$

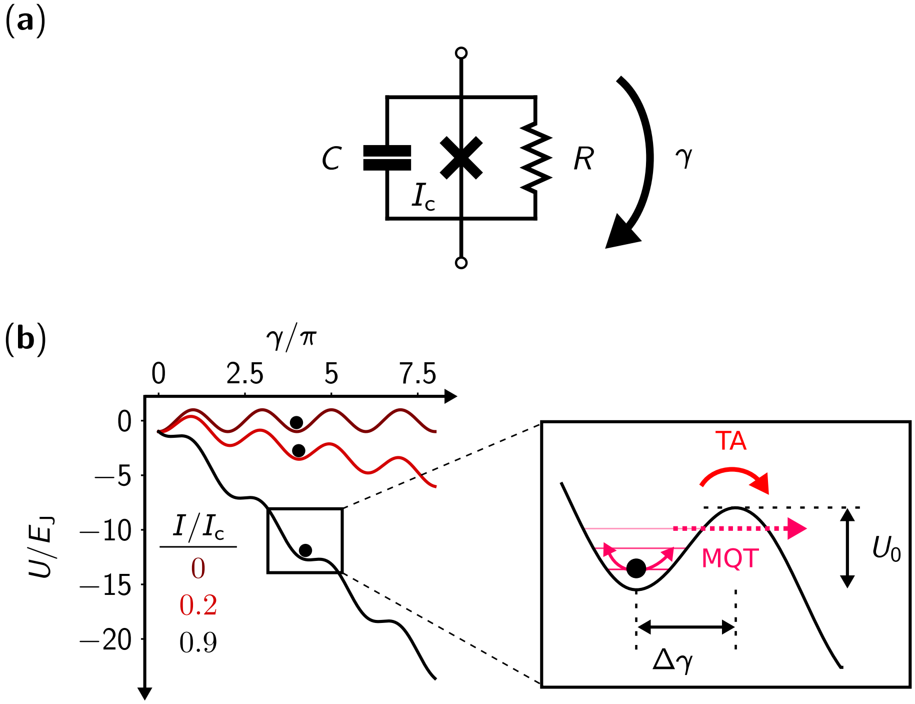

Figure 21: Josephson junctions: phase dynamcis. a) Effective circuit diagram of a Josephson junction according to the resistively-capacitively-shunted-junction (RCSJ) model, devised to describe the dynamics of the superconducting phase difference across the junction γ. The model consists of a parallel circuit of an ideal junction with critical current I_c and sinusoidal current-phase relation (cross symbol), which is shunted by a capacitor with capacitance C, and a resistor with resistance R. The shunt capacitor accounts for the geometric capacitance arising between the electrodes, while the shunt resistor introduces finite dissipation induced by the tunneling of normal-conducting quasiparticles. **b)** The left-hand panel depicts the washboard potential $U = -E_\mathrm{J}(\cos(\gamma) + I\gamma/I_\mathrm{c})$ arising in the RCSJ model, normalized by the Josephson energy $E_\mathrm{J} = \Phi_0 I_\mathrm{c}/(2\pi)$, as a function of the phase difference γ for three different bias currents $I/I_\mathrm{c} \in \{0, 0.2, 0.9\}$. As long as the phase particle, which represents the phase difference γ, is trapped in one of the local minima, a non-resistive supercurrent flows across the junction. Once the bias current exceeds the critical current $I/I_\mathrm{c} > 1$, the phase particle starts moving along the potential, entering the running state. Since the phase changes with time, the junction becomes resistive with a finite voltage drop across it. The escape of the particle can be premature, even before $I/I_\mathrm{c} > 1$, either triggered by thermal activation (TA), or by macroscopic quantum tunneling (MQT), as indictaed by the right-hand panel. In both cases, the escape probability is related to the remaining barrier height U_0.

which can be identified as the self-resonance frequency of the equivalent junction circuit. The quality factor Q is a measure of damping and depends not only on the resistance, but also on the capacitance

$$Q = \omega_\mathrm{p} R C. \tag{133}$$

A better understanding of the dynamics described by Eq. 131 can be gained by mapping the differential equation into the equation of motion of an effective phase particle moving in a one-dimensional potential. In this analogy, the phase difference γ becomes the position variable of the particle, and the time derivative $\dot{\gamma}$ becomes its velocity. By introducing the mass of the particle $m = \hbar^2 C/(4e^2)$, the effective potential U becomes

$$U = -E_\mathrm{J}(\cos(\gamma) + I\gamma/I_\mathrm{c}), \tag{134}$$

where $E_\mathrm{J} = \phi_0 I_\mathrm{c}/(2\pi)$ is again the Josephson energy. Due to its shape, the potential is referred to as the washboard potential.

The right-hand panel in Fig. 21b depicts the normalized washboard potential U as a function of the phase difference γ for three different bias currents $I/I_\mathrm{c} \in \{0, 0.2, 0.9\}$. For small bias currents, the particle remains trapped in one of the local minima, which corresponds to the zero-voltage state of the junction. According to the Josepshon equation, the immobility of the phase particle describes the flow of a finite supercurrent across the junction without dissipation. However, with increasing bias current, the potential is tilted towards increasingly negative slopes. As soon as the bias current surpasses the critical current ($I > I_\mathrm{c}$), the derivative becomes negative at all positions, and the particle starts to move downhill, in some occasions referred to as the running state. Since the velocity of the particle is non-zero, a finite voltage drop occurs across the junction and the JJ switches into the normal-conducting state.

Notably, due to the second term in Eq. 131, the particle is subject to fricition directed opposite to the direction of motion. Depending on the amount of friction, the phase particle can be retrapped after it has been escaped, and the motion of the particle can be diffusive rather than ballistic.

Escape dynamics

In contrast to the classical and ideal scenario, in which the particle escapes from the local minimum it is trapped in not before the bias current reaches the critical current ($I/I_\mathrm{c} > 1$), an escape can be triggered prematurely by two effects: Thermal activation (TA) and macroscopic quantum tunneling (MQT). While the first effect can be understood classically, the existence of the second effect unambiguously implies, that the macroscopic phase describing the superconducting condensate is a quantum mechnanical observable [44].

Figure 21b (right-hand panel) shows a magnification of one of the minima for a bias current close to the critical current ($I/I_\mathrm{c} = 0.9$). Since the phase particle is a quantum object with a finite uncertainty between position and momentum, the energy eigenstates of the particle in the potential wells are discrete and anharmonic

[43, 44], indicated by the horizontal pink lines. Even in the energetic ground state, the phase particle (black dot) is not resting, but constantly in motion, signified by the pink arrows. The frequency of this motion ω_0 is determined by the curvature of the potential around the minimum, and is therefore similar to the plasma frequency ω_p, but generally bias current dependent:

$$\omega_0(I) = \omega_\mathrm{p} \left(1 - \frac{I}{I_\mathrm{c}}\right)^{1/4} \tag{135}$$

The oscillation frequency of the particle is closely related to an attempt frequency, which is on the order of gigahertz typically, and determines the characteristic time scale of the switching event.

The probability that an escape occurs depends on the thermal energy of the particle and the remaining barrier height U_0, as indicated in the right-hand panel of Fig. 21b. For a sinusoidal current-phase relation, and assuming that the switching occurs for bias currents close to the critical current only, the remaining barrier height is well approximated by

$$U_0(I) \approx E_\mathrm{J} \left(1 - \frac{I}{I_\mathrm{c}}\right)^{3/2} . \tag{136}$$

In general, the relation between the barrier height and the bias current depends on the shape of the current-phase relation.

At finite but low temperatures ($k_\mathrm{B}T \ll E_\mathrm{J}$), the escape rate over the barrier due to thermal activation Γ_TA is a simple Arrhenius law

$$\Gamma_\mathrm{TA}(T, I) = \underbrace{b_t \frac{\omega_0(I)}{2\pi}}_{\Gamma_0} \exp\left(-\frac{U_0(I)}{k_\mathrm{B}T}\right), \tag{137}$$

where the temperature dependence of the attempt frequency Γ_0 is captured by a thermal coefficient b_t [63]. With decreasing temperature, thermally activated escapes of the phase particle are suppressed exponentially. At the so-called crossover temperature $T^\star = \hbar\omega_0/(2\pi k_\mathrm{B})$, the remaining switching events start to be dominated by macroscopic quantum tunneling through the barrier [24]. Although the escape dynamics due to MQT are generally very rich, the resulting escape rate can be estimated within a Wentzel-Kramers-Brioullin approximation. However, a simpler and mathematically more convenient approximation can be found by substituting the physical temperature T in Eq. 137 with a fixed temperature T_esc

$$\Gamma_\mathrm{MQT}(I) = \Gamma_0(I) \exp\left(-\frac{U_0(I)}{k_\mathrm{B}T_\mathrm{esc}}\right), \tag{138}$$

representing the temperature independent tunneling process.

Escape probability:

Another consequence of the premature switching into the resistive state of a JJ is, that the maximal bias current extracted from transport measurements is not necessarily the critical current, but, in particular for small JJs, a significantly smaller value. In order to distinguish between the two quantities, the measured value is referred to as the switching current I_{sw}. Under some conditions, the deviation between the measured value and the actual critical current of the junction can be significant. A series of repetitive transport measurements will result in an asymmetric distribution of switchting currents around a mean value $\bar{I}_{\mathrm{sw}}$, with a finite width σ_{sw} similar to a standard deviation.

Following the description of Kurkijärvi *et al.*, summarized in Ref. [36], the switching current probability distribution as a function of the bias current I is derived from the thermal activation of a particle above a barrier. Although the model theory was initially developed for thermal processes only, the introduction of a temperature T_{esc} extends the theory to MQT.

The probability $W(t)$ that an escape has not yet occured after time t, is given by

$$W(t) = \exp\left(-\int_0^t \mathit{\Gamma}_{\mathrm{sw}}(T, I\{t'\})\mathrm{d}t'\right). \tag{139}$$

Here, $\mathit{\Gamma}_{\mathrm{sw}}$ is the switching rate at which the junction switches into the resistive state, or, in the picture of the mechanical analogon, the phase particle enters the running state. In case every escape event triggers a switching, the switching rate is identical to the escape rate. However, in the presence of friction and retrapping, both rates can differ significantly.

Since the bias current is often swept at a constant rate, which is much slower than the attempt frequency ($\dot{I} \ll \mathit{\Gamma}_0$), the time dependence can be substituted with a bias current dependence, and the probability becomes

$$W(I) = \exp\left(-\frac{1}{\dot{I}}\int_0^I \mathit{\Gamma}_{\mathrm{sw}}(T, I')\mathrm{d}I'\right). \tag{140}$$

The probability $P(I)$ for the particle to escape, or equivalently for the junction to switch into the resistive state at a given bias current I, is given by the derivative of Eq. 140

$$P(I) = -\frac{\mathrm{d}W(I)}{\mathrm{d}I} = \frac{\mathit{\Gamma}_{\mathrm{sw}}(T, I)}{\dot{I}}W(I). \tag{141}$$

According to Eq. 141, the switching probability is the product of two probabilities: The probability that the junction switches in the bias current interval $I + \mathrm{d}I$, determined by the first factor, and the probability that the junction has not yet switched. In order to calculate $P(I)$, Eq. 141 has to be solved numerically due to the nonlinear bias current dependence of the remaining barrier height U_0 given in Eq. 136 for a sinusoidal current-phase relation. However, an analytical, and hence more convenient expression with only three free parameters can be found by assuming a linear dependence between U_0 and I [2]:

$$P(I) = A \exp\left(\frac{I - \bar{I}_{\text{sw}}}{b} - \exp\left[\frac{I - \bar{I}_{\text{sw}}}{b}\right]\right) \tag{142}$$

As previously mentioned, $\bar{I}_{\text{sw}}$ is the bias current at which switching occurs with the highest probability, while the parameter b is related to the width σ_{sw} of the full distribution defined by Eq. 141. The third parameter A is a scaling parameter that determines the amplitude of the distribution, as it is not normalized in the presented form.

Figure 22a depicts the switching current distribution $P(I)$ of an ideal JJ with sinusoidal current-phase relation, as a function of the bias current I, numerically calculated according to Eq. 141. The switching rate Γ_{sw} is assumed to be a combination of escapes that are triggered by thermal activation and by macroscopic quantum tunneling:

$$\Gamma_{\text{sw}} = \Gamma_{\text{TA}} + \Gamma_{\text{MQT}}. \tag{143}$$

Again, the underlying consequence of this assumption is, that every escape triggers a switching into the resistive state. The temperature T of the JJ is assumed to be low compared to the critical temperature $T/T_{\text{c}} = 0.02$, which, in the presented case is that of thin film aluminum $T_{\text{c}} = 1.4\,\text{K}$. In order to account for MQT, a finite escape temperature $T_{\text{esc}} = 0.3\,\text{K}$ is considered, similar to the value reported in Ref. [63]. The resulting switching current probability function has a characteristic, asymmetric shape, with a slower rise below $\bar{I}_{\text{sw}}$, and a steeper descent above it. The width of the distribution σ_{sw} gives insight into the dynamics of the escape. The white dashed line is a fit to the calculated data according to the analytical expression given in Eq. 142, from which $\bar{I}_{\text{sw}}$ and σ_{sw} are extracted. The junction parameters entering the calculation are the critical current $I_{\text{c}} = 5\,\mu\text{A}$, the value of the shunt capacitance $C = 1\,\text{fF}$ and the (constant) bias current sweeping rate $\dot{I} = 200\,\mu\text{A/s}$.

In Fig. 22b, the switching current distribution is plotted for different temperatures $T/T_{\text{c}} \in \{0.02, 0.32, 0.52, 0.62, 0.72, 0.82\}$. With increasing temperature, the critical current of the JJ decreases, causing a reduction of the amplitude of the washboard potential E_{J}, and with that, the barrier height U_0, as well as a decrease of the plasma frequency ω_{p}. As a result, the bias current with the highest switching probability appears at lower values, alongside with a broadening of the switching current distribution. The extracted values for $\bar{I}_{\text{sw}}$ are depicted in panel c as a function of temperature, and are normalized by the critical current.

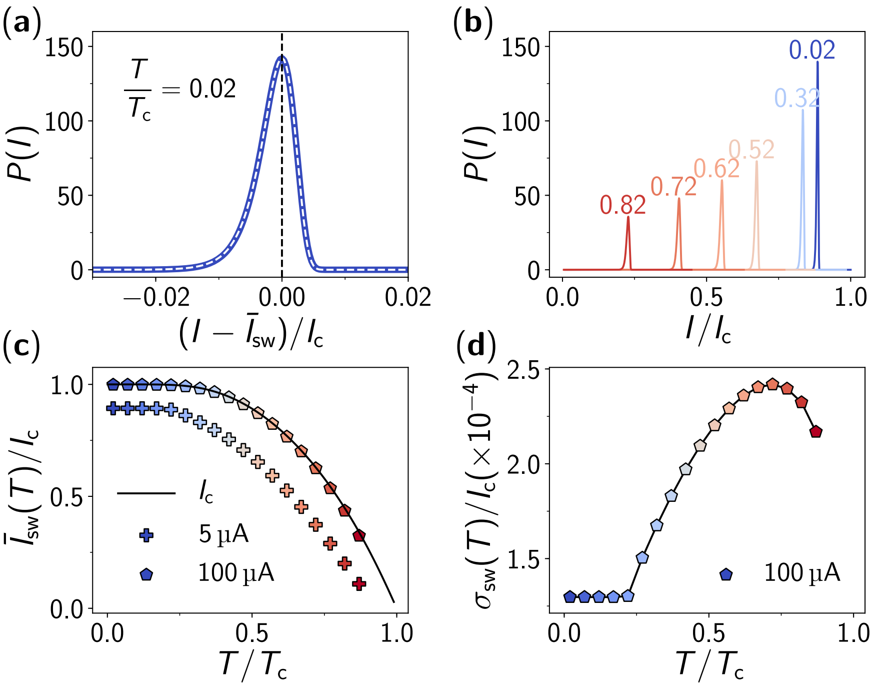

Figure 22: Josephson junctions: escape dynamics. a) Switching current distribution $P(I)$ of an ideal JJ, numerically calculated according to Eq. 141 as a function of the bias current I. The distribution is plotted around the switching current with highest probability $\bar{I}_{sw}$, normalized by the critical current $I_c = 5\,\mu A$. While the physical temperature of the JJ is assumed to be low compared to the critical temperature $T/T_c = 0.02$, macroscopic quantum tunneling (MQT) is taking into account by considering a non-zero escape temperature $T_{esc} = 0.3\,K$ (see Eq. 138). The shunt capacitance is $C = 1\,fF$, the critical temperature is $T_c = 1.4\,K$ and the bias current sweeping rate is $\dot{I} = 200 \mu A/\text{second}$. The white dashed line indicates a fit to the distribution using the analytical expression given in Eq. 142. **b)** Switching current distributions $P(I)$ as a function of normalized bias current, calculated for different physical temperatures T. With increasing temperature, the critical current is suppressed alongside with the plasma frequency ω_p of the JJ. Consequently, the escape happens at lower bias currents and the increasing thermal energy causes a broadening of the distribution. **c)** Normalized switching current $\bar{I}_{sw}/I_c$ as a function of temperature T, extracted from fits to the calculated distributions similar to panel a and b. The color of the scatter points indicate the physical temperature, and the black dashed line indicates the BCS temperature dependence of I_c [60]. For the JJ with larger critical current $I_c = 100\,\mu A$ (pentagons), the switching currents are very close to the critical current, while for the smaller JJ $I_c = 5\,\mu A$ (crosses), a significant premature switching is observed. The offset at low temperatures is due to quantum tunneling.**d)** Normalized standard deviation of the switching current distribution σ_{sw} as a function of temperature. At low temperatures, MQT dominates, and σ_{sw} remains constant. With increasing temperature, thermally activated escapes start to dominate and the distribution width increases. The decrease at temperatures close to T_c is due to the strong temperature dependence of the critical current.

The same numerical calculations were performed for two JJ, that differ in their critical current only, with $I_c \in \{5\,\mu A, 100\,\mu A\}$. For the JJ with larger critical current, the extracted switching currents are very close to the BCS temperature dependence of the actual critical current, indictaed by the black solid line. Since the energy scales corresponding to TA and MQT are low compared to the Josephson energy E_J, a bias current close to the critical current is required to reduce the barrier height U_0 sufficiently. As opposed to this, the switching current of the JJ with smaller critical current deviates from the critical current significantly. At low temperatures, the deviation is caused by the presence of MQT, until thermally activated escapes start to dominate the switching.

The competition between MQT and TA becomes particularly evident in the temperature dependence of the distribution width, depicted in Fig. 22d. At low temperatures, the width remains constant, indicating a constant escape rate due to the temperature independent MQT. Hence, in the absence of MQT, the width would decrease further with decreasing temperature. The transition into the regime in which the escape is dominated by TA occurs around the assumed and fictional escape temperature $T_{esc} = 0.3\,K$ associated to MQT. Since the temperature is normalized by the critical temperature, I would like to emphasize that the size of the constant plateau depends on the choice of the critical temperature. At temperatures close to the critical temperature, the distribution width decreases again since the critical current approaches zero. Similar to the asymmetry of the switching current distribution, caused by the upper bound given by the critical current, the distribution is squeezed from below.

D.2 Device overview

The critical current density of superconducting grAl films, as shown in Fig. 1.19, was obtained from switching current measurements performed on various dc SQUIDs. The parameters of the film, i.e. the film thickness t and the normal-state resistivity ρ_n (measured at room temperature), and the dimensions of the two geometric constrictions, i.e. the widths w_1 and w_2, as well as the lengths l_1 and l_2, are listed in Tab. 6.

The rather large fluctuations in the measured switching currents, even for devices with almost identical constriction dimensions, suggest, that the switching dynamics are strongly influenced by the film microstructure. Although not significant, there seems to be a trend in the data indicating a slight decrease of the switching current with the length of the geometric constriction. A possible explanation could be an increase in the statistical probability of finding an increasingly weaker inter-grain coupling between two (effective) grains.

Table 6: Device parameters for the grAl dc SQUIDs from which the critical current densities are extracted (shown in Fig. 1.19). The parameters are: film thickness t, normal-state resistivity ρ_n, measured switching current in zero-field $\bar{I}_\mathrm{sw}(0)$, geometric dimensions of the two constrictions width w_i and length l_i ($i \in \{1,2\}$).

device	t (nm)	ρ_n (µΩcm)	$\bar{I}_\mathrm{sw}(0)$ (µA)	w_1 (nm)	w_2 (nm)	l_1 (nm)	l_2 (nm)
1	30 ± 5	250 ± 40	47.4 ± 0.5	65 ± 5	43 ± 5	57 ± 5	61 ± 5
2			52.3 ± 0.5	73 ± 5	81 ± 5	65 ± 5	62 ± 5
3			63.2 ± 0.6	84 ± 5	80 ± 5	63 ± 5	59 ± 5
4			40.9 ± 0.4	77 ± 5	77 ± 5	154 ± 5	150 ± 5
5			20.4 ± 0.2	57 ± 5	64 ± 5	150 ± 5	149 ± 5
6			22.2 ± 0.2	80 ± 5	78 ± 5	236 ± 5	235 ± 5
7			47.1 ± 0.5	77 ± 5	75 ± 5	248 ± 5	239 ± 5
8			20.6 ± 0.2	58 ± 5	62 ± 5	246 ± 5	245 ± 5
9	20 ± 5	1520 ± 200	4.01 ± 0.04	79 ± 5	79 ± 5	70 ± 5	61 ± 5
10			2.94 ± 0.03	99 ± 5	105 ± 5	90 ± 5	100 ± 5
11			3.20 ± 0.03	86 ± 5	84 ± 5	158 ± 5	148 ± 5
12	20 ± 5	3200 ± 720	0.91 ± 0.01	54 ± 5	57 ± 5	170 ± 5	165 ± 5
13			1.10 ± 0.01	76 ± 5	76 ± 5	257 ± 5	258 ± 5
14			0.93 ± 0.01	76 ± 5	74 ± 5	261 ± 5	258 ± 5
15	30 ± 5	5550 ± 450	1.1 ± 0.01	80 ± 5	78 ± 5	68 ± 5	67 ± 5
16			0.79 ± 0.01	76 ± 5	80 ± 5	65 ± 5	69 ± 5
17			0.57 ± 0.01	36 ± 5	44 ± 5	67 ± 5	58 ± 5
18			0.24 ± 0.01	53 ± 5	55 ± 5	160 ± 5	160 ± 5
19			0.68 ± 0.01	73 ± 5	73 ± 5	165 ± 5	164 ± 5
20			0.17 ± 0.01	56 ± 5	59 ± 5	256 ± 5	254 ± 5
21			0.86 ± 0.01	70 ± 5	73 ± 5	265 ± 5	261 ± 5

E Superconducting Quantum Interference Devices - SQUIDs

In a Superconducting Quantum Interference Device (SQUID), two physical effects find a combined application: The Josephson dynamics of a weak link as described in the previous section, and the quantization of the magnetic flux enclosed in a superconducting loop in number of the magnetic flux quantum Φ_0. As a consequence, the response of a SQUID becomes a periodic function of the flux Φ enclosed in its loop, which itself is related to the external magnetic field, rendering SQUIDs among the most sensitive magnetic field detectors existing [7]. The arising periodicity is attributed to an interference effect between the two loop branches, and the circulating current induced by the application of an external magnetic field, resulting in an interference pattern similar to that of an optical double slit experiment.

The physical implementation of a SQUID comes in two ways, either with a single JJ or two JJs embedded in a superconducting loop. Historically, the two implementations are distinguished nominally by the readout scheme used to measure the magnetic flux, with devices containing a single JJ labeld radio frequency or *rf SQUIDs* [16, 55], and devices with two JJs labeled direct current or *dc SQUIDs* [32, 59]. In the first case, the SQUID used to be inductively coupled to a resonant tank circuit, with the response of the SQUID altering the transition frequency of the auxiliary system, while in the latter case, the information about the enclosed magnetic flux used to be extracted from switching current measurements as discussed in the previous section.

Depending on the application, SQUIDs are operated in the resistive or in the nonresistive state. Similar to a single JJ, the SQUID enters the resistive state above a critical bias current in case of a dc SQUID, or a critical circulating current in case of an rf SQUID. However, the main drawback of this state of operation is the loss of quantum coherence due to dissipation. With every measurement, the prepared macroscopic quantum state of the superconducting condensate is obliterated. In the framework of cQED, the nonresistive state of operation is therefore favored, which enables the implementation of non-destructive readout schemes [29].

At a first glance, a dc SQUID is quite similar to an effective JJ with a nonconstant, flux dependent critical current. Analogously, the Josephson dynamics of the two weak links give rise to a nonlinear kinetic inductance, which can be tuned with the external magnetic field. Embedded into a tank circuit, the resonance frequency of the circuit becomes a function of the external magnetic field, and similar to an rf SQUID, the information about the magnetic flux is encoded in the resonance frequency of the device when used as detector for magnetic fields. In quantum information processing with superconducting circuits, where various circuits are connected to a processor, a precise control over the frequency detuning between the different components of the circuit is an essential prerequisite. Therefore, the flux tunablity offered by a dc SQUID is used in superconducting quantum circuits.

From the perspective of transport measurements however, the SQUID contains more degrees of freedom, and the switching dynamics are more complicated, and generally sensitive to perturbations close to the plasma frequency. Although the critical current is a measure of the maximal direct current the superconductor can carry without resistance, the switching into the resistive state is a dynamical process, and contains information about the properties of the superconducting material the SQUID is made of, as well as about the electro-magnetic environment, as discussed in Ref. [18].

E.1 Magnetic flux quantization

The superconducting wavefunction has to be unambiguous and single-valued in every point in space and time. Therefore, the change of phase within one cycle around a loop made from a superconducting material has to be an integer multiple of 2π. The very consequence of this constraint is the quantization of the flux inside a superconducting loop in integer numbers of the magnetic flux quantum $\Phi_0 \approx 2.068 \times 10^{-15}$ Wb [10, 14], similar to the quantization of the electron's orbital angular momentum in the potential of an atom.

In the absence of a JJ in the loop, the external magnetic field is expelled by a circulating current induced in the loop, and the enclosed magnetic flux remains zero. However, in the presence of a JJ, quanta of magnetic flux Φ_0 can tunnel into the loop. As soon as the flux enclosed in the loop reaches half a flux quantum, the induced screening current changes its orientation since it becomes energetically favorable to increase the external flux rather than to expel it.

E.2 direct current SQUIDs

A direct current superconducting quantum interference device (dc SQUID) consists of two Josephson Junctions (JJ), embedded in parallel in a superconducting loop, see Fig. 23. In analogy to a single JJ, the supercurrent across the dc SQUID is related to the phase difference γ between the superconducting electrodes connected to the

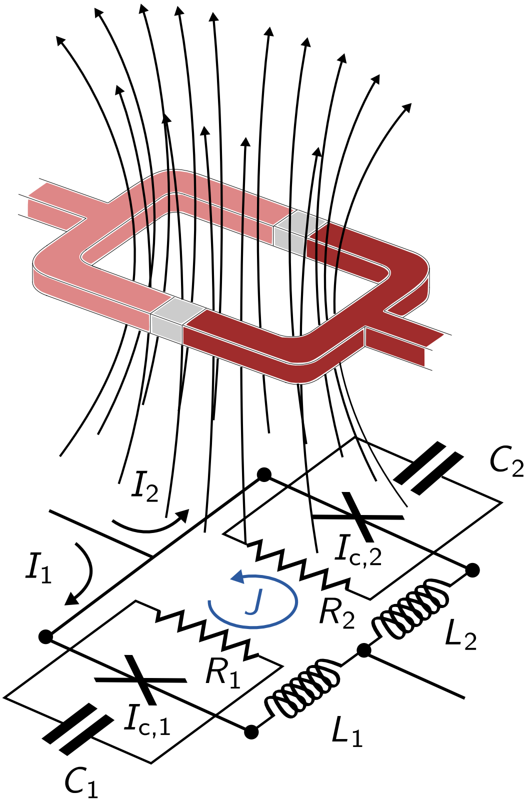

Figure 23: Direct current superconducting quantum interference device. The top part shows the artistic portrayal of a dc SQUID, consisting of two JJs (grey regions) embedded in a superconducting loop. The leads connect the SQUID loop in such a way that the JJs are connected in parallel, and are colored in different shades of red to emphasize the potential difference in phase of their macroscopic wavefunctions. The external magnetic field is indicated by the black arrows piercing through the loop from below. In the lower part of the image, an effective circuit model is depicted, based on which the static and dynamic properties of the SQUID are derived. Each JJ is modeled individually by a parallel circuit of an ideal JJ with critical current $I_{c,i}$, a capacitor C_i, and a resistor R_i, similar to Sec. D.1. Additionally, the inductance of the loop itself is accounted for by an inductor with inductance L_i in each of the two SQUID branches. The penetration of the loop area by an external magnetic field induces a screening current J in the loop wires. In case the loop inductance is significant compared to the kinetic inductance of the JJs ($L/L_J \geq 1$), screening effects start to dominate the flux modulation of the critical current.

loop. However, to the contrary, the effective critical current of the dc SQUID I_c is not constant, but a periodic function of the magnetic flux Φ enclosed in the loop.

$$I = I_\mathrm{c}(\Phi)\sin(\gamma) \tag{144}$$

To the same effect the critical current of a single JJ is related to its kinetic inductance, the kinetic inductance corresponding to the dc SQUID is a function of its critical current, too, and, hence becomes a function of the magnetic flux.

$$L_\mathrm{J,sq} = \frac{\Phi_0}{2\pi I_\mathrm{c}(\Phi)} \tag{145}$$

Therefore, a better understanding of the flux modulation of the critical current is vital for a better understanding of the applicability of a dc SQUID in the context of cQED and other fields of research.

The flux modulation of the critical current is derived from an effective circuit model, shown in Fig. 23. The circuit model consists of two JJs, both modeled in the spirit of the RCSJ-model, described in Sec. D.1, with critical currents $I_\mathrm{c,1}$ and $I_\mathrm{c,2}$, junction capacitances $C_\mathrm{J,1}$ and $C_\mathrm{J,2}$ and junction resistances R_1 and R_2. While the junction capacitances and the resistances are irrelevant for the derivation of the critical current, they become important quantities for the description of the switching dynamics of the SQUID into the normal-conducting state. The loop wires contribute with an additional inductance in each branch, denoted L_1 and L_2. For materials with low normal-state resistivity, for instance pure aluminum, the loop inductance is mainly geometric, and therefore neglectable. However, it contributes significantly in case of superconducting materials with high intrinsic kinetic inductance, for instance granular aluminum, or niobium.

Critical current flux modulation:

The supercurrent I across the SQUID is the sum of currents in both branches, denoted I_1 and I_2

$$I = I_{c,1}\sin(\gamma_1) + I_{c,2}\sin(\gamma_2). \tag{146}$$

In agreement with Eq. 1.13, γ_1 and γ_2 are the gauge invariant phase differences across the JJs. The application of an external magnetic field induces a circulating screening current J inside the SQUID loop, which is given by half the difference of the currents flowing in the SQUID branches

$$J = \frac{I_1 - I_2}{2}. \tag{147}$$

Due to the circulating current, the phase differences γ_1 and γ_2 are not independent, but are related via the magnetic flux enclosed in the loop.

$$\gamma_1 - \gamma_2 = 2\pi \Phi_\mathrm{T} / \Phi_0 \tag{148}$$

The magnetic flux Φ is a combination of two contributions: The applied external magnetic flux Φ_ext, and the magnetic flux induced by the currents I_1 and I_2 flowing through the effective loop inductances $L_1' = L_1 - M$ and $L_2' = L_2 - M$, where M is the mutual inductance between the SQUID branches.

$$\Phi = \Phi_\mathrm{ext} + LJ + \eta L \frac{I}{2} \tag{149}$$

Here, $L = L_1' + L_2'$ is the total inductance, and η, with $0 \leq \eta \leq 1$ is a parameter that takes a finite asymmetry between the loop inductances into account (not to be confused with the measurement efficiency).

$$L_1' = (1 - \eta)\frac{L}{2} \tag{150}$$

$$L_2' = (1 + \eta)\frac{L}{2} \tag{151}$$

In analogy to the asymmetry in the loop inductances, a finite asymmetry between the critical currents of the JJs is considered by introducing a critical current asymmetry parameter α:

$$I_\mathrm{c,1} = \bar{I}_\mathrm{c}(1 - \alpha) \tag{152}$$

$$I_\mathrm{c,2} = \bar{I}_\mathrm{c}(1 + \alpha), \tag{153}$$

where $\bar{I}_\mathrm{c}$ is the critical current mean value. Inserting Eqs. 149 to 153 into Eqs. 146 to 148 yields expressions for the total current I, and the screening current J

$$I/\bar{I}_\mathrm{c} = (1 - \alpha)\sin(\gamma_1) + (1 + \alpha)\sin(\gamma_2) \tag{154}$$

$$2J/\bar{I}_\mathrm{c} = -(1 - \alpha)\sin(\gamma_1) + (1 + \alpha)\sin(\gamma_2) \tag{155}$$

and an expression for the relation between the phase differences

$$\gamma_2 = \gamma_1 - 2\pi \frac{\Phi_\mathrm{ext}}{\Phi_0} - \pi\beta \frac{J}{\bar{I}_\mathrm{c}} - \pi\beta\eta \frac{I}{2\bar{I}_\mathrm{c}}, \tag{156}$$

as a function of the asymmetry parameters α and η_L, and the screening parameter $\beta = 2L\bar{I}_\mathrm{c}/\Phi_0$. Notably, in some publications, the screening parameter is expressed in terms of the maximal critical current of the SQUID $I_\mathrm{c,max} = 2\bar{I}_\mathrm{c}$, instead of the mean critical current $\bar{I}_\mathrm{c}$ of the individual JJs.

Negligible screening: $\beta = 0$

In case the loop inductance is small compared to the Josephson inductance of each junction ($L \ll L_\mathrm{J}$), according to Eq. 149, the external magnetic flux and the total flux are identical in good approximation. The induced screening current J inside the loop changes its direction every time the external magnetic flux increases by half integer multiples of the flux quantum Φ_0, which is expressed in a simplified relation for the single junction phase differences

$$\gamma_1 - \gamma_2 = 2\pi \left(\frac{\Phi_\mathrm{ext}}{\Phi_0} + s \right) \; , s \in \mathbb{N}. \tag{157}$$

Inserting Eq.(157) into Eq. 146, and identifying the average phase difference $\gamma = (\gamma_1 + \gamma_2)/2$ as the phase difference across the SQUID in the spirit of Eq. 144, yields an analytical expression the flux dependent critical current $I_c(\Phi_{ext})$

$$I_\mathrm{c}(\Phi_\mathrm{ext}) = 2\bar{I}_\mathrm{c} \left| \cos \left(\frac{\pi \Phi_\mathrm{ext}}{\Phi_0} \right) \right| \sqrt{1 + \alpha^2 \tan^2 \left(\frac{\pi \Phi_\mathrm{ext}}{\Phi_0} \right)}. \tag{158}$$

Figure 24 (a) depicts the periodic flux modulation of the critical current as a function of the critical current asymmetry parameter $\alpha \in (0, 0.2, 0.4, 0.6)$. While the maximal value $\max(I_\mathrm{c}) = 2\bar{I}_\mathrm{c}$ is independent of α_c, the asymmetry limits the minimal value found at half a flux quantum, reaching zero for symmetric devices only. Inserting Eq. 158 into Eq. 145 yields an expression for the flux dependent kinetic inductance of the SQUID

$$L_\mathrm{J}(\Phi_\mathrm{ext}) = \frac{L_{J,0}}{\left| \cos \left(\pi \frac{\Phi_\mathrm{ext}}{\Phi_0} \right) \right| \sqrt{1 + \alpha^2 \tan \left(\pi \frac{\Phi_\mathrm{ext}}{\Phi_0} \right)^2}}, \tag{159}$$

with the zero-field inductance $L_\mathrm{J,0}$ determined by the critical currents of the individual JJs

$$L_\mathrm{J,0} = \frac{\Phi_0}{2\pi(2\bar{I}_\mathrm{c})}. \tag{160}$$

Suppressing the critical current by means of an external magnetic field increases the corresponding kinetic inductance, until it reaches a maximal value at half a flux quantum of enclosed flux. According to Eq. 159, the consequence of the critical current asymmetry is a reduction of the critical current modulation depth and, therefore prevents the divergence of the corresponding kinetic inductance at half a flux quantum enclosed in the loop.

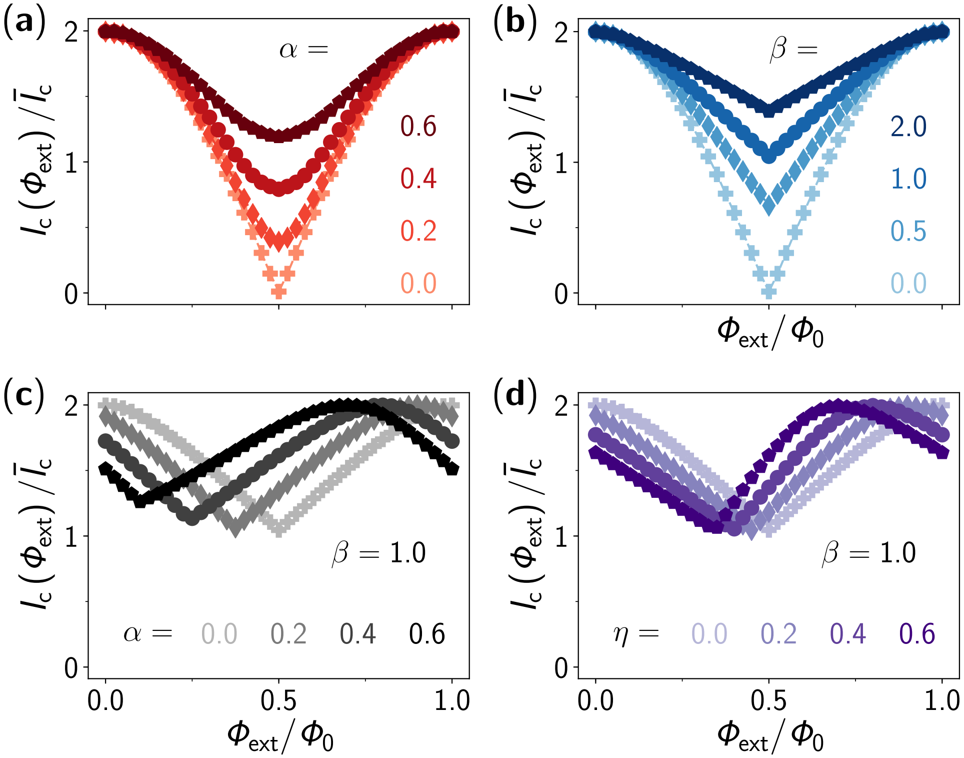

Figure 24: Critical current flux modulation of a dc SQUID. Normalized critical current of a dc SQUID $I_c/\bar{I}_c$ as a function of the applied external magnetic flux in number of magnetic flux quanta Φ_{ext}/Φ_0, numerically calculated for different values of **a)** the critical current asymmetry α, **b)** the screening parameter $\beta = 2L\bar{I}_c/\Phi_0$, **c)** a variable critical current asymmetry and a fixed screening parameter $\beta = 1$, and in **d)** a fixed screening parameter $\beta = 1$ and an asymmetry η between the loop inductance in both SQUID branches. In general, the modulation depth decreases with α and β, but with a significantly different slope around the minimum at half a quantum of external flux. For a combination of a finite screening $\beta = 1$ and critical current asymmetry, the position of the minimum shifts to lower flux values with increasing α. Depending on the relative size of α and β, the shape is either rounded or sharp at the minimum. In case of an increasing asymmetry in the loop inductance η, the position of the maximum shifts more significantly than that of the minimu.

Finite screening: $\beta \neq 0$

In the presence of considerable screening of the external magnetic field due to the loop inductance L, and, especially in case of an asymmetry η_{L} between the inductance in the two SQUID branches, a numerical calculation of the critical current flux modulation is necessary. Following the detailed description presented in Ref. [59], the screening current J is first eliminated in Eq. 156 by inserting the expressions for the total current and the screening current given in Eq. 154 and Eq. 155, respectively:

$$\gamma_2 = \gamma_1 - 2\pi \frac{\Phi_{\mathrm{ext}}}{\Phi_0} - \frac{\pi\beta}{2}(1+\eta)\frac{I}{\bar{I}_{\mathrm{c}}} + \pi\beta(1-\alpha)\sin\gamma_1. \tag{161}$$

The critical current of the SQUID is calculated for every value of the magnetic flux Φ_{ext} individually, by finding the roots of the function

$$F(I,\gamma_1) = \frac{I}{\bar{I}_{\mathrm{c}}} - (1-\alpha_{\mathrm{c}})\sin\gamma_1 - (1+\alpha)\sin\gamma_2 \tag{162}$$

For a given set of values for the bias current $0 \leq I/I_{\mathrm{c}} \leq 2$ and phase difference $0 \leq \gamma_1 \leq 2\pi$, the maximal bias current $\max(I)$ at which the function F possesses a root in γ_1 still, necessarily is the critical current. Consequently, the extracted combination of I and γ_1 will satisfy $\partial F/\partial\gamma_1 = 0$ at the same time, with the derivative given by

$$\frac{\partial F(I,\gamma_1)}{\partial\gamma_1} = -(1-\alpha)\cos\gamma_1 - (1+\alpha)\left[1+\pi\beta(1-\alpha)\cos\gamma_1\right]\cos\gamma_2. \tag{163}$$

Figure 24b-d show the critical current modulation with external flux in the presence of finite screening $\beta \neq 0$, for a symmetry SQUID ($\alpha = \eta = 0$) in panel (b), as well as in combination with a critical current asymmetry ($\alpha \neq 0$, $\eta_{\mathrm{L}} = 0$) in panel (c), and an asymmetry in the loop inductance ($\alpha = 0$, $\eta \neq 0$) in panel (d). In all combinations of SQUID parameters, the critical current reaches a maximal value $2\bar{I}_{\mathrm{c}}$ determined by the sum of the critical currents of the individual JJs. Similar to the reduction of the modulation depth ΔI_{c}, the difference between the minimal and the maximal critical current, with increasing critical current asymmetry α, depicted in Fig. 24a, the modulation depth decreases with increasing screening parameter β, too. However, while the shape of the minimum is round for $\alpha > 0$, it remains sharp for all values of β, which is the main characteristic to distinguish between both cases. For combinations of finite screening and asymmetry, the position of the minimal and maximal critical currents with respect to the applied magnetic flux shift, as indicated in panel (c) and (d).

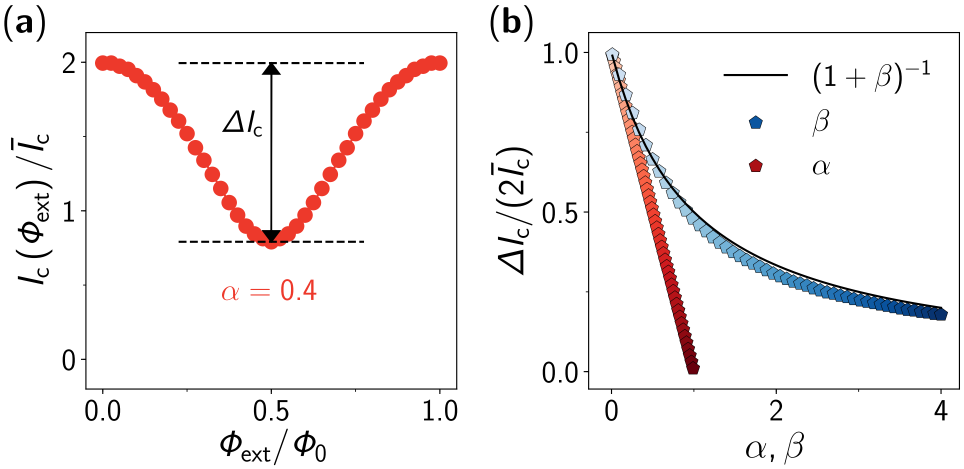

Figure 25: Critical current modulation depth. a) Normalized critical current of a dc SQUID $I_c/\bar{I}_c$ as a function of the applied external magnetic flux in number of magnetic flux quanta Φ_{ext}/Φ_0, numerically calculated for a critical current asymmetry $\alpha = 0.4$. The modulation depth of the critical current ΔI_c is defined as the difference between the minimal and the maximal value. **b)** Relative critical current modulation depth $\Delta I_c/(2\bar{I}_c)$ as a function of the critical current asymmetry parameter α, and the screening parameter β. The values are extracted from numerical calculations, as shown in a), by either varying α or β while keeping the other equal to zero. The loop inductance asymmetry is neglected ($\eta = 0$) in both cases. While the modulation depth decreases linearly with α, eventually approaching no modulation for $\alpha = 1$, it decreases slower with increasing screening parameter β. The solid black line indicates the power law according to Eq. 164, which is in good agreement with the numerical calculation.

Provided the screening due to the loop inductance dominates over the critical current asymmetry, the relative modulation depth is related to the screening parameter β [25]

$$\frac{\Delta I_c}{2\bar{I}_c} \approx \frac{1}{1+\beta}, \tag{164}$$

and the inductance of the loop L can be inferred from the measured modulation depth. Figure 25 depicts the definition of the modulation depth with the aid of the critical current calculated for $\alpha = 0.4$ in panel (a), and the dependence of ΔI_c on the parameters α and β in panel (b). With increasing critical current asymmetry, the modulation depth decreases linearly (red curve), until it vanishes for $\alpha = 1$. Of course this limit is only theoretical, since it requires one of the critical currents to become either zero or infinity. The dependence on the screening parameter (blue curve) is a power law, in agreement with Eq. 164, which is indicated by the solid black line for comparison reasons. Despite the different dependence on α and β, I would like to point out, that the relation between β and the circuit parameters (L and

$\bar{I}_c$) is linear, while it is nonlinear in case of α ($I_{c,1}$ and $I_{c,2}$). For that reason, plotting the modulation depth against $I_{c,2}$, which I assume to increase in order to change the value of α, instead of plotting it against α, would result in a similar power law dependence.

F Josephson Junction and SQUID arrays

A Josephson junction array (JJA) or, alternatively a SQUID array (SQA), is an electrical network formed by the interconnection of multiple ($N \geq 3$) Josephson circuit elements of the same kind [60]. Although the term *array* does not constrain the dimensionality of the network, in the scope of this thesis I will use the term synonymously and solely to describe one-dimensional chains of JJs or SQUIDs. However, even in the one-dimensional case, the potentially large number of degrees of freedom can give rise to rich many-body phenomena [52].

Since JJs and SQUIDs are quantum objects in general, the dynamics of JJAs can be either semi-classical, provided the Josephson energy of a single element dominates over the charging energy ($E_\mathrm{J} \gg E_\mathrm{c}$), or quantum mechanical in the opposite case ($E_\mathrm{J} \ll E_\mathrm{c}$). Since charge and phase are conjugate variables in a supercondutor, the suppression of charge fluctuations can induce a superconductor-to-insultator transition [17, 58]. The applications of JJAs are manifold, but are highly dependent on the parameter regime. Classical arrays are used for the implementation of large inductors, denoted superinductors if the corresponding impedance of the array is larger than the resistance quantum ($Z \geq R_\mathrm{Q}$) [42, 45], or alternatively as weak sources of nonlinearity in superconducting parametric amplifiers [5, 66, 68], while quantum arrays are utilized to investigate the Coulomb blockade of Cooper pairs [30], the formation of charge solitons [1, 11], and quantum phase slips [50].

Similar to the phonon spectrum present in a crystalline solid state, the number of independent degrees of freedom N determines the total number of eigenmodes of the circuit. The dependence of the eigenenergies E_m, or alternatively the corresponding frequency of the eigenmodes ω_m on the mode number m is referred to as the *dispersion relation* of the array. In general, the dispersion relation is nonlinear and depends not only on the parameters of the circuit elements, the Josephson energy E_J and charging energy E_c, but also on the boundary conditions. In contrast to the solid state, the boundary condition on both ends of the array can be determined deliberately, either by a capacitive or a galvanic coupling to the environment. The choice of coupling will determine the standing-wave pattern of current and voltage along the array.

For long arrays ($N \gg 1$), the circuit topology gives rise to low-frequency eigenmodes, for which the effective wavelengths are much larger than the distance between neighboring circuit elements, and, hence the modes are similar to the acoustic harmonics of a string. Although the eigenmodes of a JJA are generally nonlinear in power, the otherwise much larger phase fluctuations across single JJs is diluted over many elements, which reduces the nonlinearity of the mode significantly [15]. In the context of cQED, the control of this nonlinearity is used to enhance the saturation power of Josephson parameteric amplifiers, which is discussed in more detail in Ch. 3.

Despite the exact application, first and foremost, a mathematical description of the array based on an effective circuit model is required, which is introduced in the following section. The eigenmodes are calculated from the linearized Lagrangian of the circuit model, while the nonlinearity arising from the cosine potential of the JJs is introduced perturbatively, with only the first order nonlinearity being considered. Besides the microwave properties of the closed system, the external coupling rates to a microwave input port are of interest provided the eigenmodes of the JJA are readout directly.

F.1 Dispersion relation

The dispersion relation or eigenmode spectrum of a one-dimensional array of JJs, or equivalently dc SQUIDs, is calculated numerically from the linearized Lagrangian of an effective circuit model, which is based on the quantum-phase model [17]. The circuit model consists of N junctions with assigned critical current $I_{\mathrm{c},i}$ and corresponding Josephson energy $E_{\mathrm{J},i} = \Phi_0 I_{\mathrm{c},i}/(2\pi)$ for the ith element, and is shown in Fig. 26a. The junction capacitance $C_{\mathrm{J},i}$ arising between the superconducting electrodes is in parallel with the nonlinear inductive contribution for each Josephson element. The interconnections between the Josephson elements are described as superconducting islands with capacitance C_0 to ground. For simplicity, the inductive contribution of the islands is neglected. For a quantum mechanical treatment, the node charges and phases associated to the superconducting islands, $\hat{Q}_i$ and $\hat{\varphi}_i$, are conjugate variables (see App. A).

In case of dc SQUID-junctions with small loop inductance and screening parameter ($\beta \ll 1$), the critical currents and corresponding Josephson energies become functions of the external magnetic flux Φ_{ext}, but apart from this, the treatment is identical. Hence, I use the terms JJA and SQA interchangeably throughout my thesis.

Although identical circuit elements are desired in the scope of my thesis, which is why I will drop the node index i for the circuit parameters, an intentional periodic variation of the circuit parameters can induce band structures into the dispersion relation similar to photonic crystals [31], which has recently been exploited to build travelling wave parametric amplifiers based on SQUID arrays [49].

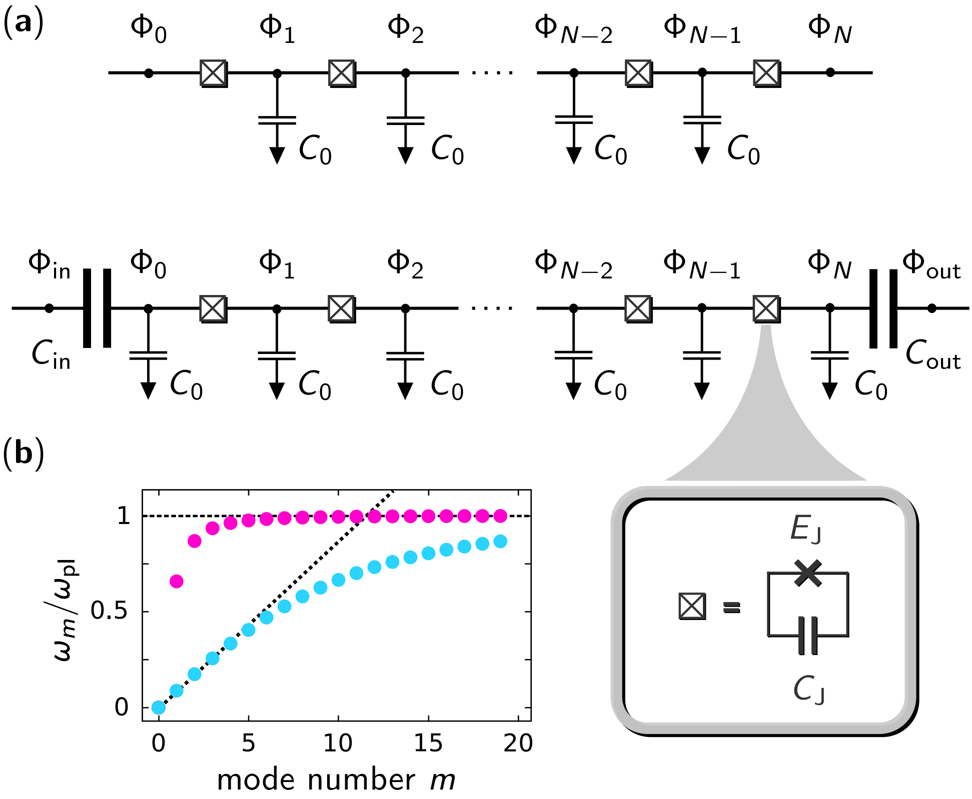

Figure 26: Josephson junction arrays. a) Schematic circuit diagram of a one-dimensional chain of N identical Josephson elements (crossed box). As indicated by the grey box, the Josephson elements represent either single JJs with constant Josephson energy $E_\mathrm{J} = \Phi_0 I_\mathrm{c}/(2\pi)$ and ideal current phase relation (cross), that are shunted by the junction capacitance C_J with charging energy $E_\mathrm{c} = e^2/(2C_\mathrm{J})$, or flux tunable dc SQUID junctions. Provided the screening parameter of the SQUID is small ($\beta \ll 1$), the SQUID behaves similar to a JJ with flux dependent critical current (see App. E). The island connecting the Josephson elements exhibit a capacitance to ground C_0. The boundary condition on both ends of the array depends on the coupling mechanism, and is either galvanic (top panel) or capacitive (bottom panel). In the latter case, the coupling capacitors are C_{in} and C_{out}. **b)** Numerically calculated dispersion relation of a short ($N = 180$, blue) and long ($N = 1800$, red) array. The eigenfrequencies ω_m are normalized by the plasma frequency $\omega_{\mathrm{pl}} \approx \sqrt{8E_\mathrm{J}E_\mathrm{c}}$, the self-resonance frequency of each Josephson element. The capacitance ratio is $C_\mathrm{J}/C_0 = 2500$. For the short array, most eigenmodes accumulate close to the plasma frequency, while the long array exhibits an almost linear dispersion relation for the first few modes, indicated by the black dashed line.

Boundary conditions:

The boundary conditions on both ends of the array depend on the coupling mechanisms, which can be either capacitive or galvanic, resulting in an antinode of the voltage or the current at these locations, respectively. Provided the coupling is galvanic on both ends, the Lagrangian is

$$\mathcal{L} = \sum_{i=1}^{N-1} \frac{C_0}{2}\dot{\Phi}_i^2 + \sum_{i=0}^{N-1} \frac{C_\mathrm{J}}{2} \left(\dot{\Phi}_{i+1} - \dot{\Phi}_i\right)^2 - E_\mathrm{J}\cos(\phi_{i+1} - \phi_i). \tag{165}$$

Here, ϕ_i is the superconducting phase of the i th island, which is related to the node flux $\Phi_i = \Phi_0\phi_i/(2\pi)$ introduced in Sec. 1.1.1. Since the voltage is related to the time derivative of the node flux, and has to vanish for a galvanic coupling, the boundary condition translates into $\Phi_0 = \Phi_N = 0$. For a capacitive coupling at both ends, the Lagrangian is

$$\begin{aligned}\mathcal{L} = &\sum_{i=1}^{N-1} \frac{C_0}{2}\dot{\Phi}_i^2 + \frac{C_\mathrm{in}}{2}\left(\dot{\Phi}_0 - \dot{\Phi}_\mathrm{in}\right)^2 + \frac{C_\mathrm{out}}{2}\left(\dot{\Phi}_\mathrm{out} - \dot{\Phi}_N\right)^2 \\ &+ \sum_{i=0}^{N-1} \frac{C_\mathrm{J}}{2}\left(\dot{\Phi}_{i+1} - \dot{\Phi}_i\right)^2 - E_\mathrm{J}\cos(\phi_{i+1} - \phi_i).\end{aligned} \tag{166}$$

Here, C_in and C_out are the coupling capacitors at the two ends of the array. In the absence of a voltage drive, the coupling capacitors are grounded ($\Phi_\mathrm{in} = \Phi_\mathrm{out} = 0$).

Linearized Lagrangian:

In the limit of small circulating currents with respect to the critical current of the junctions $I \ll I_\mathrm{c}$, the phase drop $\phi_{i+1} - \phi_i$ across each junction becomes small even in regions of maximal current, and the Lagrangian is linerized by approximating the nonlinear cosine potentials with harmonic potentials. The corresponding coefficients are the linear Josephson inductances L_J as introduced in Sec. 1.1.2.

$$\mathcal{L} = \sum_{i=1}^{N} \frac{C_0}{2}\dot{\Phi}_i^2 + \sum_{i=0}^{N} \frac{C_\mathrm{J}}{2}\left(\dot{\Phi}_{i+1} - \dot{\Phi}_i\right)^2 - \frac{1}{2L_\mathrm{J}}(\Phi_{i+1} - \Phi_i)^2. \tag{167}$$

Since the linearization does not affect the role of the capacitive contributions, the Lagrangian of a capacitively coupled array given in Eq. 166 can be linearized analogously. In order to solve for the eigenfrequencies of the system, the linear Lagrangian given in Eq. 167 is expressed in a more compact form by introducing the node flux vector $\vec{\Phi} = (\Phi_0, ..., \Phi_N)$, as well as the inverse inductance and capacitance matrices $\tilde{L}^{-1}$ and $\tilde{C}$, respectively. The matrix representation of the Lagrangian is

$$\mathcal{L} = \frac{1}{2}\dot{\vec{\Phi}}^{\mathrm{T}}\tilde{C}\dot{\vec{\Phi}} - \frac{1}{2}\vec{\Phi}^{\mathrm{T}}\tilde{L}^{-1}\vec{\Phi}. \tag{168}$$

The matrices contain the information about the distribution of the circuit parameters along the array, and are of dimension $(N-1)\times(N-1)$ and $N \times N$ depending on the coupling mechanism. For the galvanically coupled array, the capacitance matrix in its simplest form is

$$\tilde{C} = \begin{pmatrix} 2C_{\mathrm{J}}+C_0 & -C_{\mathrm{J}} & 0 & \dots & & & \\ -C_{\mathrm{J}} & 2C_{\mathrm{J}}+C_0 & -C_{\mathrm{J}} & 0 & \dots & & \\ 0 & -C_{\mathrm{J}} & 2C_{\mathrm{J}}+C_0 & -C_{\mathrm{J}} & 0 & \dots & \\ \vdots & \ddots & \ddots & \ddots & \ddots & \ddots & \ddots \end{pmatrix}, \tag{169}$$

and the inverse inductance matrix is

$$\tilde{L}^{-1} = \begin{pmatrix} \frac{2}{L_{\mathrm{J}}} & -\frac{1}{L_{\mathrm{J}}} & 0 & \dots & & & \\ -\frac{1}{L_{\mathrm{J}}} & \frac{2}{L_{\mathrm{J}}} & -\frac{1}{L_{\mathrm{J}}} & 0 & \dots & & \\ 0 & -\frac{1}{L_{\mathrm{J}}} & \frac{2}{L_{\mathrm{J}}} & -\frac{1}{L_{\mathrm{J}}} & 0 & \dots & \\ \vdots & \ddots & \ddots & \ddots & \ddots & \ddots & \ddots \end{pmatrix}. \tag{170}$$

While the inverse inductance matrix reflects the reality of nearest neighbour inductive coupling, the capacitance matrix is a simplification. In experimental realizations of JJAs, especially in microstrip geometries where the distance to the ground is much larger than the distance between neighboring elements, the ground can mediate long-range Coulomb-interactions between the charges on the superconducting islands. A more complete picture is discussed in Ref. [35], which potentially results in a quantitatively better agreement between the experimental observation and the model prediction.

Diagonalization:

Starting from Eq. 168, the eigenenergies E_m of the system can be calculated either by deriving the Hamiltonian by means of a Legendre transformation introducing the canonical momenta $Q_i = \frac{\partial \mathcal{L}}{\partial \dot{\Phi}_i} = C_{ij}\dot{\Phi}_j$ first, before it is diagonalized, or by diagonalizing the Lagrangian directly. While the Hamiltonian is

$$H_0 = \frac{1}{2}\vec{Q}^{\mathrm{T}}\tilde{C}^{-1}\vec{Q} + \frac{1}{2}\vec{\Phi}^{\mathrm{T}}\tilde{L}^{-1}\vec{\Phi}, \tag{171}$$

the diagonalization of the Lagrangian is realized by performing a coordinate transformation of the form

$$\vec{Y} = \tilde{C}^{1/2}\vec{\Phi}, \tag{172}$$

where $\tilde{C}^{1/2}$ is the square root of the capacitance matrix satisfying $\tilde{C}^{1/2} \cdot \tilde{C}^{1/2} = \tilde{C}$. The transformed Lagrangian in matrix representation is

$$\mathcal{L} = \frac{1}{2}\dot{\vec{Y}}^{\mathrm{T}}\dot{\vec{Y}} - \frac{1}{2}\vec{Y}^{\mathrm{T}}\tilde{C}^{-1/2}\tilde{L}^{-1}\tilde{C}^{-1/2}\vec{Y}, \tag{173}$$

from which the energy eigenvalues $E_m = \hbar\omega_m$ and the corresponding eigenvectors $\vec{\Psi}_m$ are found by solving the eigenvalue problem [64]

$$\underbrace{\tilde{C}^{-1/2}\tilde{L}^{-1}\tilde{C}^{-1/2}}_{\tilde{\Omega}}\vec{\Psi}_m = \omega_m^2\vec{\Psi}_m. \tag{174}$$

Since the matrix $\tilde{\Omega}$ is orthogonal, implying $\tilde{\Omega}^{\mathrm{T}} = \tilde{\Omega}^{-1}$, the resulting eigenvectors $\vec{\Psi}_m$ are orthogonal, too, and the eigenvalues are real. In the case under consideration, the eigenvectors $\vec{\Psi}_m$ are related to the node flux eigenvectors of the array, $\vec{\Phi}_m$, via the capacitance matrix and the eigenfrequencies

$$\vec{\Phi}_m = \sqrt{\frac{\hbar}{2\omega_m}}\tilde{C}^{-1/2}\vec{\Psi}_m, \tag{175}$$

and describe the (classical) standing-wave pattern of each mode along the array. Since the current I through, and the voltage drop V across the i th circuit element is related to the gradient of the magnetic flux $\Delta\Phi_i = \Phi_{i+1} - \Phi_i$ and its derivative $\Delta\dot{\Phi}$, respectively, the magnetic flux eigenvectors give insight into the standing-wave pattern of current and voltage.

Until now, the description of the array was classical. In the quantum mechanical case, as discussed in more detail in Ref. [64], the flux eigenvectors are promoted to operators, which can be describe in terms of pairs of bosonic single-mode field amplitude creation and annihilation operators $\hat{a}_m^\dagger$ and $\hat{a}_m$, respectively,

$$\hat{\vec{\Phi}}_m = \sqrt{\frac{\hbar}{2\omega_m}}\tilde{C}^{-1/2}\vec{\Psi}_m\left(\hat{a}_m + \hat{a}_m^\dagger\right). \tag{176}$$

Hence, the entries in the eigenvectors can be thought of as the zero-point fluctuations of the flux, or equivalently the phase across each JJ. The node flux vector $\vec{\Phi}$, as introduced in context of the matrix representation of the Lagrangian in Eq. 173, can be expressed as the sum of these

$$\hat{\vec{\Phi}} = \sum_m \hat{\vec{\Phi}}_m. \tag{177}$$

By inserting Eq. 177 into Eq. 171, the linear Hamiltonian expressed in second quantization is

$$\hat{H} = \sum_{m=0}^{N-1} \hbar\omega_m \hat{a}_m^{\dagger}\hat{a}_m. \tag{178}$$

Energy spectrum:

Two examples for the dispersion relation of a JJA are given in Fig. 26b, showing the eigenenergies ω_m of the first twenty eigenmodes, normalized by the plasma frequency ω_{pl}, for a shorter array with $N = 180$ (pink) and a longer array with $N = 1800$ (cyan) JJs. Notably, due to the additional capacitance to ground C_0, the plasma frequency of the array is reduced

$$\omega_{\mathrm{pl}} = \frac{1}{\sqrt{L_{\mathrm{J}}(C_{\mathrm{J}} + C_0/4)}}, \tag{179}$$

although the change is significant only if the capacitance to ground is comparable to the junction capacitance. For the arrays studied in this thesis, the capacitance to ground is at least two orders of magnitude smaller, and its contribution to the plasma frequency is negligible.

The dispersion relation of the longer array exhibits an almost linear regime at the beginning, with an approximately equidistant detuning between the modes, becoming appreciably nonlinear only after the sixth eigenmode. By comparing this results with the shorter array, it becomes evident that the number of modes in this linear regime, as well as the frequency detuning between them, depend on the total number of Josephson elements N. Moreover, the slope of the linear regime, indicated by the black dashed line, is controlled by the ratio of junction capacitance to ground capacitance, which is $C_{\mathrm{J}}/C_0 = 2500$ in the given examples. Hence, in case $C_{\mathrm{J}} \gg C_0$ and in the light of the large number of degrees of freedom, it is legit to state that the vast majority of eigenmodes accumulate close to the plasma frequency, while a few eigenmodes are addressable individually only.

Standing-wave pattern:

Figure 27a depicts the first four eigenvectors $\vec{\Phi}_m$ ($m \in \{0, 1, 2, 3\}$) as a function of the node number i, numerically calculated for a JJA with $N = 180$ elements and symmetric capacitive coupling on both ends ($C_{\mathrm{in}} = C_{\mathrm{out}} \ll C_{\mathrm{J}}$). Due to the boundary conditions, the voltage exhibits an antinode on both ends for all modes, with the fundamental mode being a $\lambda/2$ mode. Neighboring voltage antinodes are

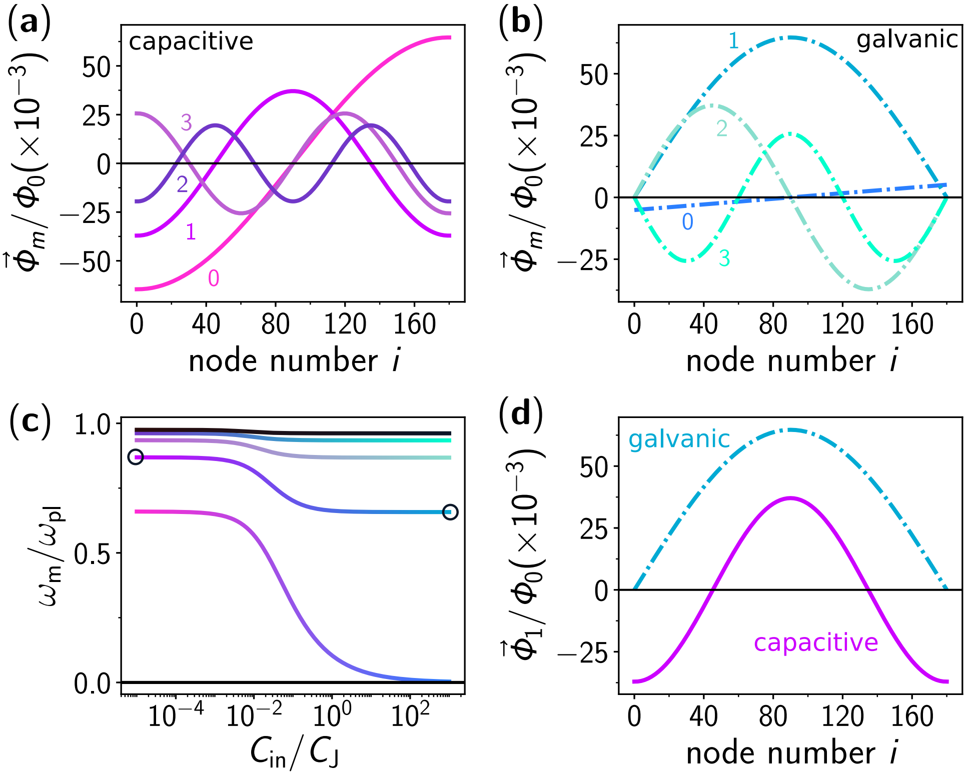

Figure 27: JJA: capacitive vs. galvanic coupling. a) Magnetic flux eigenvectors $\vec{\Phi}_m$ normalized by the magnetic flux quantum Φ_0 for the first four eigenmodes of a capacitively coupled JJA with $N = 180$ elements, plotted against the node number i as defined in Fig. 26a (bottom panel). The coupling capacitances on both ends are identical and assumed to be small compared to the junction capacitance ($C_\mathrm{in} = C_\mathrm{out} \ll C_\mathrm{J}$). Since the current I and voltage V are proportional to the gradient of the magnetic flux and its derivative, respectively, the standing-wave patterns of the eigenvectors give insight into the modal distribution of I and V. Therefore, voltage antinodes are located at the positions of the maxima, while current antinodes are located at the roots of the distribution. The effective wavelength $\lambda_{\mathrm{eff},m}$ of the mode is given by the standing-wave pattern and the physical length of the JJA. For a long array, the lowest frequency modes resemble the harmonics of an accoustic system with open boundary conditions ($\lambda/2$, λ, $3\lambda/2, ...$). **b)** Magnetic flux eigenvectors of a galvanically coupled JJA. In contrast to the capacitively coupled array, the first eigenmode is a dc mode and all eigenmodes with standing-wave pattern exhibit current antinodes on both ends. **c)** Dispersion relation of a capacitively coupled array as a function of the ratio between input and junction capacitance. Again $C_\mathrm{in} = C_\mathrm{out}$, and the eigenfrequencies are normalized by the plasma frequency ω_pl. With increasing coupling capacitance, the capacitively coupled array effectively turns into a galvanically coupled array, as indicated by the standing-wave pattern of the second eigenmode shown in **d)**.

separated by a current antinode, with the total number of voltage antinodes given by $m+2$. Hence, while the even modes exhibit a maximum of the current in the center of the array, the odd modes exhibit a voltage maximum. The amplitude of the standing-wave pattern decreases with increasing mode number m. As opposed to this, for a galvanically coupled array, shown in Fig. 27b, current antinodes are located on both ends, and the fundamental mode is a dc mode with linear standing-wave pattern and zero frequency $\omega_m = 0$.

The transtition between the two coupling regimes is indicated in Fig. 27c with the aid of the eigenenergies of the first six modes of a JJA, plotted against the coupling capacitance C_{in}. With increasing coupling capacitance, the energy spectrum transits from the dispersion relation of a capacitively coupled JJA into that of a galvanically coupled array. As indicated by the black solid line, the fundamental mode approaches zero-frequency, although it will never actually reach zero. The transition occurs in the region in which the frequency dependent impedance of the coupling capacitance is larger than that of the junction capacitance, but smaller than that of the ground capacitance. The parameter induced change of boundary conditions is further emphasized in Fig. 27d, by a comparison between the standing-wave patterns of the second overall mode for the two extremal conditions indicated by the black circles in panel c. The previously λ mode turns into a $\lambda/2$ mode.

F.2 Kerr coefficients

The nonlinearity in JJAs arises from the cosine potential of the individual Josephson elements. Since the nonlinearity of a single JJ depends on the phase fluctuations across the junction, the nonlinearity in a JJA is much lower in magnitude in general, and is therefore treated perturbatively

$$\hat{H} = \hat{H}_0 + \hat{H}_1, \tag{180}$$

where $\hat{H}_0$ is the linear Hamiltonian given in Eq. 178, and the perturbation term is

$$\hat{H}_1 = -\frac{E_\mathrm{J}}{24}\sum_{i=0}^{N-1}\left(\hat{\phi}_{i+1}-\hat{\phi}_i\right)^4 = -\frac{E_\mathrm{J}}{24}\left(\frac{2e}{\hbar}\right)^4\sum_{i=0}^{N-1}\left(\hat{\Phi}_{i+1}-\hat{\Phi}_i\right)^4. \tag{181}$$

By inserting the expression for the node flux operators

$$\hat{\Phi}_i = \sum_{m,j}\tilde{C}_{i,j}^{-1/2}\Psi_{m,j}\sqrt{\frac{\hbar}{2\omega_j}}\left(\hat{a}_j+\hat{a}_j^\dagger\right), \tag{182}$$

into the nonlinear Hamiltonian given in Eq. 181, and applying the rotating-wave approximation yields the nonlinear Hamiltonian

$$\mathbf{H} = \sum_{m=0}^{N-1} \hbar\omega_m \hat{a}_m^\dagger \hat{a}_m + \underbrace{\frac{\hbar}{2} K_{m,m}\omega_m \hat{a}_m^\dagger \hat{a}_m \hat{a}_m^\dagger \hat{a}_m}_{\text{self-Kerr}} + \underbrace{\sum_{m,k=0}^{N-1} \frac{\hbar}{2} K_{m,k}\omega_m \hat{a}_m^\dagger \hat{a}_m \hat{a}_k^\dagger \hat{a}_k}_{\text{cross-Kerr}}, \tag{183}$$

given in Eq. 3.1 in the main text. Notably, the terms considered describe interactions between two modes at most, even though the nonlinear Hamiltonian in Eq.181 gives rise to further interactions. The terms neglected describe the interaction of two modes via a third one, and the pairwise creation and annihilation of photons in four different modes [64].

The coefficients in front of the second and the third term are referred to as the self-Kerr and the cross-Kerr coefficients, respectively. As mentioned during the introduction, the two effects describe the frequency dependence of the m th eigenfrequency on the average photon number occupying the same mode m or another mode k, respectively. The Kerr coefficients are identified as

$$K_{m,m} = -\frac{2\hbar\pi^4 E_\mathrm{J}\eta_{mmmm}}{\Phi_0^4 C_\mathrm{J}^2 \omega_m^2}, \tag{184}$$

and

$$K_{m,k} = -\frac{4\hbar\pi^4 E_\mathrm{J}\eta_{mmkk}}{\Phi_0^4 C_\mathrm{J}^2 \omega_m \omega_k}, \tag{185}$$

where η_{mmkk} is a numerical factor that takes the standing-wave pattern into account. In particular, the higher the mode number, the larger is the average phase fluctuation across each JJ, and the larger the nonlinearity is, as can be seen from panel a and b in Fig. 27. The numerical factor is

$$\begin{aligned}\eta_{mmkk} =& C_\mathrm{J}^2 \sum_{i=1}^{N} \left[\left(\sum_{j=0}^{N} \left(\tilde{C}_{i,j}^{-1/2} - \tilde{C}_{i-1,j}^{-1/2} \right) \Psi_{j,m} \right)^2 \right.\\ & \left. \times \left(\sum_{j=0}^{N} \left(\tilde{C}_{i,j}^{-1/2} - \tilde{C}_{i-1,j}^{-1/2} \right) \Psi_{j,k} \right)^2 \right].\end{aligned} \tag{186}$$

Here $\Psi_{j,m}$ is the j th entry of the m th eigenvector $\vec{\Psi}_m$, and $\tilde{C}_{i,j}^{-1/2}$ is the entry in the i th row and the j th column of the square root of the inverse capacitance matrix. Generally speaking, the Kerr coefficients increase with increasing mode number m, but saturate as soon as the dispersion relation approaches the plasma frequency.

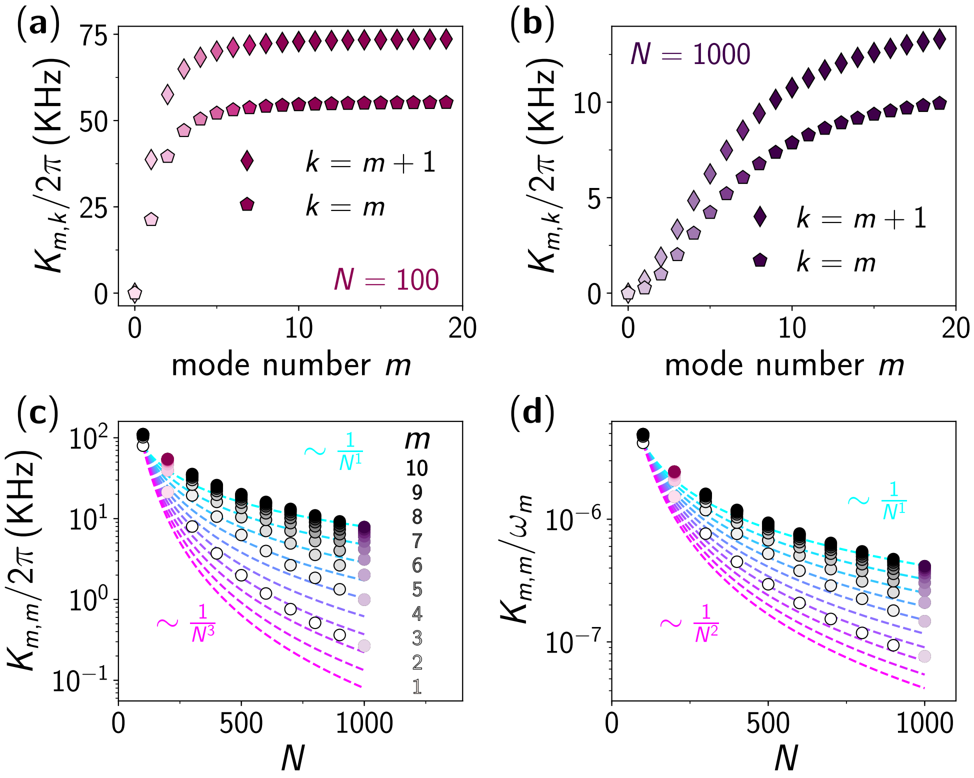

Figure 28: JJA: Kerr coefficients. Self-Kerr and next neighbor cross-Kerr coefficients $|K|_{m,m}$ (circles) and $|K|_{m,m+1}$ (diamonds), respectively, numerically calculated as a function of the mode number m for an array with $N = 100$ (panel **a**) and with $N = 1000$ JJs (panel **b**). Both arrays are assumed to be galvanically grounded on both ends. The Josephson inductance is $L_\mathrm{J} = 50\,(\mathrm{pH})$, the junction capacitance is $C_\mathrm{J} = 1\,\mathrm{pF}$ and the capacitance to ground is $C_0 = C_\mathrm{J}/2500$. Similar to the dispersion relation of the short array shown in Fig. 26b (blue), the Kerr coefficients quickly saturate and accumulate close to a maximal value for $m \geq 4$. For the longer array, the saturation is slower, and the overall magnitude of the coefficients is lower. **c)** Self-Kerr coefficients of the first 10 eigenmodes, expect for the fundamental (dc) mode, as a function of the total number of Josephson elements N. The other circuit parameters remain again fixed. With increasing length, the self-Kerr coefficients decrease. In shades of pink and purple are the solutions presented in panel a and b, respectively. The dashed lines indicate curves of the type $\sim 1/N^\epsilon$, with $\epsilon \in [1, 3]$. The comparison to the numerical solutions emphasizes the much stronger decrease in nonlinearity for the first mode. **d)** The ratios between the self-Kerr coefficients and the corresponding eigenfrequencies $|K|_{m,m}/\omega_m$ show, that the reduction in frequency is faster than the reduction in nonlinearity. Furthermore, the small magnitude of the ratios for the given circuit parameters justify the perturbative treatment of the nonlinearity.

Scaling with the array length N:

The frequencies ω_m and the Kerr-coefficients $K_{m,m}$ and $K_{m,k}$ of the eigenmodes are essential variables when designing experiments involving JJAs. Since they are not independent, but are both controlled by the circuit parameters and the length of the array, a compromise might has to be found if one or the other underlies experimental constraints. If an overall low nonlinearity is desired, which is a common condition in Josephson parametric amplifiers and superconducting qubits, the natural choice seems to be an increase of the array length. Despite the following discussion, a detailed analysis on the scaling of the nonlinearity with N, even in circuits containing additional linear inductive elements, can be found in Ref. [56].

Figure 28 panel a and b depict the self-Kerr and next neighbor cross-Kerr coefficients $|K|_{m,m}$ and $|K|_{m,m+1}$, respectively, as a function of the mode number m for two arrays with identical circuit parameters $L_\mathrm{J} = 50\,\mathrm{pH}$, $C_\mathrm{J} = 1\,\mathrm{pF}$, and $C_0 = C_\mathrm{J}/2500$, but different total number of Josephson elements, $N = 100$ (panel a) and $N = 1000$ (panel b). Similar to the comparison of the dispersion relation of a relatively short to a much longer array in Fig. 26b, the Kerr coefficients saturate much earlier in terms of the mode number in the short array, while the absolute values are much lower for the long array. In Fig. 28 panel c, the self-Kerr coefficients of the first 10 modes, except for the fundamental (dc) mode, are plotted on a log scale for arrays with increasing total length N. The dependence clearly shows that the reduction in nonlinearity is the strongest for the first mode ($m = 1$), by more than two orders of magnitude between the shortest ($N = 100$) and the longest ($N = 1000$) array. With increasing mode number, the reduction with length is less pronounced. The dashed lines indicate curves of the type $\sim 1/N^\epsilon$, with $\epsilon \in [1, 3]$, in order to emphasize the scaling of the nonlinearity with length.

Besides the reduction in nonlinearity, the frequency of the corresponding mode decreases with length, too. Fig. 28d shows the ratio between the self-Kerr coefficient and the corresponding eigenmode frequency. As can be seen, the frequency of the modes decreases faster with N than the nonlinearity. Therefore, if a certain resonance frequency needs to be met, the scaling of the nonlinearity is actually much weaker than the fast decrease with $\sim N^{2.5}$ shown in Fig. 28c. Although in principle the choice of the eigenmode is free, and, so far, has an implication on the reduction of the nonlinearity only, the coupling to a microwave input port is affected by the mode number and array length, too. Especially in the context of standing-wave parametric amplifier concepts, for which the coupling rate determines the bandwidth of the amplifier, a sufficiently strong coupling needs to be ensured.

F.3 External coupling

In order to complete the picture of JJAs from the perspective of (quantum) electrical engineering, the reamining property, the coupling rate κ to a microwave input port needs to be examined. Similar to the previous treatment, the coupling rate is determined based on a numerical calculation method.

The linear microwave response of a JJA can be predicted from an effective circuit model by calculating the corresponding reflection coefficient $\Gamma(\omega)$, or denoted $S_{11}(\omega)$ in the context of electrical engineering, as a function of probe frequency ω. Provided the eigenmodes of the array are sufficiently detuned in frequency compared to the linewidth of the mode $\Delta\omega_m = \omega_{m+1} - \omega_m \gg \kappa_m$, the microwave response of each eigenmode can be examined individually in terms of its resonance frequency ω_m and external coupling rate κ_m. In analogy to a single resonance and in the absence of microwave losses, the phase of the reflection coefficient $\arg(S_{11})$ undergoes a phase roll of 2π in close vicinity to the resonance frequencies ω_m. From a fit of the numerical data to the theoretical prediction based on a simple resonator model, ω_m and κ_m are determined for each mode.

Transmission matrix approach:

In a reflection measurement of an electrical circuit, the reflection coefficient Γ is determined by the input impedance of the circuit Z_{in} as seen from the respective port, and the charactersitic impedance Z_0 of that same port [51]. However, since it is rather cumbersome to calculate the input impedance of a JJA and its frequency dependence analytically, a much more convenient approach is to numerically calculate the reflection coefficient Γ from the S_{11} entry of the scattering matrix of an effective two-port network, based on a transmission matrix approach [51]. In case only a single physical port is connected to the JJA, the second port of the transmission matrix is grounded.

Generally speaking, the transmission matrix $\tilde{T}$ of a two-port network relates the current and voltage of the first port, denoted I_1 and V_1, respectively, to the current and voltage of the second port, denoted I_2 and V_2 accordingly.

$$\begin{pmatrix} V_1 \\ I_1 \end{pmatrix} = \underbrace{\begin{pmatrix} A & B \\ C & D \end{pmatrix}}_{\tilde{T}} \begin{pmatrix} V_2 \\ I_2 \end{pmatrix} \tag{187}$$

The scattering and transmission matrix representation of a two-port network are shown in Fig. 29. Since both representations describe the same physical system, the

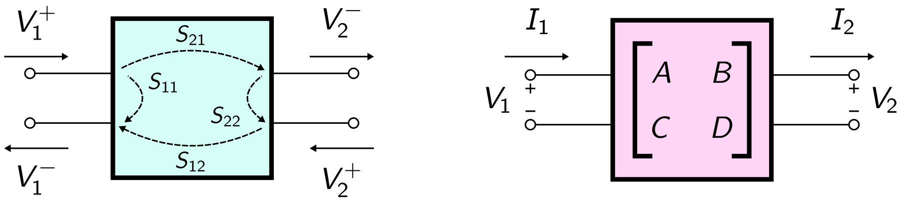

Figure 29: Scattering and transmission matrix. Scattering matrix (cyan) and transmission matrix (purple) of a two-port network. The entries of the scattering matrix are defined as the ratios of the voltages $S_{ij} = V_i^- / V_j^+$ incident to the jth port, and outgoing through the ith port, while the incident voltage on all other ports is zero $V_k^+ = 0 (k \neq j)$. Therefore, the entry S_{11} is the reflection coefficient measured from the first port. The entries of the transmission matrix relate the current and voltage of the first port, I_1 and V_1, respectively, with those of the second port, denoted I_2 and V_2. The relations between the two ports are $V_1 = AV_2 + BI_2$ and $I_1 = CV_2 + DI_2$.

entries of both matrices are related. The reflection coefficient measured from the first port is [51]

$$S_{11} = \frac{A + B/Z_0 - CZ_0 - D}{A + B/Z_0 + CZ_0 + D}, \tag{188}$$

where A, B, C and D are the entries of the transmission matrix, which are complex and frequency dependent in general, and Z_0 is again the characteristic impedance of the input port.

The convenience of this approach in the context of JJA arises from the fact, that the whole JJA can be represented by an effective two-port network with corresponding transmission matrix $\tilde{T}$, which is calculated from the transmission matrices $\tilde{T}_i$ representing each circuit element individually, simply by subsequent matrix multiplications of these matrices:

$$\tilde{T} = \prod_{i=1}^{N+1} \tilde{T}_i = \begin{pmatrix} A & B \\ C & D \end{pmatrix} \tag{189}$$

The reflection coefficient as seen from the input port connected to the array is then calculated from the four entries of the transmission matrix using Eq. 188.

According to the effective circuit model shown in Fig. 30a, the JJA can be broken down to a unit cell composed of three elements: a Josephson element represented by a parallel LC circuit, with junction capacitance C_J and generally tunable inductance $L_\mathrm{J}(\Phi_\mathrm{ext})$ to account for the flux tunability of SQUIDs, as well as the capacitance to ground C_0 and stray inductance L_s of the superconducting island connecting the

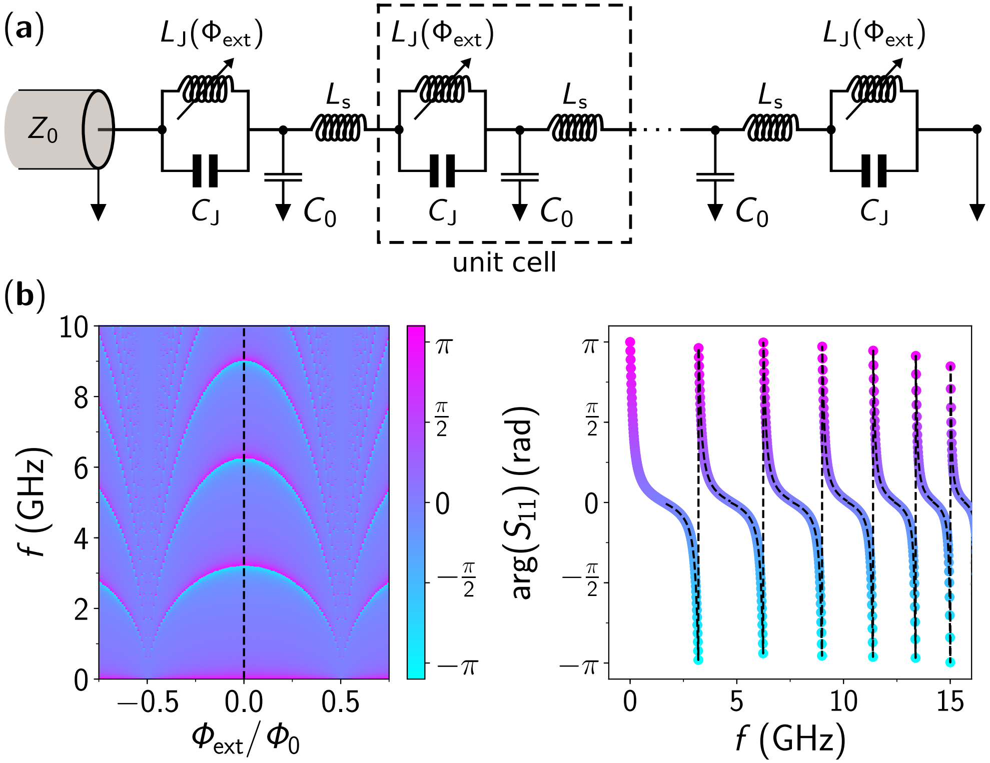

Figure 30: JJA: External coupling. a) Linear circuit model of a one-dimensional Josephson junction array. The unit cell of the array is composed of three circuit elements connected in series: a Josephson element represented by a parallel circuit of a tunable inductance $L_J(\Phi_{ext}) = L_{J,0}/|\cos(\pi\Phi_{ext}/\Phi_0)|$, shunted by the junction capacitance C_J, and a superconducting island with capacitance to ground C_0, and linear stray inductance L_s. The input port is taken into account by a semi-infinite transmission line with characteristic impedance Z_0, while the other end of the array is connected to ground. **b)** Phase of the complex reflection coefficient $\arg(S_{11})$, numerically calculated using a transmission matrix approach as a function of the probe frequency $\omega = 2\pi f$ and the external magnetic flux Φ_{ext} in numbers of the magnetic flux quantum Φ_0. The circuit parameters plugged in into the calculation are $N = 1000$, $L_{J,0} = 50\,\text{pH}$, $C_J = 1\,\text{pF}$, $C_0 = C_J/2500$, and $L_s = 10\,\text{pH}$. The individual modes are clearly visible due to the sharp phase roll-off which occurs on the order of the linewidth. Since the microwave losses are zero, the linewidth is equal to the external coupling rate κ. The right-hand panel depicts the frequency dependence of the phase extracted at zero external flux, as indicated by the black dashed line in the left-hand panel. The dashed lines are the results of individual fits to the complex reflection coefficient in close frequency vicinity of each mode according to Eq. 193 used to extract the external coupling rate.

Josephson elements. Notably, in this approach it is much simpler to include the stray inductance into the model. The transmission matrices for the three elements are

$$\begin{aligned}\tilde{T}_{\mathrm{J}} &= \begin{pmatrix} 1 & \left[\left(j\omega L_{\mathrm{J}}\right)^{-1} + j\omega C_{\mathrm{J}}\right]^{-1} \\ 0 & 1 \end{pmatrix} \\ \tilde{T}_{\mathrm{C}_0} &= \begin{pmatrix} 1 & 0 \\ j\omega C_0 & 1 \end{pmatrix} \\ \tilde{T}_{\mathrm{L}_\mathrm{s}} &= \begin{pmatrix} 1 & j\omega L_{\mathrm{s}} \\ 0 & 1 \end{pmatrix}\end{aligned} \quad . \tag{190}$$

As mentioned at the beginning, in order to recover the relfection coefficient as measured from a single port network, which is different compared to the case of a network with two physical ports, the second port has to be grounded. If the JJA is galvanically connected to ground, the voltage needs to vanish at the end node. The transmission matrix representing this termination is

$$\tilde{T}_{\mathrm{term}} = \begin{pmatrix} 0 & 0 \\ 0 & 1 \end{pmatrix} . \tag{191}$$

Summing up the calculation procedure, the transmission matrix of a JJA from which the reflection coefficient is calculated according to Eq. 188, is

$$\tilde{T} = \left(\prod_{i=1}^{N-1} \tilde{T}_{\mathrm{J}} \tilde{T}_{\mathrm{C}_0} \tilde{T}_{\mathrm{L}_\mathrm{s}} \right) \tilde{T}_{\mathrm{J}} \tilde{T}_{\mathrm{term}} . \tag{192}$$

Figure 30b depicts the phase of the reflection coefficient $\arg(S_{11})$, numerically calculated as a function of the probe frequency f, and the external magnetic flux Φ_{ext} in number of flux quanta. The flux dependence of the variable inductance considered for the calculation is that of a symmetric dc SQUID $L_{\mathrm{J}} = L_{\mathrm{J},0}/|\cos(\pi\Phi_{\mathrm{ext}}/\Phi_0)|$. The transition frequencies of the individual modes of the array are identified by the relatively sharp phase roll-off, and the characteristic sinusoidal flux dependence. For the given set of parameters, $N = 1000$, $L_{\mathrm{J},0} = 50\,\mathrm{pH}$, $C_{\mathrm{J}} = 1\,\mathrm{pF}$, $C_0 = C_{\mathrm{J}}/2500$, and $L_{\mathrm{s}} = 10\,\mathrm{pH}$, the three eigenmodes falling into the frequency domain between 1 and 10 gigahetz are well separated from each other. The right-hand panel shows a vertical slice along the probe frequency around zero-field, as indictaed by the black dashed line in the 2D colorplot. The characteristic phase roll-off by 2π is visible for the first six modes, and emphasized by the color gradient. In contrast to the 2D plot, the black dashed line(s) in panel b represent the solutions of the least-square fits to the theoretical reflection response of a single mode given in Eq. 82.

Table 7: JJA: Circuit parameters. Values for the circuit parameters of the linear model of a JJA, as shown in Fig. 30a, used for the numerical calculation of the reflection coefficient, as shown in Fig. 30a.

Length	Josephson inductance	junction capacitance	capacitance to ground	stray inductance	characteristic impedance
N	$L_{\mathrm{J},0}$	C_J	C_0	L_s	Z_0
1000	50 pH	1 pF	1/2500 pF	10 pH	50 Ω

The fits are performed for each mode individually, and the reflection coefficient in close frequency vicinity of the m th eigenmode of the array is approximated by

$$\Gamma_{\mathrm{fit},m} = \Gamma_m e^{i\phi_m} e^{is_m(\omega-\omega_m)}, \tag{193}$$

where s_m is a finite background slope in the phase of the reflection coefficient caused by the presence of the other array modes, and ϕ_m is a finite offset value of the phase. The comparison between the black dashed lines representing the fits and the calculated data shows good agreement.

Parameter scaling:

With the transmission matrix approach at hand, the dependence of the external coupling rate on the circuit parameters can be determined. For each given set of parameters, the zero-field response is calculated in form of the frequency dependent reflection coefficient. Since the available parameter space is relatively large, I will focus on two parameters: The array length N and the impedance of each Josephson element $Z_\mathrm{J} = \sqrt{L_{\mathrm{J},0}C_\mathrm{J}}$. While increasing the array length is particularly interesting for parametric amplifiers to reduce the nonlinearity in the modes, the effect on the coupling rate can be negative, for instance by reducing the available instantaneous bandwidth of the amplifier. On the other hand, the junction impedance is representative for constraints on the fabrication process. Experimentally, the achievable parameter space for the reliable fabrication of tunnel contacts is limited, in particular, usually a certain critical current density $j_\mathrm{c} = I_\mathrm{c}/A$ cannot be deceeded without risking the appearance of galvanic shorts through the barrier. If the critical current density is fixed and the junction size is varied, the plasma frequency of the junction remains constant, while its impedance changes linearly with A.

Figure 31a depicts the external coupling rate κ_m of the first seven modes of a JJA, except for the fundamental dc mode, as a function of the corresponding transition

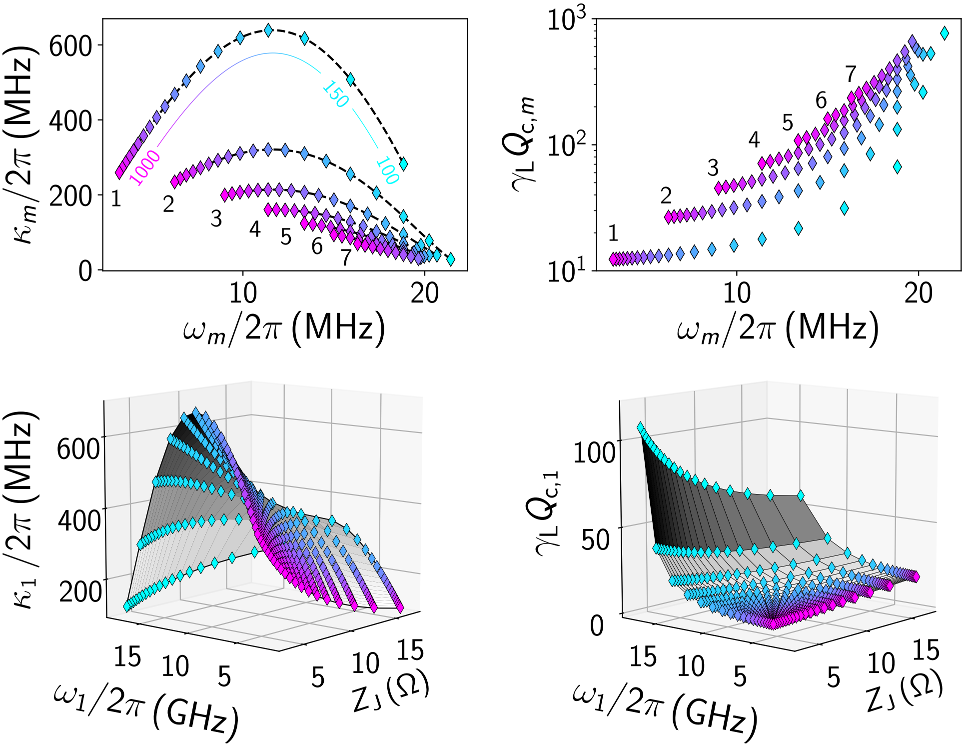

Figure 31: JJA: External coupling. a) Numerically calculated external coupling rate κ_m for the first seven eigenmodes $m \in \{1,..,7\}$ of a JJA, which is galvanically coupled to a $50-\Omega$ semi-infinite transmission line on one end, and terminated to ground on the other end. The values for κ_m and the corresponding resonance frequency ω_m are extracted from individual fits to the calculated reflection coefficient according to the theoretical prediction of a single resonant mode given in Eq. 193. With increasing array length N, from $N = 100$ (cyan) to $N = 1000$ (pink), the resonance frequencies decrease as well as the coupling rate. Around $\omega_\mathrm{pl}/2$, the coupling rate exhibits a maximum for all modes. The black dashed lines are guides for the eye. The circuit parameters are identical to the calculation shown in Fig. 30. **b)** Product of the coupling quality factor $Q_{\mathrm{c},m} = \omega_m/\kappa_m$ and the inductance participation ratio $\gamma_\mathrm{L} = L_{\mathrm{J},0}/(L_{\mathrm{J},0} + L_\mathrm{s})$. In order to guarantee convenient operation conditions if the array modes are used for parametric amplification, the product needs to be much larger than 1 [41]. **c)** External coupling rate of the first mode κ_1 for different array lengths N and junction impedances $Z_\mathrm{J} = \sqrt{L_{\mathrm{J},0}/C_\mathrm{J}}$. The plasma frequency remains fixed $L_\mathrm{J}C_\mathrm{J} = \mathrm{const.}$, which reflects the case of a constant critical current density j_c, and a variable junction size A_J. With increasing junction impedance, the maximal coupling rate reduces, as well as the frequency at which the maximum occurs. For all combinations, the prodcut $\gamma_\mathrm{L} Q_{\mathrm{c},1}$ remains well above 1, as shown in **d)**.

frequency ω_m for various array lengths $N \in [100, 1000]$. The information about the length of the array is endoded in the color of the data points, from cyan (100) to pink (1000). With increasing length, both, the transition frequencies and the coupling rates decrease. For the given set of circuit parameters, which is identical to the set used in Fig. 30b, a critical length $N \approx 300$ is required to reach the frequency range below 10 gigahertz. Interestingly, the coupling rates of all modes exhibit a maximal value around $\omega_{\mathrm{pl}}/2$, with the magnitude decreasing with the mode number. Hence, the lower the mode number the stronger the coupling to the input port.

Especially in the context of parametric amplification with superconducting resonant circuits operated close to a critical point at which the circuit enters a regime of multistability, the behaviour in vicinity of this point is crucial for the performance of the amplifier. A figure of merit for the behavior of the system in this regime, is the product between the coupling or external quality factor $Q_{\mathrm{c},m} = \omega_m/\kappa_m$, and the kinetic indutance participation ratio $\gamma_{\mathrm{L}} = L_{\mathrm{J},0}/(L_{\mathrm{J},0} + L_{\mathrm{s}})$. For a convenient operation, the product is required to be much larger than 1 [41]. Figure 31b depicts the product $\gamma_{\mathrm{L}} Q_{\mathrm{c},m}$ calculated from the data shown in panel a. For all modes, the calculated ratio is at least above 10.

In addition to the length of the array, in Fig. 31c the junction impedance is varied as well, while the product $L_{\mathrm{J},0}C_{\mathrm{J}}$, which is proportional to the plasma frequency of the junction, remains fixed. Again, this particular choice of sweeping the circuit parameters resembles the scenario of a constant critical current density j_{c} and a varying junction size. With increasing junction impedance, the external coupling rate κ_1 of the first mode κ_1 decreases for most array lengths. Only for the shortest array ($N = 100$, cyan colored), the coupling rate slightly increases. The effect on the transition frequencies is rather weak, since the plasma frequency remains fixed and the change in C_{J} primarily increases the slope of the linear regime of the dispersion relation.

The change of the coupling rate can be understood qualitatively from the change in characteristic impedance of the array. The characteristic impedance $Z_{0,\mathrm{JJA}}$ of the JJA, calculated according to the linear circuit model shown in Fig. 30a, is

$$Z_{0,\mathrm{JJA}}(\omega) = \sqrt{\frac{L_{\mathrm{J}}}{C_0(1 - L_{\mathrm{J}}C_{\mathrm{J}}\omega^2)} + \frac{L_{\mathrm{s}}}{C_0}}. \tag{194}$$

At frequencies well below the plasma frequency of the junction $L_{\mathrm{J}}C_{\mathrm{J}}\omega^2 \ll 1$, the impedance is rather constant and given by the sum of the inductive contributions L_{J} and L_{s}, and the capacitance to ground C_0. As soon as the frequency becomes close to the plasma frequency of the Josephson elements, the impedance increases rapidly until it diverges at the plasma frequency. Since the external quality factor

$Q_{\text{ext},1}$ is proportional to the ratio of the characteristic impedance of the array and the characteristic impedance of the input port

$$Q_{\text{ext},1} \sim \frac{Z_{0,\text{JJA}}}{Z_0}, \tag{195}$$

the external coupling rate is

$$\kappa_1 \sim \omega_1 \frac{Z_0}{Z_{0,\text{JJA}}}. \tag{196}$$

According to this relation, the dome-like shape of the external coupling rate as a function of the array length owing to the competition between an increasing transition frequency with decreasing length, and an increasing characteristic impedance close to the plasma frequency. Moreover, comparing the maximal values of the coupling rate between different modes, reveals a scaling with the inverse of the mode number m, and the coupling rate of the m-th mode is

$$\kappa_m \sim \frac{\omega_m}{m} \frac{Z_0}{Z_{0,\text{JJA}}}. \tag{197}$$

When designing parametric amplifiers from JJA, the scaling of the external coupling rate and the nonlinearity with the array length has to be considered.

A very efficient tuning knob is the capacitance to ground. By increasing the capacitance to ground, not only the slope of the linear regime of the dispersion relation decreases, and, hence more modes are in the desirable frequency domain between 1 and 10 gighertz, but also the characteristic impedance of the array decreases at the same time, which increases the coupling strength to the input port.

G DJJAA: Supplementary information

The following sections give additional information about the DJJAA devices discussed in the main text, for instance how the circuit parameters are estimated from additional room-temperature measurements and how the results compare to the prediction of a linear transmission matrix model, as well as a discussion about the cQED system composed of a conventional transmon qubit coupled to a dedicated readout resonator used to calibrate the noise performance of the DJJAA and the measurement efficiency of the setup.

G.1 Capacitance and inverse inductance matrices

For the DJJAA design with an in-plane center capacitance, the capacitance and inverse inductance matrices introduced in Eq. 168, $\tilde{C}$ and $\tilde{L}^{-1}$ respectively, are

$$\tilde{C} = \begin{pmatrix}
C_J' & -C_J & 0 & \dots & & & & & & \\
-C_J & C_J' & -C_J & 0 & \dots & & & & & \\
0 & -C_J & C_J' & -C_J & 0 & \dots & & & & \\
\vdots & \ddots & \ddots & \ddots & \ddots & \ddots & & & & \\
 & & 0 & -C_J & C_c' & -C_c & 0 & & & \\
 & & & 0 & -C_c & C_c' & -C_J & 0 & & \\
 & & & & 0 & -C_J & C_J' & -C_J & 0 & \\
 & & & & \ddots & \ddots & \ddots & \ddots & \ddots & \ddots \\
 & & & & & \dots & 0 & -C_J & C_J' & -C_J \\
 & & & & & & \dots & 0 & -C_J & C_J'
\end{pmatrix} \tag{198}$$

and

$$\tilde{L}^{-1} = \begin{pmatrix}
\frac{2}{L_J} & -\frac{1}{L_J} & 0 & \dots & & & & & & \\
-\frac{1}{L_J} & \frac{2}{L_J} & -\frac{1}{L_J} & 0 & \dots & & & & & \\
0 & -\frac{1}{L_J} & \frac{2}{L_J} & -\frac{1}{L_J} & 0 & \dots & & & & \\
\vdots & \ddots & \ddots & \ddots & \ddots & \ddots & \ddots & & & \\
 & & 0 & -\frac{1}{L_J} & \frac{1}{L_J} & 0 & 0 & & & \\
 & & & 0 & 0 & \frac{1}{L_J} & -\frac{1}{L_J} & 0 & & \\
 & & & & 0 & -\frac{1}{L_J} & \frac{2}{L_J} & -\frac{1}{L_J} & 0 & \\
 & & & & \ddots & \ddots & \ddots & \ddots & \ddots & \ddots \\
 & & & & & \ddots & 0 & -\frac{1}{L_J} & \frac{2}{L_J} & -\frac{1}{L_J} \\
 & & & & & & \dots & 0 & -\frac{1}{L_J} & \frac{2}{L_J}
\end{pmatrix} . \tag{199}$$

For reasons of clarity, I introduced the effective capacitances $C_\mathrm{J}' = 2C_\mathrm{J} + C_0$ and $C_\mathrm{c}' = C_\mathrm{J} + C_\mathrm{c} + C_0'$ in the representation of the capacitance matrix. The contributions due to the center capacitance are highlighted in ruby.

G.2 Kerr coefficients

For the antisymmetric modes (even mode number m), the jump in the node flux distribution, which occurs from negative to positive values at the position of the center capacitance, causes unphysical results for the dimensionless factors η_{mmmm} and, as a consequence, artificially large self-Kerr coefficients. Therefore, the self- and next-neighbor cross-Kerr coefficients are calculated by symmetrizing the node flux eigenfunctions, which does not alter the physical interpretation but avoids the numerical error.

$$\vec{\Phi}_{m,\mathrm{sym}} = \vec{\Phi}_m^\mathrm{T} \cdot \tilde{S} \tag{200}$$

Here, the diagonal matrix $\tilde{S}$ is

$$\tilde{S} = \mathrm{diag}(1, 1, ..., 1, 1, -1, -1, ..., -1, -1), \tag{201}$$

Table 8: Eigenfrequencies, self- and cross-Kerr coefficients ω_m, $|K|_{m,m}$ and $|K|_{m,m+1}$, respectively, predicted by the circuit model introduced in Sec. 3.2 using the circuit parameters of sample A and D listed in Tab. 3.2.

N	1200			1300		
m	$\frac{\omega_m}{2\pi}$ (GHz)	$\frac{\lvert K\rvert_{m,m}}{2\pi}$ (kHz)	$\frac{\lvert K\rvert_{m,m+1}}{2\pi}$ (kHz)	$\frac{\omega_m}{2\pi}$ (GHz)	$\frac{\lvert K\rvert_{m,m}}{2\pi}$ (kHz)	$\frac{\lvert K\rvert_{m,m+1}}{2\pi}$ (kHz)
0	2.123	0.2	0.6	1.881	0.2	0.5
1	2.539	0.4	1.4	2.227	0.3	1.1
2	6.539	2.8	5.9	5.773	2.3	4.8
3	7.252	3.4	6.5	6.400	2.8	5.3
4	10.530	7.6	15.2	9.359	6.3	12.5
5	11.064	8.2	13.0	9.860	6.8	10.8
6	13.525	12.7	25.0	12.153	10.7	21.0
7	13.848	13.1	18.9	12.473	11.0	16.1
8	15.591	17.0	33.3	14.152	14.6	28.6
9	15.777	17.2	23.7	14.345	14.8	20.5
10	16.988	20.2	39.8	15.546	17.6	34.6
11	17.096	20.3	27.4	15.661	17.7	24.0

Table 9: Eigenfrequencies, self- and cross-Kerr coefficients ω_m, $|K|_{m,m}$ and $|K|_{m,m+1}$, respectively, predicted by the circuit model introduced in Sec. 3.2 using the circuit parameters of sample B and C listed in Tab. 3.2.

N	1600			1800		
m	$\frac{\omega_m}{2\pi}$ (GHz)	$\frac{\lvert K\rvert_{m,m}}{2\pi}$ (kHz)	$\frac{\lvert K\rvert_{m,m+1}}{2\pi}$ (kHz)	$\frac{\omega_m}{2\pi}$ (GHz)	$\frac{\lvert K\rvert_{m,m}}{2\pi}$ (kHz)	$\frac{\lvert K\rvert_{m,m+1}}{2\pi}$ (kHz)
0	1.160	0.1	0.3	0.916	0.1	0.2
1	1.380	0.2	0.6	1.093	0.1	0.4
2	3.580	1.3	2.7	2.836	0.9	1.9
3	4.015	1.6	3.0	3.199	1.2	2.2
4	5.927	3.6	7.3	4.737	2.7	5.3
5	6.320	4.1	6.5	5.085	3.0	4.8
6	7.911	6.6	12.9	6.407	4.9	9.6
7	8.196	6.9	10.2	6.675	5.2	7.7
8	9.459	9.5	18.4	7.765	7.3	14.1
9	9.650	9.7	13.6	7.955	7.5	10.5
10	10.622	12.0	23.4	8.827	9.4	18.3
11	10.746	12.1	16.5	8.957	9.6	13.1

where the sign change occurs at the entry with index $j = N/2 + 1$. Subsequently, the eigenvectors $\vec{\Psi}_m$ are calculated by inverting Eq. 3.10. Notably, directly symmetrizing the eigenvectors $\vec{\Psi}_m$ does not prevent the numerical error. The self-Kerr and next neighbor cross-Kerr coefficients $|K|_{m,m}$ and $|K|_{m,m+1}$ are listed in Tab. 8 and Tab. 9 for the four decives discussed in the main text. For all dimers used for parametric amplification, the obtained Kerr coefficients are on the order of a few kilohertz, which is in agreement with the observed saturation power (see Sec. 1.3.4 and Sec. 3.7).

G.3 Sample holder

The DJJAAs are fabricated on sapphire wafers with a physical dimension of $7.5 \times 3.6\,\mathrm{mm}^2$, and are attached to a dedicated copper sample holder using silver paste. For the microwave connection between the $50\,\Omega$ Al transmission line patterned on the wafer and the SMA connector serving as the input port, a printed circuit board (PCB) containing a $50\,\Omega$ microstrip transmission line is used.

The PCB has a copper cladding of thickness $t_{\mathrm{copper}} = 35\,\mu\mathrm{m}$ on both sides, enclosing a low loss dielectric TMM10i ($\epsilon_{\mathrm{r}} = 9.9$) of thickness $t = 635\,\mu\mathrm{m}$, supplied by

Rogers Corporation. The height difference between the PCB and the sapphire wafer ($t = 330\,\mu\mathrm{m}$) is compensated by a small copper post below the wafer (not shown). The PCB transmission line is patterned by removing half of the top metalization on one side, sparing a strip of 0.618 mm width, which is directly soldered to the center conductor of an SMA connector, and wire bonded to the on-chip transmission line using at least two Al bonds. The other half of the PCB remains copper cladded and serves as the ground reference. For that reason, the top and the bottom metalization are galvanically connected using vias, and again, the amplifier is connected to the PCB ground using Al wire bonds. Notably, for some devices, the coupling to lossy resonant modes hosted by the sample holder and the on-chip metalization has been observed, causing a significant decrease in the amplifier performance in the corresponding frequency range. A solution was found by using silver paste instead of multiple Al wire bonds to ground the amplifier.

Each amplifier is equipped with a superconducting bias coil integrated into the lid of the sample holder, and a commercial circulator directly mounted to the SMA input port, to avoid low-frequency standing waves (see. Fig. 32b).

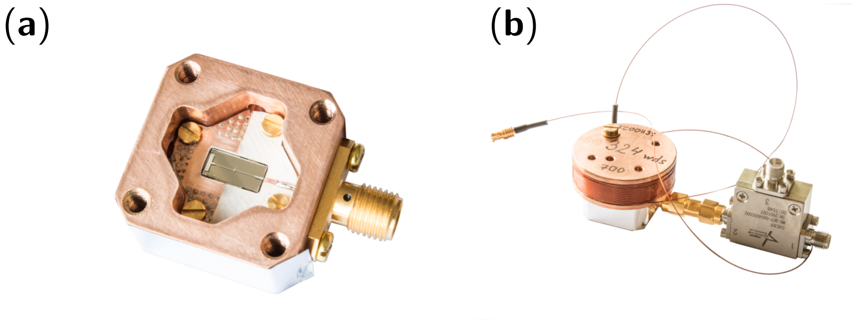

Figure 32: DJJAA: sample holder. a) Copper body of the DJJAA sample holder (without lid), hosting a printed circuit board (PCB) and a $7.5 \times 3.6\,\mathrm{mm}^2$ sapphire wafer. For the exchange of microwave photons, the PCB contains a $50-\Omega$ microstrip transmission line, soldered to the center pin of an SMA connector on one end, and wire bonded to the $50-\Omega$ on-chip microstrip transmission line of the amplifier on the other end, using at least two Al bonds. In order to ground the DJJAA, half of the PCB has a top metalization, which is galvanically connected to the bottom metallization with vias. The PCB is glued with silver paste and kept in place with four additional brass screws, the wafer is only glued with silver past. **b)** Closed sample holder. A superconducting bias coil is integrated into the lid, and a commercial circulator is directly mounted to the SMA connector of the input port to separate incident and outgoing fields.

G.4 Linear device characterization

Although the amplification of microwave signals is only possible due to the nonlinearity of the DJJAA modes, a closer look at the linear response of a device gives already vital insight into the expected performance. Moreover, comparing the obtained results with the design parameters helps to enhance the accuracy of the model prediction.

The device parameters are extracted from the measured reflection coefficient (see Fig. 3.6), as well as complementary measurements discussed in the following paragraphs. The only parameter which is fixed by design is the number of total SQUIDs N, i.e. the possibility of shorted JJs is neglected.

Critical current

The critical current of a single SQUID is estimated from room temperature transport measurements, and the Ambegaokar-Baratoff formula [60], which relates the critical current of a JJ to its normal state resistance R_n right above the critical temperature T_c, and the energy gap $\mathit{\Delta}$ in the superconducting state.

$$I_\mathrm{c}(T) = \frac{\pi \mathit{\Delta}(T)}{2eR_\mathrm{n}} \tanh\left(\frac{\mathit{\Delta}(T)}{2k_\mathbb{B}T}\right). \tag{202}$$

At temperatures well below the critical temperature T_c, the formula simplifies to

$$I_\mathrm{c}(T=0) = \frac{\pi \mathit{\Delta}(T)}{2eR_\mathrm{n}}. \tag{203}$$

The energy gap of the pure aluminum films is estimated from the BCS relation between the energy gap and the critical temperature of a supercondutor $\mathit{\Delta} = 1.76 k_\mathrm{B} T_\mathrm{c}$, with $T_\mathrm{c} = 1.4\,\mathrm{K}$. Since the normal-state resistance is measured at room temperature, there is a phenomenological correction term $R_\mathrm{n} = 1.15 R_\mathrm{n,RT}$ based on experimental observations taken from other experiments performed in our group. Another correction arises from the contribution of the pure aluminum wires connecting the JJs to the measured resistance. As deduced from the design geometry, a total of six sheets of pure aluminum has to be considered per SQUID. The resistance R_SQ attributable to the SQUIDs is

$$R_\mathrm{SQ} = R_\mathrm{n,RT} - 6NR_{\square,\mathrm{Al}}, \tag{204}$$

where N is the total number of SQUIDs, and $R_{\square,\mathrm{Al}} = 1.1\,\Omega/\square$ is the sheet resistance of the pure aluminum film measured at room temperature.

In the design with an in-plane capacitor in the center, as presented in Fig. 3.5, the total resistance of the array cannot be measured in a single transport measurement, but only the resistance from the input port to the center capacitor $R_{\mathrm{n,in}}$, and from the center capacitor to ground $R_{\mathrm{n,out}}$. However, from the difference in resistance, potential gradients in the critical current along the array can be deduced, which is expressed in the resistance asymmetry parameter

$$m_{\mathrm{asym}} = \frac{R_{\mathrm{n,in}} - R_{\mathrm{n,out}}}{R_{\mathrm{n,in}} + R_{\mathrm{n,out}}}. \tag{205}$$

Junction capacitance

The junction capacitance C_{J} is estimated from the overlap area A_{J} extracted from SEM images, similar to the example given in Fig. 3.5, and the capacitance per unit area $c_{\mathrm{J}} \approx 50\,\mathrm{fF}/\mathrm{\mu m}^2$.

$$C_{\mathrm{J}} = c_{\mathrm{J}} A_{\mathrm{J}} \tag{206}$$

The SEM images are taken from different devices fabricated in the same run, in order not damage the actual sample. For a dc SQUID, the total capacitance is twice the capacitance of a single JJ. The fabrication procedure is relatively reproducible, since the feature size is well above the resolution limit of the resist, and the obtained overlap area is around

$$A_{\mathrm{J}} = 10.5 \pm 0.4\,\mathrm{\mu m}^2, \tag{207}$$

which results in a junction capacitance of

$$C_{\mathrm{J}} = 1050 \pm 40\,\mathrm{fF} \tag{208}$$

per SQUID. The value used for the calculation of the dispersion relations shown in Fig. 3.7 is about 15% larger, which could be explained either by a different capacitance per unit area, or a smaller critical current, since the junction capacitance is adjusted such that the measured plasma frequency is reproduced.

Center capacitance

The capacitive contributions of the center capacitance, C_{c} and C_0', are deduced from finite element method simulations performed with Sonnet. While the in-plane capacitance C_{c} is controlled by the number of fingers and their length, and is adjusted according to the total length of the device, the capacitance to ground due to the capacitor plates remains unchanged. In the presented geometry, it is $C_0' \approx 33\,\mathrm{fF}$.

For the three samples the total number of SQUIDs is $N = 1200, 1600$, and 1800 (from left to right), and the critical currents per SQUID are $I_c = 7.0$µA, 3.5µA, and 2.7µA. The center capacitances are $C_c = 30\,\mathrm{fF}$, 40 fF, and 45 fF. Finally, the capacitance to ground C_0 remains the only free fitting parameter, and is extracted from the dispersion relation.

Capacitance to ground

The capacitance to ground C_0 attributed to each superconducting island remains the only free parameter in order to align the measured dispersion relation at the flux sweet spot with the model prediction. The eigenfrequencies of the DJJAA are either extracted directly from the measured reflection coefficient, or from a two-tone spectroscopy after the flux sweet spot has been determined.

The extracted value $C_0 = 0.4\,\mathrm{fF}$ stated in the main text can be compared to a value estimated from the circuit design. For a microstrip geometry, the capacitance to ground per unit length is

$$C(w) = \frac{\epsilon_{\mathrm{eff}}}{60 c_0 \ln\left(\frac{8h}{w} + \frac{w}{4h}\right)}, \tag{209}$$

where c_0 is the speed of light in vacuum, $h \approx 330\,\mu\mathrm{m}$ is the substrate height, and $w = 4\,\mu\mathrm{m}$ is the wire width. The effect of a finite film thickness is neglected, which is justified by its relative size compared to the substrate height. Since the electric fields are only partially confined inside the substrate, the effective relative permittivity ϵ_{eff} is

$$\epsilon_{\mathrm{eff}} = \frac{\epsilon_{\mathrm{r}} + 1}{2} + \frac{\epsilon_{\mathrm{r}} - 1}{2} \frac{1}{\sqrt{1 + 12\frac{h}{w}}}. \tag{210}$$

For the used sapphire substrates, the relative permittivity is $\epsilon_{\mathrm{r}} = 9.3$ for electric fields oriented perpendicular to the crystalline C-axis (hexagonal crystal structure). Instead of a capacitance per unit length, a more convenient representation is a capacitance to ground per square

$$C_{0,\square} = C(w)w \approx 0.13\,\mathrm{fF}, \tag{211}$$

with $w = 3\,\mu\mathrm{m}$. Accordingly, the value $C_0 = 0.45\,\mathrm{fF}$ extracted from the dispersion relations (see Fig. 3.7) corresponds to around $N_\square \approx 3.5$ per SQUID on average, which is in agreement with the DJJAA design shown in Fig. 3.5.

Stray inductance

Estimating the additional stray inductance due to the pure aluminum wires connecting the SQUIDs is important, as it influences the dynamics of the circuit under strong pumping, and since it determines the reliability of the lumped-element circuit model, which does not account for additional linear inductances. In general, the stray inductance contributes in form of a geometric inductance related to the wire geometry, and a kinetic inductance related to the superconducting condensate. Although these contributions cannot be distinguished in the experiment, it is possible to predict them based on the circuit design and on room temperature transport measurements.

For the given microstrip geometry, the geometric inductance per unit length L_g depends only weakly on the wire width w, and is calculated from standard microwave theory [47]

$$L_g = \frac{60}{c_0} \ln\left(\frac{8h}{w} + \frac{w}{4h}\right) \approx 1.4\,\frac{\text{pH}}{\mu\text{m}}, \tag{212}$$

where c_0 is again the speed of light in vacuum, $h \approx 330\,\mu\text{m}$ is the substrate height, and $w = 3\,\mu\text{m}$ is the wire width. Similar to the capacitance to ground, the geometric inductance per unit length is translated into a inductance per square

$$L_{g,\square} = L_g(w)w \approx 4.0\,\frac{\text{pH}}{\mu\text{m}}. \tag{213}$$

The kinetic sheet inductance is estimated from the measured sheet resistance $R_{\square,\text{Al}} = 1.1\,\Omega/\square$ and the Mattis-Bardeen formula:

$$L_{K,\square} \approx 1.3\,\frac{\text{pH}}{\square}. \tag{214}$$

Combining both contributions, and using the same number of squares as extracted from the capacitance to ground, the stray inductance per SQUID is

$$L_s = N_\square \left(L_{g,\square} + L_{K,\square}\right) \approx 19\text{pH}. \tag{215}$$

Notably, the obtained result is only a rough estimate, and should be appreciated as an orientation only. Experimentally, the flux modulation of the DJJAA modes can give insight into the kinetic inductance participation ratio, from which the stray inductance can be calculated and compared to the calculated value.

Magnetic flux calibration and Josephson inductance participation ratio

The modulation of the resonance frequencies contains information about the external magnetic flux, and the ratio between the kinetic inductance of the SQUIDs and the stray inductance, which is expressed in the kinetic inductance participation ratio γ_L. Both quantities are extracted from the measured data by comparing the observed frequency modulation to the prediction of an effective lumped-element model.

In the experiment, the magnetic flux enclosed Φ_ext inside the SQUID loops is set by the application of a bias current I_b to a superconducting field coil integrated into the lid of the device, as shown in Fig. 32. The conversion between the bias current I_b and the magnetic flux Φ_ext is possible due to the periodic modulation of the resonance frequencies. As discussed in previous sections, but especially in Sec. E.2, the action of a dc SQUID in a circuit is that of a nonlinear inductance, which depends on the magnetic flux enclosed in the SQUID loop. Since the loop inductance is negligible for the SQUIDs of the presented DJJAA design, as is experimentally validated from the almost complete suppression of the resonance frequencies, the applied magnetic flux is equal to the magnetic flux inside the loop. Therefore, the suppression of the resonance frequencies occurs at half a flux quantum $\Phi_\mathrm{ext} = 0.5\Phi_0$.

The flux modulation of each mode can be mapped onto an effective lumped element circuit model. Since the field spectra are measured at low microwave powers, a linear circuit model is sufficient to capture the features related to the flux modulation. The model consists of a flux dependent (kinetic) inductance $L_\mathrm{K,eff}(\Phi_\mathrm{ext})$ in series with a constant, magnetic flux independent stray inductance $L_\mathrm{s,eff}$, which are shunted by a capacitance C_eff, as shown in Fig. 33. The resonance frequency of the fundamental mode is

$$f_0\left(\Phi_\mathrm{ext}\right) = \frac{1}{2\pi\sqrt{C\left[L_\mathrm{s,eff} + L_\mathrm{K,eff}(0)/\left|\cos\left(\pi\Phi_\mathrm{ext}/\Phi_0\right)\right|\right]}}. \tag{216}$$

The external magnetic flux Φ_ext is due to the bias current I_b applied to the superconducting field coil. In the simplest case, the flux created by the bias current is linear

$$\Phi_\mathrm{ext} = l_\mathrm{b}(I_\mathrm{b} + I_\mathrm{offset}), \tag{217}$$

where l_b is an unknown conversion factor related to the coil geometry, e.g. the coil dimensions and the number of windings. Additionally, a potential dc offset field is accounted for by an offset bias current I_offset. The physical interpretation of this assumption is, that the offset field is homogeneous on the length scale of the array.

By introducing the resonance frequency in effective zero-field

$$f_0(\Phi_\mathrm{ext} = 0) = \frac{1}{2\pi\sqrt{C\left[L_\mathrm{s,eff} + L_\mathrm{K,eff}(\Phi_\mathrm{ext} = 0)\right]}}, \tag{218}$$

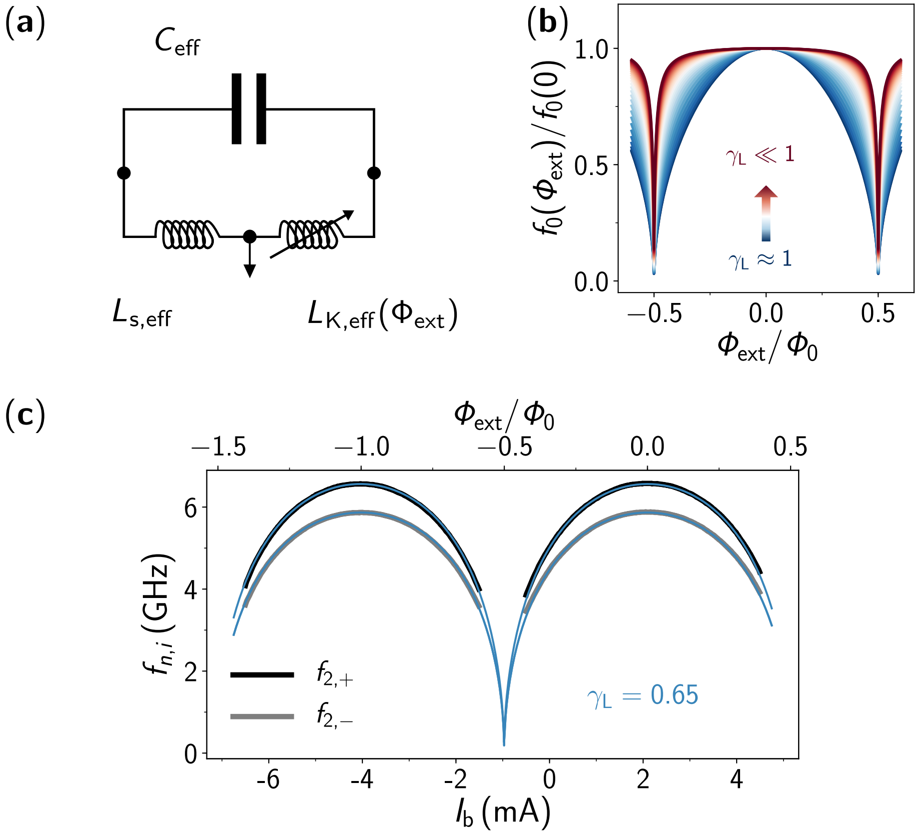

Figure 33: DJJAA: magnetic flux calibration. a) Effective lumped-element circuit model to describe individually the characteristic modulation of the DJJAA modes with the external magnetic flux. The model consists of two inductors in series, out of which one accounts for the constant stray inductance $L_{\mathrm{s,eff}}$, while the other for the tunable SQUID inductance $L_{\mathrm{K,eff}}(\Phi_{\mathrm{eff}})$. The inductors are shunted by an effective capacitance C_{eff} to form a resonant circuit. **b)** Fundamental resonance frequency $f_0(\Phi_{\mathrm{ext}})$ of the circuit as a function of the external magnetic flux Φ_{ext}, normalized by the frequency in effective zero-field $f_0(0)$, for different inductance participation ratios $\gamma_{\mathrm{L}} = L_{\mathrm{K,eff}}(0)/(L_{\mathrm{K,eff}}(0) + L_{\mathrm{s,eff}})$. If the tunable inductance dominates (blue color tones), the shape of the curve is round and sinusoidal. With increasing stray inductance, a noticeable change of the resonance frequency occurs close to half a flux quantum only. **c)** Measured resonance frequencies $f_{1,-}$ (grey markers) and $f_{1,+}$ (black markers) of the pair of modes forming the dimer with dimer index $n = 1$ for the sample with $N = 1200$ SQUIDs. The frequencies are from the field dependent reflection coefficient shown in Fig. 3.6. The blue solid lines indicate individual fits to the model prediction according to Eq. 219. From the fit parameters, the bias current I_{b} is converted into an external magnetic flux Φ_{ext} (top x-axis), and the kinetic inductance participation ratio is determined $\gamma_{\mathrm{L}} = 0.65$.

Table 10: DJJAA: normal-state resistance and kinetic inductance participation ratio. Normal-state resistance measured at room temperature, from the input port to the center capacitance $R_{\mathrm{n,in}}$, from the center capacitance to ground $R_{\mathrm{n,out}}$. The resistance asymmetry between the two array sections m is calculated according to Eq. 205. Kinetic inductance participation ratio $\gamma_{\mathrm{L,fit}}$ extracted from a fit to the frequency modulation with the applied magnetic flux (see App. G.4), and calculated according to $\gamma_{\mathrm{L}} = L_{\mathrm{J}}/(L_{\mathrm{J}} + L_{\mathrm{s}})$.

sample	A	B	C	D
N	1200	1600	1800	1300
$R_{\mathrm{n,in}}$ (kΩ)	29.03	70.96	102.25	32.4
$R_{\mathrm{n,out}}$ (kΩ)	28.41	71.3	102.91	32.38
m	1.022	0.995	0.994	1.001
$\gamma_{\mathrm{L,fit}}$	0.65	0.87	0.92 ± 2	-
γ_{L}	0.71	0.83	0.87	0.74

and using the conversion between the bias current and the external magnetic flux, and the kinetic inductance participation ratio γ_{L}, the resonance frequency of the effective circuit model can be expressed as

$$f\left(I_{\mathrm{b}}\right) = \frac{f_0(0)}{\sqrt{1 + \gamma_{\mathrm{L}}\left[1 + \left|\cos\left(\pi l_{\mathrm{b}}(I_{\mathrm{b}} + I_{\mathrm{offset}}\right)\right|^{-1}\right]}}. \tag{219}$$

Although the information contained in the flux dependence of the resonance frequency is not sufficient to determine all values of the effective circuit elements, it is sufficient to extract the kinetic inductance participation ratio γ_{L}, the conversion factor l_{b}, and the offset flux. Notably, due to the small modulation period, the offset flux is only determinable within $(-0.5\Phi_0, 0.5\Phi_0]$.

Figure 33 depicts the expected flux modulation of the fundamental frequency of the effective lumped-element circuit model according to Eq. 219, calculated for different inductance participation ratios γ_{L}. If the flux dependent inductance dominates $\gamma_{\mathrm{L}} \approx 1$ (blue colors), the observed modulation is similar to the flux modulation of the critical current, to be exact the square root of the critical current. With increasing stray inductance, the curves increasingly deviate from the ideal modulation, up to the point at which the contribution of the flux tunable inductance is noticeable close to half a flux quantum only.

G.5 Energy decay rates and dimer detuning

For the later use of the DJJAAs as parametric amplifiers, especially the external and internal coupling or decay rates of the modes take a special role. While the first determines the instantaneous bandwidth of the amplifier, the latter potentially degrades the noise added by the amplifier. The third characteristic quantity is the dimer detuning, and in particular, how it compares to the external coupling rate.

The eigenfrequencies ω_m of each mode, together with the corresponding coupling rates κ_m and γ_m, are extracted from fits to the frequency dependence of the reflection coefficient. Although the DJJAA modes remain coupled due to the non-zero cross-Kerr coefficients, the reflection coefficient of the DJJAA measured at low probe powers can still be approximated by a combination of independent and linear modes, as the Kerr coefficients are small by design. Since the two modes of a dimer belong together conceptually, the response in the immediate frequency vicinity of a pair of modes is fitted by the response of two linear modes, while the contribution of all other modes is neglected. The corresponding reflection coefficient of the n th dimer is

$$\Gamma_n(\omega) = \Gamma_{n,-}\Gamma_{n,+}e^{i\phi_0}e^{is(\omega-\bar{\omega})}, \tag{220}$$

which accounts for a finite offset phase ϕ_0 and a finite background slope s in the phase response, additionally. The frequency $\bar{\omega} = (\omega_{n,-} + \omega_{n,+})/2$ is the average of the two dimer frequencies. The other fitting parameters are the external coupling rates $\kappa_{n,-}$ and $\kappa_{n,+}$, and the internal decay rates $\gamma_{n,-}$ and $\gamma_{n,+}$. The corresponding dimer detuning $2J_n$ is defined as the frequency difference between the two modes

$$2J_n = \omega_{n,+} - \omega_{n,-}. \tag{221}$$

The applied simplification is particularly justified in the linear regime of the dispersion relation, in which the inter-dimer detuning $(\omega_{n+1,-} - \omega_{n,+})$ is much larger than the intra-dimer detuning $2J_n$, while the the two dimer modes are still well separated from each other at the same time $(J_n \approx \kappa_{n,-}, \kappa_{n,+})$.

Recalling the results of the discussion about nondegenerate parametric amplifiers (see Sec. 3.6), the gain-bandwidth product is determined by the effective coupling rate of the device, which is a combination of the coupling rates of both modes

$$\bar{\kappa}_n = 2\frac{\kappa_{n,-}\kappa_{n,+}}{\kappa_{n,-} + \kappa_{n,+}}. \tag{222}$$

Figure 34a depicts the field dependent response of the sample with $N = 1200$ SQUIDs, identical to Fig. 3.6 (left-hand panel), as well as the frequency dependence of the phase and the amplitude of the reflection coefficient, $\arg(S_{11})$ and $|S_{11}|$,

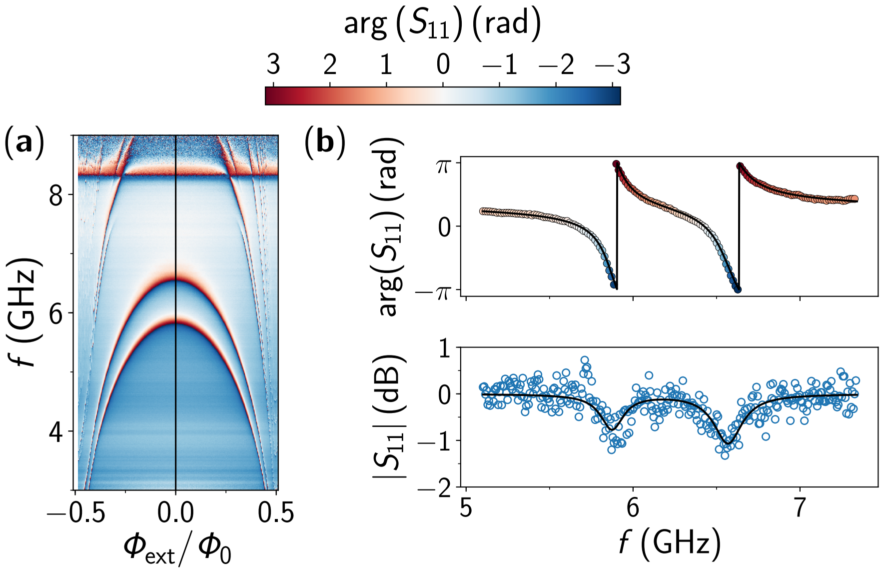

Figure 34: DJJAA: Fitting the complex reflection coefficient. a) Phase of the complex reflection coefficient arg(S_{11}) as a function of the probe tone frequency f and the external magnetic flux Φ_{ext} (see Fig. 3.6a), measured at low microwave powers. For each value of the applied external flux, the frequency dependence of the reflection coefficient is fitted to the prediction of an effective model composed of two linear cavities. **b)** Phase arg(S_{11}) (top panel) and amplitude $|S_{11}|$ (bottom panel) of the reflection coefficient measured at the flux sweet spot of the device, as indicated by the black solid line in panel a. From the fit to the model prediction (black line), the resonance frequencies $\omega_{1,1}/(2\pi) = 5.874\,\text{GHz}$ and $\omega_{1,2}/(2\pi) = 6.568\,\text{GHz}$, the external coupling rates $\kappa_1/(2\pi) = 168\,\text{MHz}$ and $\kappa_2/(2\pi) = 207\,\text{MHz}$, as well as the internal decay rates $\gamma_1/(2\pi) = 7\,\text{MHz}$ and $\gamma_2/(2\pi) = 13\,\text{MHz}$ are extracted.

respectively, measured at the flux sweet spot shown in panel b. Notably, the position of a jump in the phase response is not necessarily the position of the resonance frequency. The black solid line indicates a least-square fit to the data according to Eq. 220, from which the following device parameters are extracted:

$$\begin{aligned} \omega_{2,-}/(2\pi) &= 5.874\,\text{GHz} & \omega_{2,+}/(2\pi) &= 6.568\,\text{GHz} \\ \kappa_{2,-}/(2\pi) &= 168\,\text{MHz} & \kappa_{2,+}/(2\pi) &= 207\,\text{MHz} \\ \gamma_{2,-}/(2\pi) &= 7\,\text{MHz} & \gamma_{2,+}/(2\pi) &= 13\,\text{MHz} \end{aligned}$$

Once again I would like to mention that the fundamental dimer $n = 1$ is not visible in the measured spectrum due to its low resonance frequencies. As a side note, an enhancement of the fitting accuracy is obtained by removing features in the reflection coefficient that are unambiguously attributable to the measurement setup. The region around half a flux quantum of effective flux, where the DJJAA response is fully suppressed, serves as the reference.

A similar fit to the reflection coefficient is performed at different values of external magnetic flux in order to extract the flux dependence of the device parameters, as exemplarily shown in Figure 35. The same procedure is applied to the other devices. For comparison reasons, the parameters are extracted from two neighboring modulation periods.

The external coupling rates and the dimer detuning show a characteristic flux dependence, which is similar to the one observed for the resonance frequencies. In the whole range investigated, the dimer detuning is more than twice as large as the external coupling rates, which is not the ideal condition for pumping.

The obtained internal decay rates give insight into the electromagnetic environment of the device. Many different types of mesoscopic systems are known to induce losses to superconducting circuitry, for instance adsorbates or organic residuals from the fabrication process, defects present in the non-stoichiometric oxide of the JJ barrier and other interfaces, non-equilibrium quasiparticles, magnetic vortices, and lossy modes in the sample holder. Although the exact origin in our DJJAA devices remains unknown, measurements on samples with less JJs but identical fabrication procedure pinpoint into the direction of defects in the JJs. Independent of the origin, the observed internal decay rates are still sufficiently low compared to the external coupling rates to enable an operation of the devices as amplifiers close to the quantum limit.

External and internal quality factor

While stating the energy decay rates is convenient from the perspective of quantum optics, another common way of expressing energy decay in the context of electric circuits are the external and internal quality factors Q_c and Q_i, respectively. The quality factors are calculated as the ratio between the resonance frequencies and the decay rates, and are therefore a measure on how many oscillations the system performs until the energy has decayed to e^{-1} of its initial value, or in other words, how much energy is dissipated within one cycle. Following the established notation, the quality factors of the i th mode of the n th dimer of a device are

$$Q_{\mathrm{c},n,i} = \frac{\omega_{n,i}}{\kappa_{n,i}} \tag{223}$$

$$Q_{\mathrm{i},n,i} = \frac{\omega_{n,i}}{\kappa_{n,i}}. \tag{224}$$

Figure 36 depicts the external and internal quality factors calculated from the extracted device parameters shown in Fig. 35. Since the comparison between the two periods reveals a very similar behavior, only the data from the left period

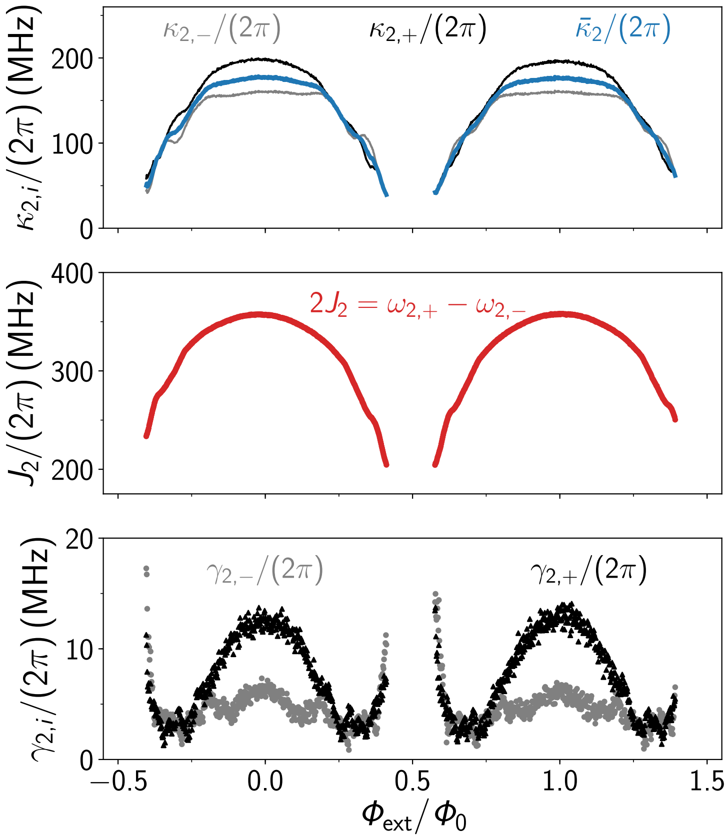

Figure 35: DJJAA: External and internal coupling rates, and dimer detuning. Field dependence of the external coupling rates $\kappa_{2,-}$ and $\kappa_{2,+}$ (top panel), the dimer detuning $2J_2 = \omega_{2,+} - \omega_{2,-}$ (central panel), and the internal decay rates $\gamma_{2,-}$ and $\gamma_{2,+}$ for the DJJAA sample A with $N = 1200$ SQUIDs (see Fig. 3.6 left-hand panel). Similar to the corresponding resonance frequencies shown in Fig. 33, the parameters associated with the lower mode (-) are indicated by grey markers, while the parameters of the higher mode (+) are indicated by black markers. The effective coupling rate $\bar{\kappa}_2 = 2\kappa_{2,-}\kappa_{2,+}/(\kappa_{2,-} + \kappa_{2,+}$ is calculated from the extracted values and plotted with blue markers. In the whole range, the dimer detuning is roughly twice the effective coupling rate. The observed change with flux in both parameters is due to the change of the resonance frequencies, and is expected for the presented design, i.e. a galvanically coupled DJJAA with in-plane center capacitance. The possible origins for the internal decay rates are manifold, ranging from organic residuals of the fabrication process, to uncontrolled degrees of freedom residing inside the JJs' oxide barriers, to interactions with lossy modes in the electromagnetic environment, for instance the sample holder.

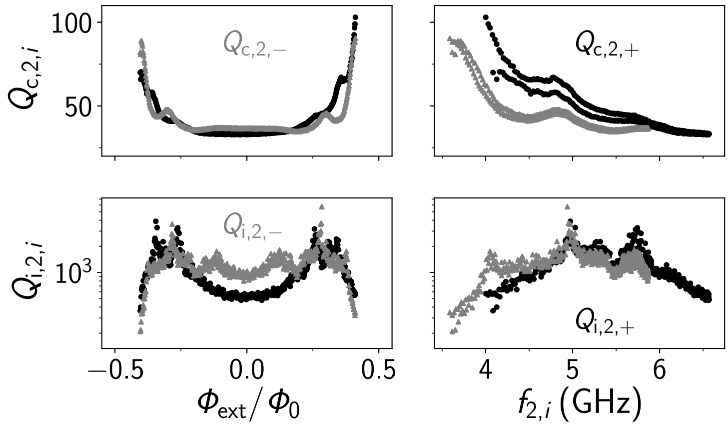

Figure 36: DJJAA: External and internal quality factor. External and internal quality factors $Q_{c,1,i}$ and $Q_{i,1,i}$, respectively, as a function of the external magnetic flux Φ_{ext} (left-hand panels) and the resonance frequency (right-hand panel). The external quality factor steadily increases away from the flux sweet spot, as the impedance of the array increases due to the increasing kinetic inductance of the SQUIDs. However, there are several ripples visible in the frequency dependence, which could be caused by a frequency dependent characteristic impedance of the input port, for instance due to standing waves. The behavior of the internal quality factor is less intuitive, as it can be affected by a variety of different external perturbations. For both modes, the internal quality factor is minimal around the flux sweet spot and close to half a flux quantum of external flux. However, this observation could be coincidence only. As the frequency dependence reveals, the two modes are exposed to a common electromagnetic environment, which is itself frequency dependent. Therefore, the drop of the internal quality factor towards higher and lower frequencies could indicate the presence of lossy modes in the sample holder.

($\Phi_{ext}/\Phi_0 \in [-0.5, 0.5]$) is plotted. Around effective zero-field, the region where the characteristic impedance of the array is the smallest, the external quality factor is largest, and for both modes around $Q_c \approx 30$.

Plotting the quality factors versus the extracted resonance frequencies reveals frequency dependent features both modes are affected by. In the external quality factors oscillations are observed, which could hint at standing waves in the input port, or more generally, the frequency dependence of the input port's characteristic impedance. In the internal quality factors several peaks and dips are observed that occur at the same frequencies for both modes. However, as the modes are hosted by the same array and possess a comparable standing-wave pattern, the coincidence of such features is not surprising.

G.6 Comparison to circuit model

Similar to the discussion about the external coupling rate in JJA, discussed in Sec. F.3, the parameters of the DJJAA devices is predicted using the transmission matrix approach. The information about each dimer is extracted by fitting Eq. 220 to the numerically calculated frequency dependence of the reflection coefficient.

Figure 37 shows the results obtained at the flux sweet spot for the three devices presented in Fig. 3.6, using the circuit parameters listed in Tab. 3.2, and assuming an additional stray inductane of $L_\mathrm{s} = 19\,\mathrm{pH}$ per SQUID. The agreement between the linear circuit model and the measured dimer parameters is satisfying, especially given the fact that no frequency dependence of the input port impedance was assumed, and no remote ground model [35].

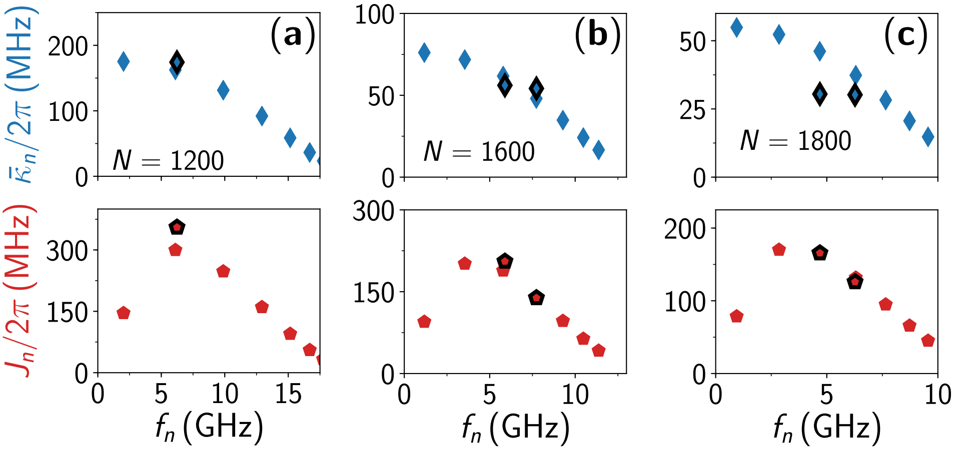

Figure 37: DJJAA: Measurement vs. prediction. The three panels depict the comparison between the measured and the predicted external coupling rates $\bar{\kappa}_n$ (blue diamonds) and dimer detunings J_n (red pentagons) for the three devices A, B, and C shown in Fig. 3.6 **a)** $N = 1200$ **b)** $N = 1600$ **c)** $N = 1800$. The measured values are highlighted by a black fringe. The corresponding circuit parameters are listed in Tab. 3.2, and the additional stray inductance is $L_\mathrm{s} = 19\,\mathrm{pH}$ per SQUID.

G.7 dc field gradients and ac flux noise

The DJJAA sample holder discussed in Sec. G.3 is made of copper and does not provide an efficient shielding against dc and ac external magnetic fields. In this section, two perturbative effects of the external magnetic field created by the environment are discussed: a finite dc gradient along the array, and a global ac field.

Magnetic field gradient:

In particular for the DJJAA devices with a center capacitance interrupting the array, a magnetic field gradient along the array can have a strong effect on the dimerization of the DJJAA modes, as can be seen in Fig. 3.6c. The effect of a magnetic field gradient can be investigated by using a position or node dependent kinetic inductance in the effective circuit model used for the transmission matrix approach (Sec. F.3).

Figure 38 depicts the comparison between the numerically calculated and the measured reflection coefficient for sample C (see Fig. 3.6c). The external flux in the i th SQUID is assumed to follow a quadratic dependence

$$\Phi_{\mathrm{ext,i}} = \Phi_{\mathrm{ext,N}} \left(\frac{i+1}{N}\right)^2 , \tag{225}$$

where $\Phi_{\mathrm{ext,N}} = 0.165\Phi_0$ is the offset field at the position of the N th SQUID as seen from the microwave input port. Although the assumption on the magnetic field gradient does not consider the design of the DJJAA devices in form of meanders, the numerical calculation does recover the main features observed in the measurement, and confirms a finite field gradient as the origin of the misalignment between the modes.

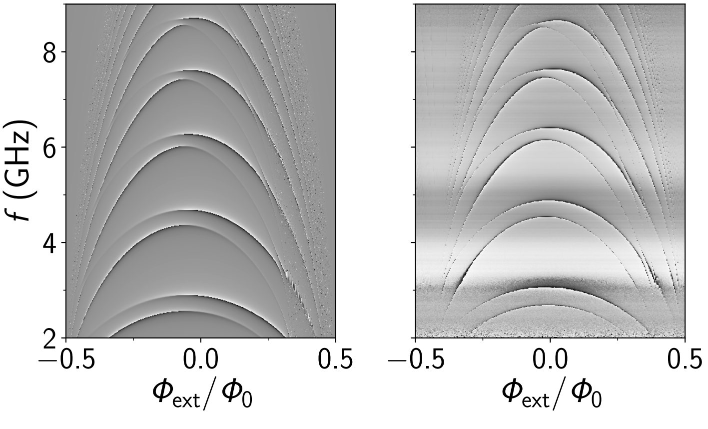

Figure 38: DJJAA: magnetic field gradient. Comparison between the phase $\arg(S_{11})$ of the numerically calculated (left-hand panel) and the measured (right-hand panel) reflection coefficient (see Fig. 3.6c). The calculations are based on the transmission matrix approach discussed in Sec. F.3, and consider a node dependent magnetic field to reflect the presence of a finite magnetic field gradient, together with a critical current asymmetry $m = 1.007$ between the parts of the array to the left and the right of the center capacitance.

Mitigating such detrimental effects is crucial for the operation of an amplifier. For the suppression of out-of-plane magnetic field components, a cylindrical outer Al shield has been build, which is anchored at the base plate of the cryostat.

ac flux noise:

In contrast to a finite magnetic field gradient, which mainly influences the dimerization and limits the achievable gain tunability, a finite alternating magnetic field threading the SQUID loops enhances the noise measured at room temperature. Time variations in the resonance frequencies translate into an fluctuating detuning of the device from the initial point of operation, and as a consequence, the observed power gain becomes a function of time.

While every SQUID is exposed to a local electromagnetic environment, caused by magnetic adsorbates and residuals from the fabrication process, there are magnetic fields which can be considered homogeneous on the length scale of the amplifier. Examples for such global and alternating sources are fluctuations in the bias current applied to the superconducting field coil, and sources residing at distant locations outside the measurement setup like pulse tubes and cellphones.

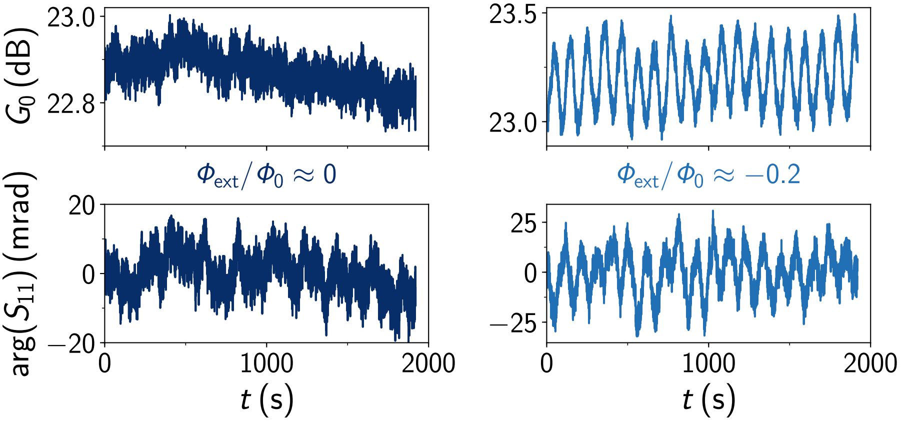

Figure 39: DJJAA: ac flux noise. Maximal power gain G_0 (top panels) and phase of the reflection coefficient $\arg(S_{11})$ (bottom panels) measured with a fixed frequency probe tone as a function of time t. The comparison between the data obtained at the flux sweet spot $\Phi_{\rm ext}/\Phi_0 \approx 0$ (left-hand panels) and the flux bias point $\Phi_{\rm ext}/\Phi_0 \approx -0.2$ (right-hand panels) demonstrates the increase in flux noise due to the increasing flux dependence of the resonance frequency of the amplifier modes. The data was measured with the higher frequency mode of the third dimer 3_+ associated to the sample shown in Fig. 3.8 using an IF bandwidth of 10 Hz.

Figure 39 depicts the long-time stability of the power gain G_0 and the phase of the reflection coefficient measured with a VNA at the flux sweet spot $\Phi_{\mathrm{ext}}/\Phi_0 \approx 0$ and another flux bias point $\Phi_{\mathrm{ext}}/\Phi_0 \approx -0.2$. The IF bandwidth of the VNA was set to 10 Hz during the measurement. At the flux sweet spot, the power gain is stable within $\Delta G = 0.1\,\mathrm{dB}$, while there appears a distinct periodic modulation with period 107 s away from the sweet spot. Besides the increase in noise associated to the increasing susceptibility of the modes to flux noise away from the flux sweet spot, the decrease in bandwidth discussed in Sec. 3.6 further enhances the observed noise.

G.8 Transmon qubit: cryogenic microwave wiring

The microwave wiring of the cryogenic setup — a commercial, dry $^3\mathrm{He}/^4\mathrm{He}$ dilution refridgerator — used for the experiments on the conventional transmon qubit to calibrate the noise performance of the DJJAA (see Sec. 3.8), is shown in Fig. 40. In order to reduce the signal level and the thermal noise seen by the samples, the signal input port and the pump port are equipped with a total of 70 dB of attenuation, from which 60 dB stem from commercial attenuators mounted at different temperature stages of the setup, and 10 dB are attributed to the stainless steel coaxial cables. Notably, not all temperature stages of the commercial cryostat are shown. Furthermore, commercial low-pass filters and custom-made infrared (IR) filters are mounted at the base plate to suppress high frequency noise and irradiation.

The signal is guided to the sample using a commercial, cryogenic circulator. In order to protect the transmons and the readout resonators from the magnetic stray fields, a combination of different outer shieldings surrounds the waveguide sample holder, which is similar to the one shown in Fig. 2.1. Reflected from the readout resonator, the signal was combined with the DJJAA pump tone using a commercial power combiner, which added at least 3 dB attenuation to the signal path. Similar to the qubit sample, the incident and amplified outgoing sample reflected from the DJJAA are separated using a circulator. In the output line, additional filtering and an isolator suppress irradiation from higher temperature stages. The outgoing signal is further amplified at 4 K using a HEMT amplifier, and again at room temperature. The noise temperatures, as certified by the manufacturer, are $T_{\mathrm{N,HEMT}} = 2 - 3\,\mathrm{K}$ and $T_{\mathrm{N,RT}} = 127\,\mathrm{K}$.

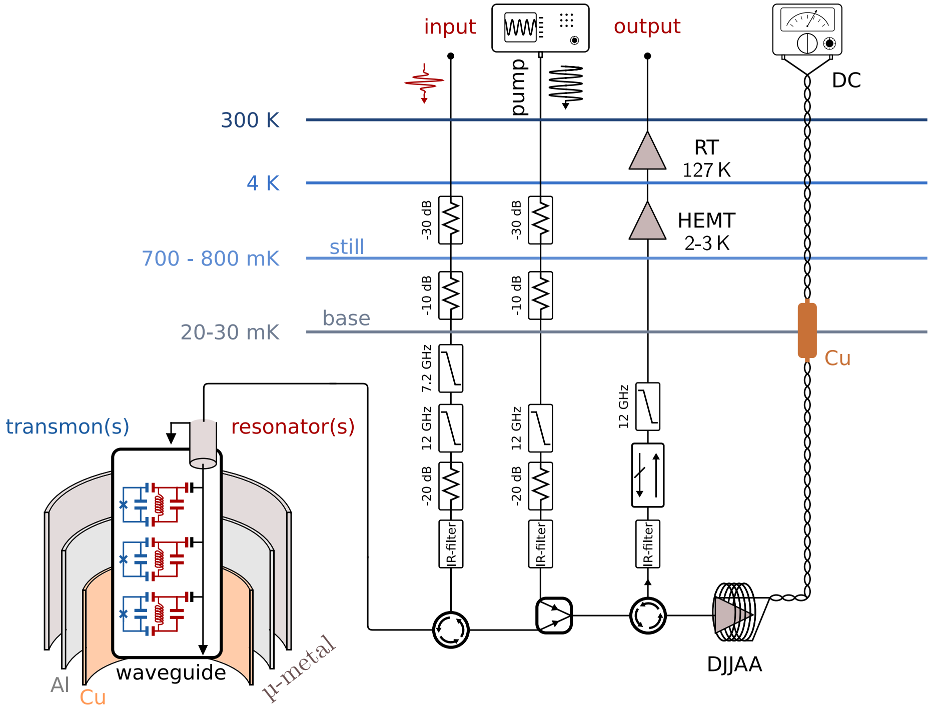

Figure 40: DJJAA: Experimental wiring for the noise performance measurement in Sec. 3.8. The input line and the pump line of the DJJAA are equipped with 60 dB of attenuation in form of commercial attenuators, distributed along the lines at different temperature stages. For thermal isolation of these stages, the microwave wiring in both lines are based on stainless steel coaxial cables, which add another ~ 10 dB of attenuation to each line. In order to filter high frequency noise, two low-pass filters are added to the input line, with an upper cut-off frequency 7.2 GHz. The pump line is only equipped with a single low-pass filter with a cut-off at 12 GHz. The signal is guided to the samples, i.e. three pairs of transmon qubits (blue) coupled to dedicated readout resonators (red) hosted in a waveguide sample holder, using a commercial circulator. As indicated by the open cylinders, the sample holder is surrounded by a combination of three different (magnetic) shieldings: copper (Cu), aluminum (Al), and a μ-metal. The signal reflected from the readout resonator(s) is combined with the DJJAA pump tone using a commercial power combiner, which attenuates the signal by at least 3 dB. The amplified outgoing signal, reflected from the DJJAA, is further amplified by a HEMT amplifier mounted at 4 K and a room-temperature amplifier. An isolator and additional filtering protect the samples from radiation coming from the output line. Depending on the measurement, the input and the output line are either connected to the microwave ports of a commercial VNA (gain measurements) or the ports of a custom-made microwave interferometer (quantum jumps). For the noise visibility measurement, only the output port is connected to a spectrum analyzer. The dc line for the superconducting field coil of the DJJAA contains a copper powder filter.

G.9 Transmon qubit: time-domain setup

The time-domain setup used to measure the quantum jump traces of the transmon qubit (see Fig. 3.14) is a custom-made, heterodyne microwave interferometer similar to the one used in Ref. [26], with its schematic shown in Fig. 41. The I and Q quadratures are determined from the time-varying difference between a signal path $\mathrm{SIG}(t)$, which has been passed through the cryostat and therefore interacted with the sample, and a reference path $\mathrm{REF}(t)$, which has not interacted with the sample:

$$I(t_0) = \int\limits_{t_0 - T_\mathrm{m}/2}^{t_0 + T_\mathrm{m}/2} \mathrm{SIG}(t)\mathrm{REF}(t)\mathrm{d}t \tag{226}$$

$$Q(t_0) = \int\limits_{t_0 - T_\mathrm{m}/2}^{t_0 + T_\mathrm{m}/2} \mathrm{SIG}(t)\mathrm{REF}\left(t + \frac{T}{4}\right)\mathrm{d}t. \tag{227}$$

Here, t_0 is the moment in time in the center of the integration window of length T_m, referred to as the integration time in the main text (see Sec. 3.8), and $T = 16\,\mathrm{ns}$ is the period of the intermediate frequency (IF) 62.5 MHz. Due to the calculation procedure for I and Q, the integration time T_m has to be an integer multiple of $T(1 + 1/4) = 20\,\mathrm{ns}$. Both microwave tones are generated using the channels of a two channel microwave source, and, since both paths are downconverted to the IF using the other channel as the local oscillator (LO), the calculated quadratures I and Q become insensitive to drifts of the individual carrier channels.

The pulse sequences for the readout and the manipulation of the transmon are synthesized by mixing the respective carrier tone with the (rectangular) pulse shape supplied by an arbitrary waveform generator (AWG). Since the process is heterodyne and single-sideband (SSB) mixers are used for the conversion, the carrier frequencies are shifted to higher frequencies by an amount determined by the IF. Both, the readout and the qubit manipulation tone are combined at room temperature. The strength of the tones is controlled by the voltage amplitudes of the AWG and the power of the carrier signal.

The output signal coming from the cryostat is first filtered using a custom-made cavity bandpass filter adjusted to the resonance frequency f_r to filter out the strong DJJAA pump tone applied at $f_\mathrm{p} = 5.509\,\mathrm{GHz}$, the filter function is shown in Fig. 41 in form of the transmission spectrum $|S_{21}|$, and subsequently downconverted to the IF. Several room-temperature amplifiers are used to increase the signal strength to a level well beyond the resolution of the analog-to-digital converter (ADC). The sampling rate of the ADC is 1250 MHz, corresponding to a time resolution of 0.8 ns.

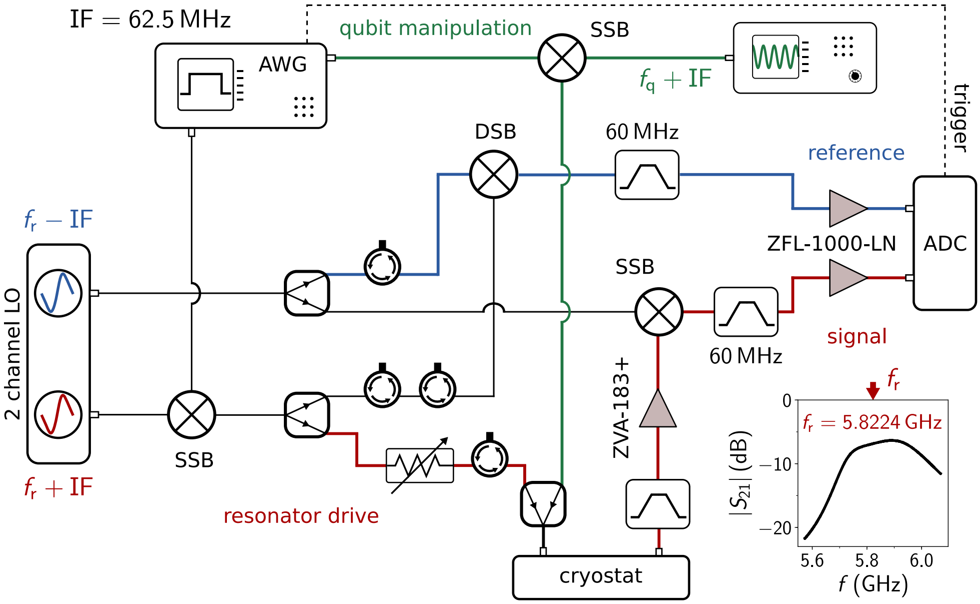

Figure 41: DJJAA: Time-domain setup. Schematic of the microwave interferometer — the time-domain setup — used to decompose the signal of the readout resonator into the I and Q quadratures. At the center of the interferometer are two paths denoted the signal (red) and the reference (blue). For the readout tone of the resonator, the continuous microwave tone of a two channel microwave source (2 channel LO), is mixed with the desired pulse shape synthesized by an arbitrary waveform generator (AWG) using a single-sideband (SSB) mixer. The signal is split into two paths, from which one serves as the local oscillator (LO) of the reference tone, and the other is guided to the fridge. The readout power is roughly adjusted by a step attenuator, and fine-tuned by the voltage amplitude of the waveform. Before the readout signal reaches the microwave input port of the cryostat (see Fig. 40 for microwave wiring), the qubit manipulation drive (green path) is combined with the signal. The signal coming from the cryostat is filtered with a custom-made cavity band-pass filter to remove the DJJAA pump tone applied at $f_p = 5.509\,\mathrm{GHz}$. The transmission spectrum around the signal frequency $f_r = 5.8224\,\mathrm{GHz}$ is shown. For the downconversion of the signal to the intermediate frequency (IF) 62.5 MHz, the second port of the microwave source (2 channel LO) is used. In that way, drifts in the two channels appear in both, the reference and the signal path. Several isolators (circulators with 50 Ω-terminations) are used to reduce unintended crosstalk between both paths.

G.10 Transmon qubit: circuit parameters and energy spectrum

The circuit parameters of the transmon qubit, the charging energy $E_{C,q}$ and the Josephson energy $E_{J,q}$, as well as the coupling rate g to the readout resonator are extracted by comparing the energy spectrum predicted by the full qubit-resonator

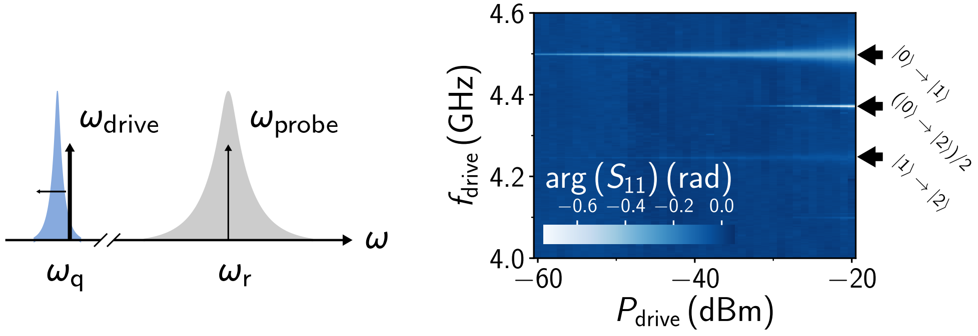

Figure 42: Transmon: spectrum. The transmon spectrum is measured by performing a two-tone spectroscopy. The response of the readout resonator is monitored with a constant and continuous probe tone applied on resonance $\omega_{\mathrm{probe}} = \omega_{\mathrm{r}}$, while a drive tone is applied in vicinity of the fundamental transmon transition frequency ω_{q}. The two Lorentzian curves By sweeping the drive tone frequency ω_{drive} and power P_{drive}, various transitions in the transmon become visible. The measured transmon spectrum is shown in the right-hand panel. At low power, the fundamental transmon frequency appears at $\omega_{\mathrm{q}} = 2\pi \times 4.505\,\mathrm{GHz}$, while a second transition appears at $\omega_2 = 4.244\,\mathrm{GHz}$ when the drive power is increased, corresponding to the transition between the first excited state and the second excited state. This observation is due to a finite population of the excited state, as discussed in Sec. 3.9. From the difference of both transitions, the qubit anharmonicity $\alpha_{\mathrm{q}} = -2\pi \times 256\,\mathrm{MHz}$ is extracted. Additionally, several multi-photon transitions are visible, for instance the $(|0\rangle \rightarrow |2\rangle)/2$ transition.

Hamiltonian expressed in the charge basis for the transmon and the Fock-basis for the readout resonator $|N, n_{\mathrm{r}}\rangle$

$$\begin{aligned}\hat{H} = &\sum_{N=-\infty}^{\infty} \left(4E_{\mathrm{c}}(N - N_{\mathrm{g}})^2 |N\rangle\langle N| - \frac{E_{\mathrm{J}}}{2} |N\rangle\langle N+1| + |N+1\rangle\langle N| \right) + \hbar\omega_{\mathrm{r}} |n_{\mathrm{r}}\rangle\langle n_{\mathrm{r}}| \\ &+ \hbar g \sum_{N=-\infty}^{\infty} N |N\rangle\langle N| \sum_{n_{\mathrm{r}}=0}^{\infty} \sqrt{n_{\mathrm{r}}+1}\, (|n_{\mathrm{r}}+1\rangle\langle n_{\mathrm{r}}| + |n_{\mathrm{r}}\rangle\langle n_{\mathrm{r}}+1|)\,,\end{aligned} \tag{228}$$

with the results obtained from the quantum optics Hamiltonian given in Eq. 1.44 [38]. The qubit parameters entering the quantum optics Hamiltonian are extracted from the energy spectrum of the transmon shown in Fig. 42, yielding the fundamental transmon transition frequency $\omega_{\mathrm{q}} = 2\pi \times 4.505\,\mathrm{GHz}$ and the anharmonicity of the spectrum $\alpha_{\mathrm{q}} = -2\pi \times 256\,\mathrm{MHz}$. The remaining parameters are the resonator frequency $\omega_{\mathrm{r}} = 2\pi \times 5.8224\,\mathrm{GHz}$ (see Fig. 1.11) and the dispersive shift $2\chi_{\mathrm{qr}} = 2\pi \times 480\,\mathrm{kHz}$ (see Fig. 1.11 and Fig. 3.12).

The results obtained by aligning the energy spectra are $E_{\mathrm{J,q}}/h = 12.5\,\mathrm{GHz}$, $E_{\mathrm{c,q}}/h = 225\,\mathrm{MHz}$ $\left(E_{\mathrm{J,q}}/E_{\mathrm{c,q}} \approx 56\right)$ and $g = 2\pi \times 39\,\mathrm{MHz}$, in good agreement with values extracted from finite element simulations of the circuit geometry (charging energy and coupling rate) and the normal-state resistance of the JJ $R_\mathrm{J} = 10.3\,\mathrm{k\Omega}$ measured at room temperature.

G.11 Transmon qubit: coherence

By applying a squared-envelope manipulation pulse of duration t to the transmon on resonance with its fundamental transition frequency $\tilde{f}_\mathrm{q}$, continous Rabi-oscillations between the transmon's ground and first excited state are observed, shown in Fig. 43a (top panel). Using a relatively weak drive strength, the duration of the π-pulse $t_\pi \approx 1.43\,\mu\mathrm{s}$ is calibrated by fitting the data (blue) with a periodic cosine function with exponentially decaying envelope (red).

Energy relaxation measurements were performed by exciting the qubit to its first excited state using the calibrated π-pulse, and gradually increasing the time interval τ between the end of the excitation pulse and the beginnig of the readout pulse. From an exponential fit (red) to the data (blue), shown in Fig. 43a (bottom panel), the energy relaxation time is found to be $T_1 \approx 8.8\,\mu\mathrm{s}$.

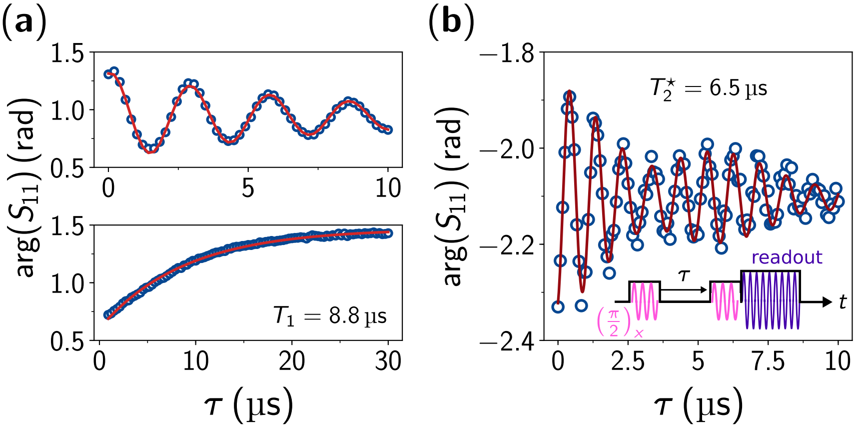

Figure 43: Transmon: quantum coherence. a) Rabi oscillations of the transmon (top panel) and energy relaxation measurement (bottom panel) following a $\pi-$pulse, both encoded in the phase response of the readout resonator. The $\pi-$pulse duration of $1.5\,\mu\mathrm{s}$ corresponds to the first minimum of the measured Rabi oscillations. From the exponential energy decay (red solid line), an energy relaxation time of $T_1 = 8.8\,\mu\mathrm{s}$ is deduced. **b)** Ramsey fringes experiment with the pulse sequence depicted in the lower right-hand corner. Two oscillations were observed with similar frequency $f_\mathrm{R}^1 = 1.03\,\mathrm{MHz}$ and $f_\mathrm{R}^2 = 1.19\,\mathrm{MHz}$, with a characteristic decay time $T_2^* = 6.5\,\mu\mathrm{s}$.

The transmon's coherence time $T_2^* \approx 6.5\,\mu\mathrm{s}$ was extracted from a Ramsey fringes measurement. As shown in Fig. 43b, two superposed oscillations with different frequencies were observed. In the case of two distinct Ramsey frequencies, an extended fit function $\varphi(\tau)$ is used to fit the measured time evolution of the phase of the reflection coefficient.

$$\begin{aligned}\varphi(\tau) = {} & \exp^{-\tau/T_2^*} (A_1 \cos\left[2\pi(f_{\mathrm{R},1}\tau) + \phi_{0,1}\right] \\ & + A_2 \cos\left[2\pi(f_{\mathrm{R},2}\tau) + \phi_{0,2}\right]) + \varphi_0.\end{aligned} \tag{229}$$

Most probably, the two Ramsey frequencies $f_{\mathrm{R},1}$ and $f_{\mathrm{R},2}$ arise from two distinct transmon frequencies, which could be caused by the coupling to mesoscopic system(s) residing in the environment of the transmon. However, the origin remains unknown.

G.12 Transmon qubit: Photon number calibration

The photon number inside the readout resonator $\bar{n}_\mathrm{r}$ of the transmon used for the calculation of the measurement photon number (see Sec. 3.8) was calibrated for a number of voltage amplitudes $\bar{V}_\mathrm{drive}$ set for the readout drive tone at room temperature. Notably, for readout and manipulation performed on the readout resonator and the qubit, square-envelope pulses were used. The integration time of the readout tone is $T_\mathrm{m} = 300\,\mathrm{ns}$, and the pulse duration for a π-pulse is $\tau_\pi = 57\,\mathrm{ns}$.

Figure 44a depicts the calibrated photon number as a function of the squared voltage amplitude, which is proportional to the average drive power $P_\mathrm{drive} \propto \bar{V}^2_\mathrm{drive}$, and increases linearly with the drive power, as expected. The change in the Ramsey frequency f_R and the reduction in coherence time T_2^* with increasing resonator population is illustrated in Fig. 44b for two different drive amplitudes. Notably, the decrease in coherence results from an increasing distribution of the coherent state in the Fock-basis causing measurement-induced dephasing, which is proportional to $\bar{V}_\mathrm{drive}$ [19] (see Sec. 1.1.6). The measured Ramsey fringes are fitted with an exponentially damped cosine

$$\varphi(\tau) = e^{-\tau/T_2^*} A \cos\left[2\pi(f_\mathrm{R}\tau) + \phi_0\right] + \varphi_0. \tag{230}$$

Here τ is the time the qubit state evolves between the $\pi/2$ pulses, T_2^* is the coherence time, A is the oscillation amplitude, f_R is the Ramsey frequency, ϕ_0 is the offset phase of the cosine oscillation and φ_0 is the global offset phase.

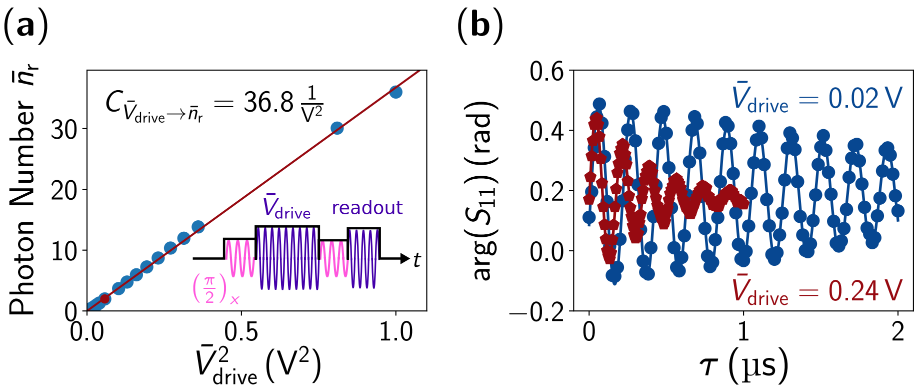

Figure 44: Transmon: photon number calibration a) Photon number calibration of the readout strength proportional to the squared voltage amplitude $\bar{V}^2_{\mathrm{drive}}$ of the readout pulse. The pulse sequence used in the experiment is depicted in the lower right corner. In-between two $(\pi/2)_x$ pulses applied to the transmon (pink), an additional tone was applied to the readout resonator with varying voltage amplitude $\bar{V}_{\mathrm{drive}}$ (purple). After this pulse sequence, the qubit state was inferred from the response of the readout resonator. From the change in frequency f_{R} observed in the Ramsey fringes (see panel b) with respect to the undriven case $f^0_{\mathrm{R}} = |f_{\mathrm{q,drive}} - f_{\mathrm{q}}|$, and using the dispersive shift χ_{qr} [see Fig. 3.12], the photon number $\bar{n}_{\mathrm{r}}$ was calibrated as a function of the applied drive power $P_{\mathrm{drive}} \propto \bar{V}^2_{\mathrm{drive}}$. **b)** Two examples of measured Ramsey fringes with $\bar{V}_{\mathrm{drive}} = 0.02\,\mathrm{V}$ (blue) and $\bar{V}_{\mathrm{drive}} = 0.24\,\mathrm{V}$ (red) visible in the phase response of the readout resonator. Besides the change in the frequency f_{R}, the measured coherence time T_2^* decreases also due to measurement-induced dephasing.

G.13 Fabrication recipe

The DJJAA samples are based on a simple, fast and reproducible positive optical-lithography fabrication, summarized in Tab. 11 and Tab. 12. The design is split into two consecutive fabrication steps, as emphasized in Sec. 3.3, using a dedicated soda lime glass based chrome mask for each step.

Firstly optical resist (S 1805) is spin coated onto a doubly polished sapphire wafer[1] with the coating parameters summarized in Tab. 11. The sapphire wafers are either cleaned in the so-called piranha solution, a mixture of sulfuric acid, water, and hydrogen peroxide, or used directly from the supplier. However, no unambiguous difference has been observed in the quality of the amplifiers. After the resist has dried on a hot plate for 60 s, it is exposed for 4 s with light of wavelength $\lambda = 365\,\mathrm{nm}$ emitted by a 500W Xe lamp. Subsequently, the exposed parts of the resist are dissolved using a $25 - 30\,\mathrm{s}$ bath in a commercial MF 319 developer, followed by a

---

[1] CrysTec

rinse in destilled water. Since the developer contains TMAH, which is a known Al etcher, the development time for the second step does not exceed 30 s.

The pure Al films are deposited in a PLASSYs electron beam shadow evaporator. Typically the transfer chamber (load lock) is prepumped for around $t \approx 1\,\mathrm{h}$ (first step) and $t \approx 3\,\mathrm{h}$ (second step) giving values for the pressure of around $p_{LL} \approx 2 - 5 \times 10^{-7}$ mbar. Before the first aluminum layer is deposited the wafer is cleaned with an oxygen/argon (10 sccm/5 sccm) plasma under a beam voltage 200 V and a beam current 10 mA for 2 : 30 min. Subsequently around 30 nm of aluminum is deposited at 1 nm/s.

For the junction fabrication the intrinsic oxide layer on-top of the first Al layer is removed by an Ar milling process (flow rate: 4.0 sccm, 400 V, 15 mA) for 2 : 30 min before the insulating barrier is grown under controlled conditions, determined by the combination of oxygen pressure and time - the exposure. In order to increase the barrier quality the pressure inside the main chamber is further reduced by Ti gettering ($p_{LL} \approx 5 - 6 \times 10^{-8}$ mbar). The second aluminum layer is slightly thicker (40 nm) to ensure a good contact.

For lift-off, the samples are stored in a preheated ($T = 90\,^{\circ}\mathrm{C}$) NEP bath for a couple of minutes. Especially after the second step, a low power (power not calibrated) ultra sonic bath is used to ensure the lift-off of the metal parts in the SQUID loops. Subsequently, the wafer is rinsed in an acetone and ethanol bath (in this order), before it is finally blown-dry with N_2-gas.

Table 11: Optical-lithography fabrication recipe: Resist application, exposure and development.

Resist application	
resist	S1805 (thickness: 500 nm, positive)
acceleration	500 rpm/s
ramp speed	500 rpm
ramp time	5 s
spin speed	4500 rpm
spin time	60 s
HP temp	115 °C
HP time	60 s

exposure	
mask type	soda lime glas based chrome mask
dose	13 mW/cm^2
wavelength	365 nm
contact mode	hard
time	4 s

Development	
developer	MF-319
time	$20 - 30$ s
rinse	destilled H_2O + N_2 blown-dry

Table 12: Optical-lithography fabrication recipe: Aluminum evaporation.

Aluminum evaporation: layer 1	
cleaning	O_2/Ar
parameters	10 sccm/5 sccm, $U_{\mathrm{beam}} = 200\,\mathrm{V}$, $I_{\mathrm{beam}} = 10\,\mathrm{mA}$
thickness	30 nm
rate	1 nm/s
angle	0 °
lift-off	
solvent	NMP or NEP
time	$5 - 10$ min
temperature	90 °C (preheated)
US-bath	2 × 4 min at lowest power
rinse	acetone + ethanol + N_2 blown-dry
Argon milling and oxidation	
cleaning	Argon milling
parameters	4.0 sccm, $U_{\mathrm{beam}} = 400\,\mathrm{V}$, $I_{\mathrm{beam}} = 10\,\mathrm{mA}$
time	2 : 30 min
partial pressure	10 mbar
time	$2 - 7$ min
Aluminum evaporation: layer 2	
thickness	40 nm
rate	1 nm/s
angle	0 °
lift-off	
solvent	NMP or NEP
time	$5 - 10$ min
temperature	90 °C (preheated)
US-bath	2 × 4 min at lowest power
rinse	acetone + ethanol + N_2 blown-dry

References

1. Amman, M., Ben-Jacob, E. & Mullen, K.: *Charge solitons in 1-D array of mesoscopic tunnel junctions*. Physics Letters A **142**, 431–437 (1989) (cit. on p. 213).
2. Bluhm, D.: *A Deconvolution Method for Switching Current Histograms as a Fast Diagnosis Tool*. PhD thesis (The Graduate School, Stony Brook University: Stony Brook, NY., 2008) (cit. on p. 199).
3. Bohr, N.: *Über die Serienspektra der Elemente*. Zeitschrift für Physik **2**, 423–469 (1920) (cit. on p. 149).
4. Caparelli, E. & Tomasi, D.: *An Analytical Calculation of the Magnetic Field Using the Biot Savart Law*. Revista Brasileira de Ensino de Fisica **23**, 284–288 (2001) (cit. on p. 186).
5. Castellanos-Beltran, M. & Lehnert, K.: *Widely tunable parametric amplifier based on a superconducting quantum interference device array resonator*. Applied Physics Letters **91**, 083509 (2007) (cit. on p. 213).
6. Clerk, A. A., Devoret, M. H., Girvin, S. M., Marquardt, F. & Schoelkopf, R. J.: *Introduction to quantum noise, measurement, and amplification*. Rev. Mod. Phys. **82**, 1155–1208 (2010) (cit. on pp. 155, 177).
7. Cleuziou, J.-P., Wernsdorfer, W., Bouchiat, V., Ondarçuhu, T. & Monthioux, M.: *Carbon nanotube superconducting quantum interference device*. Nature Nanotechnology **1**, 53–59 (2006) (cit. on p. 203).
8. Cohen-Tannoudji, C., Diu, B., Laloe, F. & Dui, B.: *Quantum Mechanics (2 vol. set)* (Wiley-Interscience, 2006) (cit. on p. 158).
9. Cottet, N.: *Energy and information in fluorescence with superconducting circuits*. PhD thesis (PSL Research University, Ecole Normale Superieure, 2018) (cit. on p. 175).
10. Deaver, B. S. & Fairbank, W. M.: *Experimental Evidence for Quantized Flux in Superconducting Cylinders*. Phys. Rev. Lett. **7**, 43–46 (1961) (cit. on p. 204).
11. Delsing, P., Chen, C. D., Haviland, D. B., Harada, Y. & Claeson, T.: *Charge solitons and quantum fluctuations in two-dimensional arrays of small Josephson junctions*. Phys. Rev. B **50**, 3959–3971 (1994) (cit. on p. 213).
12. Dirac, P. A. M.: *The fundamental equations of quantum mechanics*. Proceedings of the Royal Society of London. Series A, Containing Papers of a Mathematical and Physical Character **109**, 642–653 (1925) (cit. on p. 149).
13. Dirac, P. A. M.: *The principles of quantum mechanics* **27** (Oxford university press, 1981) (cit. on p. 149).

14. Doll, R. & Näbauer, M.: *Experimental Proof of Magnetic Flux Quantization in a Superconducting Ring*. Phys. Rev. Lett. **7**, 51–52 (1961) (cit. on p. 204).

15. Eichler, C. & Wallraff, A.: *Controlling the dynamic range of a Josephson parametric amplifier*. EPJ Quantum Technology **1**, 1–19 (2014) (cit. on pp. 155, 170, 171, 174, 213).

16. Erné, S. N., Hahlbohm, H.-D. & Lübbig, H.: *Theory of rf-biased superconducting quantum interference device for nonhysteretic regime*. Journal of Applied Physics **47**, 5440–5442 (1976) (cit. on p. 203).

17. Fazio, R. & van der Zant, H.: *Quantum phase transitions and vortex dynamics in superconducting networks*. Physics Reports **355**, 235–334 (2001) (cit. on pp. 213, 214).

18. Friedrich, F., Winkel, P., Borisov, K., Seeger, H., Sürgers, C., Pop, I. M. & Wernsdorfer, W.: *Onset of phase diffusion in high kinetic inductance granular aluminum micro-SQUIDs*. Superconductor Science and Technology **32**, 125008 (2019) (cit. on p. 204).

19. Gambetta, J., Blais, A., Schuster, D. I., Wallraff, A., Frunzio, L., Majer, J., Devoret, M. H., Girvin, S. M. & Schoelkopf, R. J.: *Qubit-photon interactions in a cavity: Measurement-induced dephasing and number splitting*. Phys. Rev. A **74**, 042318 (2006) (cit. on p. 258).

20. Gao, J.: *The physics of superconducting microwave resonators*. PhD thesis (California Institute of Technology, 2008) (cit. on p. 165).

21. Gardiner, C. W. & Collett, M. J.: *Input and output in damped quantum systems: Quantum stochastic differential equations and the master equation*. Phys. Rev. A **31**, 3761–3774 (1985) (cit. on pp. 155, 158, 177).

22. Girvin, S. M.: *Circuit QED: superconducting qubits coupled to microwave photons* (2011) (cit. on pp. 141, 155, 169).

23. Goto, H.: *Bifurcation-based adiabatic quantum computation with a nonlinear oscillator network*. Scientific Reports **6**, 21686 (2016) (cit. on p. 165).

24. Grabert, H. & Weiss, U.: *Crossover from Thermal Hopping to Quantum Tunneling*. Phys. Rev. Lett. **53**, 1787–1790 (1984) (cit. on p. 197).

25. Granata, C. & Vettoliere, A.: *Nano Superconducting Quantum Interference device: A powerful tool for nanoscale investigations*. Physics Reports **614**. Nano Superconducting Quantum Interference device: a powerful tool for nanoscale investigations, 1–69 (2016) (cit. on p. 211).

26. Grünhaupt, L.: *Granular aluminium superinductors* (KIT Scientific Publishing, 2019) (cit. on p. 254).

27. Grünhaupt, L., von Lüpke, U., Gusenkova, D., Skacel, S. T., Maleeva, N., *et al.*: *An argon ion beam milling process for native AlOx layers enabling coherent superconducting contacts*. Applied Physics Letters **111**, 072601 (2017) (cit. on pp. 184, 185, 191).

28. Haroche, S. & Raimond, J.-M.: *Exploring the quantum: Atoms, Cavities, and Photons* (Oxford university press, 2006) (cit. on p. 160).

29. Hatridge, M., Shankar, S., Mirrahimi, M., Schackert, F., Geerlings, K., *et al.*: *Quantum Back-Action of an Individual Variable-Strength Measurement*. Science **339**, 178–181 (2013) (cit. on p. 203).

30. Haviland, D. B., Andersson, K. & Ã…gren, P.: *Superconducting and Insulating Behavior in One-Dimensional Josephson Junction Arrays*. Journal of Low Temperature Physics **118**, 733–749 (2000) (cit. on p. 213).

31. Hutter, C., Tholén, E. A., Stannigel, K., Lidmar, J. & Haviland, D. B.: *Josephson junction transmission lines as tunable artificial crystals*. Phys. Rev. B **83**, 014511 (2011) (cit. on p. 214).

32. Jaklevic, R. C., Lambe, J., Silver, A. H. & Mercereau, J. E.: *Quantum Interference Effects in Josephson Tunneling*. Phys. Rev. Lett. **12**, 159–160 (1964) (cit. on p. 203).

33. Johansson, J., Nation, P. & Nori, F.: *QuTiP: An open-source Python framework for the dynamics of open quantum systems*. Computer Physics Communications **183**, 1760–1772 (2012) (cit. on p. 177).

34. Johansson, J., Nation, P. & Nori, F.: *QuTiP 2: A Python framework for the dynamics of open quantum systems*. Computer Physics Communications **184**, 1234–1240 (2013) (cit. on p. 177).

35. Krupko, Y., Nguyen, V. D., Weißl, T., Dumur, É., Puertas, J., *et al.*: *Kerr nonlinearity in a superconducting Josephson metamaterial*. Phys. Rev. B **98**, 094516 (2018) (cit. on pp. 217, 249).

36. Kurkijärvi, J.: *Intrinsic Fluctuations in a Superconducting Ring Closed with a Josephson Junction*. Phys. Rev. B **6**, 832–835 (1972) (cit. on p. 198).

37. Lecocq, F., Pop, I. M., Peng, Z., Matei, I., Crozes, T., Fournier, T., Naud, C., Guichard, W. & Buisson, O.: *Junction fabrication by shadow evaporation without a suspended bridge*. Nanotechnology **22**, 315302 (2011) (cit. on p. 190).

38. Lescanne, R., Verney, L., Ficheux, Q., Devoret, M. H., Huard, B., Mirrahimi, M. & Leghtas, Z.: *Escape of a Driven Quantum Josephson Circuit into Unconfined States*. Phys. Rev. Applied **11**, 014030 (2019) (cit. on p. 256).

39. Lindblad, G.: *On the generators of quantum dynamical semigroups*. Communications in Mathematical Physics **48**, 119–130 (1976) (cit. on p. 178).

40. Liu, G., Chien, T.-C., Cao, X., Lanes, O., Alpern, E., Pekker, D. & Hatridge, M.: *Josephson parametric converter saturation and higher order effects*. Applied Physics Letters **111**, 202603 (2017) (cit. on p. 173).
41. Manucharyan, V. E., Boaknin, E., Metcalfe, M., Vijay, R., Siddiqi, I. & Devoret, M.: *Microwave bifurcation of a Josephson junction: Embedding-circuit requirements*. Phys. Rev. B **76**, 014524 (2007) (cit. on pp. 230, 231).
42. Manucharyan, V. E., Koch, J., Glazman, L. I. & Devoret, M. H.: *Fluxonium: Single Cooper-Pair Circuit Free of Charge Offsets*. Science **326**, 113–116 (2009) (cit. on p. 213).
43. Martinis, J. M., Devoret, M. H. & Clarke, J.: *Energy-Level Quantization in the Zero-Voltage State of a Current-Biased Josephson Junction*. Phys. Rev. Lett. **55**, 1543–1546 (1985) (cit. on p. 197).
44. Martinis, J. M., Devoret, M. H. & Clarke, J.: *Experimental tests for the quantum behavior of a macroscopic degree of freedom: The phase difference across a Josephson junction*. Phys. Rev. B **35**, 4682–4698 (1987) (cit. on pp. 196, 197).
45. Masluk, N. A., Pop, I. M., Kamal, A., Minev, Z. K. & Devoret, M. H.: *Microwave Characterization of Josephson Junction Arrays: Implementing a Low Loss Superinductance*. Phys. Rev. Lett. **109**, 137002 (2012) (cit. on p. 213).
46. Nigg, S. E., Paik, H., Vlastakis, B., Kirchmair, G., Shankar, S., Frunzio, L., Devoret, M. H., Schoelkopf, R. J. & Girvin, S. M.: *Black-Box Superconducting Circuit Quantization*. Phys. Rev. Lett. **108**, 240502 (2012) (cit. on p. 141).
47. Paul, C.: *Analysis of Multiconductor Transmission Lines* `https://books.google.de/books?id=6hpoQgAACAAJ` (Wiley, 1994) (cit. on p. 240).
48. Planat, L., Dassonneville, R., Martınez, J. P., Foroughi, F., Buisson, O., Hasch-Guichard, W., Naud, C., Vijay, R., Murch, K. & Roch, N.: *Understanding the Saturation Power of Josephson Parametric Amplifiers Made from SQUID Arrays*. Phys. Rev. Applied **11**, 034014 (2019) (cit. on p. 174).
49. Planat, L., Ranadive, A., Dassonneville, R., Martınez, J. P., Léger, S., Naud, C., Buisson, O., Hasch-Guichard, W., Basko, D. M. & Roch, N.: *A photonic crystal Josephson traveling wave parametric amplifier*. arXiv (2019) (cit. on p. 214).
50. Pop, I. M., Protopopov, I., Lecocq, F., Peng, Z., Pannetier, B., Buisson, O. & Guichard, W.: *Measurement of the effect of quantum phase slips in a Josephson junction chain*. Nature Physics **6**, 589–592 (2010) (cit. on p. 213).
51. Pozar, D.: *Microwave Engineering, 4th Edition* (Wiley, 2011) (cit. on pp. 165, 225, 226).
52. Puertas Martınez, J., Léger, S., Gheeraert, N., Dassonneville, R., Planat, L., *et al.: A tunable Josephson platform to explore many-body quantum optics in circuit-QED*. npj Quantum Information **5**, 19 (2019) (cit. on p. 213).

53. Richer, S., Maleeva, N., Skacel, S. T., Pop, I. M. & DiVincenzo, D.: *Inductively shunted transmon qubit with tunable transverse and longitudinal coupling*. Phys. Rev. B **96**, 174520 (2017) (cit. on p. 183).

54. Roy, A. & Devoret, M.: *Quantum-limited parametric amplification with Josephson circuits in the regime of pump depletion*. Phys. Rev. B **98**, 045405 (2018) (cit. on p. 173).

55. Silver, A. H. & Zimmerman, J. E.: *Quantum States and Transitions in Weakly Connected Superconducting Rings*. Phys. Rev. **157**, 317–341 (1967) (cit. on p. 203).

56. Sivak, V. V., Shankar, S., Liu, G., Aumentado, J. & Devoret, M. H.: *Josephson Array-Mode Parametric Amplifier*. Phys. Rev. Applied **13**, 024014 (2020) (cit. on p. 224).

57. *Table-top dilution cryostat: Sionludi*. Néel Highlights 2012 - *Table-top dilution cryostat: Sionludi*, 4. `https://neel.cnrs.fr/IMG/pdf/Table-top_dilution.pdf` (2012) (cit. on p. 189).

58. Takahide, Y., Miyazaki, H. & Ootuka, Y.: *Superconductor-insulator crossover in Josephson junction arrays due to reduction from two to one dimension*. Phys. Rev. B **73**, 224503 (2006) (cit. on p. 213).

59. Tesche, C. D. & Clarke, J.: *dc SQUID: Noise and optimization*. Journal of Low Temperature Physics **29**, 301–331 (1977) (cit. on pp. 203, 210).

60. Tinkham, M.: *Introduction to Superconductivity* Second Edition (Dover Publications, 2004) (cit. on pp. 200, 213, 237).

61. Vool, U.: *Engineering Synthetic Quantum Operations*. PhD thesis (Yale University, 2017) (cit. on p. 155).

62. Vool, U. & Devoret, M.: *Introduction to quantum electromagnetic circuits*. International Journal of Circuit Theory and Applications **45**, 897–934 (2017) (cit. on pp. 141, 142, 144, 150).

63. Wallraff, A., Lukashenko, A., Coqui, C., Kemp, A., Duty, T. & Ustinov, A. V.: *Switching current measurements of large area Josephson tunnel junctions*. Review of Scientific Instruments **74**, 3740–3748 (2003) (cit. on pp. 197, 199).

64. Weißl, T., Küng, B., Dumur, E., Feofanov, A. K., Matei, I., Naud, C., Buisson, O., Hekking, F. W. J. & Guichard, W.: *Kerr coefficients of plasma resonances in Josephson junction chains*. Phys. Rev. B **92**, 104508 (2015) (cit. on pp. 218, 222).

65. Winkel, P., Borisov, K., Gruenhaupt, L., Rieger, D., Spiecker, M., Valenti, F., Ustinov, A. V., Wernsdorfer, W. & Pop, I. M.: *Implementation of a transmon qubit using superconducting granular aluminum*. arXiv (2019) (cit. on pp. 175, 183, 184).

66. Winkel, P., Takmakov, I., Rieger, D., Planat, L., Hasch-Guichard, W., *et al.: Nondegenerate Parametric Amplifiers Based on Dispersion-Engineered Josephson-Junction Arrays*. Phys. Rev. Applied **13**, 024015 (2020) (cit. on p. 213).
67. You, X., Sauls, J. A. & Koch, J.: *Circuit quantization in the presence of time-dependent external flux*. Phys. Rev. B **99**, 174512 (2019) (cit. on p. 149).
68. Yurke, B. & Buks, E.: *Performance of cavity-parametric amplifiers, emplyoing Kerr nonlinearities, in the presence of two-photon-loss*. J Lightwave Technol **24** (2006) (cit. on pp. 157, 213).

Acknowledgements

When I started with my master program in Alexey Ustinov's group under the supervision of Martin Weides, suddenly I found myself exposed to a group of extraordinary individuals, both highly talented and brimful of life. Although I also learned about the obstacles and difficulties of an experimental physicist, looking back at this time I will always be grateful for the opportunity you, Alexey and Martin, gave me.

It was during an ordinary lunch break when I first met Ioan, and like everyone else in the group, I was deeply impressed by his enthusiasm and the new scientific perspective he brought with him from Yale after he had eventually settled down in Karlsruhe in 2015. Hence, I felt honored when he asked me if I would be interested in a PhD project under shared supervision between him and Wolfgang, and accepting this offer really turned out to be an excellent choice. During the last years, we spent uncountable hours discussing in your office, in the lab, or even during a night I had to spent in the hospital involuntarily. You've been an excellent teacher and your enthusiasm for physics is highly contagious. I will always be thankful for your support, the inspiring atmosphere you created in the black forest quantum group, and the effort you made in helping us build our personality. Even before I started working with you, you spent several days preparing me for the personal interview with Wolfgang in Grenoble, and looking back at the first version of my talk, you started from nothing as Max Zanner would phrase it.

When I first met Wolfgang, I was a bit nervous because I couldn't really anticipate what kind of person I should expect. The only information I had was his almost ridiculously high publication record and the rumors about his work ethic, but to my surprise, I met a kind person who showed true interest in me, and I couldn't have felt more welcome. Of course, I was also impressed by the ceremony we attended, because by chance my application fell on the same date as what was called the "Wolfgang day". Meanwhile, I'm not surprised when Wolfgang is awarded with another price, not only because it happened quite frequently over the last years, but also because I was able to witness his dedication for more than three years, and I don't know a harder working person. One of my favorite personal anecdotes is going back to the first year of my PhD, I was working late on a Saturday night around 10 pm, and I saw light in your office, so I decided to "quickly" knock at your door and impress you with my own dedication. At the end, I left your office at 1 am after a long discussion about my project, and of course, you didn't seem to be particularly impressed, because science is your life, and there is no bad timing discussing about it. I'm very grateful for the opportunity you gave me, the small and big tricks you showed me, and the inspiring "let's just do it" spirit you're setting an example of every single day. How many students can consider themselves fortunate to get hands-on advice and support from their supervisors basically on a daily basis.

Moreover, I would like to express my gratitude to Nico Roch for his help and guidance in the amplifier project. Whenever we meet you have a smile on your face and I'm very proud that I was able to work with you. Also, I would like to thank Gerhard Kirchmair for becoming my second reviewer, and for the time and effort you are investing in my PhD defense.

I know that there are various standard formulations of expressing gratitude, which are usually alternated to avoid repetition. However, I don't really like this alternation, since it feels like an unnecessary focus on the figure of speech, distracting from the deep appreciation I would like to convey. Although every sentence starts with me as the subject, this section is dedicated to all the amazing people I met during the last years in the wonderful world of physics.

I would like to thank my colleague and friend Lukas Grünhaupt. We had our desks side by side during our master program, and from the beginning I felt a deep connection between us. You are an excellent scientist and probably one of the best organizers I know personally. Even though we are of the same age, you have what German teens nowadays would call a "boss aura", and I'm absolutely convinced that you will become a fantastic principle investigator sooner or later. I will carry this time in my heart, and I will always remember you as a true fighter. Definitely, I would have quit playing ping-pong in case I would have lost twenty games in a row. Chapeau!

I would like to thank Jochen Braumüller. I still remember my first cool down in the majestic silver fridge, when we closed the last shield well beyond midnight on a Saturday, which we then celebrated even longer. We shared many hotel rooms and even a bow cabin, and if my eyes are red it could be because of tears of joy filling my eyes, or because of your socks in my pillow. You have the passion and skill set to become an excellent scientist, which you combine with an infectiously positive perspective on life.

I would like to thank Dennis Rieger for being the best scientific companion I could have dreamed of. I'm still amazed how talented you are and I keep telling friends, if I will ever be in the position in which I can hire any person I know, it would be

you. But much more likely, you will be my supervisor at some point. The amplifier project wouldn't have been such a success without you, and I'm truly impressed by your enthusiasm about unsolved problems of any kind.

I would like to thank Kiril Borisov, for creating a warm atmosphere in our office, and for being a real role model. You are an exceptional person and your work ethic is extraordinary. Although you are one of the hardest working colleagues I encountered during my time at KIT, I don't remember a single day you were in a particular bad mood, or didn't take the time to help me out. I wish you the best for your new stage of life, you absolutely deserve it.

I would like to thank Felix Friedrich for being brave enough to risk a master's thesis under my supervision. We had some fun times, and the switching current measurements wouldn't have had happened without you.

I would like to thank Natasha Maleeva for being the good soul of the black forest quantum group for two wonderful, but still far too short years. Your help, especially at the beginning of my PhD project, was very important to me. You are one of the nicest persons I know, and I will always remember you with a smile on your face, and a smile on mine.

I would like to thank Martin Spiecker, for being such a brilliant mind. Whenever I had a question, I knew you would be the ideal person to discuss with about it, and you never let me down. We had some fun times in front of a whiteboard, and I will always remember you not only as a truly gifted person, but also as a humble person, a person that lives science in a way I'm not able to.

I would like to thank Daria Gusenkova for being the warm and free person you are. I enjoyed accompanying you during the last years, and seeing you grow as a person and a scientist.Let me express my appreciation by quoting my favorite message "Your life is a joke" imprinted on one of your t-shirts, which would have been a considerably more correct statement without you.

I would like to thank Francesco Valenti for being the free Italian spirit you are. I was able to learn a lot from you and I was inspired by your graphical skill set.

I would like to thank Simon Günzler for his excellent Bachelor's thesis. I truly appreciated your motivation and desire to learn, and I'm more than happy to see you now working with Dennis.

I would like to thank Ivan Takmakov. I learned a lot from you about parametric amplifiers, and I'm very happy with the work we did.

I would like to thank all my colleagues from the Nanospin group, Sasmitha, Marcel, Philip, Aljoscha, Gheorghe, Tino, Luca, Markus, Julian, Daniel, Rainer, Thomas, Michael, Moritz, Richard, Jasmin, Markus, Peter, Ioannis, Lukas, and Hannes. It's been an amazing time with all of you. The only thing I regret is that I was not able to join you for a climbing session. But maybe it was in your best interest, some things cannot be unseen.

I would like to thank Andre Schneider for being a helping hand in uncountable situations, especially during my master's thesis. Without you, maybe my master's thesis wouldn't be printed until today.

I would like to thank Nico Voss, a specialist in transport measurements and painting alike.

I would like to thank Marco Pfirrmann. Thank you Markus.

I would like to thank Steffen Schlör, a partner in crime, with technical abilities beyond my wildest dreams.

I would like to thank Jan Brehm for being the open minded person and conversational partner you are. The liberal view you have on our society was truly inspiring, you definitely broadened my horizon.

I would like to thank Hannes Rotzinger, Jürgen Lisenfeld and Sascha Lukashenko for their support, and for always having an open door to my questions.

I would like to thank Christoph Sürgers for introducing me to experimental solid state physics during my bachelor's thesis, for being an enthusiastic singer, and for being the universal weapon of the Physikalisches Institut.

I would like to thank the whole clean room staff in general for their help and support, and in particular Lucas Radke, Silvia Diewald, and Aina Quintilla, as well as the lithography team located at campus north, Lothar Hahn, Andreas Bacher, and Marie-Kristin Gamer.

I would like to thank the mechanical workshop, and in particular Michael Meyer for the many hours we spent in front of your computer designing my sample holder, and I would like to thank the administration, in particular Steffi Baatz, Claudia Alaya, and Lars Behrens.

I would like to thank former colleagues of the black forest quantum group, Fabio , Alex, Thibeau, Marc, and Julian, and some colleagues from the fluxon group. Thank you Tim, Max, Konrad, Yannick, and Micha.

I would like to thank Max Zanner for always being an optimist. Life and science can be both tough, but people like you make it easier.

I would like to thank Sebastian Skacel for igniting my interest in superconducting quantum circuits during a physical practice. Besides your scientific impact on my life, you also totally changed my perspective on porridge. Maybe it was related to the Croatian nuts, but I can tell you, I rarely had a better porridge in my life. Nevertheless, I still think that 20 for a package of nuts is crazily expensive.

I would like to thank Alex Stehli for being a great companion and discussion partner about all sorts of topics. During my time at KIT, I only met a few people I consider comparably in tune with me than we are. My hope is, that you once will truly understand and appreciate how smart you are.

I would like to thank Alex Bilmes, my first Uzbek friend, and I can tell you, that you raised the bar really high. However, I would like to take this opportunity to ask you one last time for the plov recipe. I will miss your honey, and I will miss all the small pranks.

There are a few other people I mostly interacted with during my master, but which are not forgotten. Thank you Charles, Gleb and Julius.

Christina, you are the true love of my life.

Finally, I would like to thank my family, my Mum and Dad, and my sister. Without your love and support, I couldn’t have become the person I am today.

Karlsruhe, July 2020 Patrick Winkel